Genetic Risk Variants Contributing to Arterial Calcification

Fariborz Soheili

A thesis submitted to the University of Ottawa in partial fulfillment of the requirements for the

Doctorate in Philosophy degree in Biochemistry

Department of Biochemistry, Microbiology and Immunology

Faculty of Medicine

University of Ottawa

A**bstract**

Genetic Risk Variants Contributing to Arterial Calcification

Background: Arterial calcification, characterized by the accumulation of calcium minerals in the arterial wall, is a complex process that is influenced by genetic and molecular factors. This study explores how the 9p21.3 genetic risk variants interact with statherin (STATH), matrix GLA protein (MGP), and the bisphosphonate drug alendronate to affect arterial calcification.

Results: Microarray gene expression profiling of human aortic smooth muscle cells (SMCs) revealed that *STATH* expression was silenced in carriers homozygous for 9p21.3 risk variants. STATH, like MGP, is a hydroxyapatite-binding protein produced by human SMCs that blocks bone morphogenetic protein 4 (BMP4)-dependent signaling, promotes the chondrogenic/osteogenic differentiation, and prevents SMC calcification. In mice lacking MGP (*Mgp*KO), severe arterial calcification leads to death through aortic rupture. However, the expression of human statherin in the SMCs of *Mgp*-null mice rescued the arterial calcification phenotype. To further investigate the role of MGP and potential treatments, alendronate was tested in mice lacking Mgp (*Mgp*KO mice). Unexpectedly, although alendronate treatment improved dental malocclusion, it also worsened calcification and decreased the number of CD68-positive macrophages in the arterial wall. A single dose of alendronate increased the aberrant expression of the chondrogenic/osteogenic factor *Runx2* in SMCs of the aorta of *Mgp*KO mice and alendronate treatment increased calcium endo/lysosomal accumulation in the cultured macrophages.

In mouse models, warfarin rapidly induces significant arterial calcification by inhibiting the vitamin K cycle, which prevents the γ-carboxylation of MGP, rendering it inactive. Humans with *MGP* mutations (Keutel syndrome) show a more variable and milder calcification phenotype than do mice. This difference is partially attributed to the

expression of statherin, a hydroxyapatite-binding protein absents in mice but present in human SMCs. Statherin compensates for the loss of MGP in humans and prevents severe arterial calcifications. The 9p21.3 genetic risk variants suppress statherin expression through ALU interaction, which blocks bone morphogenic protein 4 (BMP4)-dependent signaling and prevents calcification in human SMCs, contributing to the variability in arterial calcification observed in individuals with these risk alleles. The paradoxical effects of alendronate in worsening arterial calcification in *Mgp*KO mice suggest that functional MGP is necessary to prevent soft tissue calcification. These findings highlight the complex interplay between genetics, protein expression, and pharmacological interventions, offering new targets for reducing calcification in susceptible individuals.

Contributions and Copy Right

All experimental tests presented in this thesis were conducted by me, a PhD student, directly involved in these projects under the supervision of, Erin Mulvihill and Niloufar Heydarikhorneh, who served as research assistants and lab technicians in Dr. Stewart's lab. Dr. Benjamin Rotestein performed the CT imaging, and Emily Hoddinott conducted the image analysis. Naif A. M. Almontashiri and Ragnar O. Vilmundarson carried out the primary analysis of the microarray data. Additionally, I authored this thesis under the supervision of Dr. Erin Mulvihill, my supervisor. Therefore, any third-party use of information extracted from this thesis, or any derived papers is prohibited without my explicit permission and must comply with applicable laws. This project was supported by operating grants from the Canadian Institutes of Health Research (Alex Stewart Grant: 497628, 376503).

Acknowledgments

I would like to express my deepest gratitude to my supervisor, Dr. Erin Mulvihill, for her exceptional mentorship, unwavering support, and invaluable guidance throughout my research journey. Her compassionate mentorship extended beyond the laboratory, offering hope and encouragement to both me and my family.

I am grateful to Dr. Alex Stewart, who served as my former supervisor and provided tremendous support during my research. I would also like to extend my appreciation to Drs. Erin Mulvihill, Kyoung-Han Kim, and Mireille Ouimet for their invaluable guidance and support during my tenure as a member of the TAC committee. Their expertise and guidance have been crucial in shaping my research and guiding me towards success.

Furthermore, I would like to express my heartfelt thanks to professional professor from other universities (following list) and my lab mates Ragnar, Niloufar, An, and My best friends Natasha Trzaskalski, Nadya. Morrow. They have been instrumental in helping me navigate challenging times and providing me with the necessary emotional support throughout my academic journey.

Beyond all the academic and professional support, I have received, some deserve more than gratitude and respect for my parents. Their unwavering support, prayers, and infinite love have not only sustained me throughout this journey but have also played a significant role in my success. I am deeply indebted to them for their sacrifices and unwavering faith.

Finally, I would like to express my deepest appreciation to my beloved wife Niloufar. Her unwavering help and generous emotional support have made my success tangible. Her unwavering belief in me has been instrumental in pushing me towards my goals. I am immensely grateful for her presence in my life. Without her, this achievement would have been impossible. Although my daughter, Emma, had no idea what I am doing, her presence in my life made me a different, stronger, and patient man.

Finally, I would like to dedicate this dissertation to my wife and parents. Although they are not physically present to witness this moment, their absence is felt deeply. I miss them dearly, and this achievement is dedicated to their enduring love and support.

Name	University	Role
Erin Mulvihill	University of Ottawa Heart Institute	Supervisor
Alexandre Stewart	University of Ottawa Heart Institute	Former Supervisor
Kyoung-Han Kim	University of Ottawa Heart Institute	Thesis Advisor committee Member
Mireille Ouimet	University of Ottawa Heart Institute	Thesis Advisor committee Member
Nadine Wiper-Bergeron	University of Ottawa, Vice-Dean	Professionalism committee
Emilio I. Alarcon	University of Ottawa Heart Institute Director of the Biochemistry graduate program	Professionalism committee
Benjamin Rotstein	University of Ottawa Heart Institute	CT imaging
Niloufar Heydari	University of Ottawa Heart Institute	Experimental test including histology and mice handling and tissue culture
Carol A Heckman	Bowling Green State University, Ohio, USA.	The pXJ -40 primary sequencing
Siu-Pok Yee	Center for Mouse Genome Modification, University of Connecticut, Connecticut, USA	Generation Statherin transgenic mice
Karim Rahimi	Harvard Medical School, Blavatnik Institute of Genetics, Boston, USA	Gene cloning, CRISPR technology
Boris Skryabin	Transgenic Animal and Genetic Engineering Models, University of Münster, Germany	SM22-Cre transgenic mice
Michael Gotthardt	Max Delbrück Center for Molecular Medicine (MDC), Berlin, Germany	SM22-Cre transgenic mice
Roland H. Wenger	University of Zurich, Switzerland	Cre-mediated recombination
Ali Shariati	University of California, Santa Cruz, California, USA	Gene cloning, Gibson recombination
Heather Wilson	Vaccine and Infectious Disease Organization (VIDO), Saskatchewan, Canada	Modeling
Zahed Khatooni	Vaccine and Infectious Disease Organization (VIDO), Saskatchewan, Canada	Modeling

Table of Contents

List of original publications/manuscripts

1) **Fariborz Soheili**, Niloufar Heydarikhorneh, Emily L. Hoddinott, Benjamin H. Rotstein, Alexandre F. R. Stewart. Alendronate improves dental malocclusion but worsens arterial calcification in Mgp-null mice by modulating macrophage hydroxyapatite uptake into lysosomes. (Manuscript in review).

2) **Fariborz Soheili**, Niloufar Heydarikhorneh, Ragnar O. Vilmundarson, Alexandre F. R. Stewart. 9p21.3 variants drive coronary calcification by suppressing statherin expression (Manuscript in review).

3) **Fariborz Soheili**, Niloufar Heydarikhorneh, Zahra Jalili, Ragnar Vilmundarson, Samira Foladi, Fardin Fathi, Asrin Rashidi, Sona Zare, Alexandre F. R. Stewart. Structural and Clinical Analysis of Novel Tbx5 Mutations in Kurdish Patients with Isolated Cardiac Defects (Manuscript in review).

4) Ragnar Vilmundarson, Niloufar Heydarikhorneh, An Duong, Ho T, Keyhanian K, **Fariborz Soheili**, Chen HH, Alexandre F. I. Stewart. Savior Siblings Might Rescue Fetal Lethality But Not Adult Lymphoma in Irf2bp2- Null Mice. Frontiers in Immunology. 2022,4; 13:868053.

5) Ragnar Vilmundarson, An Duong, **Fariborz Soheili**, Chen Hsiao-Huei, Stewart Alexandre. IRF2BP2 3′ UTR polymorphism increases Coronary Artery Calcification in Men, Frontiers in Cardiovascular Medicine. 2021:1423. 3.

6) Asrin Rashidi, Ernst-Martin Füchtbauer, Zakaria Vahabzadeh, Farzad Soleimani, Karim Rahimi, Bahram Nikkhoo, Shohreh Fakhari, Mohammad Bagher Khadem Erfan, Asaad Azarnezhad, Arash Pooladi, **Fariborz Soheili**, Fardin Fathi, CRISPR/Cas9-mediated knockout of DYRK1B in triple negative breast cancer cells: implications for cell proliferation, apoptosis, and therapeutic sensitivity, Biochemical Engineering Journal, 2024, 213 2.

Abbreviation

ABCC6	ATP Binding Cassette Subfamily C Member 6
ACDC	Arterial Calcification due to CD73 Deficiency
ADAMTS7	A Disintegrin and Metalloproteinase with Thrombospondin Motifs 7
ADK	Adenosine Kinase
ALN	Alendronate
ALP	Alkaline Phosphatase
ALPL	alkaline phosphatase
ANK	Ankylosis
ANRIL	Antisense Noncoding RNA at the Ink4 Locus
AoSMCs	Aortic Smooth Muscle Cells
ARID5B,	AT-Rich Interaction Domain 5B
ARSE	Arylsulfatase
ASARM	Acidic Serine- and Aspartate-Rich Motif
BGLAP	bone gamma-carboxyglutamate protein
Bis	Bisphosphonate
BMDMs	Bone Marrow-Derived Macrophages
BMP2/4	Bone Marrow Protein 2/4
BS	Bone Sialoprotein
BSP	Bone Sialoprotein

CAC	Coronary Artery Calcification
CARDIoGRAM	Coronary ARtery DIsease Genome-Wide Replication And Meta-Analysis
CD39	Cluster of Differentiation 39
CDKN2A	Cyclin Dependent Kinase Inhibitors 2A
CDKN2B	Cyclin Dependent Kinase Inhibitors 2B
CDKs:	Cyclin- Dependent Kinases
cMGP	Carboxylated MGP
CNN1	contractile proteins like calponin (CNN1)
COL1A1	Collagen type I
CSN1S2	Casein α-S2
CT	Computed Tomography
DISH	Diffuse Idiopathic Skeletal Hyperostosis
dp-cMGP	Dephosphorylated Carboxylated
dp-ucMGP	Dephosphorylated Uncarboxylated
ECM:	Extra Cellular Matrix
ENPP1	Ectonucleotide Pyrophosphatase/Phosphodiesterase
ENT1	Equilibrative Nucleoside Transporter 1
ERK,	Extracellular signal-Regulated Kinase
FGF	Fibroblast Growth Factor
FIBGC	Familial Idiopathic Basal Ganglia Calcification
GACI	Generalized Arterial Calcification of Infancy

GAPDH:	Glyceraldehyde-3- Phosphate Dehydrogenase
GGCX	Gamma Glutamyl Carboxylase
GWASs	Genome-Wide Association Studies
HA	Hydroxyapatite
HA-BP	Hydroxyapatite Binding Proteins
HAoSMCs	Human Aortic Smooth Muscle Cells
HNR	Homozygous for the non-risk
HPP	Hypophosphatemia
HR	Homozygous for the Risk
HTN	Histatins
IGFBP3	Insulin-like Growth Factor Binding Protein 3
KH2	vitamin K hydroquinone
LPA	Lipoprotein(a)
MGP	Matrix Gla Protein
MAPK	Mitogen-Activated Protein Kinase
MMP16	Matrix Metalloproteinase 16A
NT5E/CD73	Ecto-5'-Nucleotidase/ Cluster of Differentiation,73
OPCs	Osteochondrogenic progenitor cells
OPN	Osteopontin
PHACTR1	Phosphatase and Actin Regulator 1
PI3K/AKT	Phosphatidylinositol 3-Kinase/Protein Kinase B
Ppi	Pyrophosphate

PRC1 and PRC2	Polycomb Repressor Complex 1 and 2
PXE	Pseudo Xanthoma Elasticum
RGD motif	Arginine-Glycine-Aspartic acid motif
RUNX2	Runt-related Transcription Factor 2
SBS	STAU1-Binding Sites
SCPP	Secretory Calcium-binding Phosphoprotein
SMD	Staufen1 mRNA Decay
SPARC	Secreted Protein Acidic and Rich in Cysteine, osteocalcin
SPARCL	SPARC-like protein
SPP1	Sialophospho Protein
STATH	Statherin
STAU1	Staufen1
TGFBR	TGFβ Receptor
TGFβ	Transforming Growth Factor Beta
TNAP	Tissue-nonspecific alkaline phosphatase
UTR	Untranslated Region
VKOR	Vitamin K Epoxide Reductase (VKOR)
VSMCs	Vascular Smooth Muscle Cells

List of Figures

List of Tables

Main findings Summary

Alendronate Treatment in *Mgp*KO Mice

Dental malocclusion improved but arterial calcification worsened.

Reduced CD68-positive macrophages in arterial walls.

Increased Runx2 Expression in Aortic muscle cells.

Promotes calcium accumulation in macrophage lysosomes.

Role of Statherin and 9p21.3 Genetic Variants

9p21.3 variants modulate statherin expression in human aortic SMCs.

Statherin compensates for MGP loss in humans, preventing severe calcification.

Human statherin expression rescued calcification in *Mgp*KO mice.

Interaction between Pyrophosphate and MGP

Pyrophosphate alone was insufficient to inhibit calcification in *Mgp*KO mice.

A complex interplay exists among pyrophosphate, MGP, and statherin in the regulation of calcification.

Conclusions:

Alendronate requires functional MGP to prevent soft-tissue calcification.

9p21.3 variants accelerate arterial calcification by suppressing statherin.

Both pyrophosphate and MGP are necessary for the effective prevention of calcification.

Chapter 1: General Introduction

1.1. Definition and Importance of Arterial Calcification

Coronary artery calcification (CAC) is a pathological process characterized by the deposition of calcium phosphate crystals, primarily hydroxyapatite (HA), within the coronary arterial walls[1]. This process serves as a strong marker of advanced atherosclerosis and a robust predictor of future cardiovascular events [1, 2]. This phenomenon significantly contributes to cardiovascular morbidity and mortality, particularly in aging populations and in those with chronic diseases. CAC significantly increases the risk of sudden death and diminishes vessel wall compliance, disrupting blood flow regulation through vasomotor mechanisms[1]. Vascular calcification transforms soft vascular tissues into rigid bone-like structures, reducing vessel elasticity and impairing cardiovascular function. Calcified coronary arteries are detectable using computed tomography angiography in individuals with symptomatic coronary atherosclerosis, often post-myocardial infarction, and in some asymptomatic cases[3, 4]. CAC progression involves complex interactions between various cell types and molecular pathways, with vascular smooth muscle cells (VSMCs) playing a central role[5].

1.2. Risk Factors and Current Interventions

The most important risk factors for CAC are male sex, age, smoking status, atherosclerosis, and osteoporosis[6, 7]. Currently, there is no effective intervention for CAC[8]. Interestingly, while statin therapy is effective in preventing atherosclerosis[9], it

paradoxically hastens the progression of CAC[10, 11]. The acceleration of coronary artery calcification (CAC) by statins is a complex process involving multiple mechanisms, affecting a broad range of individuals rather than just susceptible ones[10-13]. This unexpected effect stems largely from the statins' diverse actions beyond their primary role in lowering lipids. One key pathway involves the medication's interference with vitamin K2 production, a vital element in activating proteins that shield arteries from calcification [14, 15]. Statins also influence various types of macrophages, leading to increased calcium buildup in arterial tissues[13, 16]. This phenomenon of accelerated calcification is observed widely among statin users, regardless of their specific health profiles. Importantly, this process is generally interpreted as a sign of plaque stabilization, rather than an indication of expanding atherosclerotic lesions[16].

Genome-wide association studies (GWAS) have identified several genetic variants associated with CAC, including the prominent 9p21.3 locus[17]. These studies suggest that 40-50% of CAC variance is attributable to genetic[3] factors, highlighting the importance of understanding the genetic and molecular mechanisms underlying this condition[3].

1.3. Types of Vascular Calcification

Vascular calcification can be broadly categorized into two main types: intimal and medial calcification. Intimal calcification is closely associated with atherosclerosis and primarily affects the inner layers of the blood vessels[18, 19]. In contrast, medial calcification, also known as Mönckeberg sclerosis, occurs in the middle layer of the arterial wall and is commonly observed in patients with chronic kidney disease and diabetes[20, 21].

1.3.1. Intimal Calcification

Intimal calcification is associated with atherosclerosis and involves lipid accumulation and macrophage infiltration within vessel wall[22] [23]. This leads to the formation of calcified plaques, often observed in patients with significant cardiovascular risk factors[24].

1.3.2. Medial Calcification (Mönckeberg's Calcification)

Medial calcification, or Mönckeberg calcification, is associated with chronic kidney disease and diabetes[23]. It occurs independently of lipid accumulation and macrophage infiltration and is localized to elastin fibers[25] or smooth muscle cells in the arterial wall. This study focused on medial calcification because of its relevance to matrix Gla protein (MGP) deficiency[23, 26].

1.3.3. Animal Models in Vascular Calcification Research

Studies on the molecular mechanisms of vascular calcification have relied on animal and cell-based model systems. Intimal calcification, which is closely associated with atherosclerosis, involves calcium deposition in the intimal layer of the blood vessels. Several animal models have been developed to study this process, primarily focusing on mouse models of atherosclerosis. The most widely used are *ApoE*-deficient (*ApoE* −/−)[27, 28] and low-density lipoprotein receptor-deficient (*Ldlr* −/−) mice[27, 29, 30]. When fed with a high-fat diet, these models develop severe hypercholesterolemia and atherosclerotic lesions, exhibiting both micro- and macrocalcifications in advanced atheromatous plaques.

Their calcification patterns closely resemble those observed in human atherosclerotic plaques. Additionally, combined models have been developed, such as *ApoE*-/- or *Ldlr*-/- mice with induced chronic kidney disease (CKD)[31], which develop both arterial medial and intimal calcification in the same arterial segment, mimicking the complex calcification patterns observed in patients with both atherosclerosis and CKD. The key features of these intimal calcification models include lipid accumulation and macrophage infiltration inside the vessel wall, formation of atherosclerotic plaques with calcified regions, presence of both microcalcifications (<15 μm) and larger calcified areas, and involvement of various cell types, including vascular smooth muscle cells (VSMCs), macrophages, and circulating progenitor cells[27-30].

Animal models for studying medial vascular calcification are important for advancing our understanding of this complex pathological process. Several rodent models have been developed to mimic the progression of medial calcifications observed in human diseases. One of the most widely used models is the matrix Gla protein (MGP) knockout mouse (*Mgp*KO), which develops spontaneous and severe arterial calcification beginning at two weeks of age[32]. These mice exhibit widespread medial calcification and typically die within 6-8 weeks of age due to aortic rupture[32]. Additionally, warfarin-induced calcification models in rats have been used to study vitamin K-dependent processes in vascular calcification deficiency[33, 34] and in rats that experience uremia either by near-total nephrectomy (5/6th type of nephrectomy) [9]or by high-adenine diet exposure[35].

Genetic models targeting pyrophosphate metabolism, such as *Enpp1*-deficient or *Abcc6*-deficient mice, develop severe arterial calcification and mimic human diseases such as generalized arterial calcification of infancy[36, 37].

1.4. Pathophysiology of Coronary Artery Calcification (CAC)

Medial coronary artery calcification (CAC) pathophysiology is a complex progressive process characterized by calcium phosphate deposition within the arterial medial layer. This mechanism is distinct from atherosclerosis and primarily involves the phenotypic transformation of vascular smooth muscle cells (VSMCs) from a contractile to an osteogenic state. This transformation leads to the precipitation of calcium phosphate and the formation of hydroxyapatite crystals within the arterial wall. Imbalances in calcium-phosphate homeostasis and dysregulation of calcification inhibitors such as the Matrix Gla Protein further exacerbate this process. As calcification progresses, it increases arterial stiffness, impaired vasomotor function, and compromised hemodynamics.

1.4.1. Vascular smooth muscle cells (VSMCs)

Vascular smooth muscle cells (VSMCs) play a central role in CAC progression[17]. Hydroxyapatite is a normal physiological product released from SMCs that is cleared from the extracellular space by macrophages[18]. VSMCs are crucial regulators of calcium homeostasis within the vascular environment and actively manage calcium levels through multiple mechanisms. These include the uptake and storage of excess calcium in the endoplasmic reticulum, secretion of hydroxyapatite to eliminate surplus calcium, and

production of key calcification inhibitors, such as pyrophosphate (PPi) and Matrix Gla protein (MGP)[38, 39]. However, in the presence of pro-calcific signals, such as inflammatory cytokines and elevated phosphate levels, this initiates the growth of hydroxyapatite crystals, activates bone morphogenic protein (BMP2 and BMP4) signaling, and induces osteochondrogenic conversion of SMCs[40], ultimately leading to calcified arteries. VSMCs undergo phenotypic transformation into osteoblast-like cells[41].

This transition is characterized by a significant reduction in the expression of contractile VSMC markers, such as myocardin and alpha-smooth muscle actin, accompanied by the expression of chondrogenic/osteogenic markers, such as osteopontin and runt-related transcription factor 2 (RUNX2), which drive the production of hydroxyapatite crystals within the arterial wall and alkaline phosphatase (ALP), which degrades pyrophosphate[19, 42, 43]. This pathological progression is driven by the activation of circulating bone morphogenic proteins (BMPs), a process triggered by hydroxyapatite. Indeed, the potency of a BMP2-containing collagen scaffold biomaterial used for bone regeneration was markedly enhanced by the inclusion of a small quantity of hydroxyapatite[44, 45].

1.4.2. Macrophage Function in Medial Vascular Calcification

While macrophages are primarily associated with intimal calcification in atherosclerosis, their role in medial calcification is less direct but still significant[46]. Medial calcification or Mönckeberg's sclerosis, primarily involves vascular smooth muscle cells (VSMCs) and occurs independently of lipid accumulation or macrophage infiltration[21, 47, 48]. Macrophages indirectly influence medial calcification through several mechanisms.

They release pro-inflammatory cytokines and extracellular vesicles that promote the phenotypic switching of VSMCs to osteoblast-like cells, a key process in medial calcification[49].

In addition, macrophages modulate the expression and activity of calcification inhibitors and inducers, thereby affecting the calcification process[50, 51]. In chronic kidney disease, a common cause of medial calcification, uremic toxins can activate macrophages, leading to increased inflammation and oxidative stress, which indirectly promotes VSMC transdifferentiating and calcification [37]. Macrophages play a role in the clearance of apoptotic bodies and matrix vesicles that serve as nucleation sites for calcium deposition. Impaired clearance of these structures by dysfunctional macrophages may contribute to medial calcification[50].

1.5. Molecular Mechanisms of Arterial Calcification

Arterial calcification is a complex process involving multiple molecular mechanisms that contribute to the hardening and loss of arterial elasticity. Several of the molecular pathways have been delineated and are described below.

1.5.1. Bone Morphogenetic Proteins (BMPs)

Bone morphogenetic proteins (BMPs) are members of the transforming growth factor-beta (TGF-β) superfamily and play important roles in various biological processes, including vascular calcification[52]. The BMP signaling pathway is initiated when BMP ligands such as BMP-2 and BMP-4 bind to heteromeric complexes of type I and type II serine-threonine

kinase receptors on the cell surface[52]. Upon ligand binding, type II receptors phosphorylate and activate type I receptors, which in turn phosphorylate the cytosolic BMP effector proteins SMAD 1, 5, and 8 (SMAD 1/5/8)[53, 54]. These phosphorylated SMADs form a complex with the common mediator Smad 4 and translocate to the nucleus. In the nucleus, this complex interacts with various transcription factors and co-regulators to activate specific target genes, including inhibitors of DNA-binding (*Id*) genes. This activation leads to the expression of chondrogenic/osteogenic markers, such as RUNX2, Osteopontin, and alkaline phosphatase, promoting osteoblastic differentiation and mineralization[55]. The BMP signaling pathway is tightly regulated by various extracellular and intracellular modulators, including antagonists such as the matrix Gla protein (MGP), which can bind to BMP ligands and prevent their interaction with receptors, thus inhibiting the pathway and potentially mitigating vascular calcification[56].

1.5.2. Runt-related transcription factor 2 (RUNX2)

RUNX2 is a transcription factor involved in chondrogenic/osteogenic differentiation of VSMCs and plays a significant role in vascular calcification[47, 57]. As an early marker of osteogenesis, RUNX2 is upregulated during the phenotypic switch of VSMCs from a contractile to an osteoblast-like state, which is essential for the formation of bone-like structures within the vasculature[47]. This transformation is characterized by the expression of bone matrix proteins such as collagen type I (COL1A1), osteopontin (SPP1), and osteocalcin (BGLAP), all of which are regulated by RUNX2 [47] and ALP[21].

RUNX2's role in calcification involves regulating several signaling pathways and

interacting with other transcription factors[47]. It modulates chondrogenic/osteogenic differentiation by interacting with coactivators and corepressors, thereby influencing the transcription of the genes necessary for bone formation. RUNX2 also interacts with signaling molecules, such as BMP2, ERK/MAPK, and PI3K/AKT, which affect its post-translational modifications, such as phosphorylation and ubiquitination, thereby regulating its activity[47, 58]. These interactions enhance RUNX2's ability to promote the expression of chondrogenic/osteogenic genes in VSMCs, contributing to the deposition of hydroxyapatite crystals within the arterial walls. Under pathological conditions where pyrophosphate is degraded and hydroxyapatite is unmasked, SMCs undergo aberrant conversion to a bone-like phenotype expressing the osteogenic factor *Runx2* and produce more hydroxyapatite to further harden the extracellular matrix, as in bone[47, 59]. This pathological progression is driven by the activation of circulating bone morphogenic proteins (BMPs), which are triggered by hydroxyapatite[45, 60]. Indeed, the potency of the BMP2-containing collagen scaffold biomaterial used for bone regeneration was markedly enhanced by including a small quantity of hydroxyapatite[44].

The absence of RUNX2 significantly inhibited vascular calcification. Studies have shown that knocking out *Runx2* in VSMCs reduces chondrogenic/osteogenic differentiation and calcification[47]. This indicates that RUNX2 is an early marker and a necessary driver of calcification processes in the vasculature. In the absence of RUNX2, chondrogenic/osteogenic transformation and mineral deposition are substantially impaired, highlighting its indispensable role in vascular calcification[47, 61]. Understanding these mechanisms highlights potential therapeutic targets for preventing or mitigating the

vascular calcification associated with cardiovascular diseases[47, 61]. •

1.5.3. Alkaline phosphatase (ALP)

Alkaline phosphatase (ALP) plays a significant role in mineralizing the extracellular matrix by degrading pyrophosphate and increasing local inorganic phosphate concentrations, which are necessary for hydroxyapatite crystal formation[21, 42, 62]. The activity of this enzyme is upregulated during the chondrogenic/osteogenic transition of VSMCs, contributing to the deposition of calcium phosphate crystals. This phenotypic switch increases the expression of chondrogenic/osteogenic proteins such as RUNX2 and ALP, which promote the nucleation and growth of hydroxyapatite crystals within arterial walls[21, 62, 63]. Elevated levels of calcium and phosphate ions in the vascular environment enhance hydroxyapatite deposition, which is facilitated by the upregulation of phosphate transporters and other chondrogenic/osteogenic factors in VSMCs[21, 62, 64]. This transformation involves changes in gene expression and alterations in cellular metabolism and signaling pathways that favor mineral deposition[21, 62]. Understanding these mechanisms provides insight into potential therapeutic targets for preventing or mitigating arterial calcification.

1.6. Calcification Inhibitors

Calcification inhibitors are critical in preventing the pathological deposition of calcium phosphate crystals in vascular tissues. These inhibitors are essential for maintaining a delicate balance between normal and pathological calcification. These inhibitors can be

broadly categorized into two main groups: hydroxyapatite-binding proteins and molecules involved in pyrophosphate (PPi) metabolism.

1.6.1. Pyrophosphate Pathway Disruption and Calcification.

Inorganic pyrophosphate (PPi) is important in preventing pathological calcification, including CAC [65]. A complex network of proteins and enzymes regulates this potent endogenous inhibitor of calcium phosphate deposition. Extracellular ATP serves as the primary source for PPi synthesis, primarily through the action of ectonucleotide pyrophosphatase/phosphodiesterase 1 (ENPP1), which converts ATP to PPi in the extracellular matrix[66, 67].

PPi is primarily synthesized from extracellular ATP by the enzyme ectonucleotide pyrophosphatase/phosphodiesterase 1 (ENPP1). This process occurs in the extracellular matrix and is vital for maintaining adequate PPi levels to inhibit unwanted mineralization. Once produced, PPi acts as a powerful inhibitor of hydroxyapatite crystal formation and growth, effectively preventing the initiation and progression of vascular calcification (Figure 1.1). As a potent physiological inhibitor of hydroxyapatite formation in soft tissues, PPi serves as a natural defense mechanism against ectopic mineralization by preventing the growth of calcium phosphate crystals[65]. A delicate balance between PPi and inorganic phosphate (Pi) is critical for regulating mineral deposition in the vasculature. PPi antagonizes the ability of Pi to crystallize with calcium and reduce VSMC differentiation into osteoblast-like cells[65]. Extracellular ATP serves as the primary source for PPi synthesis, primarily through the action of ectonucleotide

pyrophosphatase/phosphodiesterase 1 (ENPP1), which converts ATP to PPi in the extracellular matrix[68, 69]. The importance of PPi in preventing calcification is evident in several genetic disorders characterized by PPi deficiency, which leads to ectopic calcification[65, 70]. These disorders include pseudoxanthoma elasticum [37, 71](PXE), generalized arterial calcification of infancy (GACI)[72], and arterial calcification due to CD73 deficiency (ACDC) [73] (Table 1.1, Figure 1.1).

Table 1 1.Ectopic arterial calcification is caused by mutations in genes involved in pyrophosphate metabolism.

Genetic Disease	Protein	Role	Ectopic Calcification
GACI	ENPP1	Synthesis of ppi	Medial Arterial
PEX/GACI	ABCC6	Transporter	Elastic fibers in skin, arteries
ACDC	CD73/ NT5E	Hydrolysis of AMP	Medial Arterial and Periarticular
FIBGC	Pit-2	Phosphate Transporter	Basal Ganglia and cortex
PA	ANK	Transporter	Craniofacial Bones, Articular cartilage
CPPD	ANK	Transporter	Medial Arterial
HPP	TANP/ALPL	phosphatase activity	Death, Lack of skeletal mineralization
Arterial Calcification, and SP	CD39/E-NTPD	Modulate adenosine levels	Soft tissue
GACI: Generalized Arterial Calcification of Infancy, ACDC: Arterial Calcification due to Deficiency of CD73, FIBGC: Familial Idiopathic Basal Ganglia Calcification, PA: Progressive Ankylosis PEX: pseudoxanthoma Elasticum, HPP: Hypophosphatasia, CPPD: calcium pyrophosphate deposition disease (Gain-of-function mutations) progressive ankylosis (Loss-of-function mutations), SP: Spastic Paraplegia			

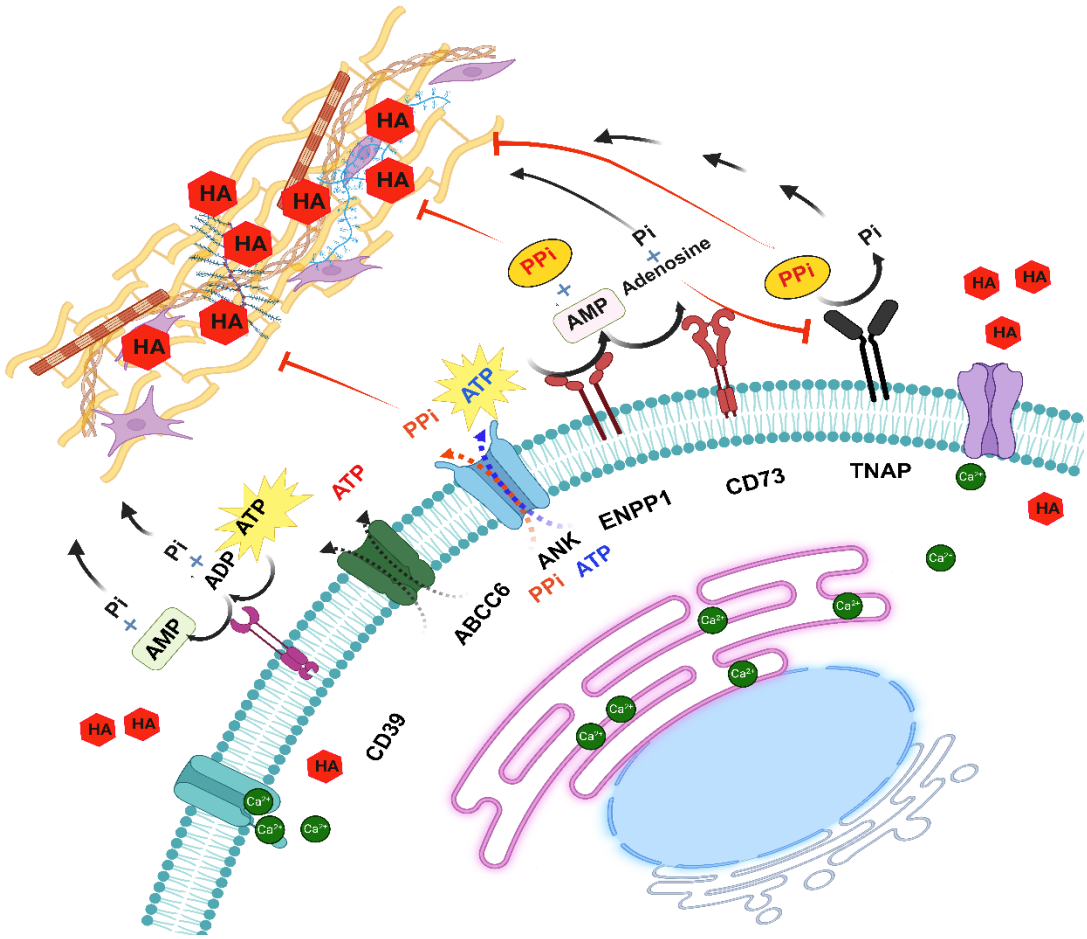

Figure 1.1. Regulating PPi/Pi Balance and Preventing Arterial in SMCs.

In VSMCs, ATP is released into the extracellular space via various transporters. ENPP1, an enzyme present on the cell surface, hydrolyzes ATP to produce PPi and AMP. ABCC6 and ANKH proteins in VSMCs transport ATP, which is then converted to PPi by ENPP1, contributing to the pool of extracellular PPi. PPi acts as an inhibitor of hydroxyapatite crystal formation, which is crucial for preventing tissue calcification. TNAP, another enzyme on the cell surface, breaks down PPi into Pi. Proper regulation of TNAP is essential for maintaining the balance between PPi and Pi and preventing excessive calcification. Mutations in genes such as ABCC6, ENPP1, and ANKH can disrupt this balance, leading to reduced PPi levels and the promotion of calcification in the arterial walls. CD73 then converts AMP to Pi and adenosine, which inhibits TNAP. Thus, VSMCs play a critical role in generating PPi and maintaining their balance with Pi, which prevents unwanted calcification in arteries and ensures normal vascular function. Created in BioRender. Soheili, F. (2025) https://BioRender.com/z00g679

1.6.1.1. Ectonucleotide pyrophosphatase/phosphodiesterase 1 (ENPP1):

Smooth muscle cells (SMCs) contain the enzyme ENPP1, which is the primary enzyme that generates PPi by hydrolyzing ATP to AMP and PPi in the extracellular space where negatively charged pyrophosphate binds to hydroxyapatite, prevents its accumulation and facilitates its clearance to prevent of calcification (Figure 1.1).[37, 74, 75]. Loss of ENPP1 causes generalized arterial calcification of infancy (GACI) type 1[76]. In the absence of ENPP1, humans and mice cannot produce PPi, which leads to severe arterial calcification and early death[36]. Administering bisphosphonates, which are synthetic analogs of PPi typically used for osteoporosis treatment, can help reduce arterial calcification and improve survival in ENPP1-deficient infants. Patients with GACI type 1 and Enpp1 mutant mouse models have almost zero plasma PPi, indicating the essential role of ENPP1 in PPi generation[25].[36]

1.6.1.2. ATP-binding cassette subfamily C member 6 (ABCC6)

ABCC6 (ATP-binding cassette subfamily C member 6) is a transmembrane protein primarily expressed in the liver and kidneys that functions as an ATP-dependent efflux pump that transports substrates from inside cells to the extracellular space (Figure 1.1)[37, 77, 78]. Although not an enzyme, it plays a critical role in regulating tissue calcification by influencing PPi levels, a potent inhibitor of mineralization. Mutations in *ABCC6* are associated with genetic disorders, such as pseudoxanthoma elasticum (PXE) and GACI, both characterized by ectopic calcification[37, 77, 78]. Although the exact mechanism by which ABCC6 prevents calcification is not fully understood, it is believed to be involved in ATP

release, which is subsequently converted to PPi by other enzymes[37, 77, 78].

1.6.1.3. CD73 deficiency (NT5E)

NT5E mutation, also known as CD73, contributes to arterial calcification due to a deficiency of CD73 (ACDC)[73]. Loss of CD73 function results in reduced adenosine levels, which diminishes adenosine-mediated inhibition of TNAP activity, leading to a greater breakdown of PPi[73]. CD73 is a glycosylphosphatidylinositol (GPI)-anchored glycoprotein that functions as an ectoenzyme in the plasma membrane[73]. It regulates the extracellular production of adenosine by catalyzing the hydrolysis of AMP to adenosine and inorganic phosphate[73]. CD73 is widely expressed in various tissues and cell types, including endothelial cells, lymphocytes, and fibroblasts[73]. Its primary function is in the purinergic signaling pathway, where it works in tandem with CD39 (ectonucleoside triphosphate diphosphohydrolase-1) to convert extracellular ATP to adenosine[73]. This process is important for regulating inflammation, immune response, and vascular function[73]. In the context of vascular calcification, CD73 deficiency has been associated with a rare condition called "arterial calcification due to deficiency of CD73" (ACDC), highlighting its importance in maintaining vascular health and preventing ectopic calcification[73] (Figure 1.1).

1.6.1.4. CD39 or Ecto-nucleoside triphosphate diphosphohydrolase-

CD39, also known as ecto-nucleoside triphosphate diphosphohydrolase-1 (E-NTPD ase1) [79], is a crucial enzyme in the extracellular purinergic signaling pathway. In the context of vascular health, CD39 activity is particularly important, as it works in tandem with CD73

to modulate extracellular adenosine levels, which can influence vascular calcification processes[73] [79]. CD39's structure requires proper glycosylation. The N-terminal intracytoplasmic domain also undergoes palmitoylation, allowing its association with lipid rafts[80]. Oriented towards the extracellular space, CD39 efficiently hydrolyzes extracellular nucleotides such as ATP and ADP [79, 80]. In vascular health, CD39 activity is particularly important, as it works in tandem with CD73 to modulate extracellular adenosine levels, which can influence vascular calcification processes [79] (Figure 1.1).

1.6.1.5. Progressive ankylosis protein (ANK)

Progressive ankylosis protein (ANK) is a transmembrane protein that plays a significant role in regulating extracellular pyrophosphate (PPi) levels and preventing ectopic calcification[65, 81]. Containing multiple transmembrane domains and ankyrin repeat motifs involved in protein-protein interactions, ANK functions primarily by mediating the efflux of intracellular PPi to the extracellular space[65, 81, 82]. This mechanism helps to maintain extracellular PPi levels, which are essential for inhibiting mineralization and calcification. ANK works synergistically with other enzymes, such as ENPP1, TNAP, and CD73, to regulate extracellular PPi and adenosine concentrations, a process critical for preventing ectopic calcification, particularly in vascular tissues. While ANK is primarily thought to transport PPi, evidence suggests that it may also be involved in the transport of other compounds, such as ATP, as indicated by increased extracellular ATP levels upon ANK overexpression in chondrocytes[82-84] (Figure 1.1).

1.6.1.6. Tissue-non-specific Alkaline Phosphatase (TNAP):

TNAP plays a pivotal role in both physiological and pathological mineralization processes, particularly in vascular calcification. As an ectoenzyme, TNAP hydrolyzes various phosphate compounds, including inorganic pyrophosphate (PPi), pyridoxal-5'-phosphate (PLP), phosphorylated osteopontin (p-OPN), and adenosine tri-/di-/monophosphate (ATP/ADP/AMP). In mineralization, TNAP acts as a crucial gatekeeper for apatite crystallization and bone formation through multiple mechanisms. It hydrolyzes PPi, a potent inhibitor of mineralization, thereby reducing its inhibitory effects. Simultaneously, TNAP provides the inorganic phosphate (Pi) necessary for hydroxyapatite formation, thus regulating the delicate balance between PPi and Pi. The relationship among tissue-nonspecific alkaline phosphatase (TNAP), ectopic calcification, and hypophosphatasia (HPP) presents a complex and seemingly paradoxical scenario. Increased TNAP activity can lead to ectopic soft tissue calcification by reducing pyrophosphate (PPi) levels, which are potent inhibitors of mineralization. TNAP upregulation in smooth muscle cells (SMCs) plays a substantial role in various models of arterial calcification, and TNAP overexpression in vascular muscle cells or endothelial cells can induce massive and lethal arterial calcification in mice. However, *Tnap* deficiency, which causes HPP and skeletal hypomineralization, can paradoxically prevent ectopic calcification in the soft tissues. This apparent contradiction is further elucidated by studies showing that crossing *Alpl*-deficient mice (Tnap-deficient) with mice deficient in PPi-producing enzymes (such as ENPP1 or ANK) reduces ectopic calcification in PPi-deficient mice, whereas mineralization defects are prevented in PPi-deficient mice. These findings highlight the delicate balance required

in PPi metabolism for proper tissue-specific mineralization, and the complex interplay between TNAP and other factors in regulating both physiological and pathological calcification processes (Figure 1.1).

1.6.1.7. Equilibrative Nucleoside Transporter 1 (ENT1),

ENT1, encoded by *SLC29A1*, is a transmembrane protein that facilitates the sodium-independent bidirectional transport of purine and pyrimidine nucleosides across cell membranes[85]. ENT1 is widely distributed in various tissues, including the cardiovascular system[85]. This transporter plays essential roles in nucleotide synthesis, adenosine signaling, and absorption and distribution of xenobiotics. Its activity can be modulated by factors, such as ethanol and protein kinases, defining a role for ENT1 in not only cardiovascular disease as well as cancer treatment, and drug transport. ENT1 has been implicated in the adenosine-mediated cardioprotection of arterial calcification. Studies have shown that the absence of ENT1 can provide whole-heart protection against ischemia, suggesting that ENT1 plays a role in modulating purine nucleoside-dependent signaling that may influence vascular health[85]. Although the direct link between ENT1 and arterial calcification has not been fully elucidated, its involvement in adenosine signaling and cardiovascular protection suggests that it may indirectly influence calcification processes by regulating local adenosine levels and subsequent cellular response[85] (Figure 1.1).

1.6.2. Hydroxyapatite Binding Proteins

Hydroxyapatite-binding proteins play a critical role in preventing and regulating arterial calcification by inhibiting the deposition of calcium phosphate crystals, specifically

hydroxyapatite, in the vascular tissues[86]. In VSMCs, these proteins are particularly important for maintaining a delicate balance between mineralization and tissue integrity[87, 88]. This distinction in protein expression in different states helps elucidate the different roles of hydroxyapatite-binding proteins in vascular calcification, as some proteins are primarily protective in healthy arteries, whereas others become active or upregulated in response to calcification and tissue damage[25].While several proteins involved in arterial calcification like osteopontin[89-91] and bone sialoprotein[92], have been characterized in calcified SMCs or osteonectin expression which is present in both healthy and calcified SMCs[93-96];the role of statherin in calcification is unclear. Table 1.2 provides a detailed explanation of the key hydroxyapatite-binding proteins related to arterial calcification.

Table 1.2.Characteristics of Hydroxyapatite Binding Proteins Produced by Arterial SMCs

protein	MW	Function in Arterial SMCs	Expression Pattern	Pathologies	HA Binding Domain
MGP[32]	10	Inhibits HA formation Inhibits BMP signaling	Expressed in healthy SMCs Upregulated in calcified tissues	Vascular calcification Atherosclerosis	Gla domain
OPN[89-91]	44	Inhibits HA crystal growth Inhibits SMC osteogenesis	Low in healthy SMCs Upregulated in vascular calcification	Vascular calcification Atherosclerosis	Multiple acidic regions
SPARC[89-91]	32	Modulates collagen mineralization inhibits calcification	Expressed in normal SMCs Upregulated in calcified tissues	Vascular calcification Atherosclerosis	EF-hand calcium-binding domain
BSP[92]	33	Promotes HA nucleation	Primarily associated with pathologic conditions	Vascular calcification Atherosclerosis	RGD sequence acidic AA clusters
BGLAP	5.3	Modulates collagen mineralization	Expressed in healthy SMCs	Not confirmed	Gla domain

HA: hydroxyapatite MW: Molecular Weight (KDa); BMP: Bone Morphogenetic Protein; RGD: Arginine-Glycine-Aspartic acid. AA: amino acid, MGP: Matrix Gla Proteins, OPN: Osteopontin, SPARC: Osteonectin, BSP: Bone Sialoprotein, Statherin, Osteocalcin/ Bne gamma-carboxyglutamic acid-containing protein ((BGLAP)

1.6.2.1. Matrix Gla protein

Matrix Gla protein (MGP) was initially extracted from demineralized bovine bone matrix[32]. It is characterized by the presence of vitamin K-dependent modified amino acids, specifically γ-carboxylation acid (Gla), at positions 37, 41, 48, and 52[97, 98]. This protein has a molecular weight of 14 kDa and contains a disulfide bond within its amino acid structure[99]. Moreover, sequence analyses revealed similarities between the MGP and Bone Gla proteins (BGP or osteocalcin), suggesting that these proteins may have evolved from a common ancestral gene through mechanisms of duplication and divergence[99].In humans, MGP contains five glutamic acid residues, which are crucial for its affinity for calcium phosphate crystals and bone morphogenetic proteins. These glutamate residues are converted to Gla residues through post-translational modifications mediated by vitamin K-dependent carboxylase[99] (Figure 1.2). During this process, the co-factor vitamin K hydroquinone (KH2) is oxidized, resulting in the addition of a carboxyl group at the γ-position of the glutamate residue[97, 98, 100]. After oxidation, vitamin K can be recycled by the enzyme vitamin K epoxide reductase (VKOR), which restores it to continue the cycle. The production of Gla proteins may be inhibited by derivatives of 4-hydroxycoumarin that affect the VKOR enzyme, such as warfarin, a widely used anticoagulant [33, 101-105]. For example, warfarin, a vitamin K antagonist, prevents this process and induces arterial calcification within two weeks in rats[33](Figure 1.3). Additionally, MGP undergoes phosphorylation at serine residues 3, 6, and 9 (Figure 1.2). Although phosphorylation is known to modulate the activity of extracellular matrix proteins [97, 98, 100], these modifications

remain unclear. Furthermore, matrix Gla protein (MGP) is phosphorylated at three serine residues (positions 3, 6, and 9) within the conserved Ser-X-Glu/Ser(P) motif by a Golgi-associated casein kinase. This motif is also found in other secreted proteins such as casein and salivary proteins. Proteins secreted into the extracellular environment, such as MGP, are typically partially phosphorylated, which allows for the dynamic regulation of their activity. In contrast, proteins secreted into milk or saliva are usually fully phosphorylated at all the target serine residues. This evolutionarily conserved sequence, present in sharks and humans, underscores its significance in regulating protein function[106].The Golgi-associated casein kinase responsible for this phosphorylation is distinct from the cytosolic casein kinases and specifically targets secreted proteins. Phosphorylation is critical for MGP's ability of MGP to bind hydroxyapatite and prevent arterial calcification. By regulating MGP activity in extracellular environments such as vascular tissues, this process plays a vital role in inhibiting calcification and maintaining tissue health[106, 107].MGP plays a crucial role in preventing calcification through two primary mechanisms. First, it inhibits hydroxyapatite formation by binding to nascent crystals in the extracellular matrix, effectively preventing their growth and accumulation[108]. This action is particularly vital for maintaining the elasticity of the blood vessels by preventing calcium deposition, which would otherwise contribute to conditions such as atherosclerosis and arterial calcification[108]. Second, MGP inhibits bone morphogenetic protein (BMP) signaling, specifically BMP-2 and BMP-4[25, 107, 109-112], which are known to promote the chondrogenic/osteogenic differentiation of VSMCs[53]. This inhibition is critical because it

prevents the transformation of VSMCs into osteoblast-like cells, which otherwise would contribute significantly to calcification[53]. Through these dual mechanisms, MGP serves as a potent inhibitor of ectopic calcification, maintaining the integrity and function of soft tissues, particularly in the cardiovascular system.

1.6.2.2. *Mgp* Knockout Mice

The *Mgp*KO mouse model was developed by Karsenty *et al.* in 1997 to investigate extracellular matrix (ECM) calcification and the molecular factors that govern this process[113]. Matrix Gla protein (MGP) is a small extracellular protein, weighing 14 kDa, produced by VSMCs and chondrocytes. Gene targeting at the *Mgp* locus in embryonic stem cells led to the replacement of a 3.4 kb region that included the proximal promoter, as well as exons 1, 2, and 3, and most of exon 4 [25, 107, 109-112]. *Mgp*KO mice exhibit severe arterial calcifications and abnormal mineralization in cartilaginous tissues, resulting in death within two months due to cardiovascular disease. Additionally, these mice displayed short stature, fractures, and osteopenia (a condition with lower-than-normal bone mass or bone mineral density that can increase the risk of developing osteoporosis). The insights gained from studying *Mgp*-deficient mice are fundamental for understanding the physiological significance of MGP[25, 107, 109-112].

1.6.2.3. Keutel Syndrome

In 1972, Keutel first described Keutel syndrome as an autosomal recessive disorder characterized by peripheral pulmonary stenosis, brachytelephalangism (characterized by

the presence of unusually short or underdeveloped terminal phalanges, which are bones at the tips of fingers or toes), neural hearing loss, abnormal cartilage calcification, and ossification[114]. Munroe conducted a genome search in 1999 using homozygosity mapping in two consanguineous families of Turkish origin, identifying Matrix Gla Protein (MGP) as a candidate gene[115]. Subsequent mutational analysis of MGP in probands and their families revealed mutations associated with absent or nonfunctional MGP[115]. Postmortem examinations of the two siblings showed concentric calcifications in the coronary, pulmonary, hepatic, renal, meningeal, and cerebral arteries[25, 116-119]. Additionally, the first reported case of aortic calcification occurred in a 6-year-old female patient[120], a critical extracellular matrix (ECM) protein that functions as a potent inhibitor of tissue calcification. Mutations in this gene lead to loss of function, causing ectopic mineralization in cartilaginous and vascular tissues, which manifests as the classical KS phenotype[48-51].

1.6.2.3. Variability of Arterial Calcification in Keutel Syndrome:

The absence of functional MGP in null mice led to widespread vascular and cartilage calcification, mirroring the clinical presentation observed in patients with KS. The extent and severity of calcification in Keutel Syndrome exhibits significant variability among the affected individuals[48-51]. Although cartilaginous tissue calcification is a consistent feature of Keutel Syndrome, vascular calcification shows more heterogeneity[116]. Some patients exhibit calcifications in the coronary, pulmonary, and peripheral arteries, whereas others show no or only mild vascular involvement[116]. This variability suggests that additional genetic or environmental factors may modify disease severity.

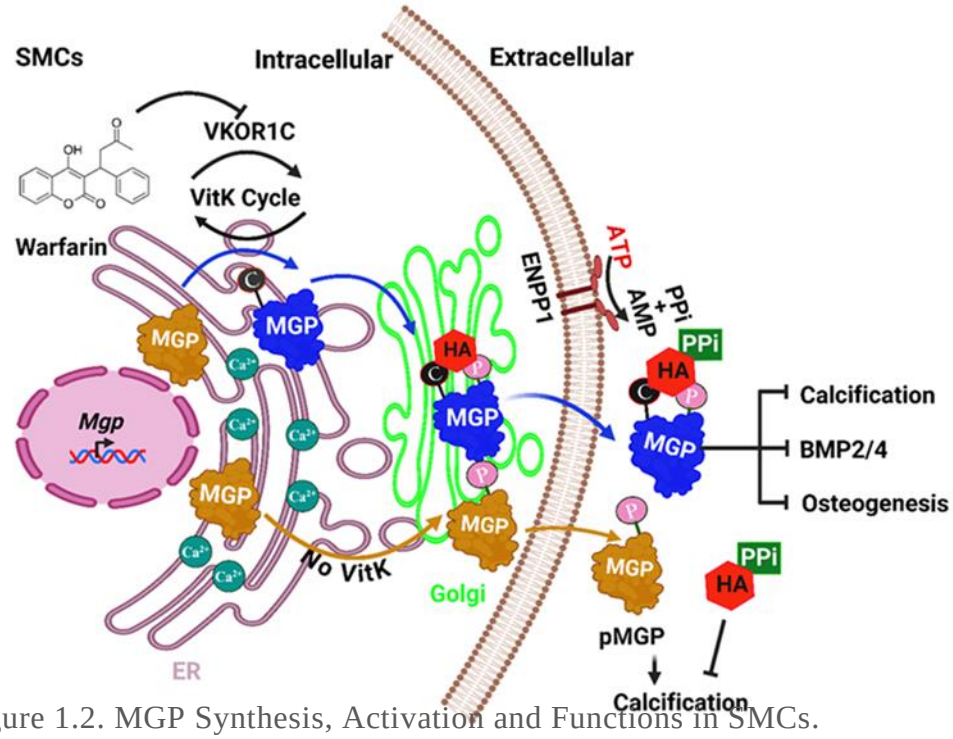

Figure 1.2. MGP Synthesis, Activation and Functions in SMCs.

This illustration depicts the complex activation process of Matrix Gla Protein (MGP) and its proposed function in preventing vascular calcification. This pathway begins with MGP synthesis in the endoplasmic reticulum, followed by vitamin K-dependent γ-carboxylation to form dp-cMGP. Subsequent phosphorylation in the Golgi apparatus produces p-cMGP, which is then secreted into the extracellular environment. Once active, p-cMGP inhibits soft-tissue calcification, prevents VSMC transdifferentiation, and modulates BMP signaling. In contrast, the inactive form dp-ucMGP is a marker of vitamin K deficiency. This process highlights the crucial role of vitamin K in MGP activation and the maintenance of vascular health.

1.7. Alendronate's Role in Vascular Calcification

Alendronate, a nitrogen-containing bisphosphonate, plays a dual role in inhibiting bone resorption and modulating cellular processes in vascular calcification[121, 122]. Structurally, alendronate ($C_4H_{13}NO_7P_2$) is designed to bind hydroxyapatite crystals in bone, preventing their dissolution[123]. [121]. Its primary mechanism of action involves the inhibition of farnesyl pyrophosphate synthase[123] (FPPS) an enzyme in the mevalonate pathway, which is essential for the prenylation of small GTPases such as Rab proteins[123-125]. This inhibition disrupts osteoclast-mediated bone resorption by impairing vesicular trafficking, cytoskeletal organization, and survival of osteoclasts[124]. Alendronate is widely used to treat and prevent osteoporosis by increasing the bone mineral density and reducing the fracture risk[122, 124].

In addition to its effects on osteoclasts, alendronate also affects other myeloid lineage cells, including macrophages[124]. Nitrogen-containing bisphosphonates reduce the prenylation of Rab GTPases in macrophages, altering endosomal trafficking and potentially affecting lysosomal function[124]. This mechanism may have broader implications for cellular hydroxyapatite handling processes, particularly in pathological calcifications.

1.7.1. Alendronate Therapeutic Applications

1.7.1.1. Osteoporosis Treatment

Alendronate is a cornerstone therapy for osteoporosis, a condition characterized by weakened bones and an increased fracture risk. Inhibition of osteoclast activity enhances bone density and reduces the likelihood of fractures in postmenopausal women and other at-risk populations[124, 126].

1.7.1.2. Generalized Arterial Calcification of Infancy (GACI)

Alendronate has shown promise for the treatment of generalized arterial calcification of infancy (GACI), a rare autosomal recessive disorder caused by mutations in *ENPP1*. ENPP1 deficiency leads to reduced levels of pyrophosphate (PPi), a natural inhibitor of hydroxyapatite formation, resulting in pathological arterial calcification. Alendronate mimics PPi's inhibitory effects of PPi on hydroxyapatite deposition, effectively reducing arterial calcification in experimental models and rescuing infants from calcification[76, 127].

1.7.1.3. Warfarin-Induced Arterial Calcification

Warfarin-induced arterial calcification is another condition for which alendronate has demonstrated efficacy. Warfarin inhibits the vitamin K cycle, preventing γ-carboxylation of Matrix Gla Protein (MGP), an essential inhibitor of vascular calcification. This results

in unregulated calcium phosphate deposition in arterial walls. Alendronate compensated for MGP dysfunction by binding hydroxyapatite and preventing its deposition, thereby rescuing arterial calcification in the experimental models[20, 33] (Figures 1.2 and 1.3).

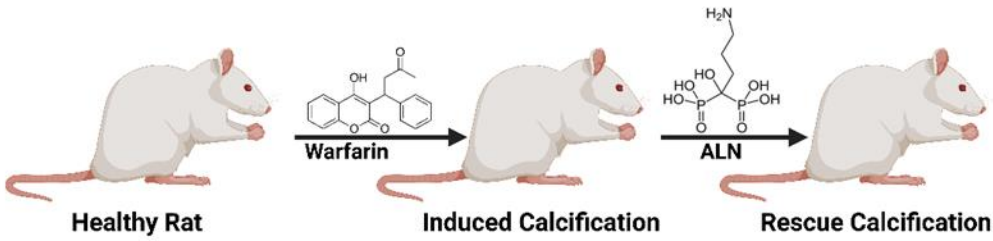

Figure 1.3.Rescue of Warfarin induced arterial calcification in rats by ALN.

In a study by Price *et al*., alendronate effectively inhibited arterial calcification induced by warfarin in rats. The concentrations used were comparable to those that inhibited bone resorption, highlighting the potential of alendronate to prevent vascular calcification without affecting the serum calcium and phosphate levels[33].

1.7.1.4. Impact of Alendronate on Arterial Calcification in *Mgp*KO Mice

Mice lacking Mgp (*Mgp*KO) exhibit severe arterial calcification due to unopposed BMP signaling and die within two months of aortic rupture or heart failure. While selective BMP inhibitors can delay this phenotype, alendronate has not been explored as a potential therapeutic agent.[57]

1.8. Other hydroxyapatite binding protein

In addition to Matrix Gla Protein (MGP), vascular smooth muscle cells (VSMCs) produce other proteins that can bind to hydroxyapatite and help prevent calcification (Table 1.2):

1.8.1. Osteopontin (OPN)

Osteopontin (OPN or SPP1) is another important player in the inhibition of hydroxyapatite formation[128, 129]. This acidic phosphoprotein is expressed in various tissues, including bones and vascular tissues, and plays a significant role in regulating calcification, particularly arterial calcification[40, 89, 113]. OPN's mechanism of action of OPN is twofold, contributing to its effectiveness as both an inhibitor and regulator of calcification.

First, OPN acts by directly binding to hydroxyapatite crystals, effectively preventing their further growth[40]. This binding action helps regulate the size and extent of calcification in the vascular wall, serving as a critical control mechanism against excessive mineral deposition[129]. Second, OPN inhibits the chondrogenic/osteogenic differentiation of VSMCs[129]. This reduces the ability of these cells to adopt bone-like characteristics and form calcium deposits in arteries, further preventing pathological calcification[129].

Interestingly, OPN is upregulated in response to vascular injury and inflammation, highlighting its role in the body's defense against pathological calcification[129]. This adaptive response underscores the importance of OPN in maintaining vascular health under stressful conditions[89, 129]. The protective role of OPN has been further substantiated by

studies in OPN-null mice, which exhibit enhanced vascular calcification[89, 129]. These findings provide strong evidence that OPN functions as a protective factor against arterial calcification, emphasizing its significance in maintaining vascular health and preventing related cardiovascular diseases[89].

1.8.2. Osteonectin (SPARC)

Osteonectin, also known as secreted protein acidic and rich in cysteine (SPARC), is a multifunctional glycoprotein that plays a significant role in the regulation of both bone and vascular calcification[91, 93]. This protein has been identified in calcified vascular lesions and in areas where VSMCs undergo chondrogenic/osteogenic differentiation, suggesting its involvement in the complex processes of tissue mineralization[91, 93, 96].

The mechanism of action of osteonectin in calcification regulation involves two steps. First, it modulates collagen mineralization by binding to collagen fibers in the extracellular matrix. This interaction with collagen and calcium ions allows osteonectin to regulate hydroxyapatite deposition in vascular tissues, thus influencing the mineralization process[91, 93]. Second, osteonectin inhibits calcification in vascular tissues by preventing excessive calcification by limiting hydroxyapatite deposition and modulating the matrix environment in a manner that discourages mineralization[91, 93].

Osteonectin expression patterns and functional characteristics underscore its multifaceted role in the regulation of calcification. It is abundantly expressed in tissues characterized by

high turnover, such as active osteoblasts, bone marrow progenitor cells, and hypertrophic chondrocytes[91, 96]. In the context of vascular calcification, the upregulation of osteonectin in calcified tissues and its presence in VSMCs undergoing chondrogenic/osteogenic differentiation highlight its importance in maintaining vascular health[91, 93].

Studies have shown that the role of osteonectin extends beyond its structural support. It is involved in cell-matrix interactions, collagen binding, and the modulation of cell proliferation[91, 96]. These functions, combined with their ability to influence matrix metalloproteinase production and activity, suggest that osteonectin plays a crucial role in tissue remodeling and preventing pathological calcification[91, 93].

1.8.4. Bone Sialoprotein (BSP)

Bone sialoprotein (BSP) is an extracellular matrix (ECM) protein that plays a role in the promotion of hydroxyapatite crystal nucleation[87]. Although its primary function is associated with bone formation, BSP has also been identified as expressed in calcified vascular tissues, particularly advanced atherosclerotic plaques[87]. This dual presence underscores its potential involvement in both physiological and pathological calcification processes[87, 92].

The mechanism of action of BSP in vascular calcification is multifaceted and distinct from that of many other proteins involved in this process. Unlike proteins that inhibit calcification, BSP actively promotes the nucleation of hydroxyapatite crystals[87, 92, 95]. In

the vascular context, BSP expression is closely associated with areas of intense mineral deposition, particularly in regions in which VSMCs undergo chondrogenic/osteogenic differentiation[87]. This suggests that BSP plays a pivotal role in the initiation and progression of vascular calcification[87, 92].

The presence of BSP in calcified arteries is strongly associated with pathological calcifications. Elevated levels of BSP in the vasculature are frequently observed in conditions characterized by abnormal mineral deposition, such as atherosclerosis and chronic kidney disease (CKD)[91, 130]. This association implies that BSP may serve as both a marker and a mediator of pathological vascular calcification[87, 92].

1.8.5. Osteocalcin

Osteocalcin (OC) is a peptide composed of 49 amino acids secreted by osteoblasts into the bone matrix and bloodstream[94]. During posttranslational modification, the enzyme gamma-glutamyl carboxylase, which requires vitamin K as a cofactor, carboxylates glutamic acid residues on osteocalcin prohormone[131]. This modification results in the formation of γ-carboxyglutamic acid (Gla) residues, with human osteocalcin containing three Gla residues per molecule[132]. Once carboxylated, osteocalcin is cleaved from its prohormone form and secreted by osteoblasts, thereby aiding bone matrix formation[131]. Additionally, some uncarboxylated osteocalcin is released into the bloodstream, where it enhances insulin secretion from pancreatic beta cells, thereby influencing glucose metabolism[131, 133]. Osteocalcin, a 5.7 kDa peptide, is the most abundant non-collagenous protein in the bone

matrix. After synthesis, OC is released into circulation, where it has a short half-life and is rapidly cleared by the kidneys within approximately five minutes[18, 132]. Various fragments of intact molecules are also present in the circulation. Serum OC is considered a specific and sensitive marker for bone formation, as it is found in bone tissue and its levels increase during periods of rapid skeletal growth[133].

The hydroxyapatite-binding function of OC, which is essential for bone mineralization, requires posttranslational carboxylation of three glutamic acid residues to γ-carboxyglutamic acid by a vitamin K-dependent carboxylase. Insufficient dietary intake of vitamin K leads to higher levels of undercarboxylated osteocalcin (Glu-OC) in children[133]. No definitive association has been determined between OC and vascular calcification or atherosclerosis. However, the presence of OC-positive cells and histological staining showed a consistent positive correlation with calcification or atherosclerosis[134].

1.8.6. Fetuin-A

Fetuin-A is a glycoprotein that acts as a systemic inhibitor of calcification, particularly in blood and extracellular fluid[135]. It is primarily synthesized by the liver and circulates in the plasma, where it helps maintain calcium and phosphate homeostasis[136]. Although not produced by SMCs, fetuin-A prevents hydroxyapatite formation by binding to calcium-phosphate complexes in the bloodstream and preventing their deposition in arterial walls[136].

The mechanism of action of fetuin-A involves two key processes: formation of protein-mineral complexes and protection against vascular calcification[135-138]. In the first process, fetuin-A binds to calcium and phosphate, forming soluble protein-mineral complexes that prevent the precipitation of hydroxyapatite crystals in the blood and vascular tissues. Macrophages then clear these complexes to prevent the accumulation of mineral deposits in the vascular wall[135-137]. In the second process, fetuin-A protects the arteries from calcification by inhibiting the nucleation and growth of hydroxyapatite[139].

Fetuin-A deficiency is associated with increased vascular calcification, particularly in patients with chronic kidney disease (CKD)[140]. Its ability to form soluble complexes with calcium and phosphate prevents the formation of hydroxyapatite crystals, which are key components of vascular calcification[135, 139]. This protective function is especially important in the context of diseases, such as CKD, where disruptions in mineral metabolism can lead to accelerated vascular calcification[135, 137, 139, 140].

.9. Genome-Wide Association Studies (GWAS) and Coronary Artery Calcification

In addition to the previously mentioned monogenic rare mutations which contribute to calcification, genome-wide association studies (GWAS) have significantly advanced our understanding of the genetic basis of coronary artery calcification, a critical indicator of cardiovascular risk. CAC is a quantifiable measure of subclinical atherosclerosis and is strongly predictive of coronary artery disease events[141] (Figure 1.4). These studies suggest

that 40-50% of CAC variance is attributable to genetic factors, highlighting the importance of understanding the genetic and molecular mechanisms underlying this condition[3].

1.9.1. GWAS Findings for CAC

GWAS have identified several genetic variants associated with CAC, including the prominent 9p21.3 locus[142, 143]. This locus was the first to be associated with an elevated risk of coronary atherosclerosis and has been linked to both symptomatic and asymptomatic CAC and aortic calcification[141]. Variants at this locus affect *ANRIL* expression, a long non-coding RNA that regulates the cell cycle and VSMC proliferation[144]. Risk alleles at 9p21.3 are linked with decreased expression of *CDKN2A* and *CDKN2B*, genes encoding tumor suppressors p16 and p15, respectively[83, 144, 145]. These changes promoted VSMC proliferation, plaque instability, and calcification.

1.9.2. Cohort Studies and Meta-Analyses

GWAS utilizes high-density single nucleotide polymorphism (SNP) arrays to genotype extensive cohorts, thereby identifying the genetic variants associated with CAC risk. GWAS initially covered a broad range of CAD studies but has gradually focused on CAC research. CAC specifically. A fundamental meta-analysis of GWAS data for CAD by Schunkert et al. (2011) identified 13 novel loci and corroborated 10 previously reported loci (Figure 1.4). This foundational work has catalyzed subsequent CAC-specific investigations[141]. O'Donnell *et al.* (2011) conducted a GWAS meta-analysis targeting CAC

in 9,961 participants from five independent community-based cohorts and identified several loci associated with CAC, including 9p21 and *PHACTR1*[143] (Figure 1.5 A). The 9p21.3 remains as strongly associated with CAC. A recent study by de Vries et al. (2023) identified six genetic loci (including two considered novel) associated with CAC (Figure 1.5 B), which confirmed that 9p21.3 shows the highest association with CAC.

1.9.3. Multi-Ancestry Studies

The largest multi-ancestry GWAS meta-analysis, involving 35,776 individuals (26,909 of European ancestry and 8,867 of African ancestry), elucidated substantial genetic contributions to CAC. This study identified 11 independent risk loci for CAC, including eight novel loci linked to various biological pathways, such as bone mineralization regulation, vitamin D receptor signaling, riboflavin metabolism, phosphate catabolism and homeostasis, and hormone secretion pathways. Among the 43 candidate genes identified, five novel loci (*ENPP1/ENPP3, IGFBP3, ARID5B, ADK*, and *FGF23*) were previously unassociated with coronary artery disease[142].

1.9.4. Population Variability

The prevalence of the minor allele frequencies (MAF) for the 9p21.3 risk locus varies across populations: European (50%), Sub-Saharan African (50%), African American (24%), Asian (47%), and Han Chinese (37%). This variation underscores the importance

of conducting multi-ethnic GWAS to fully understand the genetic architecture of CAC[146, 147].

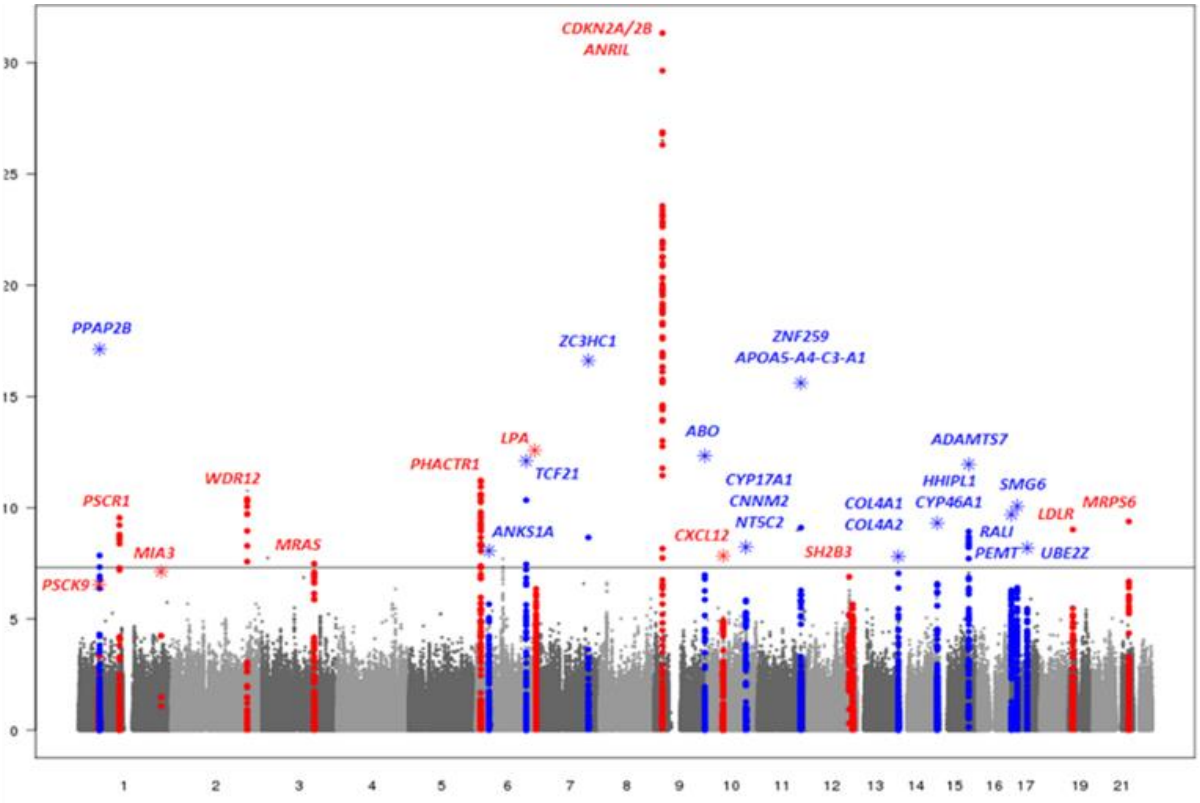

Figure 1.4 Visualization of Significant SNPs in CAD Using Manhattan Plot from CARDIoGRAM Data (GWAS of log(CAD + 1)).

A Manhattan plot was generated using the CARDIoGRAM data to visualize significant SNPs associated with CAD[141]. In the Manhattan plot, each genetic variant is included as a dot, with the position on the x axis corresponding to their genomic position and the position on the y axis corresponding to the significance of the association, denoted by –log10

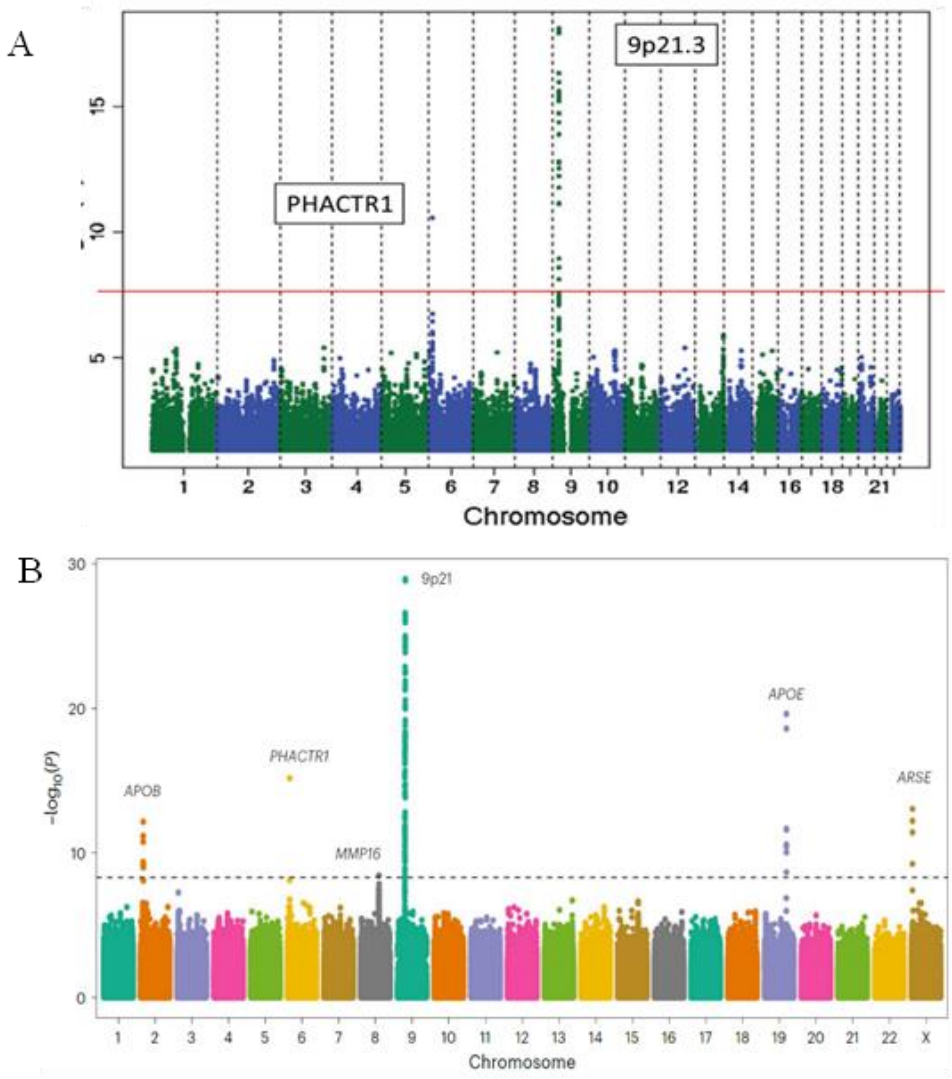

Figure 1.5. **Genome-Wide Association Study of Coronary Artery Calcification: Manhattan Plot Visualization.**

A) Donnell *et al*.'s study[143] was genome-wide association study meta-analysis for coronary artery calcification (CAC) conducted in 9,961 participants from five independent community-based cohorts, with replication in three additional independent cohorts (n=6,032). B) Results of a genome-wide association study conducted on 22,400 diverse

individuals from 10 different studies[142]. It shows six genetic loci associated with CAC score at a significance level of P < 5 × 10^-9.

1.9.5. Functional Insights into the Mechanisms underlying GWAS signals

Recent functional studies have provided insights into how the 9p21.3 locus influences CAC[142, 143]. Variants at this locus affect ANRIL expression, which in turn regulates the cell cycle and VSMC proliferation[148]. These changes promoted VSMC proliferation, plaque instability, and calcification[148]. Elevated circulating levels of ANRIL may also predict later onset of type 2 diabetes[149]. The 9p21.3 locus is one of the most significant genetic regions associated with CAC and CAD[141]. This locus contains up to 33 enhancers with CAD or type 2 diabetes risk variants and encompasses 59 linked single-nucleotide polymorphisms (SNPs) [141, 150]. It is located approximately 100,000 base pairs upstream of the cell cycle suppressor genes[151, 152] *CDKN2A*, and *CDKN2B*, and overlaps with the 3' region of ANRIL, a non-coding RNA gene[141, 14]. This locus contained a functional enhancer[141].

The genetic structure and function of the 9p21.3 risk variants affect ANRIL expression, a long non-coding RNA that regulates the cell cycle and VSMC proliferation[153]. Risk alleles are associated with decreased expression of *CDKN2A* and *CDKN2B*, which are genes encoding tumor suppressors p16 and p15[146, 148]. These changes promote VSMC proliferation, plaque instability, and calcification[154, 155]. The risk allele contains a functional enhancer that significantly increases the reporter gene expression in primary aortic smooth muscle cells[145].

ANRIL Function and Structure: ANRIL may act as a scaffold to guide effector proteins to the chromatin. Its functions depend on an Alu motif in ANRIL RNA, mirrored several thousand-fold in the genome[154]. *ANRIL* produces alternative transcripts such as DQ485453, DQ485454, and EU741058[144]. Homozygous risk allele carriers showed increased expression of short *ANRIL* variants (2.2-fold) and decreased expression of long variants (1.2-fold)[155] (Figure 1.6). Besides CAC and CAD, 9p21.3 risk variants are associated with aortic aneurysm[156-158], intracranial aneurysm[159], and periodontitis [160-162]. Recent studies have reported 9p21.3 risk variants influencing plasma lipid profile and lipid uptake in vascular elevated circulating levels of ANRIL may predict later onset of type 2 diabetes cells[149, 163].

1.9.6. The Role of ANRIL Transcripts in mRNA Decay and Gene Regulation

ANRIL transcripts play a significant role in modulating mRNA decay through a process known as Staufen1 (STAU1)-mediated mRNA decay (SMD) in mammalian cells. This mechanism involves STAU1, a double-stranded RNA-binding protein, which recognizes specific binding sites within the 3'-untranslated region (3'UTR) [164] of target mRNAs. These binding sites can be formed through intramolecular base pairing of 3'UTR sequences or intermolecular pairing with long non-coding RNAs (lncRNAs), particularly via partially complementary Alu elements[165]. The formation of STAU1-binding sites is a complex process that often results from imperfect base-pairing between an Alu element in the 3'UTR of an SMD target and another Alu element in a cytoplasmic polyadenylated lncRNA. This

interaction highlights the intricate relationships between different RNA species in the cellular regulatory networks. Researchers have extensively investigated the diverse secondary structures recognized by STAU1 proteins, revealing the complexity and specificity of these interactions,[165, 166].

Alu elements exert a broad influence on gene regulation through various means, including Alu-mediated silencing. These elements can regulate gene expression through promoters or unspliced transcripts, often triggering epigenetic modifications, such as DNA methylation and histone changes. These alterations can lead to transcriptional silencing or attenuation of nearby genes, demonstrating the far-reaching effects of Alu elements on gene expression[154, 165].

The abundance of Alu elements in gene-rich regions further underscores their importance as regulatory platforms. They exert a significant influence over transcriptional control and have the potential to function as enhancers or silencers, depending on their specific context and modifications. This versatility in function emphasizes the important role of Alu elements in fine-tuning gene expression and cellular processes.

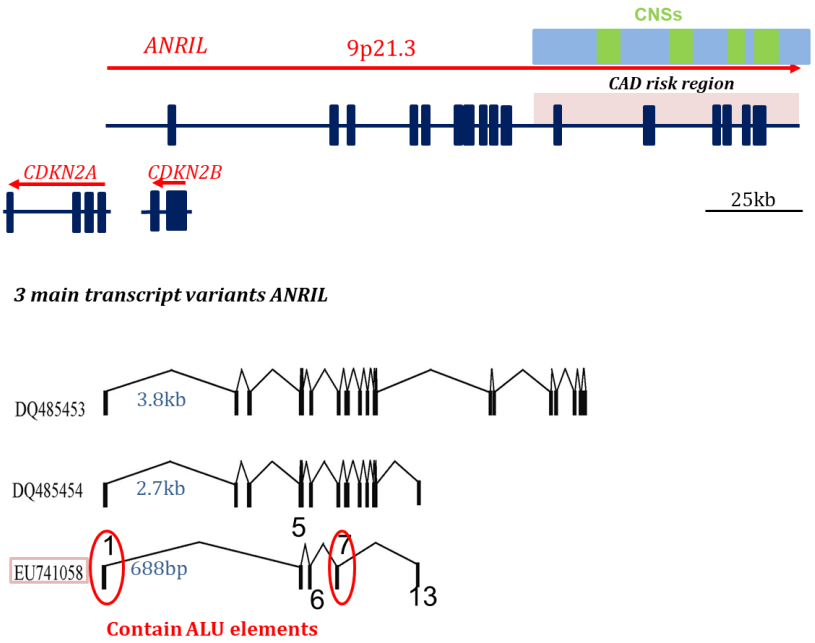

Figure 1.6. Alu motifs in ANRIL lncRNAs transregulate many genes.

9p21.3 covers the 3′ end of a long noncoding RNA transcript antisense to *CDKN2B*, whose expression has been linked to the locus. *ANRIL* produces alternative transcripts DQ485453, DQ485454, and EU741058. In the subjects homozygous for the risk allele compared to individuals homozygous for the reference allele, it was shown by Jarinova *et al* (2009) that expression levels of the two short variants of ANRIL were increased around 2.2-fold. Consistently, in individuals homozygous for the risk allele, the expression of the shortest *ANRIL* transcript, EU741058, was significantly greater, while expression levels of the long variant were decreased by approximately 1.2-fold in subjects homozygous for the risk allele versus the reference allele[155].

1.9.7. Other Significant Genetic Variants

Beyond the 9p21.3 locus, other significant genetic variants have been identified as contributors to CAC. A recent study by de Vries *et al.* (2023) identified six genetic loci

(including two novel loci) associated with CAC scores at a significance level of $P < 5 \times 10{-}9$ in a pooled analysis of 22,400 individuals from 10 studies. This study confirmed previously identified loci, such as *9p21, PHACTR1, LPA*, and *ADAMTS7*, while discovering two novel loci, ARSE and MMP16.[142, 167] (Figure 1.5B). Functional validation studies have confirmed the role of these newly identified genes in CAC development. For instance, ARSE promotes chondrogenic/osteogenic phenotype switching in VSMCs, contributing to vascular calcification[142, 167]. MMP16 appeared to inhibit this transition. MMP16 is expressed in coronary artery VSMCs, and MMP16 expression decreases by approximately 75% when VSMCs are grown in chondrogenic/osteogenic media compared with normal media. Silencing MMP16 did not affect the chondrogenic/osteogenic phenotype or calcification[142, 167].

1.10. Statherin: a newly discovered Hydroxyapatite binding protein in HAoSMCs

Statherin is a protein previously thought to be confined to expression within the salivary glands. Statherin contains a hydroxyapatite binding motif, which also plays a crucial role in oral health by preventing calcification in the mouth. It binds tightly to hydroxyapatite surfaces in saliva, inhibiting the formation and growth of calcium phosphate crystals, which helps prevent dental plaque and calculus formation (Figure 1.7, sections 1.10.1 and 1.10.2).

While primates retained and conserved the STATH gene, it became a pseudogene in the rodent lineage after the rodent-primate split (Figure 1.8 and 1.10.3). This unexpected

finding may explain the difference between the severe arterial calcification in *Mgp*-KO mice and the rare phenotype observed in humans lacking MGP.

1.10.1. Statherin differentially expressed by 9p21.3 genotype in primary human aortic smooth muscle cells

The microarray results of primary human aortic smooth muscle cells (HAoSMCs) for various genotypes of 9p21.3 (Figure 1.9) showed that HAoSMCs with normal genotyping of the 9p21.3 risk genotype expressed only two mRNAs for hydroxyapatite-binding proteins at similar levels: matrix GLA protein (MGP) and statherin (Table 1.3). Among the genes affected by the 9p21.3 homo risk genotype, statherin ranked highest (Table 1.3). Table 1.3 shows normalized fluorescence intensity Values, which reflects relative gene expression levels rather than absolute transcript counts. Measure the relative abundance of RNA transcripts by detecting fluorescence signals from labeled cDNA hybridized to complementary probes on the chip. Whole-genome microarray expression analysis showed that HAoSMCs homozygous for the 9p21.3 risk variants expressed very low levels of statherin, whereas heterozygous cells expressed intermediate levels, and cells homozygous for the non-risk allele expressed statherin at levels similar to MGP. Interestingly, whole-genome expression analysis of HAoSMCs for 9p21.3 genetic variants revealed that statherin was the most differentially expressed hydroxyapatite-binding protein mRNA according to 9p21.3 risk genotypes (Stewart Lab unpublished) (Table 1.3). Statherin exhibited a 25-fold higher expression in HAoSMCs homozygous for the non-risk (HNR)

allele of 9p21.3 compared to cells homozygous for the risk (HR) allele. In HNR-HAoSMCs, statherin is expressed at levels similar to MGP, another well-known secreted hydroxyapatite-binding protein that limits arterial calcification. Statherin is the only hydroxyapatite-binding secreted protein gene affected by the 9p21.3 genotype, which may explain the variability of arterial calcification in Keutel syndrome patients. However, the mechanism underlying this difference remains unclear.

In mouse models, warfarin rapidly induced significant arterial calcification within two weeks, affecting the medial layer of the aorta and heart in a dose- and time-dependent manner. The rapid onset of calcification in rodents treated with warfarin is a well-established model for studying vascular calcification. Warfarin, by inhibiting the vitamin K cycle, exacerbates this condition by preventing the γ-carboxylation of MGP, rendering it inactive. In contrast, humans exhibit a complex relationship between MGP deficiency and arterial calcification. The effects of warfarin on arterial calcification in humans appear to be gradual and variable. Long-term warfarin treatment is associated with an increase in systemic calcification, including in the coronary and peripheral vasculature, but the process seems to occur over a longer period than the rapid onset observed in mice. There is significant variability in the extent of calcification among warfarin-treated human patients, suggesting that other factors may influence this process. People with high calcification are likely to be homozygous for the 9p21.3 risk variants, which inhibit statherin expression.

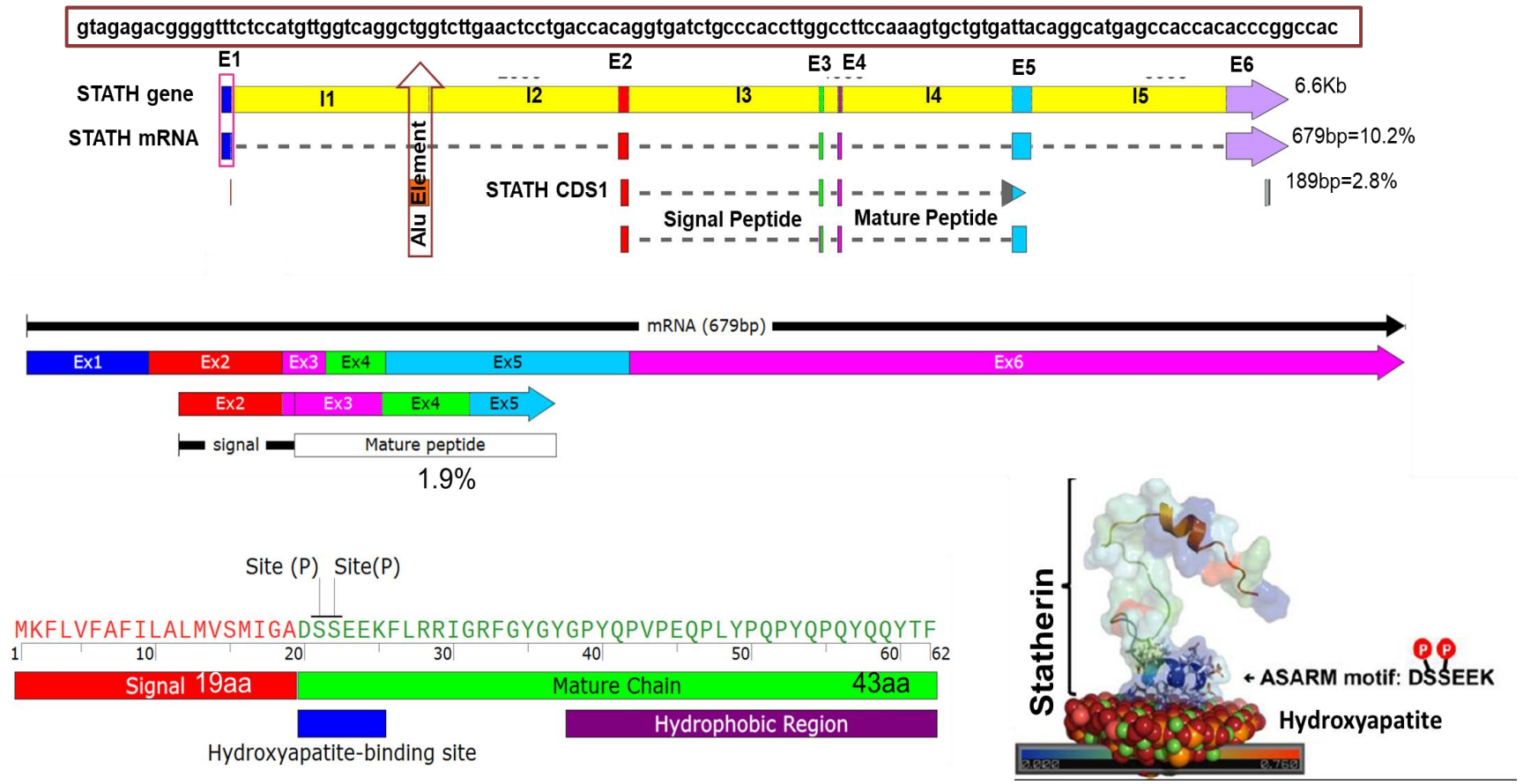

Figure 1.7. **Overview of statherin gene and protein structures**

This figure illustrates statherin from DNA to protein, highlighting key processes, such as transcription, RNA splicing, and translation.

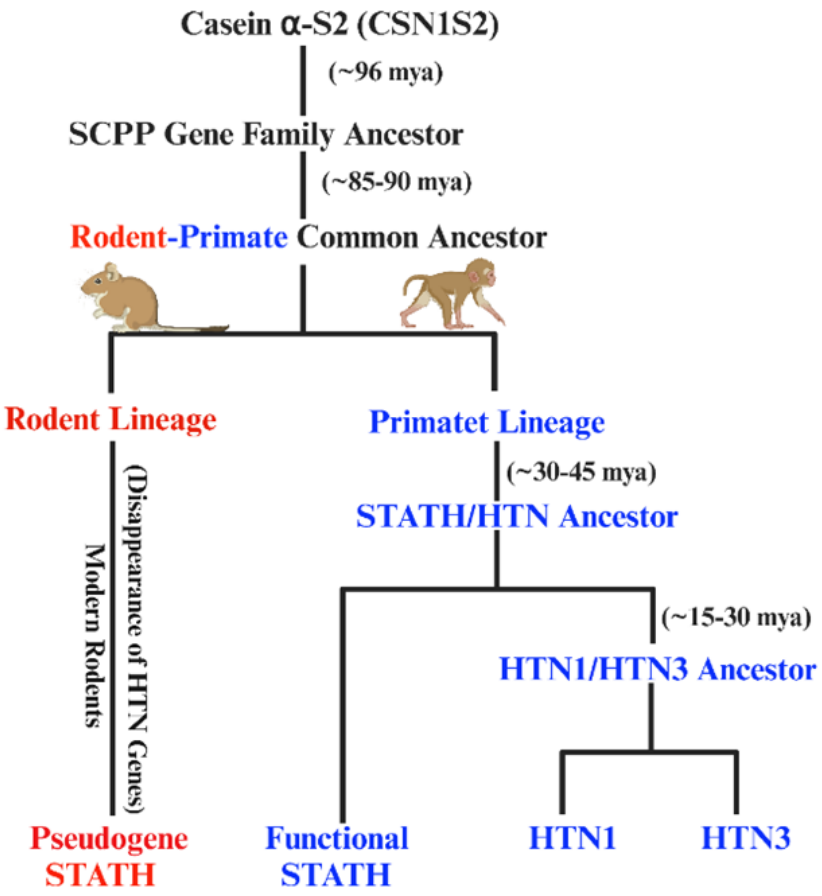

Figure 1.8. **Phylogenetic tree of vertebrate SCPP gene family**

This diagram illustrates the evolutionary relationships and divergence times of various secretory calcium-binding phosphoprotein (*SCPP*) genes across different vertebrate species. The tree highlights the emergence and diversification of genes, such as statherin (*STATH*), histatin (*HTN*), and other related genes from a common ancestor. Branch lengths represent evolutionary time, with estimated divergence times indicated at key node.

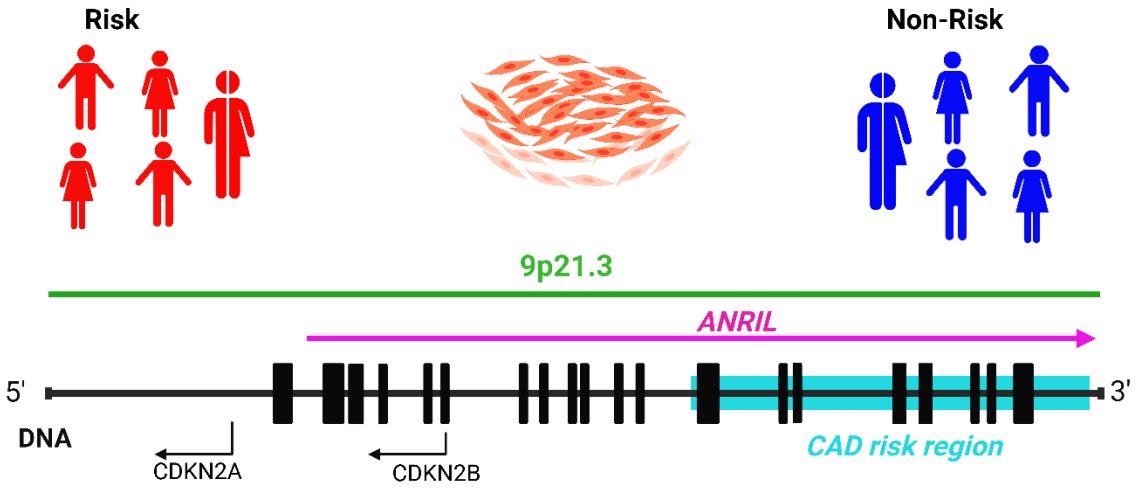

Figure 1.9. Microarray analysis of different genotypes of 9p21.3 genes.

Microarray analysis was used to compare gene expression patterns between different genotypes of the 9p21.3 risk locus in HAoSMCs. This approach allowed identification of variations in gene expression associated with the risk and non-risk alleles.

Table 1.3. ASARM motif gene expression profile of VSMCs

Table 1.3. ASARM motif gene expression profile of VSMCs						
Rank	**HR avg ± SD**	**HET avg ± SD**	**HNR avg ± SD**	**HR/HNR**	**BH**	**Gene Symbol**
1	6.5 ± 0.999	260 ± 319	176 ± 49.6	0.0369	1E-11	*STATH*
649	15.8 ± 5.87	10.7 ± 1.08	8.66 ± 1.33	1.82	0.180246	*SPP1*
4187	117 ± 154	101 ± 131	188 ± 136	0.622	0.748218	*MGP*
11282	6.06 ± 0.215	5.71 ± 0.153	5.61 ± 0.204	1.08	0.8218768	*DSPP*
11962	7.98 ± 0.869	7.1 ± 0.714	7.33 ± 0.0757	1.09	0.8300919	*IBSP*
15342	5.07 ± 0.686	4.68 ± 0.23	4.8 ± 0.141	1.06	0.8764356	*DMP1*
19560	5.28 ± 0.0972	4.8 ± 0.205	5.22 ± 0.678	1.01	0.9529179	*MEPE*

This unexpected finding may explain the discrepancy between severe arterial calcification in *Mgp*KO mice and the variant phenotype observed in humans lacking MGP and a variety of calcifications between people in the context of warfarin therapy. Interestingly, the microarray results of statherin were the most differentially expressed genes affected by 9p21.3 risk variants in HAoSMCs, making them prone to calcification.

1.10.2. Statherin: A Multifunctional Phospho-Peptide

Statherin is a multifunctional phospho-peptide encoded by the *STATH* gene on chromosome 4q13.3 in humans. This 43-amino-acid protein, weighing approximately 5.4 kDa, is rich in tyrosine, proline, and glutamine[168]. It has two domains, a polar N-terminal domain and a hydrophobic C-terminal domain. The N-terminal region contains a unique motif, DpSpSEEKFLRR, with phosphorylated serine residues that bind to hydroxyapatite, aiding in enamel protection[70, 75, 7]. The C-terminus, which becomes an alpha-helix upon

binding to tooth surfaces, inhibits bacterial growth and Candida albicans formation[137, 138]. Statherin is abundant in saliva, preventing calcium and phosphate supersaturation and contributing to oral health by modulating microbial colonization and biofilm formation[169].

1.10.2. Posttranslational Modifications

Statherin undergoes several post-translational modifications (PTMs) that significantly influence its functionality. The most critical PTM is the phosphorylation of serine residues at positions 2 and 3, which is essential for high-affinity hydroxyapatite binding[170, 171].. Proteolytic processing generates various isoforms, including SV1, SV2, and SV3, each with distinct characteristics[172-176]. Statherin can also form a cyclic derivative through transglutaminase 2 action[177]. Glycosylation adds carbohydrate chains, enhancing solubility and stability[178], [177]. N-terminal modifications include the loss of the initiating aspartic acid residue and converting N-terminal glutamine to pyroglutamic acid, which may increase the resistance to proteolytic degradation[179].

1.10.3. Evolutionary and Early Diversification of Statherin

The evolution of statherin in primates is highly conserved, reflecting its important role in oral health. A significant gene duplication event 40-50 million years ago led to separate *STATH* and *HTN1/HTN3* lineages, with another duplication 15-30 million years ago splitting *HTN1* and *HTN3*[180-182]. These genes show high sequence identity in non-coding regions but only 38-43% in coding regions, indicating accelerated evolution. Statherin

maintains the mineral balance in saliva, preventing tooth demineralization[180-182]. In contrast, rodents lost the *STATH* gene, which became a pseudogene after the rodent-primate split[182], likely due to dietary and physiological differences[181, 183, 184]. Rodents also lack histatin genes (*HTN1* and *HTN3*) [182]. Positive selection in primates for saliva-related *SCPP* genes, including *STATH* and *HTN*, contrasts with the conservation of other genes in the same locus[185, 186]. This divergence highlights different evolutionary pressures across species, with statherin being minimal or absent in carnivores like ferrets but conserved in primates and large herbivores due to dietary needs and lifespan[181, 183, 184].

1.11. Summary:

GWAS have identified several key genetic loci associated with this phenotypic switch in VSMCs during arterial calcification.The 9p21.3 locus has been extensively studied for its impact on CAC and VSMC behavior[145, 147]. This locus harbors variants associated with altered expression of ANRIL, a non-coding RNA that regulates the cell cycle and influences VSMC proliferation[155].

Collectively, these data led me to propose that, **in addition to MGP, statherin in human smooth muscle cells prevents coronary artery calcification, and its expression is modulated by the 9p21.3 variants.** This may explain the discrepancy between severe arterial calcification in *Mgp*KO mice and the varied phenotypes observed in Keutel syndrome human patients and individuals who received warfarin.

Hypothesis: Alendronate's hydroxyapatite-chelating effect alone can not prevent arterial

calcification as its efficacy is mediated through the matrix Gla protein (MGP), and that in addition to MGP and PPi, STATH in human SMCs functions to prevent CAC. Loss of statherin expression contributes to CAC risk conferred by 9p21.3 risk variants.

Significance: The mechanism by which statherin inhibits hydroxyapatite formation involves its ability to bind tightly to hydroxyapatite surfaces, thereby preventing further crystal growth and aggregation. This inhibitory action could translate into a protective effect against vascular calcification by maintaining the balance between mineralization and tissue integrity within the vasculature. Therefore, statherin may represent a novel therapeutic target for mitigating arterial calcification and associated cardiovascular diseases. Understanding how statherin functions in vascular tissues could provide new insights into the prevention of ectopic calcification and highlight its potential as an inhibitor modulated by genetic factors such as those at the 9p21.3 locus

To address this hypothesis, I propose the following research aims:

Research Aims

1. To investigate whether the hydroxyapatite-chelating effect of alendronate alone is sufficient to prevent arterial calcification or whether its anti-calcification effect is mediated through Mgp. Further, we asked whether alendronate affects endocytosis of hydroxyapatite by macrophages.
2. To assess if the short antisense noncoding RNA at the *INK4* locus (*ANRIL*) affects statherin expression, providing insight into the regulatory mechanisms at this 9p21.3

locus.

3. To determine whether expressing human statherin in smooth muscle cells can rescue arterial calcification in *Mgp*KO mice to demonstrate the potential therapeutic role of statherin.
4. To examine whether statherin inhibits BMP signaling, such as MGP, and to understand the molecular mechanisms of its calcification-inhibiting properties.

This study aimed to elucidate the regulatory mechanisms at the 9p21.3 locus, assess the therapeutic potential of statherin in rescuing arterial calcification in *Mgp*KO mice, and investigate whether statherin inhibits bone morphogenetic protein (BMP) signaling, similar to MGP. These investigations are grounded in recent advancements in genome-wide association studies (GWAS), which have highlighted the genetic and molecular underpinnings of CAC, particularly the role of vascular smooth muscle cells (VSMCs), and their phenotypic switching from a contractile to an chondrogenic/osteogenic state.

The findings from this study provide a comprehensive understanding of the genetic and molecular mechanisms involved in arterial calcification ultimately contributing to the development of novel therapeutic strategies for preventing CAC and improving cardiovascular health.

Chapter 2: Methods

2.1. Alendronate Therapy Materials and Methods

2.1.1. *Mgp*KO Mice

C57BL/6J *Mgp*+/− mice, heterozygotes for deletion of the promoter and exons 1-4 of the *Mgp* gene [32], were obtained from Jackson Laboratories (strain: B6.129S7-*Mgp*tm1Kry/KbosJ, Stock No: 023811) and maintained on a standard chow diet (Diet number 2019, Inotiv Inc.). Mice were bred at the University of Ottawa Heart Institute animal facility according to a protocol (UOHI 3630) approved by the Animal Care and Use Committee of the University of Ottawa. The University of Ottawa Heart Institute is accredited by the Canadian Council on Animal Care and meets all relevant policies and guidelines for ethical animal care. Genotypes were confirmed using a modification of the protocol #24689 from the Jackson Laboratory. The common reverse primer was extended (5'-CGA AAC TCC ACA ACC AAA TGA CTG-3') to improve the temperature match between the wild-type (5'-GAG AGG CCT GCG ATG ACT AC-3') and mutant (5'-CCT TCT ATC GCC TTC TTG ACG-3') forward primers. WT littermates were used as the controls. The PCR protocol using PCR Master Mix, 2X (Promega, #M7502) consisted of initial denaturation at 94°C for 4 min, followed by 30 cycles of denaturation at 94°C for 20 s, annealing at 60°C for the mutant allele, 58°C for the wild-type allele for 20 s, and extension at 72°C for 35 s, with a final extension step at 72°C for 5 min.

2.1.2. Alendronate Therapy

Alendronate is a nitrogen-containing bisphosphonate known to hinder the mevalonate pathway and limit osteoclastic function and activity. Alendronate sodium trihydrate acts as a bone resorption inhibitor, a farnesyl diphosphate synthase inhibitor (IC50 = 460 nM), and a CD45 protein tyrosine phosphatase inhibitor[187]. In this study, we used alendronate sodium trihydrate (C4H12NaNO7P2 · 3 H2O), which has a solubility in water of >10 mg/mL (Sigma, A4978, CAS Number 121268-17-5).[188]The compound was dissolved in deionized water, and serial dilutions were prepared to achieve the desired concentrations for injection.

2.1.2.1. Dosage Justification

The chosen dosages of alendronate (ALN) in this study are supported by its pharmacokinetic and pharmacodynamic properties, as well as preclinical evidence demonstrating its efficacy in preventing arterial calcification and bone resorption[33]. Alendronate has a long skeletal half-life, remaining active for weeks due to its incorporation into calcified tissues, which reduces the need for frequent dosing[188]. The EC50 for alendronate's inhibition of osteoclastic activity is well-established[188, 189], showing effective suppression of bone resorption at doses as low as 0.05 mg/kg in animal models.[188] Clinically, 70 mg weekly or 10 mg daily is recommended for osteoporosis treatment due to its ability to increase bone mass and reduce fracture risk[190].

For adult *Mgp*KO mice, dosages of 0.25 and 0.7 mg/kg /week were selected based on prior studies demonstrating that 0.7 mg/kg successfully rescues rats from warfarin induced arterial calcification[33]. The 0.25 mg/kg dose of alendronate was chosen because it has been shown to be effective in previous studies for preventing and reversing partially vascular calcification in warfarin induced animal models[33]. This dose balances therapeutic efficacy and safety, minimizing potential toxicity while achieving desired outcomes. Additionally, in mouse models of osteogenesis imperfecta, low doses of alendronate (0.125 mg/kg/week) were found to enhance bone strength without significantly affecting bone growth plate morphology[189].

While there are no studies specifically investigating early intervention at day 3 in *Mgp*KO mice and no established dosage has been reported for this time frame, varying dosages of alendronate were employed in this study to optimize efficacy during the critical window when calcification begins. By testing different dosages, the study aimed to identify the most effective dose for preventing or mitigating arterial calcification while minimizing potential adverse effects on bone remodeling or systemic health. This approach allows for a dose-response analysis to determine the optimal therapeutic range for alendronate during early disease progression, addressing the lack of prior studies in this specific model and intervention timeline.

2.1.2.2. Experimental Design

*Mgp*KO mice were divided into experimental and control groups (n = 8 per sex per group):

Experimental groups received subcutaneous injections of alendronate twice weekly at doses of 0.125 mg/kg (0.25 mg/kg/week) or 0.35 mg/kg (0.7 mg/kg/week), while the control group received PBS injections (Figure 2.1 A). Treatment began in the third postnatal week (weaning time) and continued for 4 weeks. The mouse weight, incisor malocclusion, and trimming frequency were monitored throughout the study (Figure 2.1 A).

To assess the effect of alendronate on postnatal development and early arterial calcification, mice received biweekly subcutaneous injections of alendronate at doses of 0.125, 0.25, 0.5, and 1 mg/kg/week from postnatal days 3 to 35 (Figure 2.1 B). The control group was treated PBS. Because the mice were treated prior to weaning and genotyping, both *Mgp*KO and littermate control heterozygotes or wild-type (WT) mice were treated simultaneously.

In a separate group, a single dose of Alendronate (0.25 mg/kg) was administered to *Mgp*KO and wild-type mouse pups on postnatal day 3 to investigate its effect on Runx2 expression in aortas harvested on postnatal day 5 (Figure 2.1 C).

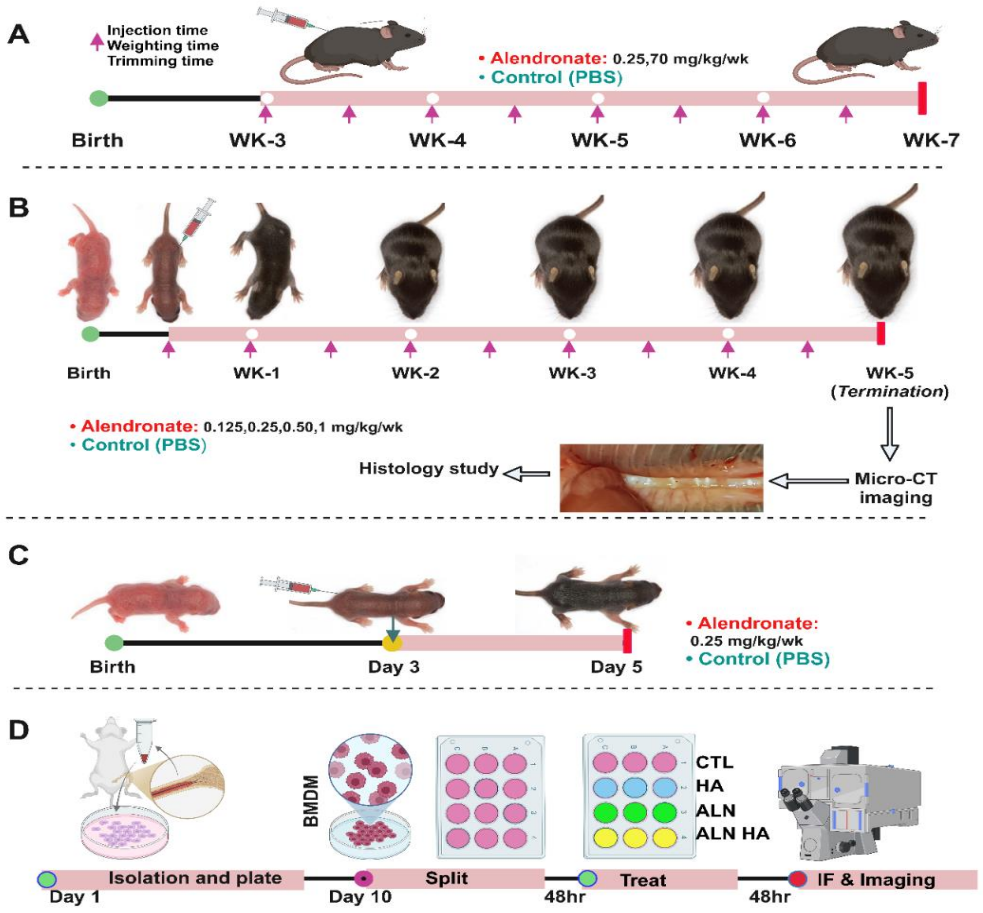

Figure 2.1. **Experimental design for alendronate therapy in *Mgp*KO mice.**

A, Weaning-initiated therapy: *Mgp*KO mice received subcutaneous alendronate injections (0.125 mg/kg or 0.35 mg/kg twice weekly) or PBS control from week 3 for 4 weeks. **B**, Postnatal therapy: Mice received alendronate injections (0.125, 0.25, 0.5, or 1 mg/kg/week) or PBS biweekly from postnatal day 3 to 35. **C**, Single-dose study: *Mgp*KO and wild-type mice received a single 0.25 mg/kg Alendronate dose on postnatal day 3, with aortas harvested on day 5 for Runx2 expression analysis. **D,** Isolation of bone marrow and differentiation into bone marrow-derived macrophages treated with ALN and HA. The timeline illustrates each experimental group's treatment schedule, monitoring parameters, and endpoints. (Created in BioRender. Soheili, F. (2024) **https://BioRender.com/i63f126)**

2.1.3. *In Vivo* Assessment of Arterial Calcification

Micro-computed tomography (μCT) imaging was performed using a Si78 PET/CT instrument (Bruker BioSpin MRI GmbH) to image and quantify arterial calcification in wild-type (n = 8/group) and *Mgp*KO mice treated with alendronate (0.25 mg/kg/week from postnatal day 3 to week 5, n = 8) or PBS (n = 8). Mice were anesthetized using 2–4% isoflurane in oxygen and placed on the scanner bed with continuous maintenance of anesthesia, warm air supply, and monitoring of the respiration rate and temperature. CT data were acquired in step and shoot mode using a 0.5 mm Al filter, 50 kV voltage, 901 μA current, and 45 ms exposure time. Image reconstruction was performed using filtered back projection to produce images with a resolution of 50 μm.

CT images were exported to PMOD 4.4 and initially evaluated for motion artifacts. A set of volumes of interest (VOIs) with fixed dimensions was placed over each of the ascending aorta (20 mm^3) and descending aorta (40 mm^3) to avoid nearby bone or other high-density tissue. Voxels with a minimum value of 150 Hounsfield units (HU) were included in the quantification of the intensity and volume for each VOI. Images were cropped to a depth of 5 mm in the sagittal plane along the spine to prepare maximum intensity projections (MIPs).

2.1.4. Histological Quantification of Calcification

Mice were euthanized by cardiac puncture under isoflurane anesthesia, and blood was

cleared by perfusion with PBS, followed by perfusion with 4% paraformaldehyde (PFA). Aortas were harvested and post-fixed in 4% PFA at 4°C for 24 h, followed by sequential dehydration in 15% and 30% sucrose in PBS, each for 24 h. Aortas were embedded and frozen in Tissue-Tek® O.C.T. compound (Thermo Fisher Inc.) and serially sectioned (n = 10 sections/mouse, 10 μm thickness) for histological analysis. To visualize calcium deposits, the sections were immersed for 2 min in Alizarin Red S solution (2% in water, Thermo Fisher Inc.) to achieve optimal staining. The sections were dehydrated by 20 immersions in acetone, followed by 20 immersions in acetone-xylene solution (1:1 v/v) and 20 immersions in pure xylene. Coverslips were added to Permount mounting medium (Thermo Fisher Inc.). Alizarin Red stained sections were imaged and analyzed using ImageJ software to quantify calcification measured as the stained area (in μm^2), mean intensity (in arbitrary units), and integrated density (area × mean intensity).

2.1.5. Immunofluorescence and Immunoblot Analysis

The antibodies used for immunofluorescence and immunoblotted studies were as follows: alpha-smooth muscle actin (α-SMCA) (Antibodies Online Inc., #ABIN185271, Rabbit), GAPDH (Santa Cruz Biotechnology Inc., #sc-59540,Mouse), RUNX2 (Antibodies Online Inc., #ABIN572068 Goat, #ABIN7260681 Rabbit), CD68 eFluor™ 660, (eBioscience™ , #50-0681-82,Mouse), Elastin (Invitrogen, #PA5-96196 Rabbit), CD45 (#eBioscience™ 14-0451-82,Rat) LAMP1/CD107a (#MAB4320,Mouse), and CD68/SR-D1 (R&D system, # MAB101141,Mouse). All antibodies used for immunofluorescence were diluted 1/100,

except for α-SMCA, which was diluted 1/200. For immunoblotting, all primary antibodies were diluted 1/2000.

For immunofluorescence, secondary Alexa Fluor™ conjugated antibodies were used at a 1/1,000 dilution: donkey anti-Goat IgG (H+L), Alexa Fluor™ 647 (Thermo Fisher Scientific # A-21447), chicken anti-Rabbit IgG (H+L) Alexa Fluor™ 488 (Thermo Fisher Scientific # A-21441), Donkey anti rat IgG (H+L) Alexa Fluor™ 555 (Thermo Fisher Scientific, # A48270) Donkey anti rabbit Alexa Fluor™ 647 (Thermo Fisher Scientific, # A-31573). For immunoblots, secondary horseradish peroxidase-conjugated antibodies were used at a 1/10,000 dilution: goat anti-mouse IgG antibody (R&D Systems, #HAF007), Rabbit anti goat (Thermo Fisher Scientific, # 31402).

We developed a modified protocol for immunofluorescence analysis followed by post-immunofluorescence Alizarin Red staining or Fluo-4 AM calcium visualization to preserve calcium deposits while enabling antigen retrieval. Following rehydration, antigen retrieval was performed overnight at 60°C using 10 mM Tris-HCl buffer (pH 9.0), which was specifically chosen to avoid EDTA-induced calcium chelation and citrate buffer. Tissue sections were permeabilized with 0.1% Triton X-100 in PBS for 20 min and blocked with 5% normal horse serum (Sigma) for 1 h at room temperature. Primary antibodies were applied overnight at 4°C, followed by three PBS washes and 1-hour incubation with fluorophore-conjugated secondary antibodies at room temperature. For calcium visualization in fixed tissues, the sections were exposed to Fluo-4 AM (2 µM) for 30 min

in the dark. Post-staining treatments included a 5-minute application of TrueView® autofluorescence quenching reagent (Vector Laboratories, Inc.) and 5-minute nuclear counterstaining with DAPI (1 µg/mL). The sections were mounted using Fluoroshield™ mounting medium (AbCam Inc.) to preserve the fluorescence. For post-immunofluorescence Alizarin Red staining, after initial immunofluorescence imaging, the slides were immersed in PBS for 5 min. The coverslips were gently removed using fine forceps or blades. Following PBS washing, the sections were stained with 2% Alizarin Red solution for 2 min, as described above.

2.1.6. Isolation of Bone Marrow-Derived Macrophages (BMDMs)

Bone marrow-derived macrophages (BMDMs) were isolated from murine femurs and tibias (Figure 2.1 D) following a modified version of the standard protocol described by Weischenfeldt and Porse [191], as we described previously [192]. Briefly, the extruded cell suspension was centrifuged at 400 × g for 5 min at 4°C, and the cell pellet was resuspended in 1 mL of red blood cell lysis buffer (155 mM NH_4Cl, 10 mM $KHCO_3$, 0.1 mM EDTA) per mouse and incubated for 7 min at room temperature. The lysis reaction was then neutralized by adding 5 mL of fetal bovine serum (FBS; Gibco, Thermo Fisher Scientific, Inc.). The cells were centrifuged again at 400 × g for 5 min at 4°C and the supernatant was discarded. RBC-depleted bone marrow cells were resuspended in culture medium and filtered through a 100 µm mesh filter. Cells were cultured at 37°C in a 5% CO_2 atmosphere in DMEM/F12 medium supplemented with 20% L929 cell-conditioned medium and 10%

FBS for 10 days to allow differentiation into macrophages. Differentiated BMDMs were harvested by incubating adherent cells with 50 mM EDTA in calcium- and magnesium-free HBSS at 4°C for 10 min, followed by gentle scraping.

2.1.7. Visualization of Hydroxyapatite Uptake in BMDM

BMDMs were seeded into 24-well plates at a density of 2.5 x 10^5 cells per well in DMEM/F12 medium supplemented with 20% L929 cell-conditioned medium and 10% FBS. After 48 h, cells were treated in DMEM/F12 medium containing high phosphate (2.5 mM) and 10% FBS, or with this medium supplemented with 50 µg/ml hydroxyapatite (HA, Sigma, H0252), 12.5 µM alendronate (Sigma,121268-17-5), or both combined for an additional 48 h.

Live BMDMs were loaded with a cell-permeable calcium indicator, Fluo-4AM (AAT Bioquest, Inc. #20552), to visualize intracellular calcium. Fluo-4AM crosses cell membranes owing to its acetoxymethyl (AM) ester group, which is cleaved by intracellular esterases that trap Fluo-4 within the cell. Upon binding calcium, Fluo-4 exhibits a significant increase in fluorescence, allowing the detection of intracellular calcium levels.

A stock solution of Fluo-4AM (2 mM in DMSO) was stored at -20°C until use, diluted to a final concentration of 1.5 µM in DMEM, and added to cells for 45 min at 37°C in a humidified atmosphere containing 5% CO_2. Following incubation, cells were washed twice with Ca^{2+}- Mg^{2+}-free PBS to remove excess dye. The anionic channel inhibitor

Probenecid (Sigma, # P8761) 2.5 mM in PBS was added to all solutions after dye loading to prevent dye efflux.

2.1.8. Macrophage Immunofluorescence Staining

To track the uptake of hydroxyapatite in macrophages, cells were labeled with Fluo-4AM and the macrophage lysosomal marker CD68. In other cells, CD68 was combined with the general lysosomal marker LAMP1 to confirm localization of CD68 in lysosomes. Cells were fixed in 4% PFA in PBS for 10 minutes at room temperature, followed by several washes in PBS and a final quenching step with 50 mM NH_4Cl and 50 mM glycine for 15 minutes to eliminate free aldehyde groups. Cells were then permeabilized in 1% Triton X100 in PBS for 15 minutes at room temperature, followed by blocking with 5% horse serum in PBS for 1 hour and processed for immunofluorescence, as described above.

2.1.9 Imaging and Analysis

Calcium uptake was assessed using high-content imaging on a PerkinElmer Operetta CLS system equipped with a 40X water immersion objective. Cells were labeled with Fluo-4AM calcium indicator and anti-CD68 as lysosome and macrophage markers or anti-LAMP1 as lysosome markers. Image acquisition and analysis were performed using Harmony software (PerkinElmer), with three wells analyzed per experimental condition. The experiment was replicated using LAMP1 as an alternative marker to validate these findings. For this confirmatory analysis, immunofluorescence data were acquired using a

Zeiss microscopy system with a 63X oil immersion objective. Quantitative evaluation, Intensity-Integrated Intensity and Intensity-MeanIntensity, colocalization of lysosome markers (LAMP1 or CD68) with FLUO-4, AM by Pearson's Correlation Coefficient, Correlation Manders lysosome, Correlation Costes tests, MAD intensity (Median Absolute Deviation of Intensity) to variability in hydroxyapatite distribution within the cell or lysosome was conducted using Cell Profiler image analysis software [193].

2.1.10. Statistical analysis

Depending on the variables compared, main effects were analyzed by one-way or two-way Analysis of Variance (ANOVA) followed by the appropriate post-hoc pairwise comparison tests (Tukey's or Dunnett's), with correction for multiple testing. Statistical analyses were carried out using the GraphPad Prism software (ver. 13).

2.2. Statherin and 9p21.3 Materials and Methods

2.2.1. Primary human and mouse aortic smooth muscle cell cultures

HAoSMCs from different donors (n=12) were purchased from Cell Applications (San Diego, CA) and Lonza (Walkersville, MD), cultured in Lonza SmGM-2 BulletKit medium, and genotyped for the 9p21.3 risk locus, as described previously[146]. Mouse aortas were dissected from 3-week-old *Mgp*KO mice, smooth muscle cells released by collagenase digestion and cultured as previously described[194].

2.2.2.RNA Isolation and Whole-genome Expression Analysis

RNA isolated from cultured HAoSMCs on the 4th passage was verified for integrity and purity on an Agilent BioAnalyzer. One sample failed quality assurance and was not carried forward. Whole-genome expression analysis used Affymetrix Human Gene 1.0 ST microarrays. Transcripts differentially expressed according to 9p21.3 genotypes were identified by the Benjamini-Hochberg FDR test at $p<0.05$. Data are available from ArrayExpress, accession E-MTAB-12709

Microarray experiments, such as those employing Affymetrix Human Gene 1.0 ST microarrays, quantify relative gene expression levels by measuring the abundance of RNA transcripts. This process involves hybridizing labeled cDNA to complementary probes on the chip, where the resulting fluorescence signals are proportional to transcript abundance. These signals, expressed as normalized fluorescence intensity values, reflect relative gene expression rather than absolute transcript counts. Normalization is applied to minimize technical biases from hybridization efficiency, scanner sensitivity, and dye labeling density, ensuring reliable comparisons across samples. Differentially expressed genes are then identified using statistical methods like the Benjamini-Hochberg False Discovery Rate (FDR) test to control for false positives.

2.2.3. *In vitro* Calcification Assay of HAoSMCs:

Confluent HAoSMCs were cultured 10 days in medium containing 1.4 mM (low

phosphate, LPi) or 2 mM inorganic phosphate (High phosphate, HPi). These concentrations were chosen based on their ability to mimic physiological and pathological conditions relevant to vascular calcification. concentration 1.4 mM is normal serum phosphate levels in healthy individuals[195]. The HPi concentration (2 mM) represents elevated phosphate levels seen in hyperphosphatemia, which is common in patients with chronic kidney disease or other conditions associated with vascular calcification[195]. Calcium deposition was measured using the Calcium Colorimetric Assay Kit (MAK022, Sigma), which was normalized to the total protein. Duplicate cell cultures were stained with Alizarin red (2%, adjusted to pH 4.1 with 0.5% ammonium hydroxide) to visualize the extent of calcification.

2.2.4. Statherin and Cre Recombinase mice

T*agln*-C*re* mice were obtained from Jackson Laboratories (strain: B6. Cg-Tg(Tagln-Cre)1Her/J, Stock No: 017491). T*agln*-C*re* (also called S*m22a*C*re*) transgenic mice express Cre recombinase under the control of the mouse smooth muscle protein 22-alpha (aka Transgelin) promoter[196]. The transgene consists of a *Tagln* (transgelin) promoter and a Cre gene modified to include translational consensus and nuclear localization signals. The *Tagln* promoter was used to drive transgene expression in smooth muscle cells. *Cre* recombinase mRNA expression closely matches the pattern of endogenous Transgelin expression, with the highest levels detected in the aorta, intestine, and uterus[196]. Low levels of *Cre* recombinase transcript are detected in all other organs, reflecting expression in vascular tissues. Recombination occurs in vascular smooth muscle cells of hepatic and

pulmonary arteries, but not in non-muscle cells. Genotypes were confirmed by Protocol 22392: Standard PCR Assay -generic Cre the Jackson Laboratory JAX®Mice Database. Wild-type control mice were provided by littermates.

Ectopic calcification in arterial smooth muscle cells represents a significant challenge in cardiovascular health, particularly in the context of Matrix Gla Protein (MGP) deficiency. To address this issue, an innovative approach utilizing human statherin, was developed with two transgenic mouse models being generated:1)wild type Statherin and 2) dominated activated or *DA-STATH*.

Statherin transgenic mice were generated by the Center for Mouse Genome Modification at the University of Connecticut Health Center using CRISPR/Cas9 technology to integrate a statherin donor vector into the Safe Harbor Site intron 1 of Rosa26. The design of the statherin donor vector (Figure 2.2, Appendix 3) was based on the Ai9 vector[197] (Addgene #22799) and consists of Rosa26 intron 1 sequences flanking a CMV enhancer and chicken β-actin (CAG) promoter, a chimeric intron that combines the first intron from the chicken β-actin gene to an intron of the rabbit β-globin gene, and three stop cassettes (3x) created using the SV40 poly-A signal sequence positioned 5' to the statherin cDNA to prevent its expression. The stop flox transgene expresses human statherin in cells expressing CRE recombinase of *Tagln*-Cre mice. Genomic DNA was purified from various tissues using the PureLing® Genomic DNA kits (Invitrogen, Inc.) and tissue-specific recombination (Appendix 3, Figure 2.3) and the statherin transgene

genotypes were confirmed by standard PCR assays. Wild-type controls were provided by littermates. Statherin protein expression was only detected in mice bearing the two copies of the STATHstopflox transgene on an *Tagln-Cre* background.

Domain-activated form where two serine residues (positions 21 and 22) were replaced with aspartic acid to mimic phosphorylation. This strategic modification was implemented to overcome the potential absence of proper kinase activity in mice for phosphorylating human statherin, as phosphorylation is crucial for its interaction with hydroxyapatite.

Wild type:

MKFLVFAFILALMVSMIGA**DSSEEK**FLRRIGRFGYGYGPYQPVPEQPLYPQPYQP

QYQQYTF

Domain-activated form

MKFLVFAFILALMVSMIGA**DDDEEK**FLRRIGRFGYGYGPYQPVPEQPLYPQPYQP

QYQQYTF

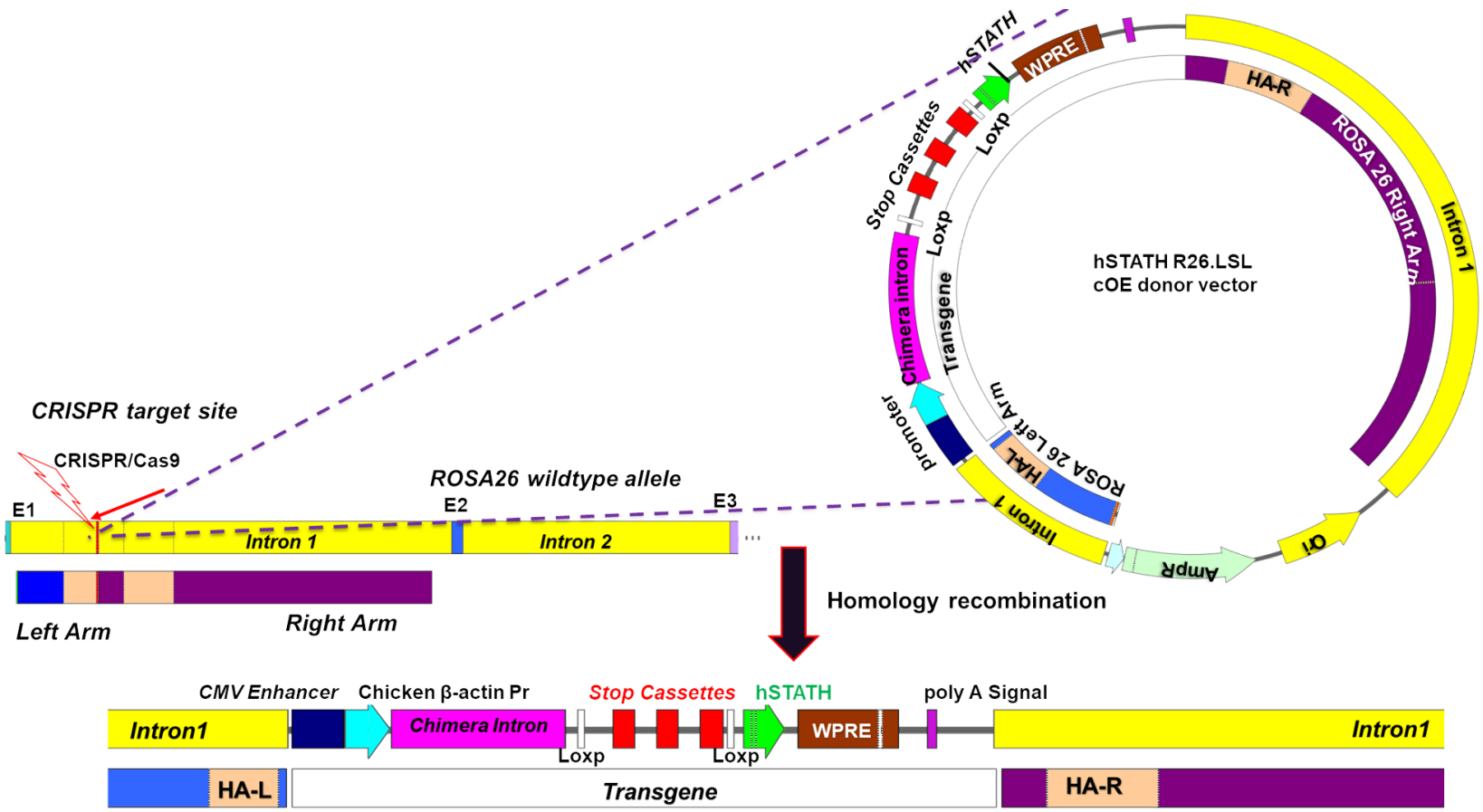

Figure 2.2. Statherin Conditional Overexpression (cOE) donor vector

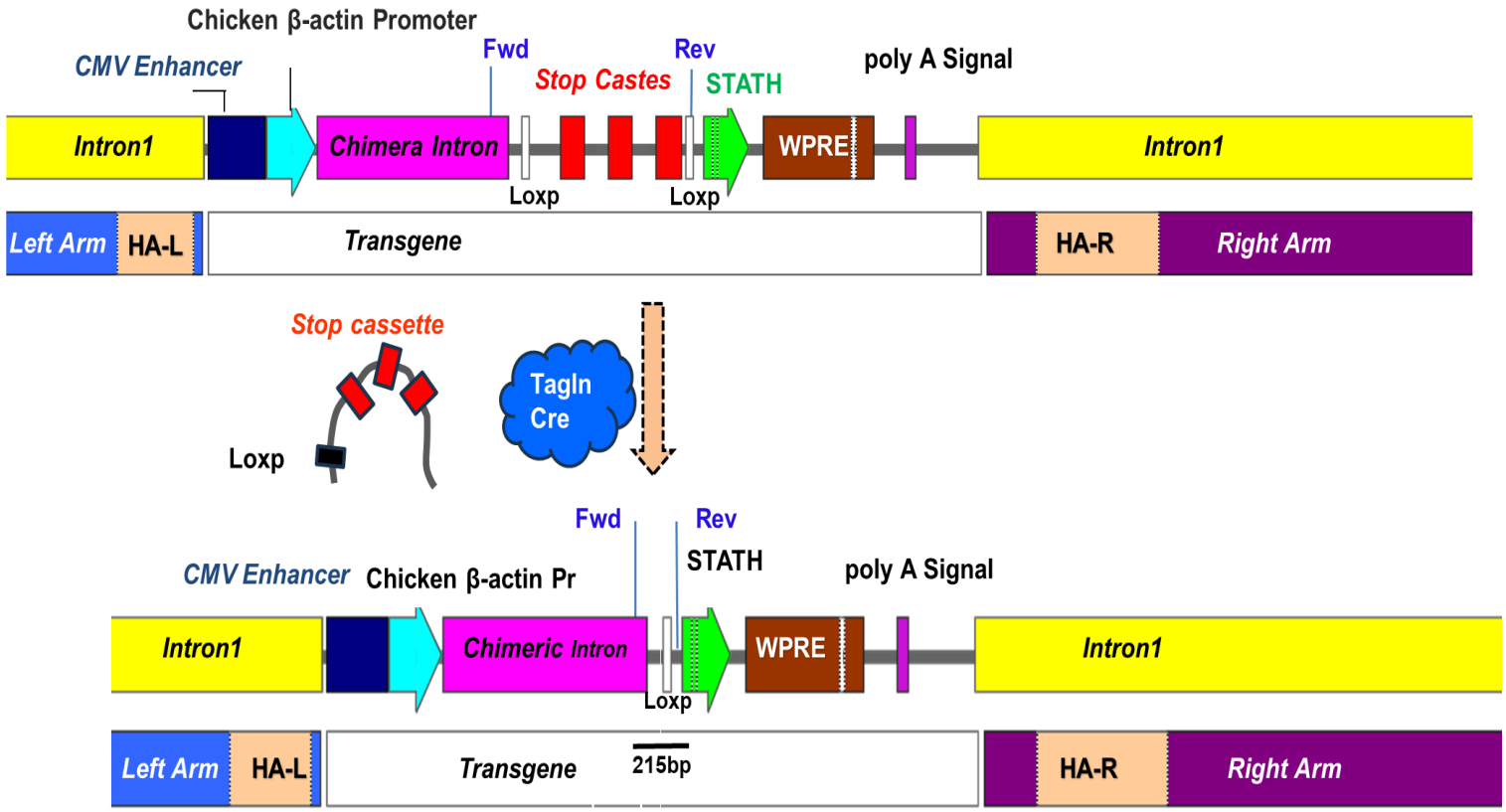

Figure 2.3. Tissue-specific contains smooth muscle expression of human STATH Transgenic mice flux

The breeding strategy is described in (Figure 2.4). In brief, to produce homozygote *Mgp*KO mice that express human statherin in smooth muscle cells, we used a two-step breeding strategy. First, *STATH* stop flox mice were bred with *Tagln*-Cre mice. Next, *Mgp*KO-/+ *STATH* stop flox *Tagln*-Cre mice were obtained by breeding *Mgp*KO-/+ heterozygotes mice to *STATH* stop flox *Tagln-Cre* and choosing rare triple heterozygote mice to interbreed. Only *Mgp*KO-/- homozygotes bearing 2 copies of the *STATH* stop flox transgene on a *Tagln-Cre* heterozygote background were rescued from arterial calcification.

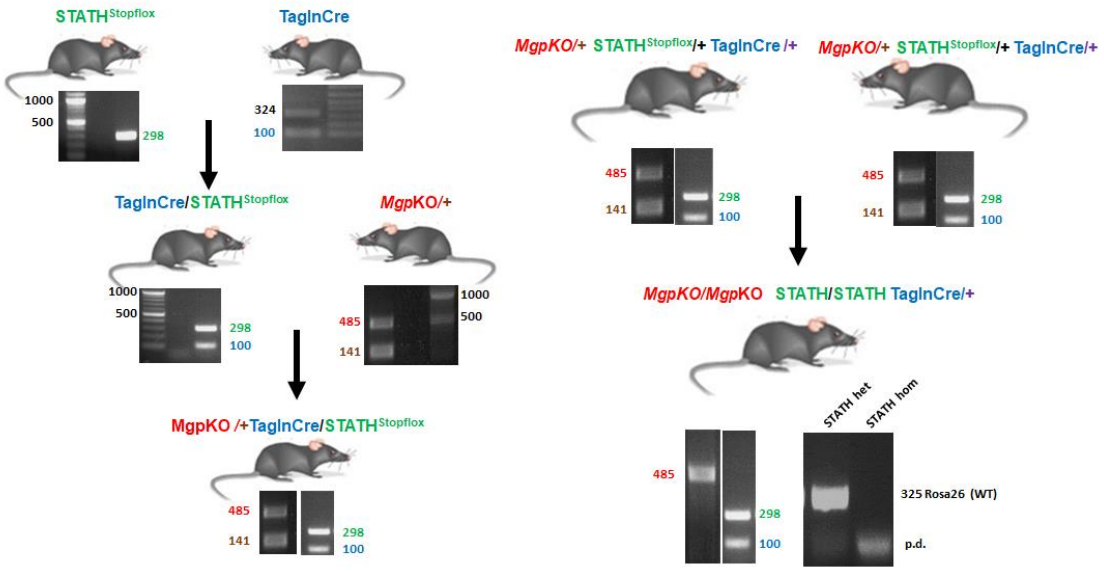

Figure 2.4. Breeding strategy.

To obtain *Mgp*KO mice with smooth muscle specific expression of human statherin (STATH). We first generated *STAH* stop-flox mice as described in Fig. 3a and bred these mice to Tagln-Cre mice. These mice were further bred onto the *Mgp*KO background to obtain triple transgenic *Mgp*KO/*STATH* stop-flox/TaglnCre heterozygote mice. These mice were crossbred to further obtain *Mgp*KO/*Mgp*KO/*STATH* stop-flox/*STATH* stop-flox/TaglnCre mice (n=4) that were identified by disruption of both alleles of the Rosa26 locus.

2.2.5. Human coronary artery and mouse aortic tissue calcification imaging

Human coronary artery sections from paraffin-embedded tissue 4 of individuals were purchased from ProteoGenix Inc. *MgpKO* mouse thoracic aortas were dissected, fixed in 4% paraformaldehyde in 20% sucrose at 4°C overnight, then embedded and frozen in OCT compound prior to sectioning on a cryostat. Paraffin slides were deparaffinized and then rinsed with distilled water and then treated in the same manner as OCT slides. The slides were treated with Alizarin Red Solution (40 mM in water) for 90 seconds. Following removal of excess dye, sections were dehydrated in acetone for 20 dips followed by 20 dips in an Acetone-toluene solution at a ratio of 1:1. The sections were then cleaned in toluene for 3 min and mounted using synthetic mounting medium. Under a transmitted light microscope (Zeiss Germany), the calcified region appeared orange to red in color, and images were captured and area of calcification was quantified using ImageJ software[198].

2.2.6. Generation of statherin expression plasmids

A pcDNA3.1 CMV-driven expression vector containing the human statherin cDNA (GenScript Inc., OHu04093C) was modified to contain additional 5' untranslated sequence of the statherin cDNA and a Kozak consensus initiation codon, but it failed to express statherin protein in HEK293 cells (Figure 2.5 A, Appendix 3). The human statherin gene contains 5 introns and 6 exons for a 679-nucleotide mRNA coding for a 62 amino acid protein (Figure 1.7).

Short transcripts are known to require splicing of introns to produce mRNA that is exported from the nucleus to produce protein[199]. To obtain a transcript with an intron, the statherin cDNA was released from the pcDNA3.1 vector using EcoR1 and BamH1 enzymes and cloned into the EcoR1/BglII linearized pXJ40 vector that contains the CMV enhancer/promoter and the rabbit beta-globin intron[200] (gift of Pierre Chambon) and statherin protein was obtained (Figure 2.5 B, Appendix 3). To insert the Alu sequence from the first intron of the *STATH* gene, a double stranded fragment with cohesive MfeI sites was synthesized (IDT Inc.) and cloned into the MfeI site of pXJ40 *hSTATH* in the beta-globin intron sequence.

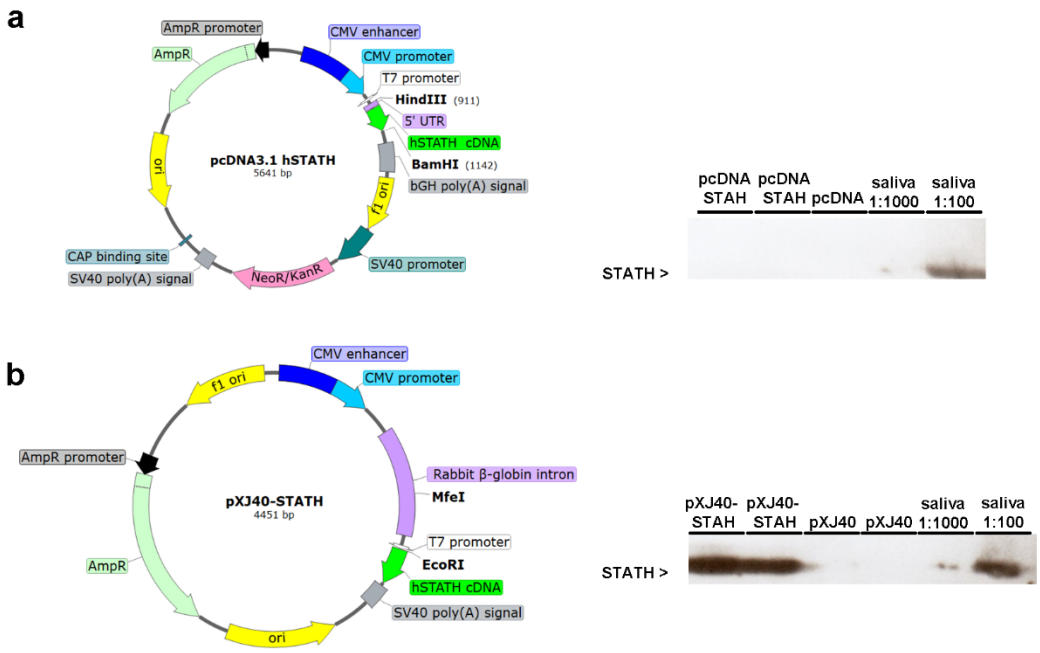

Figure 2.5. Statherin protein expression requires an intron.

a, pcDNA3.1 plasmid is a CMV-driven eukaryotic expression vector lacking an intron. No statherin protein was detected from HEK293 cells transfected with this vector. **b**, pXJ40 vector is a CMV-driven eukaryotic expression vector bearing the rabbit b-globin intron and produced robust statherin expression.

2.2.7. Lentiviral expression of statherin in *Mgp*KO mouse AoSMCs

The beta-globin intron-*STATH* cDNA from the pXJ-40 STATH vector was subcloned into pLenti-CMV-RFP-2A-Puro vector (Figure 2.6, Appendix 3) by a proprietary recombinational cloning method using specialized recombinase enzymes by Applied Biological Materials Inc. (Richmond, BC, Canada). Primary vascular smooth muscle cells isolated from the aorta of *Mgp*KO mice were plated in complete optimal medium (FBS 10% serum and pen/strep) in 12-well plates and cultured at 37°C with 5% CO_2, 24 hours prior to lentiviral infection. The cultured VSMCs wells were then transduced with the pLenti-CMV-Beta-globin intron-*STATH*-RFP-2A-Puro lentiviral particles and a multiplicity of infection (MOI) of 10 particles per cell in complete medium containing 8 µg/ml polybrene. To control for viral infection, SMCs were also transduced with pLenti-CMV-RFP-2A-Puro viral particles at an MOI=10 and compared to uninfected cells as a negative control. Media was changed every 24 hours after infection and 72 hours post-infection, the efficiency of transduction was evaluated by flow cytometry of live cells on a FACS ARIA™ III cell sorter (BD Biosciences Inc.) using the phycoerythrin-Alexa fluor 647 (PE-A) excitation and emission settings to sort red fluorescent protein (RFP)

expressing cells, providing an estimate of the percentage of cells that were transduced (Figure 2.7**)**. Because fewer than 20% of cells were transduced, to enrich for lentiviral-transduced cells (Figure 2.7**)** infected cells were cultured under puromycin selection (2.5µg/ml) for an additional 3 days in medium supplemented with low (1.0 mM) or high (2.0 mM) inorganic phosphate.

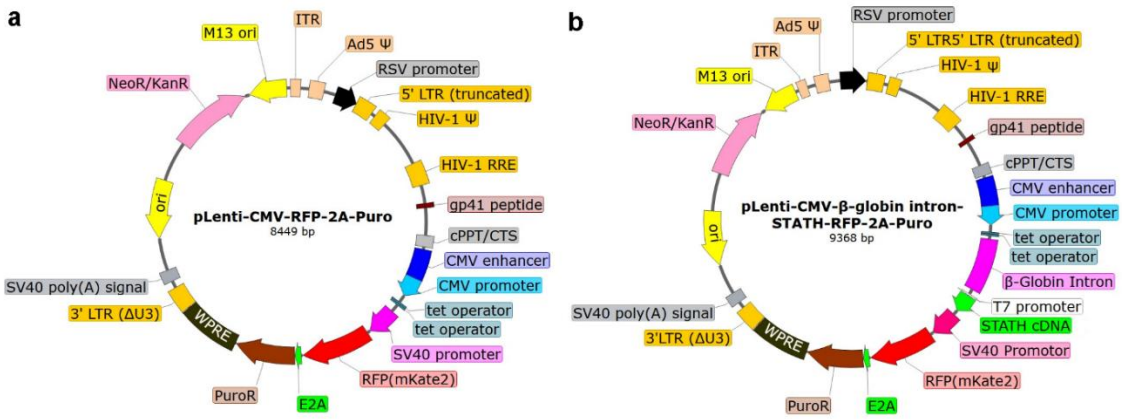

Figure 2.6. Lentiviral vectors for STATH over-expression.

The pLenti-CMV-RFP-2A-Puro vector carries a red fluorescence protein cDNA under the control of an SV40 promoter. The Puromycin selection gene is under the control of an e2A promoter. The rabbit β-globin intron-*STATH* cDNA was incorporated into the lentiviral vector to generate the pLenti-CMV- β-globin intron-STATH-RFP-2A-Puro vector. RFP and STATH expression were confirmed by immunofluorescence (Figure. 3.18 C).

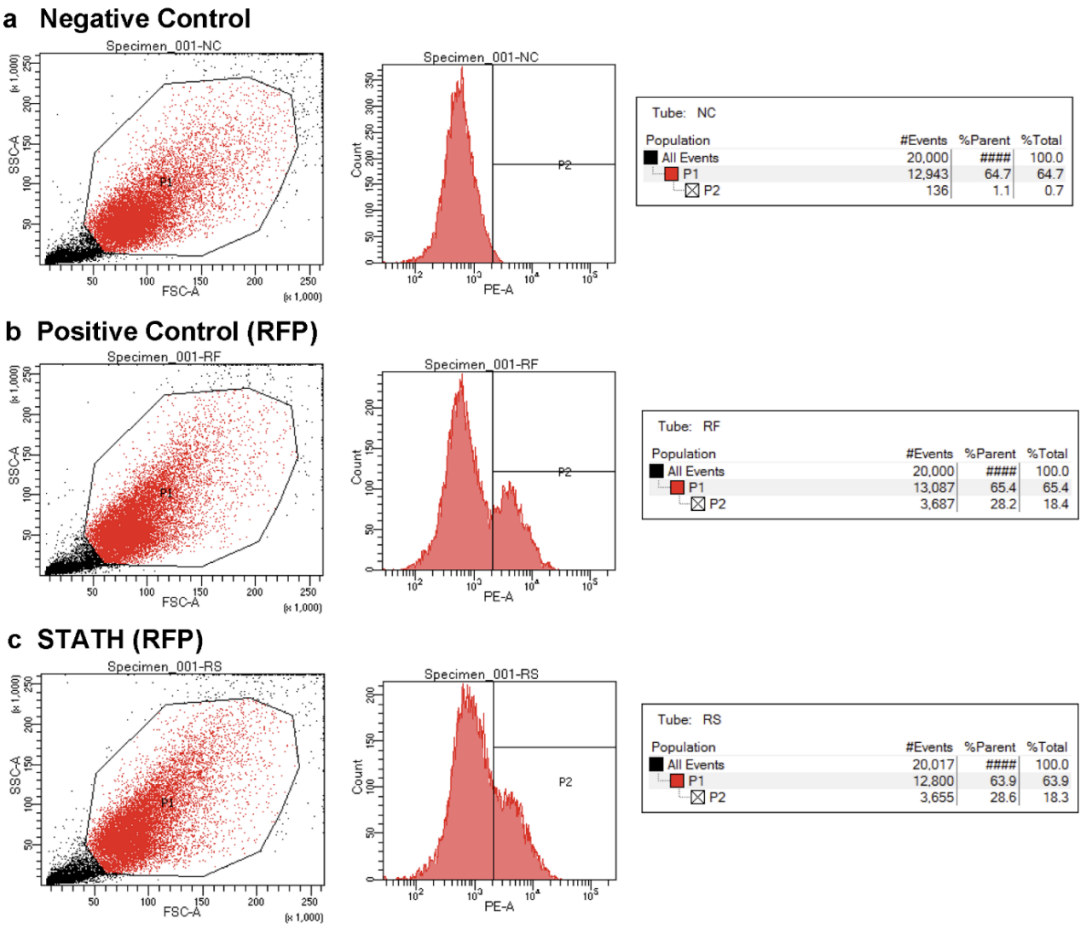

Figure 2.7. Flow cytometry revealed less than 20% infection of *Mgp*KO aortic SMCs.

a, Negative control, b, red fluorescent protein (RFP) from control lentivirus, c, RFP from STATH lentiviral vector. Leftmost panels are scatter plots after sorting for size and scatter (P1), middle plots show peaks after sorting for red fluorescence (P2) and rightmost plots shows percent of sorted cells.

2.2.8. *In vitro* Calcification Assay for *Mgp*KO mouse AoSMCs

Culture medium was removed from lentiviral-transduced and control SMC monolayers, cells were washed twice with phosphate-buffered saline (PBS; Lonza, Basel, Switzerland),

then fixed in cold neutral buffered formalin (10%; Merck Millipore, USA) for 30 minutes (min). Fixing solution was removed, cells were rinsed twice with distilled water and stained with alizarin red S staining solution 40 mM in water (Merck Millipore, USA) in the dark for thirty minutes at room temperature. Unbound Alizarin Red dye was removed by rinsing cells three times with distilled water. Calcium was quantified by adding 400 µl of 10% acetic acid (v/v) to each well and incubating them at room temperature for 30 minutes with agitation. Immediately following vortexing for 30 seconds, the slurry was covered with 500 ul mineral oil (Sigma–Aldrich), agitated in bathwater at 85°C for 10 minutes, and then chilled on ice for 5 minutes. The slurry was centrifuged at 12000g for 20 minutes, and 300 µl of the supernatant was transferred into a 1.5 mL microcentrifuge, where it was mixed with 122.5 µl of 10% NH_4OH (v/v) (to keep the pH between 4.1 and 4.5). Absorption of a 135 µl aliquot of the mixture was read at 405 nm in triplicate in 96-well plates (Fisher Lifesciences) and compared to a standard curve obtained by serial dilutions of Alizarin red solution, as described[201].

2.2.9. Immunofluorescence Imaging of Cultured Cells and Tissues

Cells were cultured on sterile glass coverslips and grown to a near-confluent state. Immunofluorescence analysis was conducted following the previously established protocol [202]. After discarding the culture medium, cells were fixed with 4% paraformaldehyde in PBS 15 min for primary SMCs and 10 minutes for HEK293 at room temperature. Paraformaldehyde was quenched using 50 mM NH_4Cl for 15 min at room temperature,

cells were washed with PBS then permeabilized with 0.1% Triton X-100 detergent in 1X PBS for 20 minutes for primary SMCs and 10 minuntes for HEK293 then washed with PBS. After blocking with 5% horse serum, cells were incubated with the anti-STATH primary antibody (rabbit polyclonal anti STATH antibody (HPA044569 SIGMA), 1:100, overnight at 4°C Next, cells were washed with PBS and incubated with the secondary antibody for 1 hour at room temperature (Alexa Fluor®488 Donkey Anti-Rabbit IgG), then cells were washed with PBS, After applying all primary antibodies: MGP mouse monoclonal antibody (MBS7601404 My BioSource) 1:50, Goat Smooth Muscle Actin Antibody (ABIN185271 Antibody online) 1:200, or Transgelin (10493-1-AP Proteintech), secondary antibodies were applied: donkey anti-goat Alexa Fluor® 647, (Invitrogen A21447), donkey anti-mouse Alexa Fluor® 555 (Invitrogen A-31570), donkey anti-rabbit 488 (Invitrogen R37118) were applied and slides were stained with DAPI. Slides were washed in PBS once for 5 minutes and then treated with TrueVIEW® autofluorescence quenching kit and the anti-fade mounting medium (Vector labs Inc.) and covered with a coverslip. Images were obtained on a Zeiss Axio-Imager.Z1 fluorescence microscope.

Deparafinized human and OCT-embedded mouse tissue sections were warmed to room temperature, washed twice with PBS and subjected to the citric acid antigen retrieval method. Sections were then washed twice in PBS-T (PBS with 0.4% Triton X-100) for 10 minutes and then blocked in PBS with 5% serum for 30 minutes at room temperature.

In a humidified chamber, primary antibody in 1% animal serum PBS-T was applied

overnight at 4°C, then washed twice in PBS-T for 10 minutes each time. Sections were then incubated for 1-2 hours at room temperature with a secondary antibody diluted in 1% serum PBS-T, washed twice with 1% serum PBS-T for 10 minutes each time. When a second and third primary antibody was used, sequential incubations were used based on the appropriately matched secondary antibodies. After applying all primary and secondary antibodies, slides were dyed with DAPI, and washed in PBS once for 5 minutes. Slides were treated with autofluorescence quencher and anti-fade and imaged as above.

2.2.10. Statherin effect on BMP signalling

To investigate the effect of statherin on BMP signaling, HEK293 cells were co-transfected with a BMP-responsive luciferase reporter plasmid [203] (Appendix 3, Map 9) (500 ng) with or without a Bmp4 expression plasmid[204] (50ng) (Appendix 3, Map 10**)** and the pXJ40-*STATH* expression plasmid or an empty vector (pXJ40) (12.5 ng, 25 ng and 50 ng) using Lipofectamine 3000 reagent (Invitrogen Inc.). The BMP-responsive luciferase reporter plasmid contains a luciferase gene under the control of a promoter which contains a direct target sequence (from mouse Id1 promoter) for BMP[203] (Appendix 3, Map 9). 24 hours after transfection, cells were harvested, and luciferase activity was measured as described previously[205]. HEK293 cells were plated at 0.5×10^6/ml, 1 ml per well, in 12-well-plates in DMEM (low glucose, Gibco) medium with 10% FBS and Pen-Strep and allowed to adhere overnight.

2.2.10. Immunoblot Analysis

Protein was extracted from cells lysed in RIPA buffer containing protease inhibitor mixture (Roche, Branchburg, NJ, USA), protein concentrations were measured using BCA protein assay (Pierce, Rockford, IL, USA). Proteins were size fractionated by SDS polyacrylamide gel electrophoresis followed by electroblotting to PVDF membranes and visualized using the following antibodies: a rabbit anti-STATH antibody (Sigma, HPA044569), BMP-4 (3H2.3) (Santa Cruz Biotechnology sc-12721), goat anti-alpha-smooth muscle actin (ABIN185271 Antibody Online), anti-GAPDH mouse monoclonal (Santa Cruz Biotechnology, #sc-59540), and anti-β-actin mouse monoclonal (Sigma, #A2228). Primary antibodies were used at 1/5,000 dilution. Secondary horseradish peroxidase-conjugated antibodies were used at a 1/10,000 dilution: goat anti-mouse IgG antibody (R&D Systems, #HAF007) and goat anti-rabbit IgG (H+L) antibody (Life Technologies, #31460) and revealed by chemiluminescence using the Super Signal West Dura substrate (Thermos Fisher Scientific). Bands were quantified by densitometry using the ImageJ software[198], and each lane signal was normalized to loading control prior to fold conversion. Fold changes were compared to the average of baseline values.

2.2.11. Statistical Analysis

Pairwise comparisons were performed using Student's t-test, unless multiple comparisons were required, in which case ANOVA (Analysis of Variance) was followed by Tukey's test for post-hoc pairwise comparisons corrected for multiple testing. Kaplan-Meier survival curves were defined as the probability of surviving at each time interval. Kaplan-Meier survival analysis was used to compare *Mgp*KO mice to *Mgp*KO/KO *STATH Tagln-Cre* mice. GraphPad software (ver. 9.5.1) was used for statistical analysis.

Chapter 3: Results

3.1. Alendronate therapy

3.1. 1. Survival analysis and progression of vascular calcification in MgpKO mice

The Kaplan-Meier survival analysis revealed a significantly reduced lifespan in Matrix Gla Protein knockout (*Mgp* KO) mice compared to wild-type controls (Figure 3.1 A). All *Mgp* KO mice (n=83) died before reaching 3 months of age, with median survival time of 7 weeks, which is consistent with other studies showing a survival age of 6 to 8 weeks. This stark contrast in survival rates underscores the critical role of MGP in maintaining vascular health and overall longevity. The progression of vascular calcification in *MgpKO* mice was assessed during growth and with advancing age (Figure 3.1 B). Quantification using Alizarin red staining (n=16 mice per age group) demonstrated a rapid and progressive increase in calcification as the mice matured.

Our findings indicate a direct correlation between the extent of calcification and mortality rates in these mice. The observed acceleration of vascular calcification with age in *Mgp* KO mice provides compelling evidence for the crucial role of MGP in preventing pathological mineralization of blood vessels. This progressive calcification appears to be a key factor contributing to the premature mortality observed in the *Mgp*KO population. These results collectively highlight the essential function of MGP in maintaining vascular integrity and its significant impact on lifespan, emphasizing the potential implications for understanding and managing vascular calcification-related disorders in clinical settings.

3.1. 2. MgpKO Mice Have Heterogeneous Calcium Deposits in their Thoracic Aorta

To assess arterial calcification in *Mgp*KO mice, CT imaging of live mice was used in combination with Alizarin red staining of histological sections through the aorta. CT imaging revealed clusters of high density within the aorta of *Mgp*KO mice at 5 weeks of age (Figure 3.2 A, arrow). Dissection of the thoracic aorta (Figure 3.2 B) revealed white calcified nodules (an example outlined in a red dashed box) versus clear less calcified internodal areas (an example outlined in a blue dashed box); further histological sections through these regions (Figure 3.2 C and 3.2 D, respectively) stained with the calcium-sensitive dye Alizarin red confirmed the prevalence of calcification in the white nodes that corresponded to the branch-points of intervertebral arteries (Alizarin red-positive areas quantified in Figure 3.2 E**)**. Interestingly, these calcified nodes also correspond to areas of oscillatory blood flow (i.e., the lesser curvature of the aortic arch and branch openings) that

were reported to accumulate the highest macrophage density during postnatal development (see below and

Figure 3.6) [46].

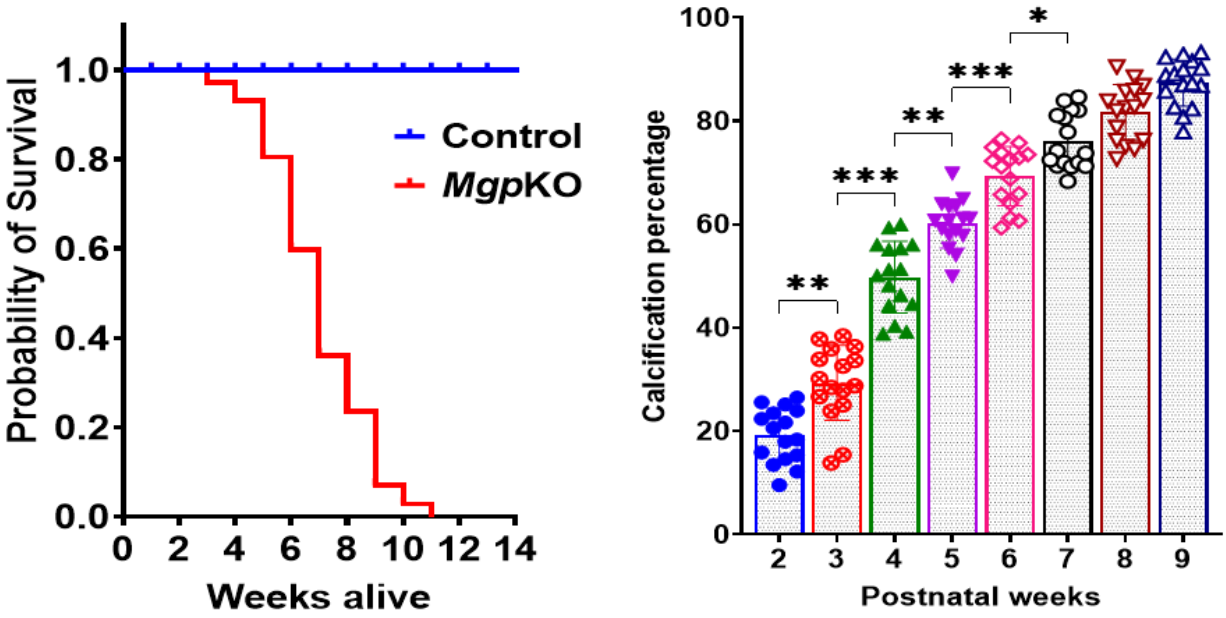

Figure 3.1. Survival Analysis and Vascular Calcification Progression in *Mgp* KO Mice.

A) The Kaplan-Meier survival curve shows the dramatically reduced lifespan of *Mgp*KO mice compared to wild-type controls. All *Mgp*KO mice (n=83) died before reaching 3 months of age, with 70% succumbing before 8 weeks. B) A graph depicts the rapid progression of vascular calcification in *Mgp*KO mice during growth with Alizarin red quantification. (n=16 mice/age group).

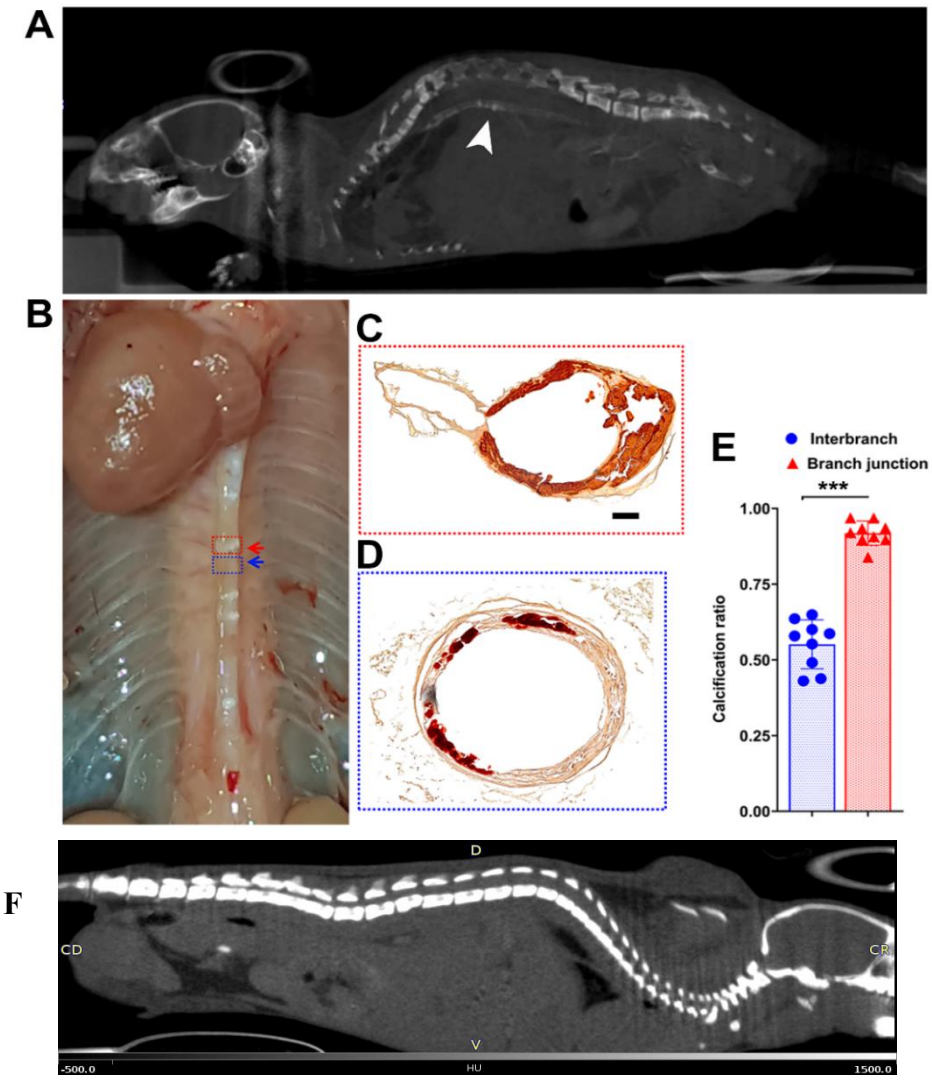

Figure 3.2. Heterogeneous regional aortic calcification in *Mgp*KO mice.

A, Micro-CT imaging revealed nodes of calcification in the aorta (white arrowhead). **B**, Dissection reveals white calcified nodes (red arrow and red dashed box) and minimally calcified internodes (blue arrow and blue dashed box). **C**, Alizarin red staining of the calcified nodes (red box) reveals their occurrence at the branch points of intervertebral arteries. **D**, Internodes (blue box) lie between branches of intervertebral arteries. **E**, Quantification reveals higher calcification at branch junctions compared to the internodal areas in 5-week-old *Mgp*KO mice. (One way ANOVA, $F_{(1, 8)} = 4.012$, $p<0.0001$). F, Micro-CT imaging showed wild type mice with no calcification.

*3.1.3. Renal Artery Calcification in Mgp*KO *Mice*

The micro-CT scan and Alizarin red staining of *Mgp*KO mice revealed significant calcification in specific vascular regions (Figure 3.3). Notably, calcification was observed at the entrance of the renal arteries into the kidneys, indicating mineralization of these critical vessels. Additionally, extensive calcification was detected along the length of the aorta. These findings demonstrate the widespread nature of vascular calcification in (*Mgp*KO) mice, particularly affecting major arteries. Micro-CT scanning provided a detailed three-dimensional visualization of the calcification patterns, while alizarin red staining confirmed the presence of calcium deposits in these vascular tissues. These results clearly illustrate the consequences of MGP deficiency on vascular health, showing pronounced calcification in both the renal vasculature and the aorta of the knockout mice.

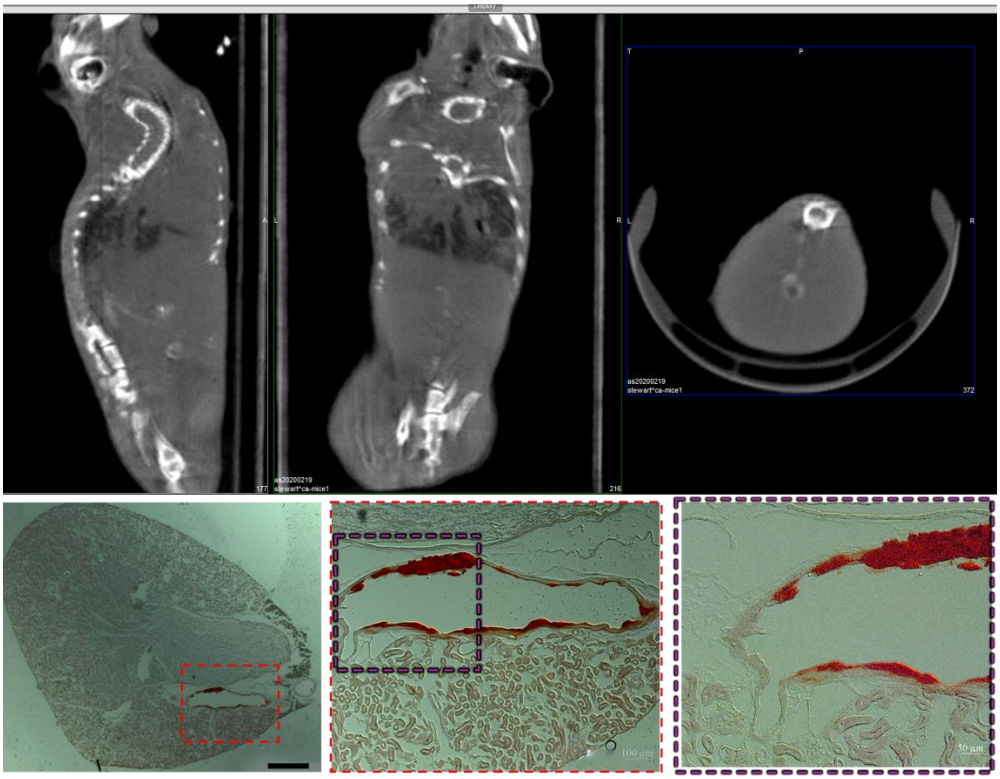

Figure 3.3. Renal calcification analysis in kidney tissue.

A) Micro-CT imaging reveals calcification deposits within the kidney structure. B-D) Alizarin red staining confirms the presence of calcium deposits in kidney sections at increasing magnifications: B) Low magnification overview, C) Medium magnification showing regional distribution, D) High magnification detailing non-uniformity calcium deposits in renal arteries like other arteries in *Mgp*KO mice.

3.1.4. Alendronate Therapy Started at 3 Weeks of Age Improved Incisor Malocclusion but Worsened Arterial Calcification in MgpKO Mice

*Mgp*KO mice develop craniofacial abnormalities resulting in misaligned and maloccluded incisors,[206] necessitating repeated incisor trimming. Alendronate administered twice weekly at a dose of 0.25 or 0.7 mg/kg per week starting at three weeks of age (at the time of weaning) showed a dose-dependent improvement in malocclusion of the incisors in *Mgp*KO mice of both sexes, requiring or no teeth trimming, in contrast to their PBS-treated controls (Figure 3.4 A-C). Despite this marked improvement in craniofacial development, alendronate worsened aortic calcification (Figure 3.4 D, E). In addition, *Mgp*KO mice have stunted growth compared to heterozygotes or WT littermates that was improved, but not normalized, by alendronate treatment (Figure 3.5).

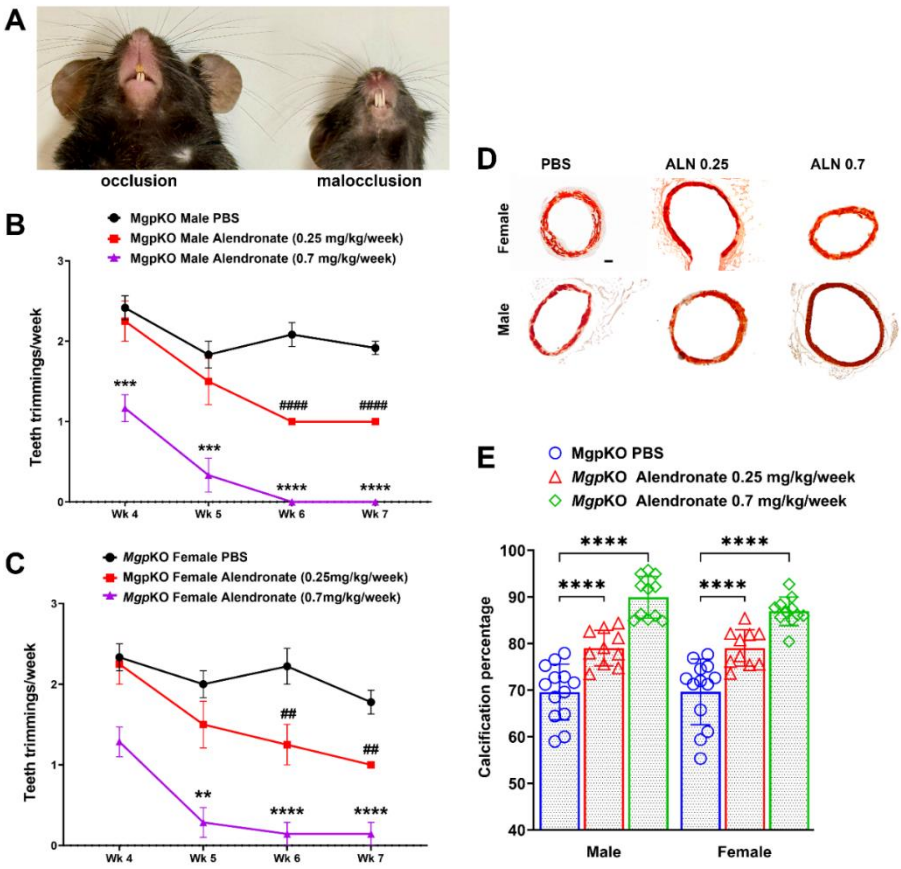

Figure 3.4. Alendronate therapy initiated at three weeks of age.

Alendronate ameliorates malocclusion but exacerbates arterial calcification in *Mgp*KO mice. **A**, Malocclusion of the incisors in *Mgp*KO mice required frequent trimming (B, C). Alendronate therapy started at 3 weeks of age ameliorated incisor alignment in both male (B) and female (C) *Mgp*KO mice in a dose-dependent fashion compared to the PBS control group (n = 8/group/sex, three-way repeated measures ANOVA with Tukey's multiple comparisons test, ##, or ** $p<0.01$; ***, $p<0.001$, ####, or ****, $p<0.0001$). Main effects of treatment (0.70 mg/kg/week), $F_{(1, 20)} = 414.8$, $p < 0.0001$; Time $F_{(3, 20)} = 56.93$, $p < 0.0001$; time x treatment $F_{(3, 20)} = 6.566$, $p = 0.0029$; sex $F_{(1, 20)} = 0.4455$, $p = 0.5121$. Main effects of treatment (0.25 mg/kg/week), $F_{(1, 12)} = 46.53$, $p < 0.0001$; Time $F_{(3, 12)} = 9.923$, $p = 0.0014$; time x treatment $F_{(3, 12)} = 3.979$, $p=0.0351$; dosage $F_{(1, 20)} = 269.4$, $p = 0.0008$; time x dosage $F_{(3, 20)} = 4.024$, $p = 0.0216$. **D**, Alendronate treatment worsened aortic calcification in *Mgp*KO mice of both sexes. Scale bar, 100 µm. **E**, Quantification of Alizarin red staining by ImageJ analysis (Two-way ANOVA with Dunnett's multiple comparisons test, main effect of treatment, $F_{(2, 62)} = 82.40$, $p<0.0001$, sex $F_{(1, 62)} = 0.6176$, $p = 0.4349$, and interaction $F_{(2, 62)} = 0.6618$, $p = 0.5195$. WT: n = 13/sex/group, *Mgp*KO: n=10/sex/group).

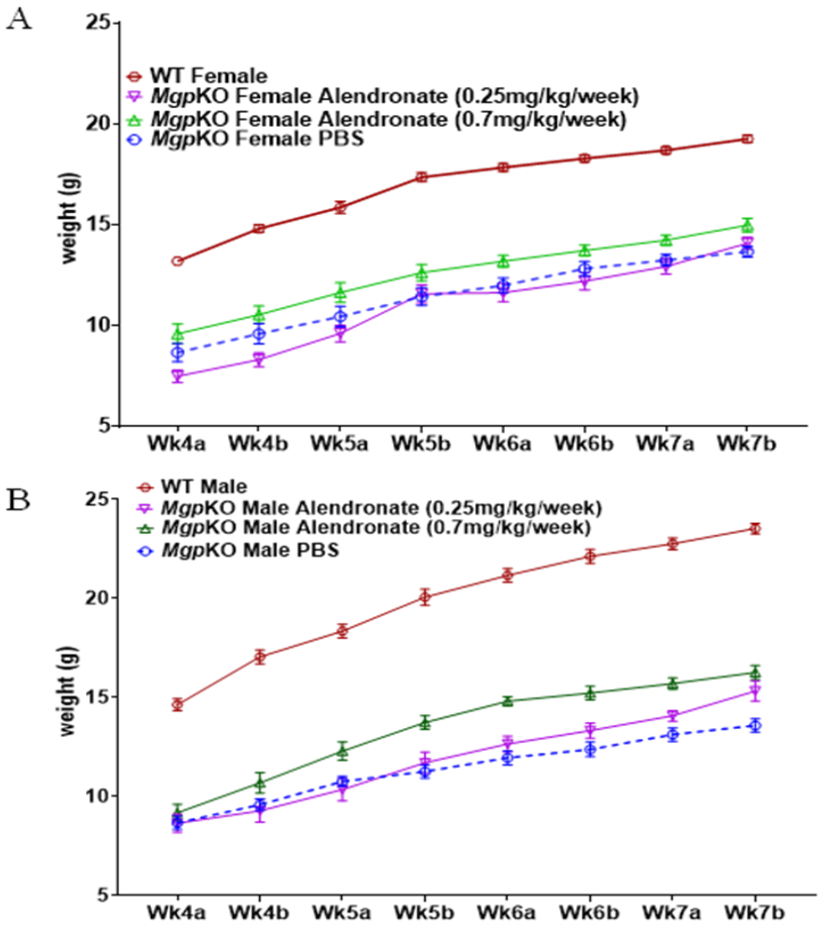

Figure 3.5. Alendronate Enhances Weight Gain in *Mgp*KO Mice.

Alendronate Improves Weight Gain but Does Not Fully Restore Body Weight Progression in *Mgp*KO Mice. Administering alendronate to *Mgp*KO mice from the weaning period showed dose-dependent improvements in weight gain. Both female (**A**) and male (**B**) *Mgp*KO mice treated with 0.7 mg/kg/week alendronate exhibited more significant weight gain compared to those treated with the 0.25 mg/kg/week dose and the untreated *Mgp*KO control group. However, despite the improvement, the body weight of the treated *Mgp*KO mice did not reach the levels observed in healthy mice. Furthermore, male *Mgp*KO mice showed an earlier and more pronounced response to alendronate treatment compared to their female counterparts. The statistical analysis comparing *Mgp*KO PBS with treated groups. Female: Treatment $F_{(2, 128)} = 15.75$, $P<0.0001$; Time $F_{(7, 128)} = 52.02$, $P<0.0001$; Interaction $F_{(14, 128)} = 0.6290$, $P=0.8368$. Male: Treatment $F_{(2, 136)} = 49.29$, $P<0.0001$; time $F_{(7, 136)} = 72.20$, $P<0.0001$; Interaction $F_{(14, 136)} = 2.538$, $P=0.0030$,

3.1.5. Early Postnatal Alendronate Also Worsened Arterial Calcification in MgpKO Mice

Since calcium deposits appear starting at postnatal day 6-7 in *Mgp*KO mice [25, 60], we asked whether earlier intervention prior to the onset of calcification with the same (Figure 3.6 A-C), lower or higher doses of Alendronate (Figure 3.6 E) as were used after weaning would prevent or delay arterial calcification. CT imaging revealed that earlier treatment with alendronate (0.25 mg/kg/week) reduced but did not eliminate the calcified lesions in both the ascending and descending aortas (Figure 3.6 B). Notably, calcification was less concentrated at the vertebral artery branch points and redistributed throughout the aorta including more caudal regions, as reflected by reduced signal variability (Figure 3.6 C). Consistent with this notion, redistribution of calcified lesions throughout the aorta by alendronate treatment was reflected by an increased percent area of the descending thoracic aorta that was calcified (i.e., Alizarin red-positive area). Further, alendronate increased the calcified area of the aortic wall in a dose-dependent fashion (Figure 3.6 D, E). Of note, arterial calcification was not detected in WT or *Mgp* heterozygotes littermates injected with PBS or alendronate.

Like the effect of late alendronate administration, early postnatal administration at the lower doses (0.125 and 0.25 mg/kg/week) also ameliorated incisor malocclusion (Figure 3.6 F). Of note, the incisors normally appear on postnatal day 11 and surprisingly, higher doses of alendronate (>0.5 mg/kg/week) disrupted proper tooth development: only

1 pair of lower incisors appeared at 0.5 mg/kg/week and no incisor developed at 1 or 2 mg/kg/week of alendronate (Figure 3.6 G). Similarly, body weight progression was improved but not normalized in *Mgp*KO mice by the lower dosage of Alendronate, whereas higher doses were detrimental in both *Mgp*KO, *Mgp* heterozygotes and WT mice (Figure 3.7).

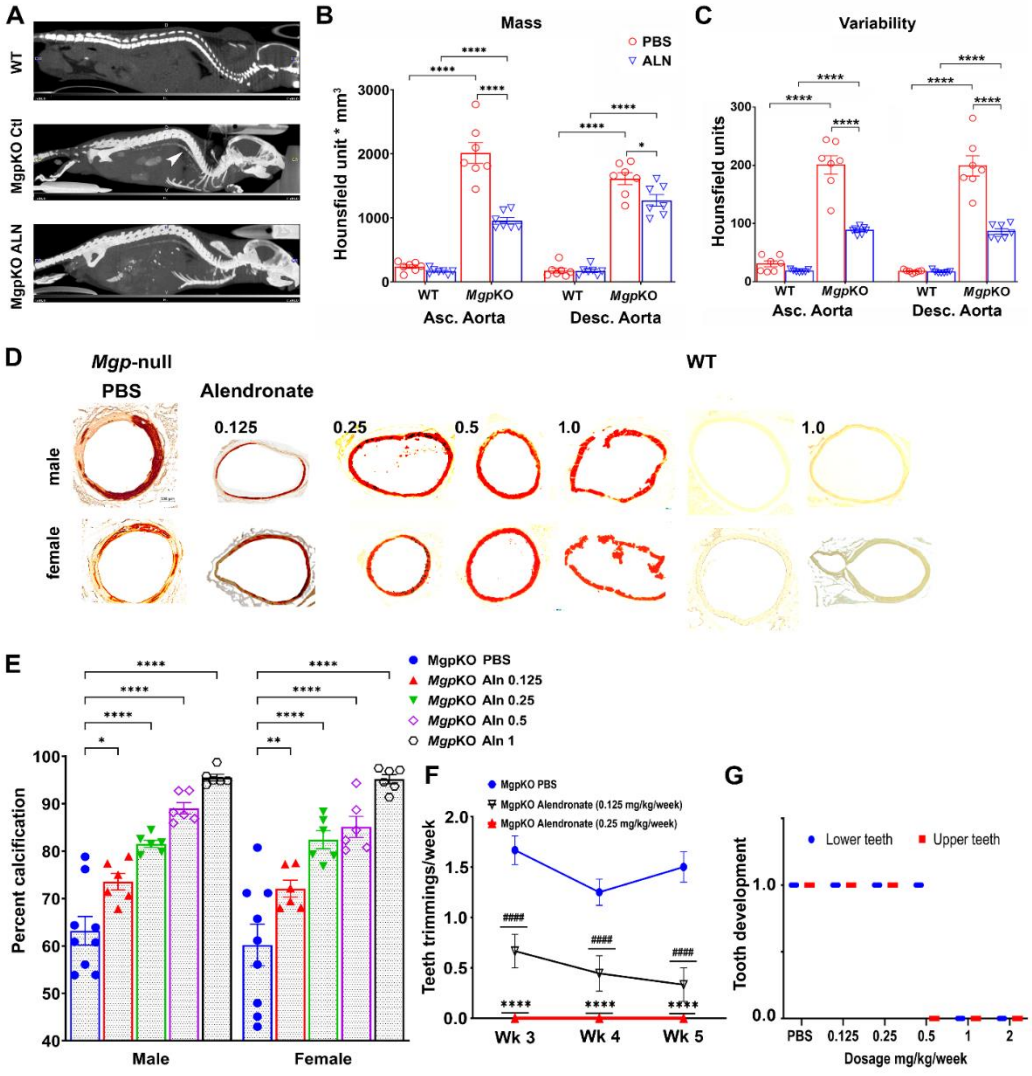

Figure 3.6. Alendronate therapy initiated on postnatal day 3 age.

It affects tooth development and worsens vascular calcification in *Mgp*KO mice. **A**, CT imaging reveals uniform aortic calcification in *Mgp*KO mice treated with Alendronate (0.25 mg/kg/week from day 3) as compared to PBS-treated *Mgp*KO mice that exhibit heterogeneous calcification (arrowhead) at 5 weeks of age. Wild-type (WT) mice show no aortic calcification either with PBS or Alendronate treatment. **B**, Alendronate reduced aortic calcification mass in the ascending and descending aorta. Data were analyzed by two-way ANOVA followed by pairwise comparisons using Tukey's test. Ascending aorta: Main effects of genotype $F_{(1, 24)}$ = 218.7, $p < 0.0001$; treatment $F_{(1, 24)} = 42.34$, $p<0.0001$; interaction $F_{(1, 24)} = 32.18$, $p < 0.0001$. Descending aorta: Main effects of genotype $F_{(1, 24)} = 332.2$, $p < 0.0001$; treatment $F_{(1, 24)}$ = 6.112, $p < 0.05$; interaction $F_{(1, 24)} = 5.801$, $p < 0.05$. *, $p < 0.05$, ****, $p < 0.0001$. **C**, Alendronate reduced variability, consistent with more uniform calcium distribution. Ascending aorta: Main effects of genotype $F_{(1, 24)} = 202.7$, $p < 0.0001$; treatment $F_{(1, 24)} = 54.74$, $p<0.0001$; interaction $F_{(1, 24)} = 35.28$, $p < 0.0001$. Descending aorta: Main effects of genotype $F_{(1, 24)}$ = 193.3, $p < 0.0001$; treatment $F_{(1, 24)} = 39.80$, $p < 0.0001$; interaction $F_{(1, 24)} = 38.22$, $p < 0.0001$. ****, $p < 0.0001$. **D**, Alendronate-treated *Mgp*KO mice of both sexes exhibit dose-dependent increased global and uniform calcification by Alizarin red staining, while PBS-treated mice show focal calcification. No calcification was detected in WT mice. **E**, Quantitation of arterial calcification by Alizarin red staining reveals exacerbation of calcification with Alendronate treatment in both sexes. Two-way ANOVA, Treatment $F_{(4, 66)} = 53.54$, $p < 0.0001$; sex $F_{(1, 66)}$ = 0.8550, $p = 0.3591$; interaction $F_{(4, 66)} = 0.2545$, $p = 0.9057$; n= 6 mice / Alendronate treatment and n = 9 PBS-treated control mice. **F**, Lower Alendronate doses (0.125 and 0.25 mg/kg/week) ameliorate malocclusion in *Mgp*KO mice. Three-way repeated measures ANOVA compared main effects of treatment, sex, dosage and duration and pairwise comparisons used Tukey's test (****, or ####, $p < 0.0001$). Treatment (0.25 mg/kg/week), $F_{(1, 15)} = 75.62$, $p<0.0001$; Treatment (0.125 mg/kg/week), $F_{(0.5205, 2.603)} = 149.4$, $p=0.0026$; Dosage, $F_{(0.5915, 2.957)}$ = 135.0,**$p=0.0017$. Sex and duration were not significant. **G**, Alendronate doses exceeding 0.5 mg/kg/week inhibit tooth development (pairs of upper and lower incisors) in both wild-type and *Mgp*KO mice.

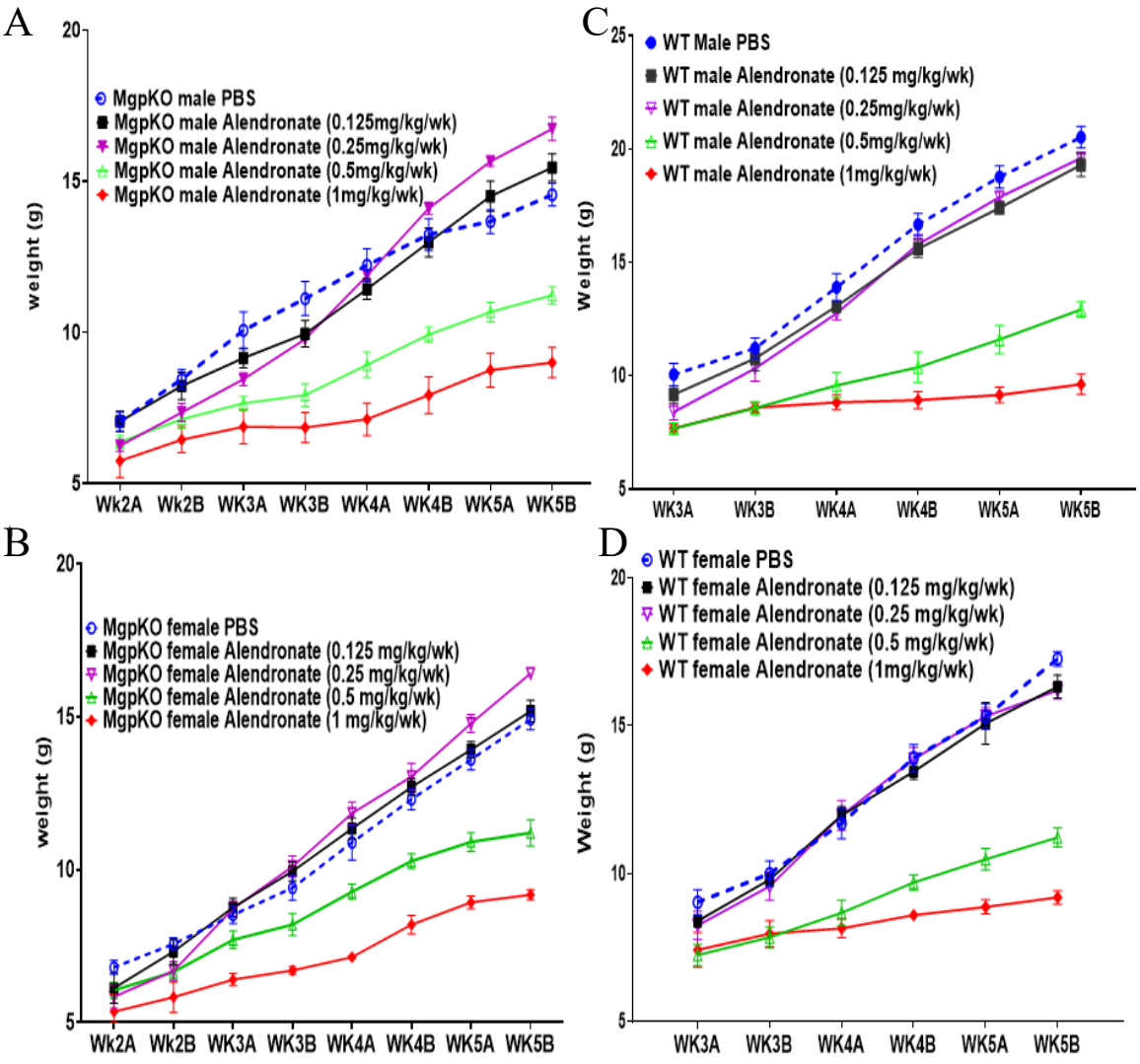

Figure 3.7. Body weight changes following alendronate injected at day-3

. Concentrations exceeding 0.5 mg/kg/week prevent growth development in both groups (A-D). However, concentrations surpassing 0.125 or 0.25 mg/kg/week led to improved weight gain in male (A) and female (B) *Mgp*KO mice, with a more pronounced effect observed in male mice $p<0.0001$, but male (C) and female (D) wild type mice do not react to these low concentrations. Nevertheless, Alendronate fails to induce weight gain in both sexes of *Mgp*KO mice sufficiently to reach the normal level observed in wild-type mice.

Runx2 is an early transcription factor that drives the normal chondrogenic/osteogenic program of osteoblast differentiation, as well as the pathological chondrogenic/osteogenic conversion of smooth muscle cells observed in arterial calcification [40, 207-209]. In line with the hastened arterial calcification in *Mgp*KO mice by Alendronate, we found that exposure to a single dose of Alendronate given to 3-day old *Mgp*KO mice is sufficient to activate increased Runx2 expression in the aorta harvested 2 days later, as revealed by immunoblot (Figure 3.8 A, B). Immunofluorescence detected RUNX2 -positive nuclear staining in aortic smooth muscle cells of Alendronate-treated *Mgp*KO mice (Figure 3.8 C), but not in WT or PBS-treated *Mgp*KO mice.

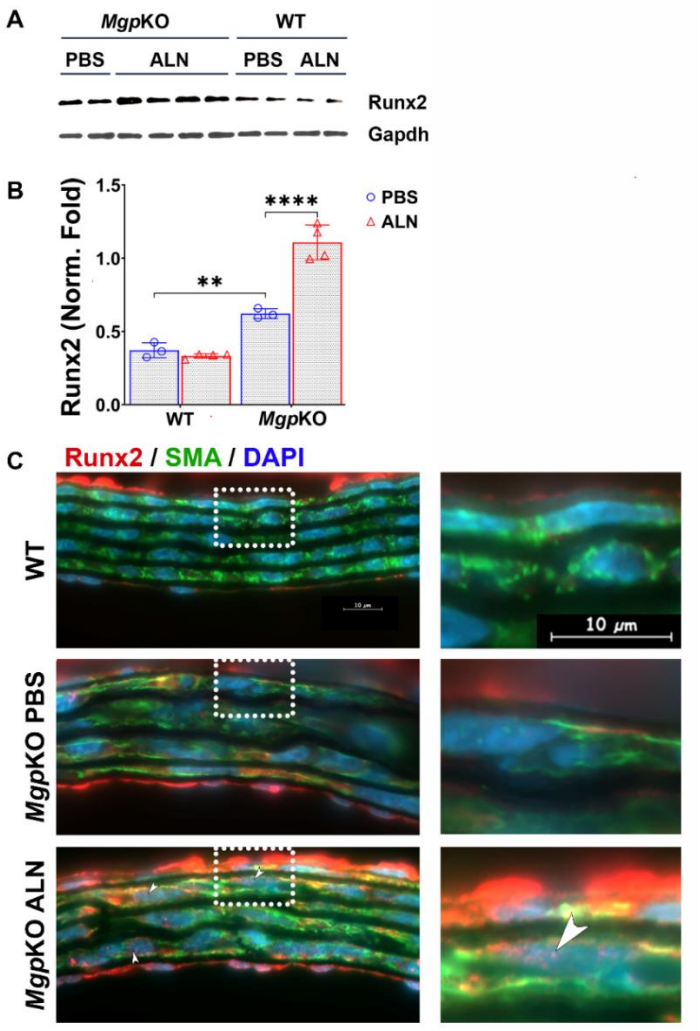

Figure 3.8. Acute elevation of Runx2 expression in *Mgp*KO aorta following single-dose Alendronate administration.

A, Representative Western blot analysis demonstrating RUNX2 protein expression levels in aortic tissue from *Mgp*KO and wild-type (WT) mice 48 hours post-alendronate administration (single dose on postnatal day 3). **B**, Densitometric quantitation of Runx2 protein levels normalized to Gapdh. n=4 for Alendronate-treated groups, n=3 for PBS-treated control groups. Data were analyzed by two-way ANOVA followed by Tukey's multiple comparisons test. Treatment, $F_{(1, 10)} = 33.94$, $p = 0.0002$; genotype $F_{(1, 10)} = 177.7$, $p < 0.0001$; interaction, $F_{(1, 10)} = 46.64$, $p < 0.0001$. **, p<0.01; ****, $p < 0.0001$. **C**, Immunofluorescence staining revealed increased RUNX2 expression in aortic tissue of 5-day-old *Mgp*KO mice following a single dose of Alendronate. Dashed insets enlarged on the right. White arrowheads indicate nuclear localization of RUNX2.

3.1.6. Early Alendronate Treatment Does Not Ameliorate Calcification in the Ears

Since ear ossification has been reported in humans with Keutel syndrome resulting from the loss of MGP [119], we asked whether calcification of the ears also occurs in *Mgp*KO mice and what effect postnatal Alendronate therapy (0.25 mg/kg/week) would have on this process. Alizarin red staining of ear sections revealed extensive interstitial calcification in PBS-treated *Mgp*KO mice beneath the auricular cartilage, a region rich in blood vessels (Figure 3.9 A). Elastin immunofluorescence staining confirmed that calcified regions occurred predominantly in areas of low elastin density and not in the elastin-dense auricular cartilage *per se* (Figure 3.9 B). Alendronate worsened calcification in the ears of *Mgp*KO mice (Figure 3.9 C). No such ectopic calcification was detected in WT mice. Calcium deposits in the ears of *Mgp*KO mice were also visualized by CT imaging (Figure 3.10). Our observation of ectopic ear calcification in *Mgp*KO mice corroborates the human Keutel syndrome phenotype. Further, our data indicate a deleterious effect of Alendronate treatment on soft tissue calcification in the context of *Mgp* deficiency.

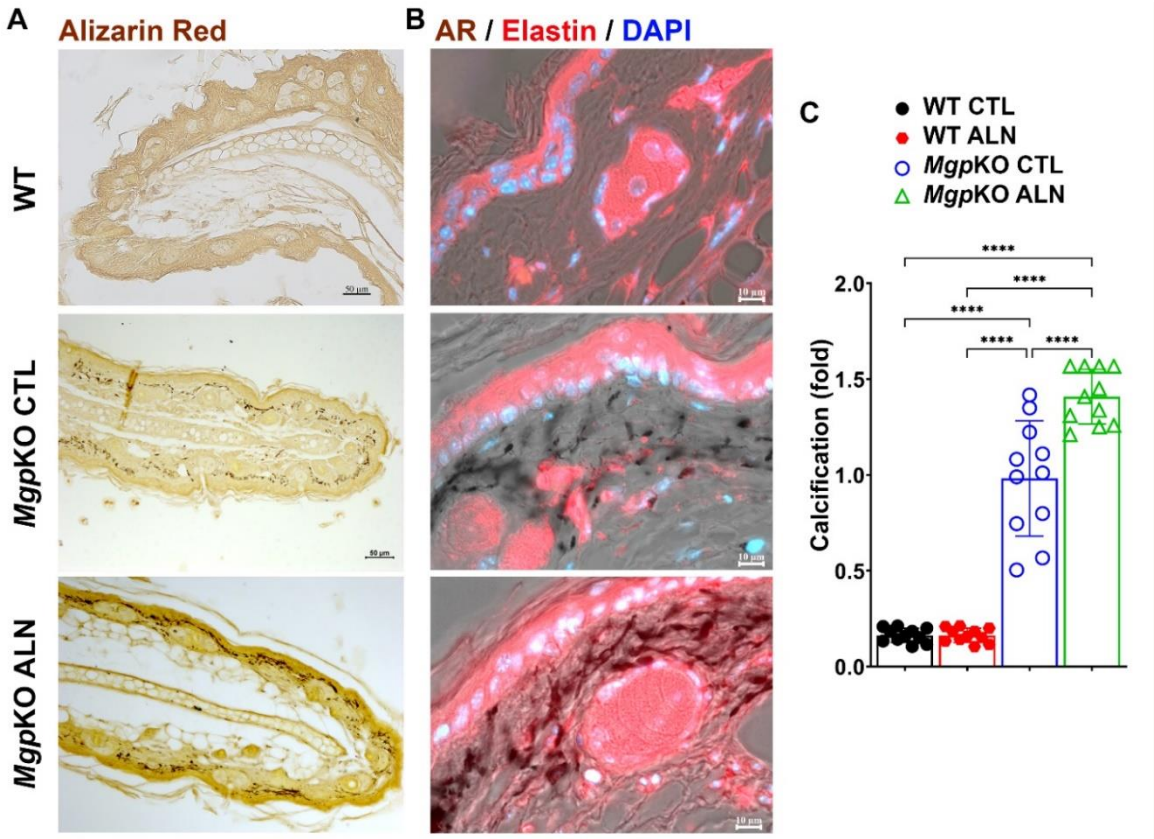

Figure 3.9. Postnatal Alendronate therapy exacerbates ear calcification in *Mgp*KO mice.

A, Alizarin red staining of sections through the ears reveals calcification in *Mgp*KO mice treated twice weekly with PBS from postnatal day 3 to week 5 (*Mgp*KO control) whereas Alendronate treatment did not improve soft tissue calcification (*Mgp*KO ALN). **B**, Elastin immunofluorescence staining (red) reveals that the calcified regions (AR, Alizarin red) lie in the areas of low elastin density in the ear tissue. DAPI reveals the nuclei. **C**, Quantification of calcification by Alizarin red staining. (n = 8 *Mgp*KO treated, n=10 WT and n = 11 *Mgp*KO control mice per group). Two-way ANOVA, treatment, $F_{(1,40)} = 414.2$, $p < 0.0001$; genotype, $F_{(1,40)} = 17.71$, $p < 0.0001$; interaction, $F_{(1,40)} = 17.71$, $p < 0.0001$. Tukey's multiple comparisons test, ****, $p < 0.0001$.

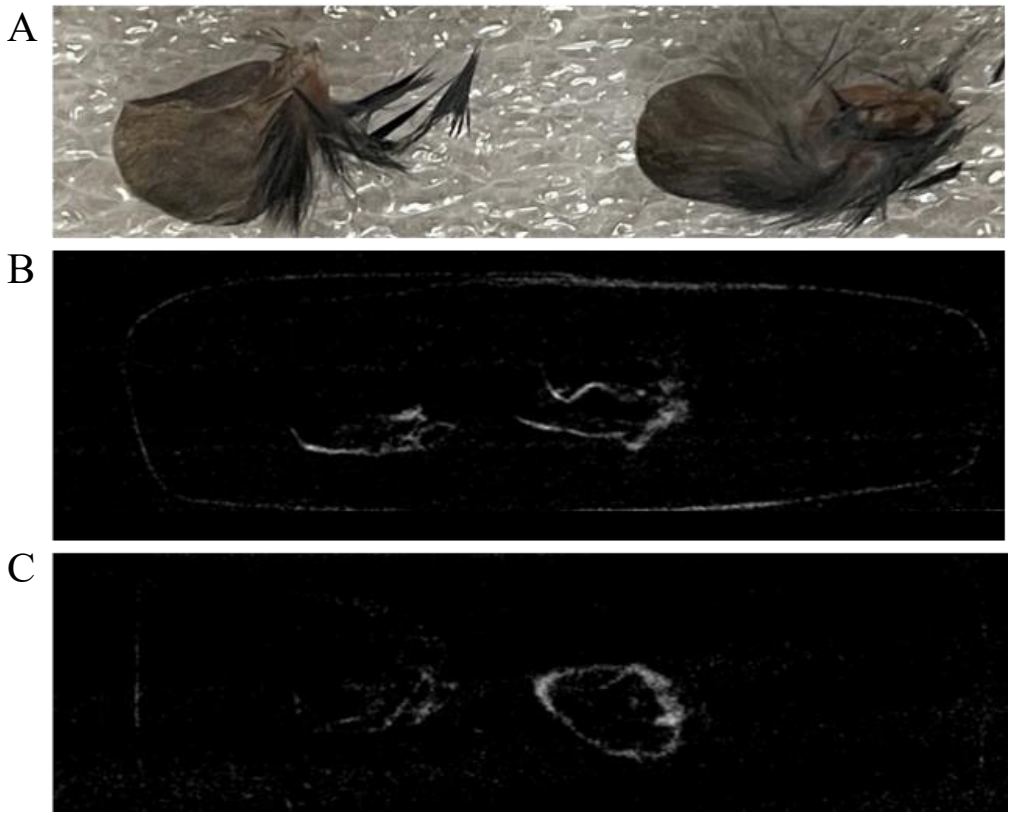

Figure 3.10. Sagittal and Coronal CT Analysis of Ectopic Calcification Patterns in Excised *Mgp*KO Mouse Ears.

A, A standard photograph provides a baseline visual reference of the excised *Mgp*KO mouse ears. CT imaging shows the highest intensity voxels have consistent density with calcification. **B**, the sagittal plane, providing a side view of the isolated ear, allows for visualization of calcification along the edges of the ear pinna, appearing as bright, dense areas on the CT scan and the longitudinal extent of calcification in the ear cartilage, from base to tip. **C**, Coronal Plane Imaging: The coronal plane, offering a front-to-back view of the excised ear, highlights: Cross-sectional calcification patterns throughout the ear structure, and Potential asymmetries in calcification between different regions of the ear.

3.1.7. Alendronate Therapy Alters Tissue-resident Macrophage Phenotype

To address how alendronate therapy affects macrophages at calcified lesions, the macrophage-specific markers CD68 (a lysosome-specific marker) and CD45 (a cell-surface marker) were used to examine macrophages at the branch points of vertebral arteries where calcified lesions often occur (Figure 3.2 B, C). Calcified lesions were imaged using the calcium-binding fluorescent dye Fluo-4AM. Similar CD45-positive macrophages were detected at calcified lesions of *Mgp*KO mice treated with either PBS or Alendronate. Surprisingly, CD68-positive macrophages were detected in PBS-treated *Mgp*KO mice but not in alendronate treated *Mgp*KO mice (Figure 3.11), suggesting that chronic alendronate treatment suppresses the expression of this lysosomal marker in macrophages.

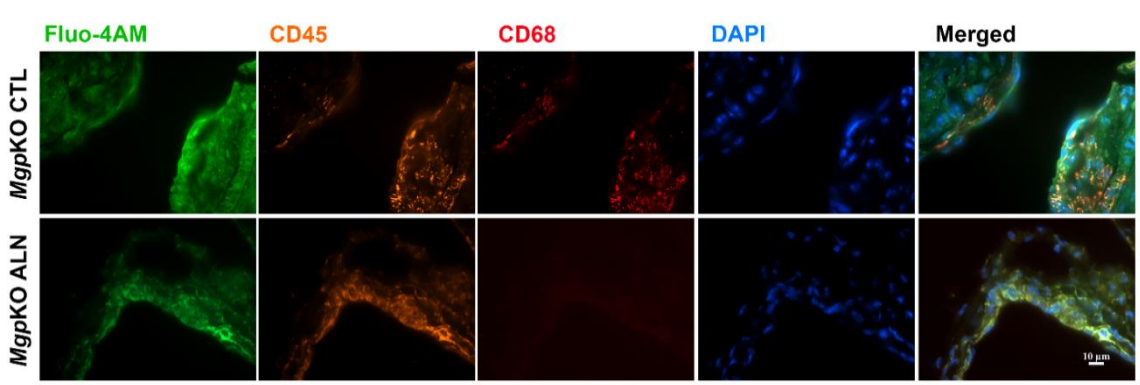

Figure 3.11. Postnatal alendronate treatment suppresses CD68 expressions in macrophages of *Mgp*KO-mice.

Immunofluorescence reveals macrophage markers CD45 (orange) and CD68 (red) and calcium deposits by Fluo-4AM (green) in aortic tissue sections at 5 weeks of age from PBS-treated *Mgp*KO control mice (*Mgp*KO CTL) and MgpKO (*Mgp*KO ALN) mice treated with Alendronate (0.25 mg/kg/week from day 3). Nuclei were revealed by DAPI (blue). Scale bar, 10 µm.

3.1.8. Alendronate Increases Calcium Accumulation in Primary Macrophages

Macrophages take up hydroxyapatite (HA) in lysosomes and degrade it to its constituent components, calcium and phosphate [210]. Endocytosis of micrometer-sized HA particles activates a pro-inflammatory [211-213] and pro-glycolytic [214] phenotype in macrophages, whereas endocytosis of smaller nanometer-sized HA particles activates an anti-inflammatory phenotype [214, 215]. Interestingly, Alendronate suppresses the M1 inflammatory phenotype in RAW 264.7 macrophages [216], although the effect of alendronate on macrophage HA uptake has not been reported.

Alendronate inhibits farnesyl pyrophosphate synthase and thereby suppresses the

prenylation of the small GTPase Rab proteins in macrophages [124]. Since the Rab proteins play an essential role of sorting endosomes and lysosomes, we asked whether Alendronate would affect macrophage endocytosis of HA. Primary macrophages from wild type mice were cultured and exposed to nanometer-sized HA (50 μg/ml) in the presence or absence of Alendronate (12.5 μM) for 48 hours. HA uptake was imaged and quantified using the calcium-sensitive fluorescent dye Fluo-4AM and lysosomes were visualized using the macrophage and lysosome-specific marker CD68 (Figure 3.12). In addition, Fluo-4AM localization to lysosomes was confirmed using another lysosome-specific maker Lamp1 (Figure 3.13). The Fluo-4AM signal showed that HA uptake by macrophages was promoted by Alendronate treatment (Figure 3.12 A, B). Further, Alendronate markedly increased the CD68 lysosome content of cells (Figure 3.12 C). The Pearson correlation coefficient between the calcium and lysosomal signals was markedly increased with Alendronate treatment, indicating that calcium accumulates in the lysosomes (Figure 3.12 D). Of note, the median absolute deviation (MAD) value of the intensities of Fluo-4AM within the lysosomes was reduced by Alendronate treatment, indicating that the calcium signal becomes concentrated in lysosomes (Figure 3.12 E) rather than in extra-lysosomal compartments. The accumulation of calcium signal in alendronate-treated macrophages suggests either that macrophages more actively take up hydroxyapatite in the CD68-positive endo/lysosomes, or that the ability of the endo/lysosomes to dissolve the hydroxyapatite becomes impaired. Since dissolution of hydroxyapatite requires acidification of the lysosomes, perhaps alendronate impedes this process. Of note, treating

macrophages with higher doses of alendronate at 50 or 100 μM caused extensive cell death (data not shown), in line with prior reports of 100 μM alendronate inducing macrophage apoptosis [217].

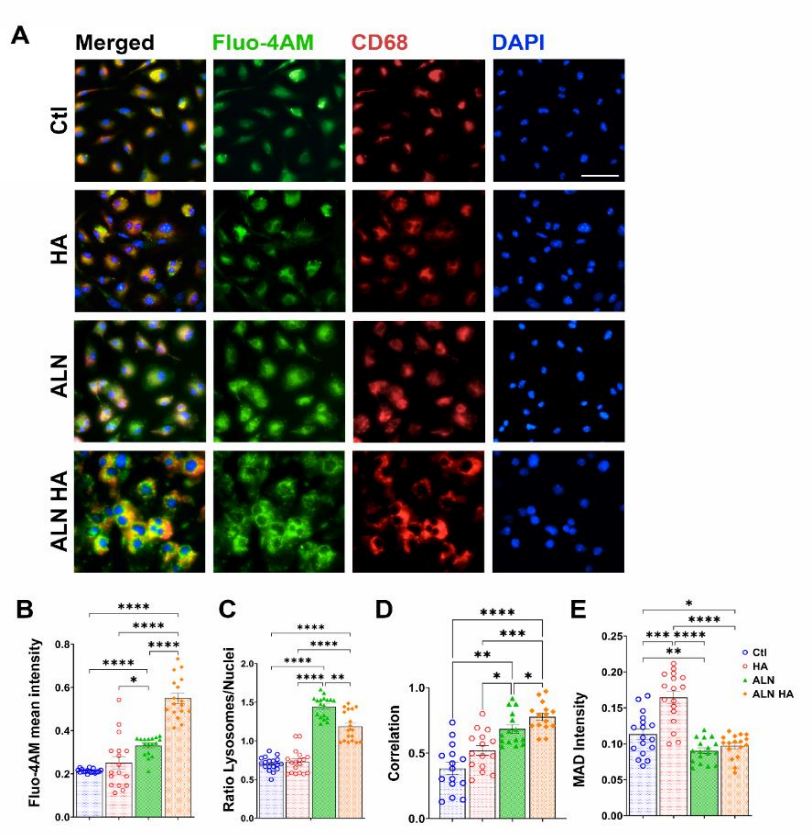

Figure 3.2. Alendronate alters calcium handling of cultured primary macrophages CD68 marker.

A, Representative immunofluorescence images showing calcium uptake (Fluo-4AM, green) by primary cultured bone marrow-derived macrophages under four treatment conditions for 48 hours: control, hydroxyapatite (HA, 50 µg/ml), Alendronate (ALN, 12.5 µM), and combined ALN and HA treatment. CD68 (red) indicates lysosomes, and DAPI (blue) marks nuclei. Scale bar = 20 µm. **B**, Quantification of mean Fluo-4AM intensity within cells. ALN treatment significantly increases Fluo-4AM signal intensity, with a synergistic effect observed in the ALN+HA group (n = 50 fields per condition, $F_{(1.718, 27.49)} = 102.5$, $p < 0.0001$, two-way ANOVA follow by Tukey's post-hoc test). **C**, ALN treatment significantly increases lysosome numbers independent of cell density (n = 30 fields of view per condition, repeated measures ANOVA $F_{(1.937, 32.94)} = 103.2$ $p < 0.0001$). **D**, Pearson's correlation analysis between lysosomal (CD68) and calcium (Fluo-4AM) signals showed progressive treatment-dependent increased spatial correlation (Control < HA < ALN < ALN+HA) between lysosomes and hydroxyapatite with ALN and ALN+HA treatments (n = 40 cells per condition, Repeated measures ANOVA, $F_{(2.380, 33.31)} = 22.40$ $p < 0.0001$ with Tukey's post-hoc test). **E**, Median Absolute Deviation (MAD) of Fluo-4AM intensity, demonstrating more uniform calcium distribution in ALN and ALN+HA treatments (n = 50 view per condition, Repeated measures ANOVA with Tukey's post-hoc test $F_{(1.688, 27.01)} = 44.81$ $p < 0.0001$).

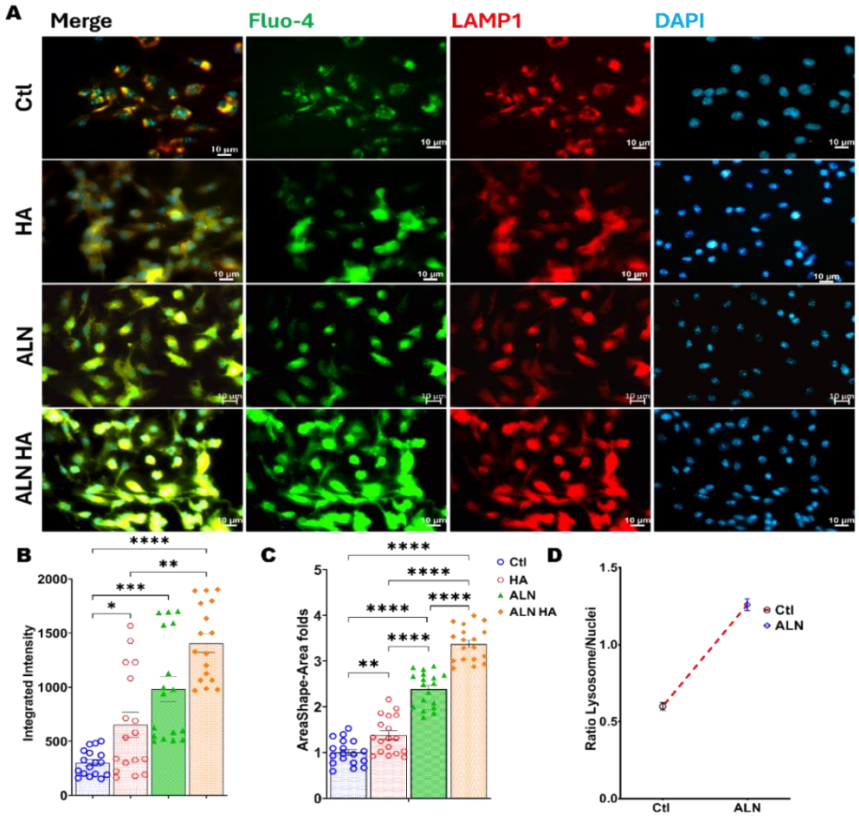

Figure 3.3. **Alendronate alters calcium handling in cultured primary macrophages.** LAMP-1 marker.

A, Representative immunofluorescence images showing calcium uptake (Fluo-4AM, green) by primary cultured bone marrow-derived macrophages under four treatment conditions for 48 hours: control, hydroxyapatite (HA, 50 µg/ml), Alendronate (ALN, 12.5 µM), and combined ALN and HA treatment. LAMP-1 (red) indicates lysosomes, and DAPI (blue) marks nuclei. Scale bar = 20 µm. **B**, Quantification of mean Fluo-4AM Integrated intensity which is the sum of the pixel intensity over all of the pixels in an object, within cells. ALN treatment significantly increases Fluo-4AM signal intensity, with a synergistic effect observed in the ALN+HA group (n = 50 fields per condition, Treatment: $F_{(3, 48)} = 23.88$, $p < 0.0001$, two-way ANOVA followed by Tukey's post-hoc test). **C**, Alendronate treatment increases lysosome numbers and size. The Area Shape-Area parameter indicates enlarged lysosomes, potentially due to increased hydroxyapatite uptake and storage, overall cell size expansion, or changes in cellular and lysosomal morphology in response to treatment. Treatment: $F_{(3, 68)} = 156.3$, $P<0.0001$ One-way ANOVA followed by Tukey's post-hoc test. **D**, Effect of Alendronate on Lysosome Count per Cell at Various Cell Densities. ALN treatment significantly increases lysosome numbers ratio to nuclei independent of cell density. $F_{(1, 70)} = 156.3$, $P<0.0001$, One-way ANOVA followed by Tukey's post- test).

3.2. Results: 9p21.3 Genetic Variants Suppress Smooth Muscle Statherin Expression

3.2.1. p21.3 risk variants suppress statherin.

Whole-genome expression profiling of HAoSMCs genotyped for the genetic variants at 9p21.3 identified the mRNA for the hydroxyapatite-binding protein statherin as the top differentially expressed according to 9p21.3 risk genotype (Table 1.3, Appendix 4 Table 1 and 2) and heat map (Figure. 3.13) full dataset available online at Array Express, accession E-MTAB-12709). Statherin exhibited 25-fold greater expression in HAoSMCs homozygous for the non-risk (HNR) allele of 9p21.3 than in cells homozygous for the risk (HR) allele (Benjamini-Hochberg FDR p<1E-10). Importantly, statherin is the only hydroxyapatite-binding secreted protein-coding gene whose expression is affected by the 9p21.3 genotype. In fact, in HNR HAoSMCs statherin is expressed at similar levels as MGP, another well-known hydroxyapatite-binding secreted protein important to limit arterial calcification[218, 219]. Consultation of the single cell RNAseq database confirmed that smooth muscle cells express similar levels of STATH and MGP mRNA (Figure 3.14). Also noteworthy, other than osteocalcin (BGLAP), all other hydroxyapatite-binding secreted protein coding genes were expressed at <5% the level of statherin or MGP (Figure 3.15 A). Thus, statherin may be as important as MGP to block arterial calcification. It is also noteworthy that regardless of genotype, HAoSMCs retained a smooth muscle genetic program at the time of RNA isolation, expressing high levels of smooth muscle-specific markers (Appendix 4, Table 3). Thus, the difference in susceptibility to calcification does

not reflect a loss of smooth muscle cell phenotype associated with the 9p21.3 risk variants.

In line with our microarray results, immunoblot analysis showed that statherin protein is produced by HNR HAoSMCs, but barely if at all by HR HAoSMCs (Figure 3. 15 b, c). Prior proteomic studies examining proteins secreted from vascular SMC used a cutoff greater than 15 kDa and for this reason may have failed to detect statherin (10 kDa)[220, 221]. Furthermore, tryptic digests used in standard liquid chromatography-tandem mass spectrometry assays43 would degrade statherin to peptides that would escape detection (Fig. 3.16).Consistent with the low level of statherin expression in HAoSMCs carrying 2 copies of the 9p21.3 risk variants (HR), when cultured in the presence of elevated inorganic phosphate they accumulated more calcium crystals in their extracellular matrix compared to HAoSMCs carrying 0 copy of the 9p21.3 risk variants (HNR, Figure 3.15 d, e). Like MGP[222], statherin was found to accumulate at a calcified atherosclerotic lesion in a human coronary artery (Figure. 3.15 f, g).

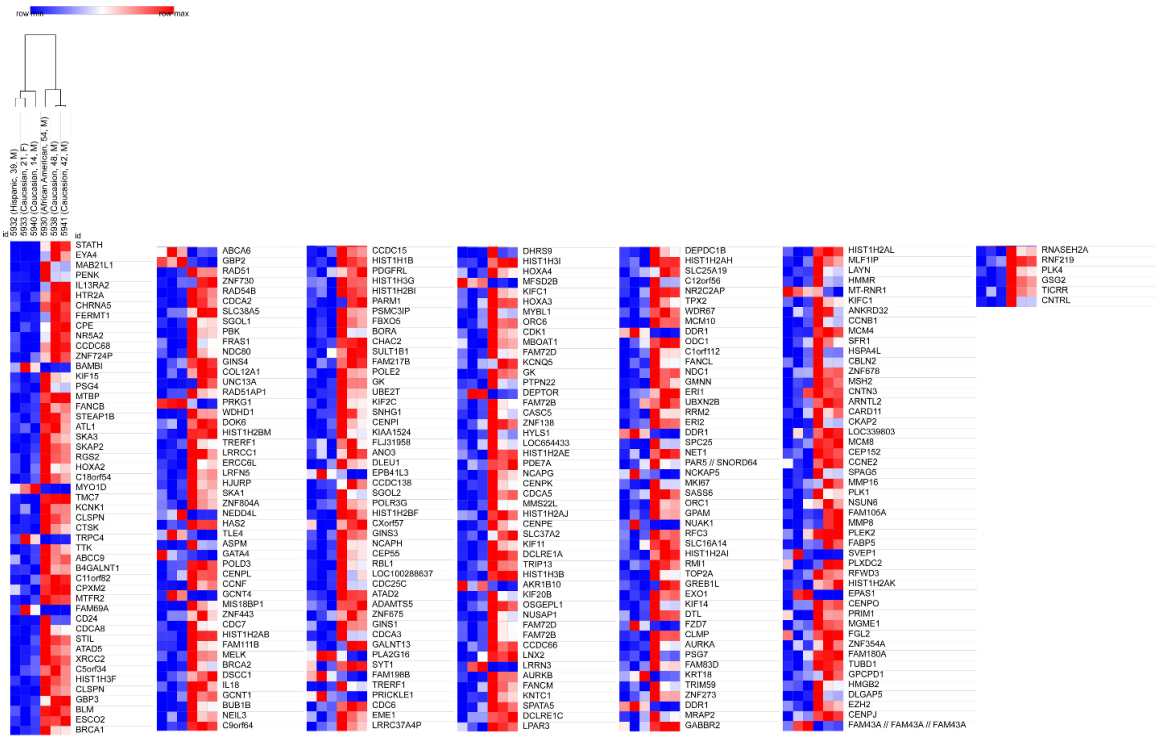

Figure 3.13. Heatmap of 295 differentially expressed genes according to 9p21.3 genotype in HAoSMCs.

First 3 samples are HR (homozygous for the risk allele) and next 3 are HNR (homozygous for the non risk allele). Note, only 30 genes were elevated in 9p21.3 HR HAoSMCs. Generated with Morpheus software using hierarchical clustering (**https://software.broadinstitute.org/morpheus/**).

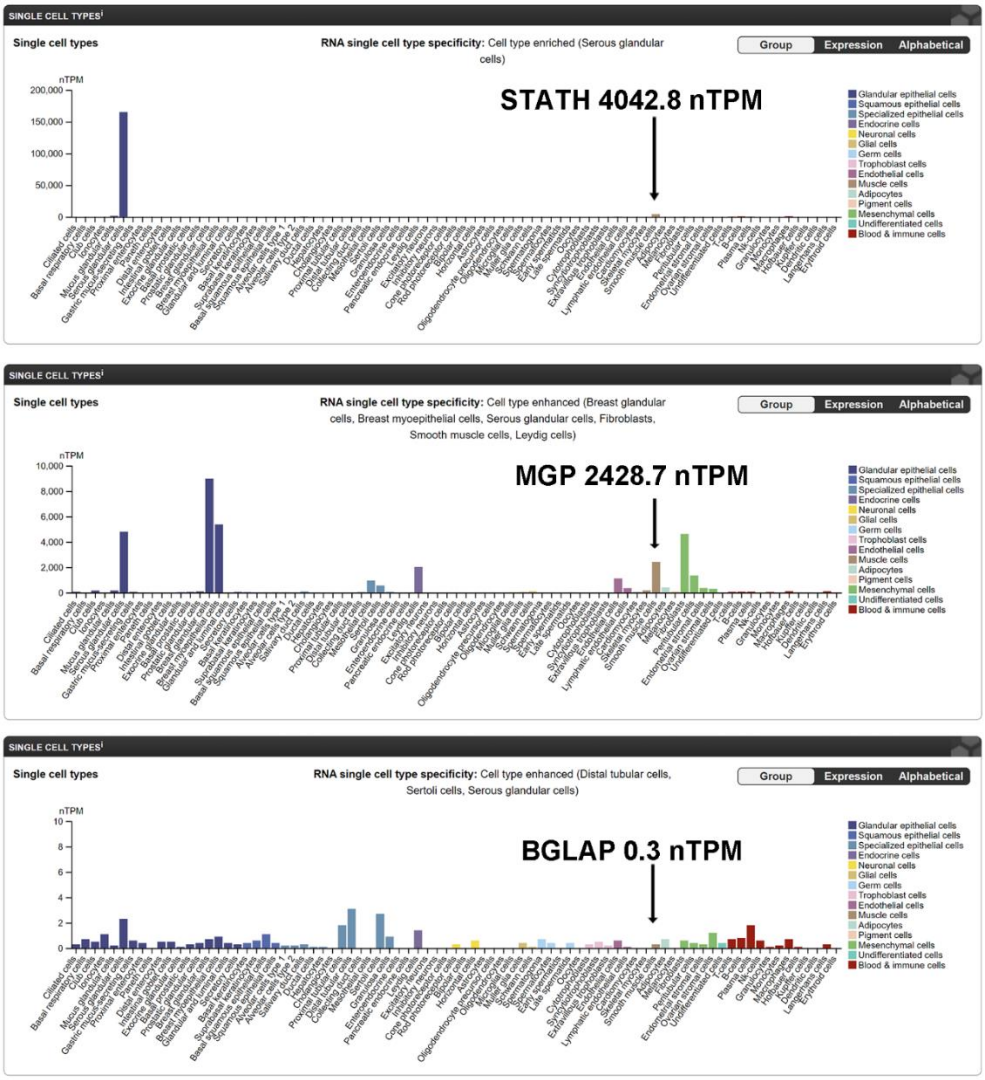

Figure 3.14. Single cell RNAseq reveals expression of STATH, MGP and BGLAP in smooth muscle cells.

(reproduced from **www.proteinatlas.org**). Transcript levels are expressed as normalized transcript per million (nTPM). Note: STATH expression in serous (salivary) glandular cells is several orders magnitude higher than in smooth muscle cells.

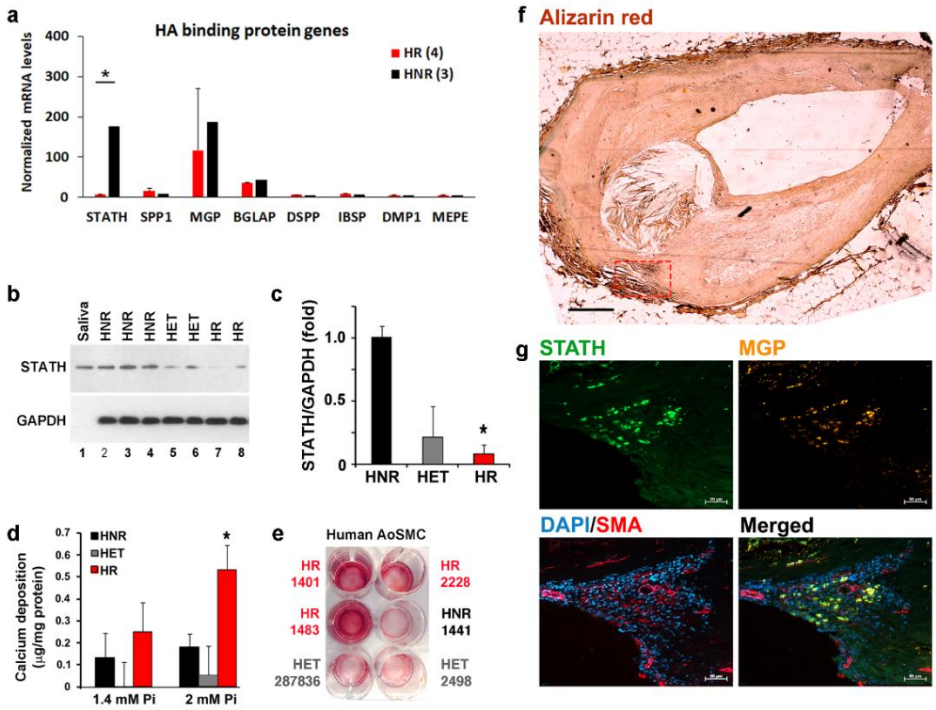

Figure 3.15. Statherin is suppressed in HAoSMCs homozygous for the 9p21.3 risk variants making them prone to calcification and accumulates at calcified coronary artery lesions.

a, Of hydroxyapatite-binding protein mRNAs detected in HAoSMCs (STATH, BGLAP and MGP) only statherin shows differential expression by the p21.3 risk genotype (n=4 Homozygous risk, HR; 4 heterozygotes, HET; 3 homozygous non-risk, HNR). Mean values ± SEM. *, Benjamini-Hochberg $p<10^{-11}$. **b**, **c**, Statherin protein is reduced in HAoSMCs bearing the homozygous risk allele (HR) as revealed by immunoblot, quantified by densitometry in (**c**). Saliva (diluted 1:600, was used as a positive control). HNR n=3; HET n=4, HR n=5; Densitometry, fold of HNR values ± SEM. *, $p<0.05$ compared to HNR by t-test. **d**, Quantitation of calcium (hydroxyapatite) deposition in confluent HAoSMCs after 10 days culture in medium containing 1.4 mM or 2.0 mM inorganic phosphate (Pi), normalized to total protein. n=3 HNR; 4 HET, 5 HR. Mean concentrations ± SEM. *, $p<0.05$ compared to HNR by t-test. **e**, Alizarin red staining reveals the extent of smooth muscle calcification under permissive (2 mM Pi) conditions. **F**, Alizarin red staining reveals a calcified lesion (boxed) within atherosclerotic plaque in a human coronary artery (representative image, n=3). Scale bar = 500 μm. **g**, Statherin (STATH, green) and MGP (ochre) are detected in the calcified lesion by immunofluorescence in an adjacent section. DAPI (4',6-diamidino-2-phenylindole, blue) stains the nuclei and SMA (α-smooth muscle actin, red) identifies smooth muscle cells. Scale bar = 50 μm.

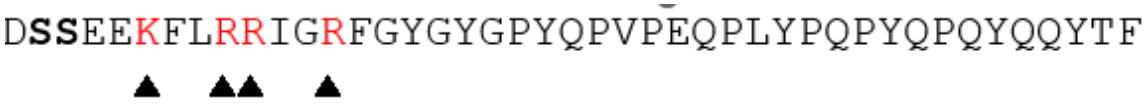

Figure 3.16. Statherin is difficult to detect by tryptic cleavage and LC-MS/MS. After removal of the signal peptide (not show), a trypsin digest cleaves C-terminal to arginine and lysine (R/K, ▲). The N-terminal DSSEEK peptide is small and highly acidic due to phosphorylation of the serine residues (bold) and may be lost during the trap column step of the injection during LC-MS/MS. The released C-terminal peptide FGYGYGPYQPVPEQPLYPQPYQPQYQQYTF is hydrophobic and carries a single charged amino acid (E, z=1). Thus, [M+2H]+2 = 1822.3459 m/z and would be unlikely to be detected in the standard MS scan range of 350 to 1600 m/z, with higher m/z usually having decreased ionization efficiency and only peptides with z=2 or greater identified. LC: Liquid Chromatography; MS/MS: Tandem Mass Spectrometry (MS/MS): Involves multiple stages of mass analysis, allowing for increased selectivity and specificity in compound identification. mass-to-charge ratio (m/z).

3.2.2. ANRIL silences statherin through an ALU element

How can genetic variants on chromosome 9 affect expression of the STATH mRNA transcribed on chromosome 4? The 9p21.3 genetic variants are located at an intergenic region associated with non-coding RNAs produced by alternative splicing that overlap with the CDKN2B (INK4) locus. Previously, we reported that the 9p21.3 risk alleles increase the expression of a short isoform of the long non-coding RNA ANRIL (antisense RNA at the INK4 locus)[155] that contains an ALU element. ANRIL was reported to regulate a host of genes in peripheral blood monocytes through the recruitment of the Polycomb repressor complex proteins to ALU elements[154]. The statherin gene contains an ALU element highly homologous to the sequences present in the short ANRIL transcript (Figure 3.17 A). To test whether the ANRIL transcript affects statherin expression, we generated a plasmid vector containing the statherin cDNA under the control of a CMV enhancer and bearing the first intron of rabbit beta globin that lacks an ALU element or one in which the beta globin intron contains the ALU element of the statherin first intron (Figure 3.17 B). It is noteworthy that plasmid vectors lacking the beta globin intron expressed no detectable statherin protein (Figure 2.5 A-B). ANRIL had no effect on statherin expression from the CMV vector lacking the ALU element but dose-dependently silenced statherin expression from the vector bearing the STATH ALU element. Thus, our results suggest the 9p21.3 risk alleles affect statherin mRNA expression through ALU-mediated repression by the short ANRIL transcript.

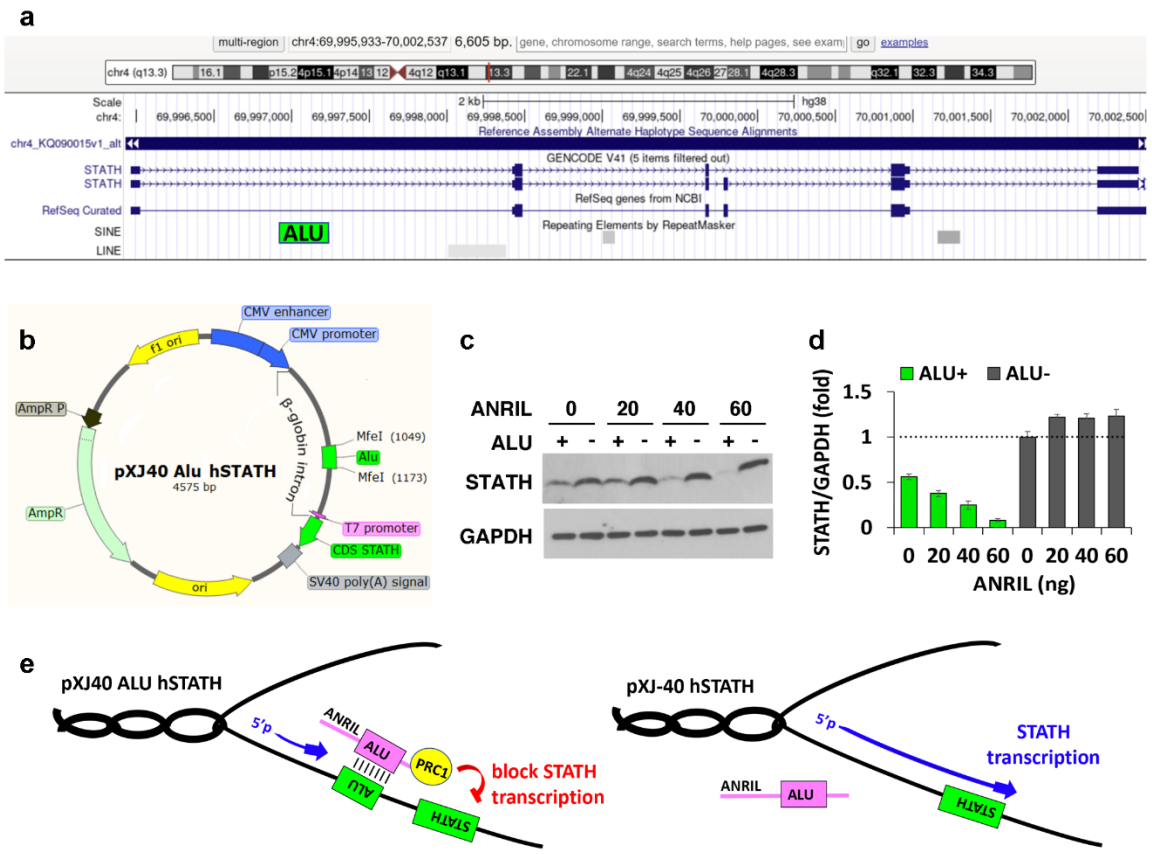

Figure 3.17. ANRIL lncRNA from the 9p21.3 locus silences Statherin expression through an Alu element in the first intron.

a, the statherin gene contains a single Alu short interspersed nuclear element (SINE) in the first intron. Screenshot from UCSC genome browser (genome.ucsc.edu) modified to show ALU element position. **b**, Construction of a CMV enhancer-driven human STATH expression vector bearing the statherin Alu element (pXJ40 Alu hSTATH) cloned into a unique MfeI site in the rabbit beta-globin intron. pXJ40 hSTAT vector lacks the Alu sequence. **c**, Cotransfection of ANRIL expression plasmid with pXJ40 Alu hSTATH (+) or pXJ40 hSTATH (-) expression plasmids shows ANRIL dose dependent suppression of statherin expression from the Alu-containing expression vector, quantified by densitometry in (**d**). **e**, Diagram of ANRIL Alu-dependent silencing of statherin transcription from pXJ40 Alu hSTATH vector, likely by recruiting Polycomb repressor complex (PRC1), as described[154]. The nascent transcript containing the phosphorylated 5' end (5'p) is shown in blue.

*3.2.3. Statherin blocks SMC calcification in vitro and in Mgp*KO *mice*

Statherin is best known as an abundant salivary protein that binds to hydroxyapatite to block the formation of calcified plaque on teeth[176]. We asked whether statherin also inhibits calcification of SMCs. A lentiviral vector bearing the CMV enhancer/beta-globin intron/human statherin cDNA and a red fluorescence protein marker (Figure 2.6**)** was used to express statherin in primary aortic smooth muscle cells of *Mgp*-null mice. Because fewer than 20% of primary SMCs were transduced by lentiviral vectors (Figure 2.6), lentiviral-transduced cells were selected with puromycin. Expression of statherin markedly reduced matrix calcification around *Mgp*-null SMCs (Figure 3.18 a-c).

Given that *Mgp*KO mice die within a few weeks after birth of severe arterial calcification and aortic and arterial dissection[32], and that the statherin gene is absent in rodents[223], we asked whether human statherin could stand in for MGP and ameliorate arterial calcification in these mice. Mice bearing a *Cre*-dependent stop-flox *STATH* transgene on the Tagln-*Cre* background (enabling CRE-dependent expression of statherin in smooth muscle cells) were bred with *Mgp*KO heterozygotes mice (for details, see online methods). Smooth muscle-specific expression of statherin prevented arterial calcification in *Mgp*KO mice (Fig. 3.18 d-i) and significantly prolonged lifespan (Fig. 3.19). However, it is important to note that tooth malocclusion and bone malformations were partially rescued by SMC-specific expression of statherin (data not shown) and mice were sacrificed at ethical timepoints.

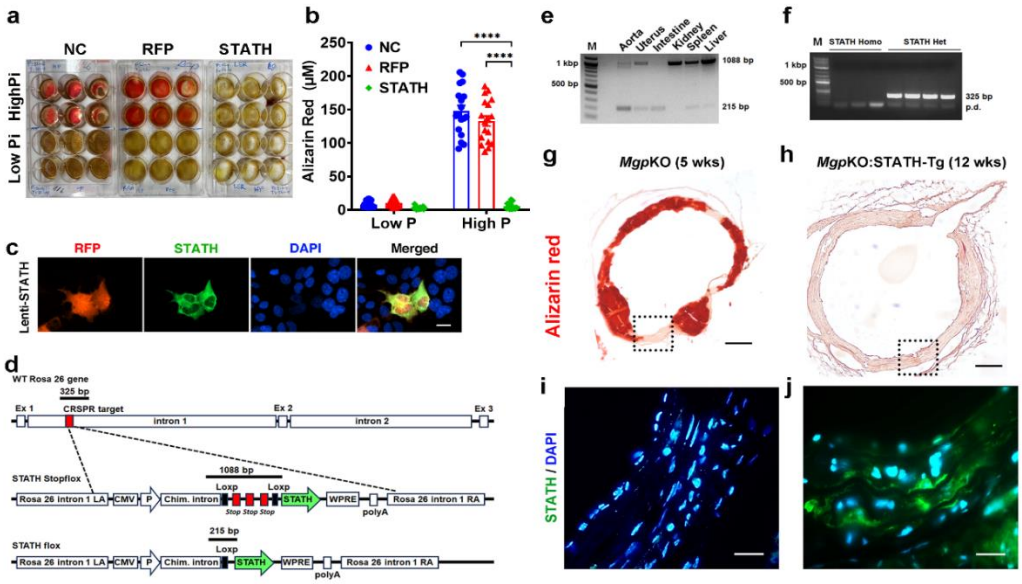

Figure 3.18. Human statherin expressed from a lentivirus (a-c) or a smooth muscle-specific transgene (d-j) reduces calcification of aortic smooth muscle cells of *Mgp*-null mice.

a, MGP-null (*Mgp*KO) AoSMCs were grown in medium containing 1.0 mM (Low Pi) or 2 mM (High Pi) inorganic phosphate for 6 days (negative control, NC) or transduced with lenti-control (RFP) or lenti–statherin (STATH), 10^6 viral particles per ml medium (moi=10) at the time of plating (n=3). **b**, Calcium deposition was assessed in separate plates, normalized to protein (n=18/group). Two-way ANOVA: phosphate medium $F_{1,102}$=527.6, p<0.0001; statherin $F_{2,102}$=151.3, p<0.0001; interaction $F_{2,102}$=126.3, p<0.0001; ****, p<0.0001 by Tukey's multiple comparisons for full statistical analysis). **c**, Immunofluorescence confirmed red fluorescent protein (RFP) and statherin (STATH, green) lentiviral over-expression in *Mgp*KO AoSMCs. DAPI stained nuclei. Scale bar, 10 μm. **d**, Generation of transgenic mice with smooth muscle-specific expression of human STATH. A conditional expression transgene was integrated to the Rosa26 locus by CRISPR/Cas9 technology and mated to TAGLN-Cre mice on an Mgp+/- background. **e**, Robust cre-dependent excision of the 3xStop cassette was achieved in smooth muscle-containing tissues (aorta, uterus, intestine). **f**, STATH protein expression was only detected in mice homozygous for the STATH transgene (STATH homo, n=4) that do not amplify a 325 bp fragment from Rosa26 observed in heterozygous mice (STATH het). **g**, Alizarin red staining of a 5-week-old MGP-null (*Mgp*KO) mouse aorta reveals extensive calcification of the artery wall. Scale bar, 100 μm. **h**, Alizarin red staining of an MGP-null mouse with smooth muscle-specific expression of human statherin (MGPKO: STATH-Tg) at 12 weeks of age was free of arterial calcification. Scale bar, 100 μm. **i**, Statherin expression is absent in non-calcified aortic tissue of MGP-null mice and **j**, present in *Mgp*KO:STATH-Tg mice.

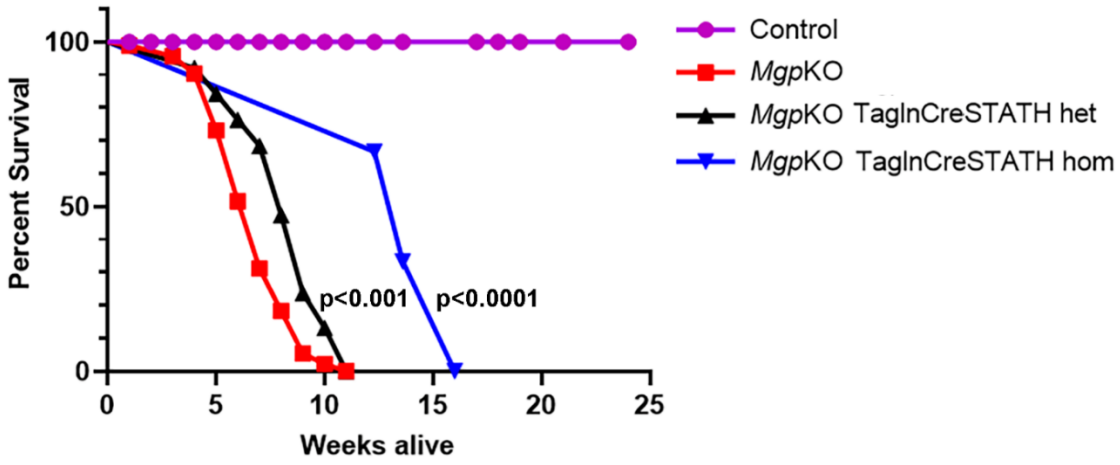

Figure 3.19. Kaplan-Meier survival analysis revealed a significant improvement in *Mgp*KO mice with SMC-specific expression of statherin.

*Mgp*KO*Tagln*CreSTATHhet mice (n=38) survived a median of 8 weeks compared to MgpKO mice (n=98) that survived a median of 7 weeks, ***, p=0.0002 by the Log-rank (Mantel-Cox) test, Chi square 13.95. Mice homozygous for the STATH transgene (*Mgp*KOTaglnCreSTATHhom, n=3) survived a median of 13.6 weeks, ****, p<0.0001 by the Log-rank (Mantel-Cox) test, Chi square 15.67, before euthanasia to evaluate arterial calcification.

Ablation of the *Mgp* gene in mice not only leads to the loss of a hydroxyapatite-binding protein, MGP is also known to inhibit signaling by bone morphogenic proteins that facilitate chondrogenic/osteogenic conversion of smooth muscle cells[53, 224, 225]. Since human statherin could block calcification of MGP-null smooth muscle cells in culture and *in vivo*, we asked whether it can also affect BMP signaling. Statherin markedly inhibited the activation of a BMP-responsive luciferase reporter in response to BMP4 over-expression (Figure 3.20). Thus, like MGP, statherin can bind hydroxyapatite

crystals[176] and our data show it inhibits BMP signaling. Taken together, our observations have identified loss of statherin expression as a key component that accounts for the effect pf 9p21.3 risk alleles to increase susceptibility to coronary artery calcification.

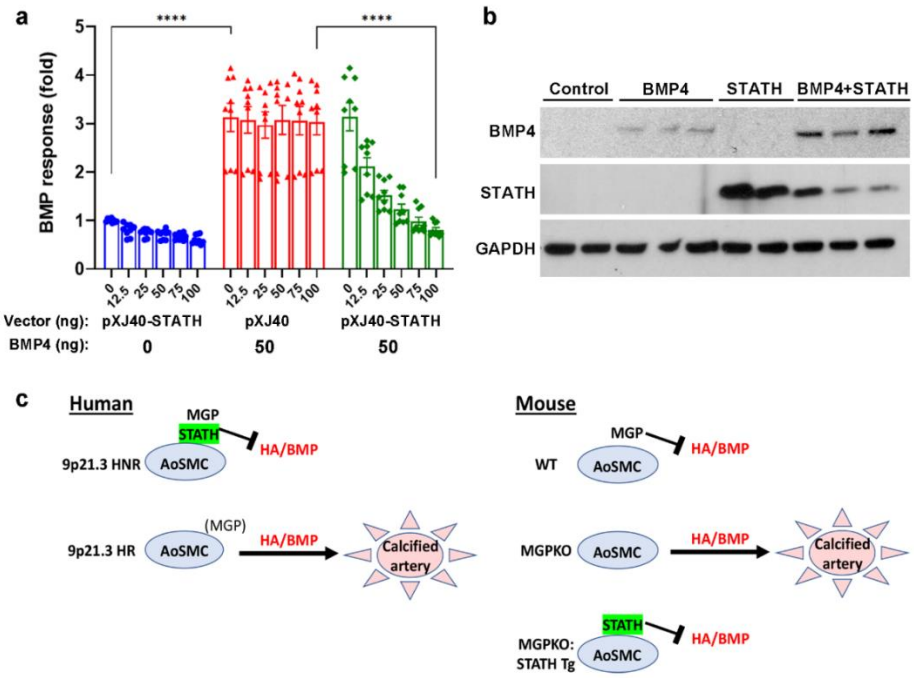

Figure 3. 19. Statherin inhibits BMP4 signaling.

a, A BMP-responsive luciferase reporter plasmid (pGL3-BRE-luciferase[203], 500 ng) was co-transfected into HEK293 cells with expression plasmids for BMP4 (pCAG BMP4[204], 50 ng) together with increasing doses of a statherin expression plasmid (pXJ40 hSTATH) or an empty control vector (pXJ40). BMP4 activation was markedly attenuated by STATH expression (ANOVA, $F_{5,144}$=10.20, p<0.0001, ****, p<0.0001 by Šídák's multiple comparisons test) but not by empty expression vector (see **Supplementary Table 6** for full statistical analysis). **b**, Immunoblot confirmed expression of BMP4 and STATH from the expression plasmids (50 ng each). **c**, Diagram distinguishing calcification risk of human and mouse aortic smooth muscle cells. 9p21.3 HNR cells express MGP and STATH that block calcification by binding to hydroxyapatite (HA) and by inhibiting BMP signaling, while 9p21.3 HR cells silence STATH by an ANRIL-mediated Alu mechanism (see **Fig. 2**) without altering MGP expression (**Fig. 1a**) and are susceptible to arterial calcification (**Fig. 1d**, **e**). Mice lack the statherin gene, so ablation of MGP

causes calcified arteries. Transgenic expression of human STATH prevents arterial calcification in mice, suggesting a therapeutic potential to this approach.

3.2.4. Other mechanisms tied to calcification at the 9p21.3 risk locus

Beyond our top hit statherin, other genes were differentially expressed according to the 9p21.3 risk genotype in HAoSMCs, the majority were downregulated in HR cells compared to HNR (265/295). While we did not pursue these mechanisms here, it is worthwhile noting them as possible candidates for future studies. Our previous study identified risk alleles that disrupt TEAD transcription factor binding and the response to TGFβ signaling at the 9p21.3 locus[145]. TGFβ signaling inhibits vascular SMC calcification in culture[226]. In addition to statherin, other genes involved in TGFβ signaling that could affect CAC[226] were also affected by 9p21.3 (Appendix 4). For example, the mRNA for BAMBI, a TGFβ decoy receptor that inhibits TGFβ signaling and promotes mineralization[227], was 7 times more abundant in HR versus HNR HAoSMCs.

3.2.5. *Mgp*KO/*Mgp*KO *DA- STATH-Cre show evidence that mutated statherin is lethal*

The *Mgp*-KO/*Mgp*KO-DA-Statherin-Cre mice, despite successful generation, exhibited complete mortality within the first month, highlighting the complexity of calcium homeostasis regulation *in vivo* (Figure 3.21).

Homology modeling of Statherin isoforms using SWISS-MODEL and Robetta [228, 229] revealed significant structural transformations between wild-type and mutated protein

configurations. The most notable change occurred at positions D21 and D22, where mutations induced a dramatic transition from a loop conformation to a structured α-helical arrangement (Figure 3.22). This structural shift was accompanied by a substantial electrostatic surface potential change, ranging from -44.226 to +44.226, fundamentally altering the protein's interaction characteristics (Figure 3.23).

The computational analysis demonstrated a marked reduction in the N-terminal region's flexibility within the mutated form, suggesting a pronounced structural rigidification. The conversion of the loop region to a -helical structure around D21 and D22 positions highlighted the profound impact of subtle sequence variations on protein architecture. Electrostatic potential distribution analysis revealed a significant transformation from a relatively neutral surface charge in the wild type to a strongly negative region in the mutant variant.

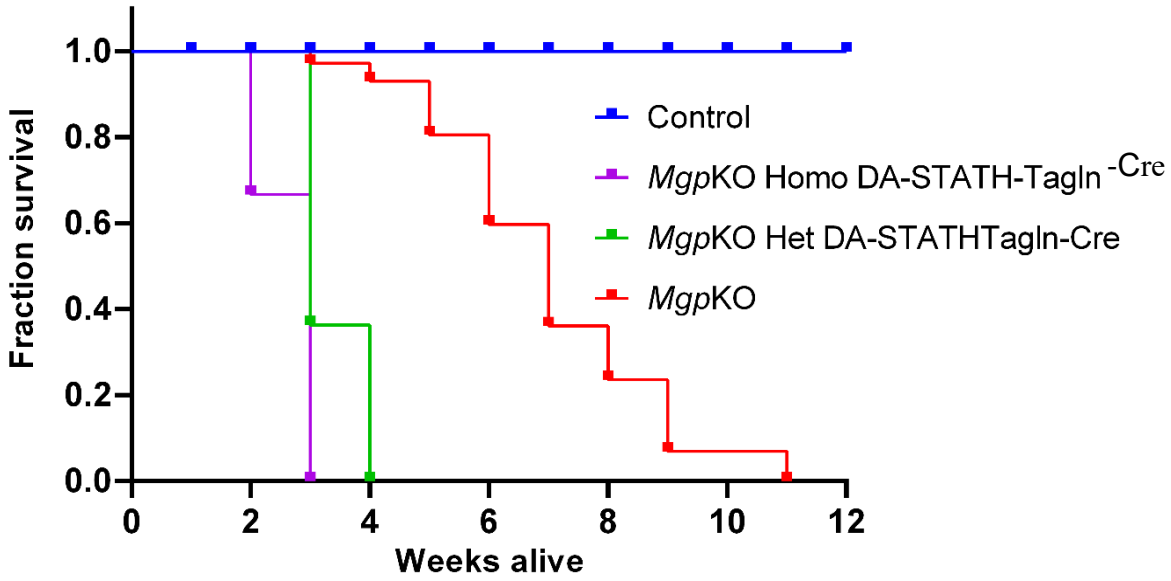

Figure 3.21. Kaplan/Mire for *Mgp*-KO/*Mgp*KO-DA-statherin-Cre.

Accelerated death (n=2) at 3 weeks age for homozygote for DA-STATH and (n=11) heterozygotes at 4 weeks age.

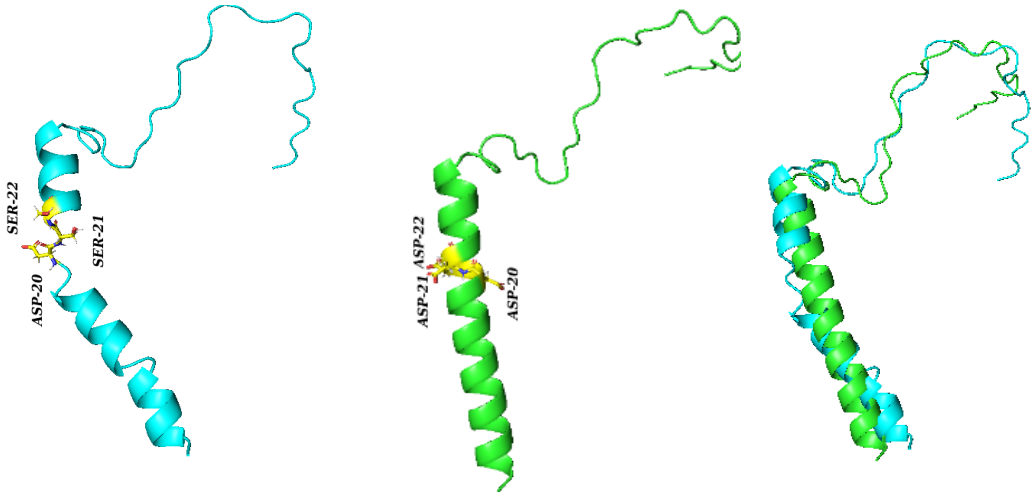

Figure 3.22. **Homology Modeling of both statherin and DA-statherin (mutated version).**

Homology modeling was conducted using two tools: SWISS-MODEL and Robetta. The analysis revealed that the mutations induce a structural change, converting the loop conformation into a helix at residues D21 and D22.

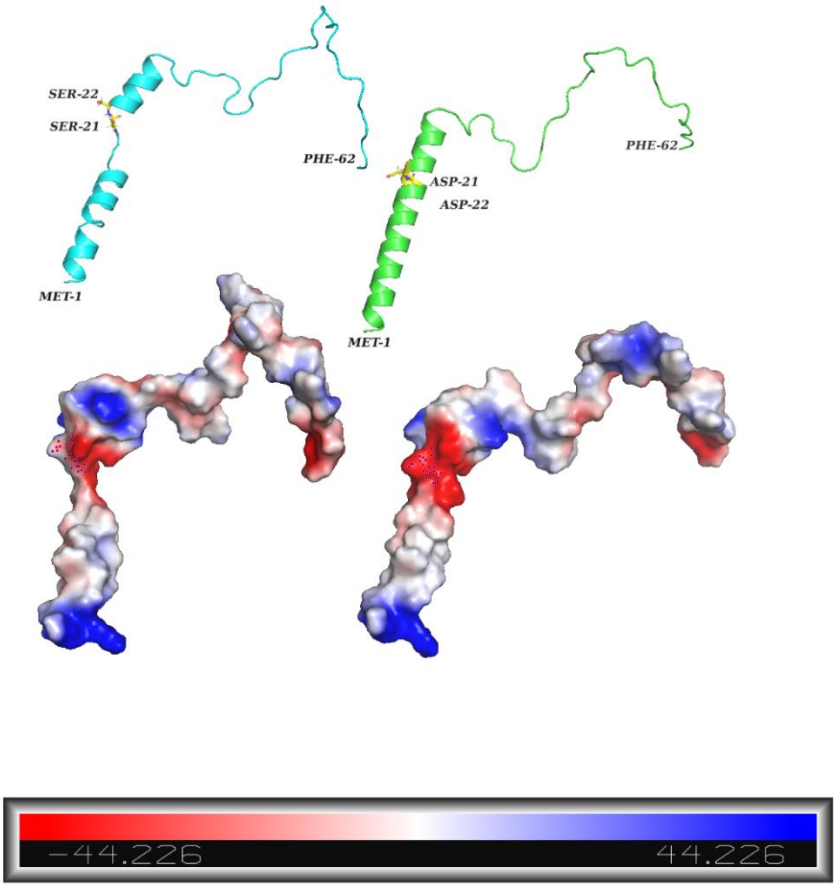

Figure 3. 22. Electrostatic Contact Map.

The contact map highlights how sequence differences may impact the charge distribution on the protein surface. In the DSS wild-type protein, the mutation to ASP introduces a relatively negative charge, converting a previously almost neutral region. This alteration in the charge distribution occurs at a specific region with different residues of the mutated Statherin. The resulting negative surface charge influences the protein's interactions with other molecules. Depending on the interaction region, this change can lead to either attractive or repulsive interactions

Chapter 4: Discussion

4.1. Alendronate therapy

This study reveals the consequence of Alendronate treatment on vascular and soft tissue calcification in the context of *Mgp* deficiency and on the uptake of hydroxyapatite by macrophages. Our results reveal several key points that have important implications for understanding the pathogenesis of vascular calcification and potential therapeutic strategies.

First, our study demonstrates that both early and late alendronate treatment ameliorates incisor malocclusion in MgpKO mice, implicating disrupted pyrophosphate metabolism—secondary to MGP deficiency—as a key contributor to tooth morphogenic defects. This conclusion is supported by the finding that substituting a synthetic pyrophosphate could restore incisor growth and alignment in the absence of MGP in a dose-dependent fashion. Specifically, a higher dose of pyrophosphate (0.7 mg/kg/week) administered after weaning improved malocclusion without tooth loss. In contrast, a lower dose (0.5 mg/kg/week) given from postnatal day 3 impaired incisor development, resulting in the absence of upper incisors. These results highlight the essential role of pyrophosphate in cementum formation[65]., Consistent with findings in Alpl-null mice ((lacking the enzyme that degrades pyrophosphate)where excess pyrophosphate causes root detachment and mimics premature tooth loss in hypophosphatasia.[65] Our data suggest that MgpKO mice are likely deficient in pyrophosphate production, possibly as a compensatory mechanism

for the loss of MGP. This concept is further supported by the findings of Parashar et al., who demonstrated that mice expressing a mutant form of MGP lacking its conserved γ-carboxylated glutamic acid residues (SM22α-Gla^mutMgp) exhibited impaired protection against phosphate-induced vascular calcification, underscoring the critical role of MGP's γ-carboxylated domain in mineral homeostasis.[230].

Alendronate's therapeutic effect is attributed its ability to bind hydroxyapatite crystals, inhibiting their growth and accumulation[231] . This action helps prevent ectopic calcification in soft tissues, such as ligaments and cranial structures, which can disrupt jaw architecture and lead to malocclusion. By reducing abnormal crystal accumulation, alendronate supports proper maxillary (upper jaw) development and promotes correct incisor alignment.

In MgpKO mice, ectopic calcification leads to jaw misalignment and uncontrolled incisor elongation, due to interference with natural attrition—a key process in rodents, whose incisors grow continuously throughout life[206]. This disruption promotes uncontrolled hydroxyapatite crystal growth in the tissues surrounding the teeth, resulting in malocclusion and aberrant incisor growth[206]. Balanced attrition from opposing teeth is essential for proper occlusion, and jaw misalignment impairs this process, leading to unchecked incisor elongation. Our findings deeply revealed that alendronate mitigates this pathology through a dose- and time-dependent mechanism: low doses reduce hydroxyapatite crystal formation while preserving normal bone remodeling, leading to

improved tooth and bone development. Importantly, osteoclasts play a vital role in bone resorption, which is essential for dental eruption, craniofacial remodeling, and maintaining the balance of bone formation and degradation[232]. High doses of alendronate excessively inhibit osteoclast activity, thereby disrupting this resorptive process and impairing normal tooth and jaw development. This imbalance can prevent necessary bone remodeling, contributing to abnormal mineralization and dental defects.

Our findings indicate that early, optimally dosed alendronate treatment can fully correct malocclusion, while later-stage interventions yield only partial benefits and may require mechanical correction (e.g., trimming). Mechanistically, alendronate is most effective during the nucleation phase of mineral formation, where it prevents new crystal foci from developing. However, its ability to reverse pre-existing calcifications is limited[33]. underscoring the importance of early intervention. Thus, this study highlights the critical role of pyrophosphate metabolism and balanced bone remodeling—mediated by osteoclasts—in dental and craniofacial development.

Second, our study reveals that the synthetic pyrophosphate Alendronate exacerbates arterial calcification in the *Mgp*KO mouse. This finding stands in stark contrast to the beneficial effects of alendronate in preventing arterial calcification in a rat model where the vitamin K inhibitor warfarin inhibits γ-carboxylation and activation of MGP, thereby inducing arterial calcification over several weeks [33]. This finding stands in stark contrast to the beneficial effects of alendronate in preventing arterial calcification in a rat model where

the vitamin K inhibitor warfarin inhibits γ-carboxylation and activation of MGP, thereby inducing arterial calcification over several weeks[33]. Furthermore, Malhotra et al. demonstrated that inhibiting BMP2/4 signaling reduced calcification by 80%, but did not completely abolish it, indicating that BMP-independent mechanisms also contribute to vascular calcification[60]. This suggests that mineral deposition can occur independently of classical cellular differentiation pathways[231]. Consistent with this, our in vivo and in vitro results show that alendronate directly interacts with hydroxyapatite (HA), forming stable complexes that are subsequently taken up by macrophages. Once internalized, this combination impairs macrophage migration and induces apoptosis, disrupting their ability to regulate mineral deposition. These dysfunctional macrophages fail to clear calcified deposits effectively, promoting uniform mineral accumulation and exacerbating calcification through non-cell-autonomous mechanisms. Supporting this concept, Khavandgar et al. (JBMR, 2014) demonstrated that MGP-deficient arteries do not show induction of target genes downstream of BMP signaling (e.g., alkaline phosphatase, ID1), challenging the traditional view that vascular calcification in MGP deficiency is solely driven by classical osteogenic pathways involving BMP signaling[25]. Moreover, the study found that compound mutants lacking both MGP and tissue-nonspecific alkaline phosphatase (TNAP) did not exhibit reduced vascular calcification, further suggesting that mineralization can proceed through TNAP-independent mechanisms[25]. Thus, even in the presence of functionally compromised MGP, pyrophosphate can inhibit calcification; however, in the complete absence of MGP—as seen in *Mgp*KO mice—pyrophosphate is

insufficient to prevent arterial calcification. This interdependence highlights the critical requirement for both MGP and pyrophosphate to maintain vascular homeostasis. Similarly, humans and mice with normal MGP but a homozygous mutation in ENPP1 (the enzyme required to synthesize pyrophosphate) develop severe arterial calcification early in life, further underscoring the essential role of pyrophosphate-MGP interactions Infancy [71, 74, 75, 233].

Third, the observation that a single dose of alendronate rapidly and aberrantly elevated the early chondrogenic/osteogenic transcription factor Runx2 in *Mgp*KO aorta, but not in wild-type or *Mgp*- heterozygotes mice, points to a specific interaction between bisphosphonate treatment and *Mgp* deficiency. The acceleration of Runx2 expression in aortic smooth muscle cells (SMCs) following alendronate treatment is particularly noteworthy since it suggests that in the absence of MGP, bisphosphonates paradoxically promote chondrogenic/osteogenic conversion of vascular SMCs. Since RUNX2 activation depends upon the action of the bone morphogenic proteins (BMP2/4), an intriguing possibility is that in the absence of MGP, hydroxyapatite and pyrophosphate activate BMP2/4 to drive chondrogenic/osteogenic conversion. Addition of a small quantity of hydroxyapatite to collagen scaffolds containing BMP2 was reported to accelerate and improve osteogenesis, suggesting that hydroxyapatite is an essential catalyst of BMP2 that works in a positive feedback for osteogenesis and calcification [44]. Expression of Runx2 mRNA was reported to precede chondrogenic/osteogenic conversion of smooth muscle cells in *Mgp*KO mice [60]. While RUNX2 protein levels were elevated in *Mgp*KO mice at 5

days and further increased by Alendronate treatment, the transcription factor Runx2 must translocate to the nucleus to activate the chondrogenic/osteogenic program [40]. Indeed, nuclear localization of RUNX2 was only observed in Alendronate treated *Mgp*KO mice at this age, consistent with an earlier activation of osteogenesis.

Fourth, the exacerbation of ear calcification in *Mgp*KO mice treated with Alendronate, particularly in capillary-rich structures, highlights the widespread effects of *Mgp* deficiency and the potential risks associated with bisphosphonate therapy. This observation aligns with findings in other conditions involving ectopic calcification with modified elastin fibers, such as calcific uremic arteriolopathy [234], emphasizing the vulnerability of capillary-rich structures to calcification processes. It is noteworthy that bisphosphonates are contraindicated in chronic kidney disease [235]. Elastin heterozygotes *Mgp*KO mice have improved arterial calcification associated with ameliorated deficits in bone development [206, 236]. The authors concluded that arterial calcification was responsible for bone deficits. Here, we found that bone deficits, or at least orofacial deficits leading to incisor malocclusion, could be rescued by bisphosphonate treatment without simultaneous rescue of arterial calcification, arguing that bone deficits may be a consequence of disrupted pyrophosphate metabolism occurring with arterial calcification.

Fifth, our study revealed the intriguing effects of Alendronate on macrophage function *in situ*. In chronically treated *Mgp*KO mice, we observed loss of CD68 immunoreactivity at the site of calcified deposits. CD68 can shuttle from the cell surface

to the endosomal/lysosomal compartment and is a lysosomal-associated protein that contains a highly glycosylated mucin-like domain involved in ligand binding [237]. Mice lacking CD68 have functional deficits in osteoclasts that accumulate vesicle-like structures and do not efficiently resorb bone [238]. Thus, loss of CD68 might be functionally relevant to arterial calcification if CD68 participates in the clearance of hydroxyapatite. Furthermore, the localization of aortic calcified lesions changed with Alendronate treatment, becoming less concentrated at branch points of the vertebral arteries and more diffuse between these nodes. Inhaled Alendronate was reported to impair lung macrophage migration and phagocytosis [239]. Macrophages accumulate at branch points of vertebral arteries during development, likely due to differences in sheer stress from oscillatory blood flow [46]. If Alendronate impairs macrophage migration and phagocytosis, this could explain why calcification increases at the internodal regions of the aorta. This is consistent with Alendronate directly interacting with hydroxyapatite, preventing crystal growth[231]. Its uptake by macrophages and subsequent accumulation within endosomes or lysosomes impairs lysosomal function, inhibiting processes such as migration, inducing apoptosis, and disrupting the mevalonate pathway[232]. Our results indicate that these processes lead to diffuse calcification and reduced calcification at branch points, converting macrocalcification into microcalcification. This transformation exacerbates arterial calcification, as the diffusion and generation of microcalcifications damage elastin (Elastocalcinosis)[25], resulting in arterial fragility, stiffness, and a lack of flexibility.

Sixth, in primary cultured bone-marrow derived macrophages acutely treated with

Alendronate, we observed an increase in the accumulation of hydroxyapatite in CD68-positive endo/lysosomes. Endocytosis of alendronate takes place by a fluid-phase endocytosis mechanism that requires acidification of the endosomes to release alendronic acid onto the cytoplasm [240]. Clearance of hydroxyapatite from the interstitial space likely also relies on endocytosis to macrophage lysosomes to dissolve hydroxyapatite to calcium and phosphate ions. It is doubtful that these ions are returned to the cytoplasm as the calcium concentration is extremely low. Instead, these ions might be released from macrophages to the extracellular space by recycling endosomes. Alendronate inhibits the prenylation of the Rab GTPases involved in endosomal sorting [124], and these changes could account for the accumulation of the calcium-sensitive dye Fluo-4AM in lysosomes that we observed in alendronate-treated macrophages. Similarly, statins act on the mevalonate pathway and impair mechanisms of endocytosis [241] as well as exocytosis [242]. What role Mgp plays in the uptake and clearance of hydroxyapatite also remains unclear. *In vivo*, smooth muscle cells release hydroxyapatite coated with Mgp. Once outside the cell, pyrophosphate produced by the secreted enzyme ENPP1 associates with the Mgp/hydroxyapatite complex and these are taken up by macrophages to be eliminated by dissolution in lysosomes. Loss of Mgp must somehow disrupt this process and supplementing Alendronate seems to make it worse. **Figure 2.13** presents our model of hydroxyapatite production and clearance.

Seventh, reconciling our in vivo findings with recent in vitro data from Bak et al. (JSB, 2024), demonstrating alendronate's inhibition of mineralization in arterial explant cultures,

requires careful consideration of several factors[231]. The divergence may stem from differences in local drug concentrations, as in vitro experiments involve direct tissue exposure to defined alendronate levels, whereas in vivo systemic distribution and bone sequestration may result in lower vascular concentrations. Furthermore, our in vivo model captures systemic effects on calcium and phosphate homeostasis, which are absent in Bak et al.'s in vitro setup[231]. Additionally, MGP deficiency alters mineral dynamics and cellular interactions in vivo, modulating alendronate's effects. As discussed in Point 5, alendronate's uptake by macrophages and subsequent accumulation within lysosomes leads to impaired lysosomal function and microcalcification, which may not be fully recapitulated in in vitro models. These differences in local drug concentrations, systemic influences, cellular interactions, and altered mineral dynamics likely contribute to the apparent discrepancy between in vitro and in vivo observations, highlighting the importance of considering tissue context when evaluating drug effects on vascular calcification.

Finaly, the observed calcification in the renal arteries of *Mgp*KO mice, as revealed by micro-CT scanning and Alizarin red staining, underscores the critical role of Matrix GLA Protein in preventing vascular mineralization in these vital vessels. The presence of calcification at the entrance of the renal arteries into the kidney is particularly significant, as it demonstrates the vulnerability of these specific arteries to mineralization in the absence of MGP. This localized calcification could have profound implications for kidney function, potentially contributing to renal complications in *Mgp*KO mice. The findings align with the established understanding of MGP's function as a potent inhibitor of vascular

calcification, especially in elastic and muscular arteries[18, 243]. The use of advanced imaging techniques in this study not only confirms previous research on the consequences of MGP deficiency but also provides a more detailed spatial understanding of calcification patterns in renal arteries. These results offer valuable insights into the pathogenesis of vascular calcification in the renal system and may inform future studies on potential therapeutic interventions for conditions like chronic kidney disease, where renal artery calcification is a significant concern.

Limitations of the Study

While our study provides significant insights into the mechanisms of alendronate action and its effects on vascular calcification in *Mgp*-deficient mice, several limitations should be noted:

Lack of Evaluation of Downstream Chondrogenic/Osteogenic Markers:

Our study did not evaluate downstream markers such as osterix, alkaline phosphatase, or BMP signaling in *Mgp*-deficient arteries post-alendronate treatment. Previous studies have demonstrated that MGP deficiency induces BMP signaling and trans-differentiation of vascular smooth muscle cells (VSMCs) toward chondrogenic/osteogenic lineages. However, mineral deposition in *Mgp*-deficient arteries often precedes upregulation of these markers, suggesting that mineralization may occur independently of classical

osteogenic pathways. Future studies should include histological or molecular analyses to confirm whether alendronate exacerbates vascular calcification through these pathways or alternative mechanisms.

Absence of Histological or Molecular Analysis of Nasal Septum Calcification and Cranial Base Synchondroses:

Although we hypothesized that alendronate may inhibit abnormal mineralization of the nasal septum and prevent premature fusion of cranial base synchondroses in *Mgp*-deficient mice, our study lacks direct evidence to support this claim. Histological or molecular analyses are necessary to determine whether alendronate impacts these regions and to elucidate its role in craniofacial development. Such analyses could provide critical insights into how alendronate indirectly corrects jaw positioning and normalizes incisor wear.

Lack of Direct Evidence Confirming Elastin Degradation at Sites of Increased Mineralization:

While our findings suggest that Elastocalcinosis contributes to arterial fragility and stiffness in *Mgp*-deficient mice treated with alendronate, we did not perform direct analyses to confirm elastin degradation at these sites. Elastin haploinsufficiency has been shown to impede arterial calcification progression, and degradation of elastic fibers is linked to ectopic calcium phosphate deposition. Future studies should focus on

identifying molecular markers of elastin degradation and assessing their correlation with mineralization patterns in affected tissues.

In summary, the first set of results reveals a complex interplay between alendronate, Mgp, and the vascular calcification process. While alendronate ameliorated deficits in incisor development in *Mgp*KO mice, it paradoxically exacerbated arterial and soft tissue calcification, suggesting an essential co-requirement for pyrophosphate and Mgp in preventing ectopic mineralization/calcification. The acute elevation of Runx2 in *Mgp*KO aorta following alendronate treatment further hints at an aberrant chondrogenic/osteogenic conversion of vascular smooth muscle cells caused by loss of Mgp that is amplified by the bisphosphonate alendronate. Furthermore, alendronate altered macrophage phenotype and increased calcium accumulation in lysosomes, conditions that could exacerbate the burden of arterial calcification. These results highlight the critical role of MGP in preventing chondrogenic/osteogenic conversion of soft tissues and underscore the potential risks of bisphosphonate therapy in conditions associated with MGP deficiency. Our study emphasizes the need for caution when considering bisphosphonate treatment in patients with or at risk for vascular calcification, particularly in the context of potential MGP dysfunction. Future research should focus on developing targeted therapies that can address both bone health and vascular calcification risks in MGP-deficient conditions, considering the complex interactions between bisphosphonates, MGP, and macrophage-mediated calcium homeostasis.

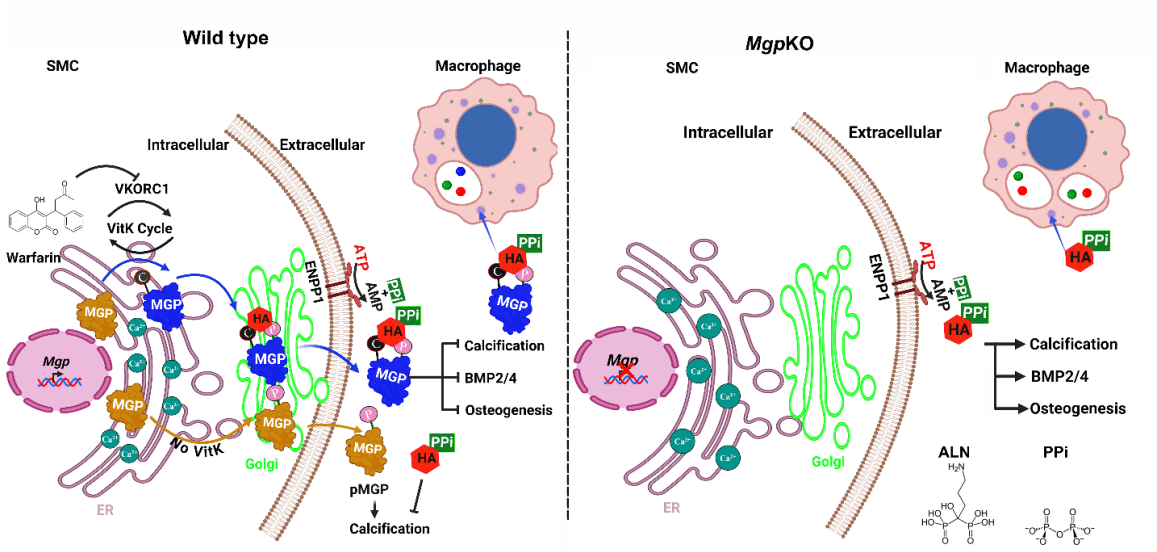

Figure 3.23. Overview of Alendronate effects in the presence or absence of Mgp.

In wild type mice, Mgp is phosphorylated and further modified by a vitamin K dependent carboxylation that enables it to bind to hydroxyapatite (HA) in the Golgi, prior to secretion from smooth muscle cells (SMC). Warfarin inhibits Vitamin K Epoxide Reductase Complex Subunit 1 (VKORC1) and prevents vitamin K activation required for Mgp carboxylation, rendering Mgp partially inactive. Pyrophosphate (PPi) is produced by ENPP1 and combines with Mgp/HA to produce a protected Mgp/HA/PPi complex that inhibits calcification, prevents Bmp2/4 activation and osteogenesis and may facilitate the clearance of HA by macrophages. In *Mgp*KO mice, the absence of Mgp renders the HA/PPi or HA/Alendronate (ALN) complex pro-calcific, stimulating Bmp2/4 and chondrogenic/osteogenic conversion of SMC. Macrophages accumulate HA/PPi in lysosomes, perhaps due to impaired clearance. Image generated with bioRender®.

4.2. Discussion: 9p21.3 Genetic Variants Suppress Smooth Muscle Cell Statherin Expression

The 9p21.3 locus was the first genetic risk locus identified for coronary atherosclerosis[244, 245]. Subsequent studies also tied this locus to coronary artery calcification[143, 246-249], aortic calcification[249], abdominal aortic and intracranial aneurysms[156, 159], and surprisingly to periodontitis[162]. The mechanisms whereby genetic variants at 9p21.3 affect the risk of these various phenotypes has gradually become apparent. 9p21.3 risk variants associate with increased expression of the short isoforms of the lncRNA ANRIL[155] that contains a conserved repetitive Alu element that was shown to regulate a diverse group of genes that also contain homologous Alu elements in their primary transcripts by a mechanism of Alu-mediated silencing[154].

Here, we identified the statherin mRNA as a target of Alu-mediated silencing by the short ANRIL isoform associated with the 9p21.3 risk genotype. Statherin, a gene that is normally absent in mice, could functionally complement the absence of Mgp in smooth muscle cells, likely by binding to hydroxyapatite and inhibiting BMP signaling required for the chondrogenic/osteogenic conversion of smooth muscle cells and the progression of arterial calcification. Our studies suggest that statherin loss could account for the susceptibility of 9p213 risk allele carriers to arterial calcification. Whether this mechanism also contributes to atherosclerosis, arterial aneurysm and periodontitis remains an open question.

The 9p21.3 locus was first discovered in association with coronary atherosclerosis[244] and acute coronary syndrome and myocardial infarction[245]. Subsequent Mendelian randomization in individuals with angiographically-defined coronary atherosclerosis revealed that the 9p21.3 risk alleles associate with the severity of atherosclerosis and not with incident myocardial infarction[250]. Subsequent studies found that these variants are prevalent in asymptomatic individuals with coronary calcification[246]. A Mendelian randomization of cases of acute coronary syndrome also revealed a strong association of these variants with coronary calcification[143]. One study provided evidence that Mendelian randomization tied the 9p21.3 risk variants only with coronary atherosclerosis with calcification, but not without calcification[248]. Calcium microprecipitation occurs in the early stages of atherosclerosis and is correlated with the severity of atherosclerosis[22, 251]. We recently identified genetic variants in another gene tied to coronary atherosclerosis[192] and selective coronary artery calcification in men asymptomatic for coronary artery disease[205]. Whether the propensity to arterial calcification precedes the onset of atherosclerosis and accounts for the association of 9p21.3 risk variants to atherosclerosis and incident myocardial infarction is an intriguing possibility.

9p21.3 variants have also been tied to the risk of aortic and intracranial aneurysms[156, 159]. Aortic aneurysm calcification markedly increases mortality[157] and cerebral aneurysms are almost always calcified[158]. We found that human aortic smooth muscle cells largely express 2 hydroxyapatite-binding protein mRNAs, statherin and MGP.

Whereas mice lacking the gene *Mgp* develop severe arterial calcification and die of aortic and arterial aneurysms and rupture[32], this is generally not the case in humans, where loss of MGP leads to Keutel syndrome, characterized by cartilage and rarely arterial calcification [115]. Our study showed that forcing human statherin expression in smooth muscle cells could complement for the loss of *Mgp* in mice and prevent arterial calcification and aneurysm. Given that ~25% of individuals of Asian or European ancestry are homozygous for the 9p21.3 risk alleles, this could explain the infrequent detection of arterial calcification in humans with Keutel syndrome and inactivating mutations of MGP[115].

Our observation of statherin accumulating at calcified plaques in human coronary arteries has also been reported for MGP[222]. Like MGP, statherin binds to hydroxyapatite via a phosphorylated serine and glutamic acid-rich motif[176]. Inflammation and activation of alkaline phosphatase at atherosclerotic lesions is known to dephosphorylate and inactivate hydroxyapatite-binding proteins and could account for the accumulation of functionally inactivated MGP and STATH at calcified lesions. Consequently, the observed accumulation could represent the deposition of functionally impaired statherin and MGP at calcified sites, rather than active inhibition. This perspective necessitates exploring non-cell-autonomous mechanisms, wherein statherin's direct interaction with mineral phases, independent of VSMC differentiation, plays a significant role[231]. Specifically, further research should rigorously investigate statherin's direct interaction with mineral phases, independent of VSMC differentiation processes, to fully elucidate its role.

Previously, we reported that 9p21.3 risk variants disrupt TGFβ-dependent activation of the cyclin dependent kinase (CDK4) inhibitor p16 in primary human aortic SMCs (HAoSMCs), leading to uncontrolled cell proliferation[146], a process that would be predicted to promote atherosclerotic lesion growth. In addition, since CDK4 phosphorylates and inactivates the TGFβ transcription factors Smad2 and Smad3[252], unopposed CDK4 activity by 9p21.3 risk variants would globally suppress TGFβ signaling in a vicious cycle and account for the effect of 9p21.3 risk variants on SMC calcification. This mechanism could also explain elevated expression of BAMBI in HR HAoSMCs. It is noteworthy that TGFβ activates statherin expression in human-derived stem cells[253], so reduced expression of statherin in HR HAoSMCs is consistent not only with the Alu-mediated suppression of the statherin mRNA identified here, but also with their impaired TGFβ-dependent gene activation, as we reported[146].

Statherin has not previously been tied to the 9p21.3 risk genotype in human arterial smooth muscle cells. Proteomic studies may have missed statherin as a 10 kDa secreted protein since they used a cutoff greater than 15 kDa[220, 221]. A recent study using human inducible pluripotent stem cells (iPSC) to generate vascular smooth muscle cells according to the 9p21.3 risk and non-risk genotypes, and further using CRISPR/Cas9-mediated deletion of the 9p21.3 risk variants, did not detect statherin as a differentially expressed transcript[254]. While we cannot account for this different result, we used primary human aortic smooth muscle cells and these likely differ from iPSC-derived smooth muscle cells. Further, deletion of the 9p21.3 region might not prevent transcription of the 9p21.3-

associated ANRIL transcripts that may retain differential expression despite the deletion of the 9p21.3 risk alleles. Since these transcripts are required for Alu-mediated targeting of differentially expressed genes, including statherin, this could explain this discrepant result.

Statherin is one of the most abundant proteins in saliva, where it functions as an anti-bacterial agent and prevents plaque accumulation on teeth[176]. We have not examined the expression of statherin in saliva according to 9p21.3 risk allele, but it is tempting to suggest that statherin levels in saliva might be influenced by the 9p21.3 genotype to account for its association with periodontitis[161, 162]. Furthermore, our demonstration of an effect of statherin to limit BMP signaling could also have implications on bone remodeling observed in periodontitis.

The observed structural modifications carry substantial functional implications for statherin's biological roles. The transition from a flexible loop to a more rigid helical structure suggests potential changes in the protein's ability to interact with minerals, proteins, and other biological molecules. This conformational shift is particularly significant in understanding how minor genetic variations can dramatically alter protein behavior and interaction potential.

The rigidification and enhanced negative charge distribution create a modified interaction surface that could substantially impact protein-mineral and protein-protein interactions. Particularly in the context of ectopic calcification prevention, these structural changes

provide critical insights into the molecular mechanisms underlying protein function. The dramatic electrostatic potential redistribution around positions 21 and 22 indicates a fundamental reconfiguration of the protein's interaction capabilities.

Taken together, our studies indicate the 9p21.3 risk variants increase susceptibility to arterial calcification through lowered expression of the anti-calcification protein statherin. Since 75% of the European, East Asian and South Asian populations are carriers of these risk variants that act by an allele-additive mechanism[250], statherin delivery could be a therapeutic approach to delay or block arterial calcification (and possibly atherosclerosis progression, and aortic and arterial aneurysm) in many people.

4.3. General discussion

Our investigations into Alendronate treatment in *Mgp*KO mice and the role of statherin in arterial calcification in the context of different genotypes of the 9p21.3 risk locus provide significant insights into the mechanisms of vascular calcification and potential therapeutic approaches. These studies highlight important differences between mice and humans in terms of arterial calcification, particularly in the context of warfarin treatment and *Mgp* deficiency.

4.3.1. Addressing Warfarin-Induced Arterial Calcification in Rodents with Alendronate

In mouse models, warfarin rapidly induces significant arterial calcification within two weeks, affecting the medial layer of the aorta and the heart in a dose- and time-dependent manner[255]. This rapid onset of calcification in rodents treated with warfarin is a well-established model for studying vascular calcification[255]. Warfarin, by inhibiting the vitamin K cycle, exacerbates this condition by preventing the γ-carboxylation of MGP, rendering it inactive[102, 219, 255]. This results in unregulated calcium-phosphate deposition in vascular tissues. Alendronate, a bisphosphonate, effectively rescues this phenotype induced by warfarin in rodents by mimicking pyrophosphate (PPi), a natural inhibitor of hydroxyapatite formation, thereby reducing calcification[33].

4.3.2. Differential Effects of Alendronate in *Mgp*KO Mice

Similarly, *Mgp*KO mice exhibit severe and lethal arterial calcification, developing extensive calcification in the medial layer of arteries, particularly the aorta[32]. This

calcification is rapid and progressive, leading to death within two months of birth due to aortic rupture or heart failure, accompanied by the transdifferentiation of vascular smooth muscle cells into osteochondrogenic lineages[32]. However, unlike warfarin-induced calcification, our study shows that *Mgp*KO mice treated with Alendronate in different dosages exhibit worsened arterial calcification, whereas mice treated with the optimal dosage improve malocclusions and lose weight but never reach normal weight.

4.3.3. Challenges of Alendronate Therapy in *Mgp*-Deficient Models

Previous studies have shown that MGP inhibits BMP4 signaling and binding hydroxyapatite prevents calcification in soft tissues like arteries[29, 53]. However, inhibition of BMP4 in *Mgp*KO mice reduces calcification by only 80%[60]. These results indicate that MGP does more than bind to hydroxyapatite and inhibit BMP4 signaling to prevent calcification.

This study indicated that Alendronate therapy cannot compensate for MGP deficiency. While Alendronate improved tooth deficits, it paradoxically worsened arterial and ear calcification in *Mgp*KO mice, potentially by disrupting the endo/lysosomal-mediated hydroxyapatite handling by macrophages and accelerating the chondrogenic/osteogenic conversion of arterial smooth muscle cells. alendronate also increased calcium endo/lysosomal accumulation in cultured macrophages and reduced CD68-positive macrophages in the arterial wall of *Mgp*KO mice treated with alendronate for five weeks. A single dose of alendronate increased the aberrant expression of the osteogenic factor

Runx2 in smooth muscle cells of the aorta of *Mgp*KO mice. Thus, alendronate requires and functions with MGP to prevent soft tissue chondrogenic/osteogenic conversion and calcification.

4.3.4. Diverse Outcomes of MGP Deficiency in Human Arterial Calcification

In contrast, humans exhibit a complex relationship between MGP deficiency and arterial calcification. The effects of warfarin on arterial calcification in humans appear to be more gradual and variable[256]. Long-term warfarin treatment is associated with an increase in systemic calcification, including in the coronary and peripheral vasculature, but the process seems to occur over a longer period compared to the rapid onset observed in mice[256, 257]. There is significant variability in the extent of calcification among warfarin-treated human patients, suggesting that other factors may influence this process.

Similarly, humans with *Mgp* mutations (Keutel syndrome) show a more variable and often milder calcification phenotype[116]. While cartilaginous tissue calcification is consistent in Keutel syndrome patients[258], vascular calcification shows significant heterogeneity. Some patients exhibit calcifications in aorta,[120] coronary, pulmonary[258], and peripheral arteries[258], while others show no or only mild vascular involvement[116, 259, 260].

4.3.5. Species-Specific Differences in Arterial Calcification: Humans vs. Mice

The difference in arterial calcification between humans and rodents can be partially attributed to statherin, a salivary phosphoprotein that prevents calcification by binding to hydroxyapatite. Humans may be less susceptible to severe arterial calcification than mice

due to statherin, even in the context of *Mgp* deficiency. This difference in calcification patterns is due to the evolutionary absence of statherin in rodents[180-182]. The evolutionary paths of primates and rodents diverged significantly with respect to statherin. While primates retained and conserved the *STATH* gene, the rodent lineage became a pseudogene after the rodent-primate split[180-182, 185]. This absence in rodents likely stems from differences in dietary needs and physiological adaptations.

4.3.6. Genetic Insights from the 9p21.3 Locus

The 9p21.3 locus, identified as a genetic risk factor for coronary atherosclerosis[250], has been extensively studied for its role in various cardiovascular conditions, including coronary artery calcification[142], aortic aneurysms[157], and periodontitis[161]. The genetic variants at this locus are associated with increased expression of the short isoforms of the long non-coding RNA ANRIL, which contains a conserved repetitive Alu element[144, 249, 261]. This element regulates a diverse group of genes that also harbor homologous Alu elements in their promoters or (unspliced) transcripts through Alu-mediated silencing[261].

4.3.7. New discovery: Mechanisms by Which 9p21.3 Genetic Variants Contribute to Coronary Calcification

Whole-genome expression profiling of human aortic smooth muscle cells (HAoSMCs) were genotyped for 9p21.3 genetic variants identified statherin, a hydroxyapatite-binding protein, as the most differentially expressed gene based on the 9p21.3 risk genotype. Statherin expression was 25 times higher in HAoSMCs homozygous for the non-risk (HNR) allele compared to those homozygous for the risk (HR) allele. Notably, statherin is

the only secreted protein-coding gene linked to hydroxyapatite binding affected by the 9p21.3 genotype, with expression levels in HNR HAoSMCs comparable to MGP, another hydroxyapatite-binding protein that limits arterial calcification.

We identified statherin mRNA as a target of Alu-mediated silencing by the short ANRIL isoform associated with the 9p21.3 risk genotype. Statherin, absent in mice, could functionally complement the absence of MGP in smooth muscle cells by binding to hydroxyapatite and inhibiting BMP signaling, which is necessary for the chondrogenic/osteogenic conversion of smooth muscle cells and the progression of arterial calcification. Our studies suggest that statherin loss may contribute to the susceptibility of 9p21.3 risk allele carriers to arterial calcification.

The rescue of *Mgp*KO mice expressing human statherin genes in arterial smooth muscle cells, and the inhibition of calcification in primary *Mgp*KO smooth muscle cells isolated from these mice by lentiviral particles expressing human statherin, support our hypothesis that statherin in human smooth muscle cells prevents calcification and that its expression is influenced by 9p21.3 risk alleles. This discovery elucidates the varied effects of warfarin on calcification and explains the significant heterogeneity of vascular calcification in Keutel syndrome, where some patients exhibit calcifications in coronary, pulmonary, and peripheral arteries, while others show no or only mild vascular involvement.

4.3.8. DA-Statherin

However, the *Mgp*KO/*Mgp*KO -DA-Statherin-Cre mice, despite successful generation, exhibited complete mortality within the first month, highlighting the complexity of calcium homeostasis regulation in vivo. The observed structural modifications carry substantial functional implications for statherin biological roles. The transition from a flexible loop to a more rigid helical structure suggests potential changes in the protein's ability to interact with minerals, proteins, and other biological molecules. This conformational shift is particularly significant in understanding how minor genetic variations can dramatically alter protein behavior and interaction potential.

The rigidification and enhanced negative charge distribution create a modified interaction surface that could substantially impact protein-mineral and protein-protein interactions. Particularly in the context of ectopic calcification prevention, these structural changes provide critical insights into the molecular mechanisms underlying protein function. The dramatic electrostatic potential redistribution around positions 21 and 22 indicates a fundamental reconfiguration of the protein's interaction capabilities.

4.3.8. Statherin expression in Homozygous

The study on statherin expression in mutant mice reveals significant impacts on their lifespan, in heterozygote and particularly in homozygous mutants where both alleles carry the mutation. These mice exhibit even shorter lifespans compared to wild-type and *Mgp*KO mice, emphasizing the essential role of functional statherin. The lack of statherin

expression in heterozygote is linked to a 5' upstream in-frame stop codon creating an upstream open reading frame (uORF), which inhibits the translation of the main open reading frame. Complete in vivo recombination at the Rosa26 locus ensures proper transgene regulation, confirmed by sequencing results. The study aligns with Voet et al.'s findings on the human STATH gene, highlighting regulatory complexities in transgene expression. Future research should explore uORFs' roles in gene regulation and their impact on mRNA stability and localization, providing deeper insights into genetic context and transgene functionality.

4.3.10. Limitations of the study

4.3.10.1: Limited number of human aortic smooth muscle cells for 9p21.3 genotypes

The gene expression profiling and genotyping analysis of the 9p21.3 locus conducted in Dr. Stewart's Laboratory had notable limitations. The study included only four subjects per group (homozygous risk, homozygous non-risk, and heterozygous) for smooth muscle cell (SMC) analysis. While our investigation aimed to elucidate the mechanistic relationship between 9p21.3 risk alleles and coronary artery calcification (CAC), the small sample size (n=4 per group) raised significant concerns among manuscript reviewers. This limited sample size potentially affects the statistical power and generalizability of our findings regarding the 9p21.3 locus's role in CAC development.

4.3.10.1: Lack of Statherin expression in heterozygous mice

The expression of statherin in mutant mice significantly impacts their lifespan compared to wild-type mice. In our study, we found that the expression of a statherin mutant (dominated activated) was undetectable in heterozygous mice, leading to a notably short lifespan. This contrasts with wild type statherin, which supports normal physiological functions. One significant limitation of our study is the discrepancy in statherin expression between heterozygous and homozygous mice. Despite successful recombination to remove the stop cassette and induce statherin expression in smooth muscle cells, statherin was not detected in over 50 heterozygous mice. In contrast, statherin was expressed in homozygous mice. Additionally, obtaining homozygous genotypes is challenging and time-consuming due to their low probability, further complicating the study.

The absence of statherin expression in heterozygotes may be due to a 5' upstream in-frame stop codon that creates an upstream open reading frame (uORF), inhibiting the translation of the main open reading frame. In homozygous mutant mice, where both alleles carry the mutation, the lifespan is even shorter, underscoring the critical role of functional statherin in sustaining life.

While some studies suggest that Cre recombinase in Rosa26 locus can lead to incomplete stop flox recombination *in vitro*[262], our results demonstrate that *in vivo* recombination at the Rosa26 locus occurs completely. This finding is important for ensuring proper regulation and functionality of transgene expression. Our sequencing results confirm that

the intended genetic modifications were successfully executed without residual unmodified alleles, allowing for accurate assessment of gene function and expression levels. These findings highlight the importance of statherin in mouse survival and suggest that minor alterations in gene expression can have profound effects on phenotype and longevity. This study also underscores the reliability of using Rosa26 as a locus for transgene insertion due to its complete recombination efficiency, essential for studying gene function in genetically modified organisms. Future studies should explore how statherin influences lifespan and health and investigate potential therapeutic applications for conditions associated with statherin deficiency or dysfunction.

The presence of an uORF created by a 5' upstream in-frame stop codon could significantly reduce the translation efficiency of the main open reading frame, explaining reduced expression in heterozygotes. However, the complete absence of detectable expression in heterozygotes while homozygotes show expression is surprising given Rosa26's reputation for robust and ubiquitous expression. Our findings align with those of Voet *et al.,* who demonstrated that expression of the human tissue factor (F3) gene on their chromosomal vector was directly proportional to vector copy number in mice[263]. This supports the idea that transgene expression can be controlled by manipulating copy number through breeding.

Voet *et al*. also reported no detectable expression of the human STATH gene in their transchromosomal mice despite its presence on the inserted PAC[263], which aligns with our

findings of low or undetectable STATH expression in heterozygotes. The lack of STATH expression could stem from several factors, including missing regulatory elements within the PAC insert or position effects from the chromosomal vector[263]. The proposed mechanism involving a 5' upstream stop codon creating an uORF is plausible since uORFs are known to modulate translation efficiency.

Several factors may contribute to observed expression patterns across both studies: (1) A threshold effect where heterozygotes' expression falls just below detection limits; (2) epigenetic factors influencing transgene expression based on copy number; (3) potential interactions between transgenes and surrounding genomic elements; and (4) specific design elements of transgene constructs affecting expression patterns.

These findings highlight the complexity of transgene expression and emphasize the importance of thorough characterization when developing genetically modified mouse models. Future investigations could include using more sensitive detection methods to check for low-level expression in heterozygotes, analyzing mRNA levels to determine if effects are transcriptional or translational, modifying transgenes to remove potential regulatory obstacles, and examining chromatin state and epigenetic marks at transgene loci.

In Voet *et al*.'s study, they used a PAC containing 62.5 kb of human genomic DNA with both CSN2 (β-casein) and STATH genes inserted into their chromosomal vector (CV), allowing controlled copy numbers ranging from 1 to 4 per cell[263]. Despite this capacity for multiple copies, Voet *et al.* reported no detectable statherin expression, indicating that even

with multiple copies present[263], regulatory mechanisms may prevent gene expression. In particular, the paper by Ji. emphasizes that uORFs may contain novel human exons and play a significant role in regulating gene expression through mechanisms that affect translation efficiency and mRNA stability[264]. This perspective enhances our understanding of how uORFs could contribute to the observed phenotypic effects associated with statherin expression and highlight the need for more efficient methods to achieve and verify statherin expression in genetically modified mice.

4.3.10.2: Computational modeling limitation

The research acknowledged significant limitations, most notably the reliance on computational modeling due to the absence of relevant crystal conformations in protein databases. The transgenic mouse model (*Mgp*KO/*Mgp*KO -DA-Statherin-Cre) further complicated the findings, with complete mortality observed within the first month, underscoring the complex nature of calcium homeostasis regulation.

Despite these limitations, the study provides valuable molecular insights into protein structural dynamics. By demonstrating how subtle sequence variations can induce substantial structural and functional changes, the research contributes significantly to our understanding of protein biology. The findings emphasize the intricate relationship between genetic sequence, protein structure, and biological function, opening new avenues for research in molecular biology and potential therapeutic interventions.

The computational approach, while not definitive, offers a preliminary understanding of protein behavior. It highlights the importance of combining computational modeling with experimental validation to fully comprehend the complex molecular mechanisms underlying protein function and genetic variation

5. Future Directions and Therapeutic Strategies

5.1. Disrupting the Alu Sequence

The Alu motif in ANRIL is crucial for its trans-regulatory functions, including promoting cell proliferation and adhesion, which contribute to arterial calcification. Targeting the Alu sequence of the ANRIL EU741058 variant, which interacts with the Alu sequence in statherin, could benefit individuals homozygous for the 9p21.3 risk alleles. This strategy may prevent or inhibit the suppression of statherin expression by the homozygous risk allele ANRIL.

Another approach could involve targeting the Alu sequence in the first intron of statherin. ANRIL regulates genes involved in atherogenesis, and its expression is associated with atherosclerosis severity. Disrupting the Alu sequence may reverse some of ANRIL's pro-atherogenic effects and restore normal statherin expression. These strategies aim to counteract the calcification-promoting effects of the 9p21.3 risk alleles by interfering with ANRIL-mediated suppression of statherin. By preserving statherin expression, these approaches could potentially reduce the risk of arterial calcification and atherosclerosis in genetically susceptible individuals.

5. 2. Expressing Statherin in the Liver

Expressing statherin in the liver, like fetuin-A, could help mitigate the arterial calcification phenotype in individuals homozygous for the 9p21.3 risk locus. This approach leverages the liver's protein production capabilities to increase circulating statherin levels. However, several considerations must be addressed:

Physiological Differences: Statherin is normally expressed in smooth muscle cells, not the liver. Expressing it in the liver may alter its post-translational modifications, potentially affecting its function or stability.

Tissue Distribution: The effectiveness of this approach depends on whether liver-expressed statherin can reach the arterial walls in sufficient quantities to exert its protective effects against calcification.

Regulatory Mechanisms: Hepatic expression may not replicate the natural regulatory mechanisms controlling statherin production in smooth muscle cells, potentially leading to suboptimal or excessive levels.

Functional Equivalence: Given potential differences in protein processing and the local microenvironment, it remains uncertain whether liver-produced statherin would function identically to that naturally expressed in smooth muscle cells. While this strategy presents an intriguing possibility for addressing arterial calcification in 9p21.3 risk allele carriers, careful evaluation through preclinical studies is necessary to assess its feasibility and

efficacy.

5. 3. Restoring Statherin Expression in Smooth Muscle Cells (SMCs):

To restore statherin expression in SMCs using gene therapy, a strategy could involve designing a statherin cDNA expression construct. This would entail cloning the full-length human statherin cDNA sequence, excluding any Alu elements present in introns or untranslated regions, and placing it under the control of a strong, SMC-specific promoter such as SM22α or smooth muscle myosin heavy chain promoter. Appropriate regulatory elements like polyadenylation signals and transcription terminators would be included.

The construct would then be packaged into a suitable viral vector, such as an adeno-associated virus (AAV) or lentiviral vector, which have shown efficacy in transducing vascular cells and can accommodate the relatively small size of the statherin cDNA. Delivery of the vector to arterial SMCs would be performed through local delivery to the arterial wall using catheter-based approaches or perivascular application during surgery, with systemic delivery as a less targeted alternative.

Expression and function would be monitored by assessing statherin mRNA and protein levels in transduced SMCs and evaluating the impact on SMC calcification and overall arterial health. The exclusion of Alu sequences in the cDNA construct is significant as it simplifies the expression cassette, potentially improving vector packaging and transgene expression efficiency, reducing the risk of unintended effects mediated by Alu elements, and enhancing mRNA stability and translation efficiency in the target cells. This approach

aims to restore statherin expression in arterial SMCs, potentially mitigating the increased calcification risk associated with statherin deficiency in individuals with certain genetic variants.

By linking these strategies, we can develop a comprehensive approach to counteract the calcification-promoting effects of the 9p21.3 risk alleles. Whether through disrupting the Alu sequence, expressing statherin in the liver, or restoring its expression in smooth muscle cells, these methods aim to preserve statherin expression and reduce the risk of arterial calcification and atherosclerosis in genetically susceptible individuals.

6. References

1. Detrano R, Guerci AD, Carr JJ, et al. Coronary calcium as a predictor of coronary events in four racial or ethnic groups. *N Engl J Med.* 2008;358:1336-1345.

2. Budoff MJ, Achenbach S, Blumenthal RS, et al. Assessment of coronary artery disease by cardiac computed tomography: a scientific statement from the American Heart Association Committee on Cardiovascular Imaging and Intervention, Council on Cardiovascular Radiology and Intervention, and Committee on Cardiac Imaging, Council on Clinical Cardiology. *Circulation.* 2006;114:1761-1791.

3. Peyser PA, Bielak LF, Chu JS, et al. Heritability of coronary artery calcium quantity measured by electron beam computed tomography in asymptomatic adults. *Circulation.* 2002;106:304-308.

4. Nurmohamed NS, Cole JH, Budoff MJ, et al. Impact of atherosclerosis imaging-quantitative computed tomography on diagnostic certainty, downstream testing, coronary revascularization, and medical therapy: the CERTAIN study. *Eur Heart J Cardiovasc Imaging.* 2024;25:857-866.

5. Shanahan CM, Crouthamel MH, Kapustin A, Giachelli CM. Arterial calcification in chronic kidney disease: key roles for calcium and phosphate. *Circ Res.* 2011;109:697-711.

6. Demer LL, Tintut Y. Mechanisms linking osteoporosis with cardiovascular calcification. *Curr Osteoporos Rep.* 2009;7:42-46.

7. Lehmann N, Mohlenkamp S, Mahabadi AA, et al. Effect of smoking and other traditional risk factors on the onset of coronary artery calcification: results of the Heinz Nixdorf recall study. *Atherosclerosis.* 2014;232:339-345.

8. Erbel R, Lehmann N, Churzidse S, et al. Progression of coronary artery calcification seems to be inevitable, but predictable - results of the Heinz Nixdorf Recall (HNR) study. *Eur Heart J.* 2014;35:2960-2971.

9. Nissen SE, Tuzcu EM, Schoenhagen P, et al. Effect of intensive compared with moderate lipid-lowering therapy on progression of coronary atherosclerosis: a randomized controlled trial. *JAMA.* 2004;291:1071-1080.

10. Schmermund A, Achenbach S, Budde T, et al. Effect of intensive versus standard lipid-lowering treatment with atorvastatin on the progression of calcified coronary atherosclerosis over 12 months: a multicenter, randomized, double-blind trial. *Circulation.* 2006;113:427-437.

11. Xian JZ, Lu M, Fong F, et al. Statin Effects on Vascular Calcification: Microarchitectural Changes in Aortic Calcium Deposits in Aged Hyperlipidemic Mice. *Arterioscler Thromb Vasc Biol.* 2021;41:e185-e192.

12. Bonetti PO, Lerman LO, Napoli C, Lerman A. Statin effects beyond lipid lowering--are they clinically relevant? *Eur Heart J.* 2003;24:225-248.

13. Ngamdu KS, Ghosalkar DS, Chung HE, et al. Long-term statin therapy is associated with severe coronary artery calcification. *PloS one.* 2023;18:e0289111.

14. Price PA, Faus SA, Williamson MK. Warfarin causes rapid calcification of the elastic lamellae in rat arteries and heart valves. *Arterioscler Thromb Vasc Biol.* 1998;18:1400-1407.

15. Okuyama H, Langsjoen PH, Hamazaki T, et al. Statins stimulate atherosclerosis and heart failure: pharmacological mechanisms. *Expert Rev Clin Pharmacol.* 2015;8:189-199.

16. Healy A, Berus JM, Christensen JL, et al. Statins Disrupt Macrophage Rac1 Regulation Leading to Increased Atherosclerotic Plaque Calcification. *Arterioscler Thromb Vasc Biol.* 2020;40:714-732.

17. O'donnell CJ, Kavousi M, Smith AV, et al. Genome-wide association study for coronary artery calcification with follow-up in myocardial infarction. *Circulation.* 2011;124:2855-2864.

18. Neven E, D'Haese PC. Vascular calcification in chronic renal failure: what have we learned from animal studies? *Circ Res.* 2011;108:249-264.

19. Durham AL, Speer MY, Scatena M, Giachelli CM, Shanahan CM. Role of smooth muscle cells in vascular calcification: implications in atherosclerosis and arterial stiffness. *Cardiovasc Res.* 2018;114:590-600.

20. Schurgers LJ, Spronk HM, Soute BA, Schiffers PM, DeMey JG, Vermeer C. Regression of warfarin-induced medial elastocalcinosis by high intake of vitamin K in rats. *Blood.* 2007;109:2823-2831.

21. Sheen CR, Kuss P, Narisawa S, et al. Pathophysiological role of vascular smooth muscle alkaline phosphatase in medial artery calcification. *J Bone Miner Res.* 2015;30:824-836.

22. Roijers RB, Debernardi N, Cleutjens JP, Schurgers LJ, Mutsaers PH, van der Vusse GJ. Microcalcifications in early intimal lesions of atherosclerotic human coronary arteries. *Am J Pathol.* 2011;178:2879-2887.

23. Amann K. Media calcification and intima calcification are distinct entities in chronic kidney disease. *Clinical Journal of the American Society of Nephrology.* 2008;3:1599-1605.

24. Virmani R, Burke A, Farb A, Kolodgie FD, Finn AV, Gold HK. Pathology of the vulnerable plaque. *Handbook of the Vulnerable Plaque*: CRC Press; 2007:35-50.

25. Khavandgar Z, Roman H, Li J, et al. Elastin haploinsufficiency impedes the progression of arterial calcification in MGP-deficient mice. *J Bone Miner Res.* 2014;29:327-337.

26. Otsuka F, Sakakura K, Yahagi K, Joner M, Virmani R. Has our understanding of calcification in human coronary atherosclerosis progressed? *Arteriosclerosis, thrombosis, and vascular biology.* 2014:ATVBAHA. 113.302642.

27. Aikawa E, Nahrendorf M, Figueiredo J-L, et al. CLINICAL PERSPECTIVE. *Circulation.* 2007;116:2841-2850.

28. Zhang SH, Reddick RL, Piedrahita JA, Maeda N. Spontaneous hypercholesterolemia and arterial lesions in mice lacking apolipoprotein E. *Science.* 1992;258:468-471.

29. Derwall M, Malhotra R, Lai CS, et al. Inhibition of bone morphogenetic protein signaling reduces vascular calcification and atherosclerosis. *Arteriosclerosis, thrombosis, and vascular biology.* 2012;32:613-622.

30. Ishibashi S, Brown MS, Goldstein JL, Gerard RD, Hammer RE, Herz J. Hypercholesterolemia in low density lipoprotein receptor knockout mice and its reversal by adenovirus-mediated gene delivery. *J Clin Invest.* 1993;92:883-893.

31. Veniant MM, Withycombe S, Young SG. Lipoprotein size and atherosclerosis susceptibility in Apoe(-/-) and Ldlr(-/-) mice. *Arterioscler Thromb Vasc Biol.* 2001;21:1567-1570.

32. Luo G, Ducy P, McKee MD, et al. Spontaneous calcification of arteries and cartilage in mice lacking matrix GLA protein. *Nature.* 1997;386:78-81.

33. Price PA, Faus SA, Williamson MK. Bisphosphonates alendronate and ibandronate inhibit artery calcification at doses comparable to those that inhibit bone resorption. *Arterioscler Thromb Vasc Biol.* 2001;21:817-824.

34. Yao Y, Shahbazian A, Bostrom KI. Proline and gamma-carboxylated glutamate residues in matrix Gla protein are critical for binding of bone morphogenetic protein-4. *Circ Res.* 2008;102:1065-1074.

35. Gravesen E, Lerche Mace M, Nordholm A, et al. Exogenous BMP7 in aortae of rats with chronic uremia ameliorates expression of profibrotic genes, but does not reverse established vascular calcification. *PloS one.* 2018;13:e0190820.

36. Li Q, Guo H, Chou DW, Berndt A, Sundberg JP, Uitto J. Mutant Enpp1asj mouse as a model for generalized arterial calcification of infancy. *Disease models & mechanisms.* 2013:dmm. 012765.

37. Nitschke Y, Baujat G, Botschen U, et al. Generalized arterial calcification of infancy and pseudoxanthoma elasticum can be caused by mutations in either ENPP1 or ABCC6. *The American Journal of Human Genetics.* 2012;90:25-39.

38. Berridge MJ. Smooth muscle cell calcium activation mechanisms. *The Journal of physiology.* 2008;586:5047-5061.

39. Kapustin AN, Shanahan CM. Calcium regulation of vascular smooth muscle cell–derived matrix vesicles. *Trends in cardiovascular medicine.* 2012;22:133-137.

40. Speer MY, Yang HY, Brabb T, et al. Smooth muscle cells give rise to osteochondrogenic precursors and chondrocytes in calcifying arteries. *Circ Res.* 2009;104:733-741.

41. Azpiazu D, Gonzalo S, Villa-Bellosta R. Tissue Non-Specific Alkaline Phosphatase and Vascular Calcification: A Potential Therapeutic Target. *Curr Cardiol Rev.* 2019;15:91-95.

42. Lee H-L, Woo KM, Ryoo H-M, Baek J-H. Tumor necrosis factor-α increases alkaline phosphatase expression in vascular smooth muscle cells via MSX2 induction. *Biochemical and biophysical research communications.* 2010;391:1087-1092.

43. Khavandgar Z, Roman H, Li J, et al. Elastin haploinsufficiency impedes the progression of arterial calcification in MGP-deficient mice. *Journal of Bone and Mineral Research.* 2014;29:327-337.

44. Liu Y, Puthia M, Sheehy EJ, et al. Sustained delivery of a heterodimer bone morphogenetic protein-2/7 via a collagen hydroxyapatite scaffold accelerates and improves critical femoral defect healing. *Acta Biomater.* 2023;162:164-181.

45. Rohanizadeh R, Chung K. Hydroxyapatite as a carrier for bone morphogenetic protein. *J Oral Implantol.* 2011;37:659-672.

46. Hernandez GE, Ma F, Martinez G, et al. Aortic intimal resident macrophages are essential for maintenance of the non-thrombogenic intravascular state. *Nat Cardiovasc Res.* 2022;1:67-84.

47. Lin ME, Chen T, Leaf EM, Speer MY, Giachelli CM. Runx2 Expression in Smooth Muscle Cells Is Required for Arterial Medial Calcification in Mice. *Am J Pathol.* 2015;185:1958-1969.

48. Wang SS, Martin LJ, Schadt EE, et al. Disruption of the aortic elastic lamina and medial calcification share genetic determinants in mice. *Circulation: Genomic and Precision Medicine.* 2009:CIRCGENETICS. 109.860270.

49. Li Y, Sun Z, Zhang L, et al. Role of Macrophages in the Progression and Regression of Vascular Calcification. *Front Pharmacol.* 2020;11:661.

50. Chinetti-Gbaguidi G, Daoudi M, Rosa M, et al. Human Alternative Macrophages Populate Calcified Areas of Atherosclerotic Lesions and Display Impaired RANKL-Induced Osteoclastic Bone Resorption Activity. *Circ Res.* 2017;121:19-30.

51. New SE, Goettsch C, Aikawa M, et al. Macrophage-derived matrix vesicles: an alternative novel mechanism for microcalcification in atherosclerotic plaques. *Circ Res.* 2013;113:72-77.

52. Miyazono K, Kamiya Y, Morikawa M. Bone morphogenetic protein receptors and signal transduction. *J Biochem.* 2010;147:35-51.

53. Kuronuma K, Yokoi A, Fukuoka T, et al. Matrix Gla protein maintains normal and malignant hematopoietic progenitor cells by interacting with bone morphogenetic protein-4. *Heliyon.* 2020;6:e03743.

54. Miyazono K. Signal transduction by bone morphogenetic protein receptors: functional roles of Smad proteins. *Bone.* 1999;25:91-93.

55. Bordukalo-Niksic T, Kufner V, Vukicevic S. The Role Of BMPs in the Regulation of Osteoclasts Resorption and Bone Remodeling: From Experimental Models to Clinical Applications. *Front Immunol.* 2022;13:869422.

56. Wang RN, Green J, Wang Z, et al. Bone Morphogenetic Protein (BMP) signaling in development and human diseases. *Genes Dis.* 2014;1:87-105.

57. Malhotra R, Burke MF, Martyn T, et al. Inhibition of bone morphogenetic protein signal transduction prevents the medial vascular calcification associated with matrix Gla protein deficiency. *PLoS One.* 2015;10.

58. Sudhakar S, Li Y, Katz MS, Elango N. Translational regulation is a control point in RUNX2/Cbfa1 gene expression. *Biochemical and biophysical research communications.* 2001;289:616-622.

59. Drissi H, Luc Q, Shakoori R, et al. Transcriptional autoregulation of the bone related CBFA1/RUNX2 gene. *Journal of cellular physiology.* 2000;184:341-350.

60. Malhotra R, Burke MF, Martyn T, et al. Inhibition of bone morphogenetic protein signal transduction prevents the medial vascular calcification associated with matrix Gla protein deficiency. *PloS one.* 2015;10:e0117098.

61. Zhang Y, Tang N, Zhou J. Intermedin1-47 inhibits high phosphate-induced vascular smooth muscle cell calcification by regulating Wnt/beta-catenin signaling. *Mol Med Rep.* 2021;24.

62. Byon CH, Javed A, Dai Q, et al. Oxidative stress induces vascular calcification through modulation of the osteogenic transcription factor Runx2 by AKT signaling. *J Biol Chem.* 2008;283:15319-15327.

63. Boström KI, Rajamannan NM, Towler DA. The regulation of valvular and vascular sclerosis by osteogenic morphogens. *Circulation research.* 2011;109:564-577.

64. Leopold JA. Vascular calcification: mechanisms of vascular smooth muscle cell calcification. *Trends in cardiovascular medicine.* 2015;25:267-274.

65. Foster BL, Nagatomo KJ, Nociti FH, Jr., et al. Central role of pyrophosphate in acellular cementum formation. *PloS one.* 2012;7:e38393.

66. Dsouza C, Moussa MS, Mikolajewicz N, Komarova SV. Extracellular ATP and its derivatives provide spatiotemporal guidance for bone adaptation to wide spectrum of physical forces. *Bone Rep.* 2022;17:101608.

67. Tan JJ, Boudreault F, Adam D, Brochiero E, Grygorczyk R. Type 2 secretory cells are primary source of ATP release in mechanically stretched lung alveolar cells. *Am J Physiol Lung Cell Mol Physiol.* 2020;318:L49-L58.

68. Dou L, Chen YF, Cowan PJ, Chen XP. Extracellular ATP signaling and clinical relevance. *Clin Immunol.* 2018;188:67-73.

69. Chivasa S, Ndimba BK, Simon WJ, Lindsey K, Slabas AR. Extracellular ATP functions as an endogenous external metabolite regulating plant cell viability. *Plant Cell.* 2005;17:3019-3034.

70. Halling Linder C, Ek-Rylander B, Krumpel M, et al. Bone Alkaline Phosphatase and Tartrate-Resistant Acid Phosphatase: Potential Co-regulators of Bone Mineralization. *Calcif Tissue Int.* 2017;101:92-101.

71. Jansen RS, Duijst S, Mahakena S, et al. ABCC6-mediated ATP secretion by the liver is the main source of the mineralization inhibitor inorganic pyrophosphate in the systemic circulation-brief report. *Arterioscler Thromb Vasc Biol.* 2014;34:1985-1989.

72. Rutsch F, Ruf N, Vaingankar S, et al. Mutations in ENPP1 are associated with'idiopathic'infantile arterial calcification. *Nature genetics.* 2003;34:379.

73. Wu T, Yin F, Guang S, He F, Yang L, Peng J. The Glycosylphosphatidylinositol biosynthesis pathway in human diseases. *Orphanet J Rare Dis.* 2020;15:129.

74. Li Q, Guo H, Chou DW, Berndt A, Sundberg JP, Uitto J. Mutant Enpp1asj mice as a model for generalized arterial calcification of infancy. *Dis Model Mech.* 2013;6:1227-1235.

75. Rutsch F, Ruf N, Vaingankar S, et al. Mutations in ENPP1 are associated with 'idiopathic' infantile arterial calcification. *Nature genetics.* 2003;34:379-381.

76. Ziegler SG, Gahl WA, Ferreira CR. Generalized Arterial Calcification of Infancy. In: Adam MP, Feldman J, Mirzaa GM, Pagon RA, Wallace SE, Amemiya A, eds. *GeneReviews((R))*. Seattle (WA)1993.

77. Aherrahrou Z, Doehring LC, Ehlers E-M, et al. An alternative splice variant in Abcc6, the gene causing dystrophic calcification, leads to protein deficiency in C3H/He mice. *Journal of Biological Chemistry.* 2008;283:7608-7615.

78. Jansen RS, Duijst S, Mahakena S, et al. ABCC6–mediated ATP secretion by the liver is the main source of the mineralization inhibitor inorganic pyrophosphate in the systemic circulation—Brief report. *Arteriosclerosis, thrombosis, and vascular biology.* 2014;34:1985-1989.

79. Rücker B, Almeida ME, Libermann TA, Zerbini LF, Wink MR, Sarkis JJ. E-NTPDases and ecto-5′-nucleotidase expression profile in rat heart left ventricle and the extracellular nucleotide hydrolysis by their nerve terminal endings. *Life sciences.* 2008;82:477-486.

80. Yeung G, Mulero JJ, McGowan DW, Bajwa SS, Ford JE. CD39L2, a gene encoding a human nucleoside diphosphatase, predominantly expressed in the heart. *Biochemistry.* 2000;39:12916-12923.

81. Rutsch F, Nitschke Y, Terkeltaub R. Genetics in arterial calcification: pieces of a puzzle and cogs in a wheel. *Circulation research.* 2011;109:578-592.

82. Szeri F, Niaziorimi F, Donnelly S, et al. The Mineralization Regulator ANKH Mediates Cellular Efflux of ATP, Not Pyrophosphate. *J Bone Miner Res.* 2022;37:1024-1031.

83. Addison WN, Masica DL, Gray JJ, McKee MD. Phosphorylation-dependent inhibition of mineralization by osteopontin ASARM peptides is regulated by PHEX cleavage. *Journal of Bone and Mineral Research.* 2010;25:695-705.

84. Szeri F, Lundkvist S, Donnelly S, et al. The membrane protein ANKH is crucial for bone mechanical performance by mediating cellular export of citrate and ATP. *PLoS Genet.* 2020;16:e1008884.

85. Seifert W, Posor Y, Schu P, et al. The progressive ankylosis protein ANK facilitates clathrin- and adaptor-mediated membrane traffic at the trans-Golgi network-to-endosome interface. *Hum Mol Genet.* 2016;25:3836-3848.

86. Liu Q, Luo Y, Zhao Y, et al. Nano-hydroxyapatite accelerates vascular calcification via lysosome impairment and autophagy dysfunction in smooth muscle cells. *Bioact Mater.* 2022;8:478-493.

87. Lee JS, Morrisett JD, Tung CH. Detection of hydroxyapatite in calcified cardiovascular tissues. *Atherosclerosis.* 2012;224:340-347.

88. Yuan Q, Jiang Y, Zhao X, et al. Increased osteopontin contributes to inhibition of bone mineralization in FGF23-deficient mice. *J Bone Miner Res.* 2014;29:693-704.

89. Ge Q, Ruan CC, Ma Y, et al. Osteopontin regulates macrophage activation and osteoclast formation in hypertensive patients with vascular calcification. *Sci Rep.* 2017;7:40253.

90. Jono S, Peinado C, Giachelli CM. Phosphorylation of osteopontin is required for inhibition of vascular smooth muscle cell calcification. *Journal of Biological Chemistry.* 2000.

91. Zhu YS, Mo TT, Jiang C, Zhang JN. Osteonectin bidirectionally regulates osteoblast mineralization. *J Orthop Surg Res.* 2023;18:761.

92. Vincent K, Durrant MC. A structural and functional model for human bone sialoprotein. *J Mol Graph Model.* 2013;39:108-117.

93. Ciceri P, Elli F, Cappelletti L, et al. Osteonectin (SPARC) Expression in Vascular Calcification: In Vitro and Ex Vivo Studies. *Calcif Tissue Int.* 2016;99:472-480.

94. Gadeau AP, Chaulet H, Daret D, Kockx M, Daniel-Lamaziere JM, Desgranges C. Time course of osteopontin, osteocalcin, and osteonectin accumulation and calcification after acute vessel wall injury. *J Histochem Cytochem.* 2001;49:79-86.

95. Hunter GK, Hauschka PV, Poole AR, Rosenberg LC, Goldberg HA. Nucleation and inhibition of hydroxyapatite formation by mineralized tissue proteins. *Biochem J.* 1996;317 (Pt 1):59-64.

96. Termine JD, Kleinman HK, Whitson SW, Conn KM, McGarvey ML, Martin GR. Osteonectin, a bone-specific protein linking mineral to collagen. *Cell.* 1981;26:99-105.

97. Price PA, Urist MR, Otawara Y. Matrix Gla protein, a new γ-carboxyglutamic acid-containing protein which is associated with the organic matrix of bone. *Biochemical and biophysical research communications.* 1983;117:765-771.

98. Price PA, Williamson MK. Primary structure of bovine matrix Gla protein, a new vitamin K-dependent bone protein. *Journal of Biological Chemistry.* 1985;260:14971-14975.

99. Hackeng TM, Rosing J, Spronk HM, Vermeer C. Total chemical synthesis of human matrix Gla protein. *Protein Sci.* 2001;10:864-870.

100. Murshed M, Schinke T, McKee MD, Karsenty G. Extracellular matrix mineralization is regulated locally; different roles of two gla-containing proteins. *The Journal of cell biology.* 2004;165:625-630.

101. Poterucha TJ, Goldhaber SZ. Warfarin and vascular calcification. *The American journal of medicine.* 2016;129:635. e631-635. e634.

102. Nigwekar SU, Bloch DB, Nazarian RM, et al. Vitamin K–dependent carboxylation of matrix Gla protein influences the risk of calciphylaxis. *Journal of the American Society of Nephrology.* 2017;28:1717-1722.

103. Schurgers LJ, Uitto J, Reutelingsperger CP. Vitamin K-dependent carboxylation of matrix Gla-protein: a crucial switch to control ectopic mineralization. *Trends Mol Med.* 2013;19:217-226.

104. Turner ME, Holden RM. Risks of Vitamin K Antagonism: Mammograms as a Powerful Tool to Assess Calcification Progression. Vol 40: Am Heart Assoc; 2020:1022-1024.

105. Weijs B, Blaauw Y, Rennenberg RJ, et al. Patients using vitamin K antagonists show increased levels of coronary calcification: an observational study in low-risk atrial fibrillation patients. *European heart journal.* 2011;32:2555-2562.

106. Price PA, Rice JS, Williamson MK. Conserved phosphorylation of serines in the Ser-X-Glu/Ser(P) sequences of the vitamin K-dependent matrix Gla protein from shark, lamb, rat, cow, and human. *Protein Sci.* 1994;3:822-830.

107. Bjorklund G, Svanberg E, Dadar M, et al. The Role of Matrix Gla Protein (MGP) in Vascular Calcification. *Curr Med Chem.* 2020;27:1647-1660.

108. Bjørklund G, Svanberg E, Dadar M, et al. The role of matrix Gla protein (MGP) in vascular calcification. *Current medicinal chemistry.* 2019.

109. Guerrero F, Herencia C, Almadén Y, et al. TGF-β prevents phosphate-induced osteogenesis through inhibition of BMP and Wnt/β-catenin pathways. *PloS one.* 2014;9:e89179.

110. Helbing T, Wiltgen G, Hornstein A, et al. Bone morphogenetic protein-modulator BMPER regulates endothelial barrier function. *Inflammation.* 2017;40:442-453.

111. Huntley R, Jensen E, Gopalakrishnan R, Mansky KC. Bone morphogenetic proteins: Their role in regulating osteoclast differentiation. *Bone Rep.* 2019;10:100207.

112. Kamiya N, Ye L, Kobayashi T, et al. BMP signaling negatively regulates bone mass through sclerostin by inhibiting the canonical Wnt pathway. *Development.* 2008;135:3801-3811.

113. Kaartinen MT, Murshed M, Karsenty G, McKee MD. Osteopontin upregulation and polymerization by transglutaminase 2 in calcified arteries of Matrix Gla protein-deficient mice. *J Histochem Cytochem.* 2007;55:375-386.

114. Keutel J, Jorgensen G, Gabriel P. [A new autosomal-recessive hereditary syndrome. Multiple peripheral pulmonary stenosis, brachytelephalangia, inner-ear deafness, ossification or calcification of cartilages]. *Dtsch Med Wochenschr.* 1971;96:1676-1681 passim.

115. Munroe PB, Olgunturk RO, Fryns JP, et al. Mutations in the gene encoding the human matrix Gla protein cause Keutel syndrome. *Nature genetics.* 1999;21:142-144.

116. Cancela ML, Laize V, Conceicao N, Kempf H, Murshed M. Keutel Syndrome, a Review of 50 Years of Literature. *Front Cell Dev Biol.* 2021;9:642136.

117. Meier M, Weng L, Alexandrakis E, Rüschoff J, Goeckenjan G. Tracheobronchial stenosis in Keutel syndrome. *European Respiratory Journal.* 2001;17:566-569.

118. Munroe PB, Olgunturk RO, Fryns J-P, et al. Mutations in the gene encoding the human matrix Gla protein cause Keutel syndrome. *Nature genetics.* 1999;21:142.

119. Parmar H, Blaser S, Unger S, Yoo SJ, Papsin B. Petrified ears in a patient with Keutel syndrome: temporal bone CT findings. *Pediatr Radiol.* 2006;36:241-243.

120. Ayyıldız P, Bilgici MNC, Ozyilmaz B, Sungur M, Baysal K, Oğur G. Keutel Syndrome: A Case Report With Aortic Calcification2012.

121. Wilkins Parker LR, Preuss CV. Alendronate. *StatPearls*. Treasure Island (FL)2024.

122. Geers J, Bing R, Pawade TA, et al. Effect of Denosumab or Alendronate on Vascular Calcification: Secondary Analysis of SALTIRE2 Randomized Controlled Trial. *Journal of the American Heart Association.* 2024;13:e032571.

123. Kavanagh KL, Guo K, Dunford JE, et al. The molecular mechanism of nitrogen-containing bisphosphonates as antiosteoporosis drugs. *Proc Natl Acad Sci U S A.* 2006;103:7829-7834.

124. Ali N, Jurczyluk J, Shay G, et al. A highly sensitive prenylation assay reveals in vivo effects of bisphosphonate drug on the Rab prenylome of macrophages outside the skeleton. *Small GTPases.* 2015;6:202-211.

125. Farnsworth CC, Seabra MC, Ericsson LH, Gelb MH, Glomset JA. Rab geranylgeranyl transferase catalyzes the geranylgeranylation of adjacent cysteines in the small GTPases Rab1A, Rab3A, and Rab5A. *Proc Natl Acad Sci U S A.* 1994;91:11963-11967.

126. Black DM, Delmas PD, Eastell R, et al. Once-yearly zoledronic acid for treatment of postmenopausal osteoporosis. *N Engl J Med.* 2007;356:1809-1822.

127. Ramirez-Suarez KI, Cohen SA, Barrera CA, Levine MA, Goldberg DJ, Otero HJ. Longitudinal assessment of vascular calcification in generalized arterial calcification of infancy. *Pediatr Radiol.* 2022;52:2329-2341.

128. Scatena M, Liaw L, Giachelli CM. Osteopontin: a multifunctional molecule regulating chronic inflammation and vascular disease. *Arterioscler Thromb Vasc Biol.* 2007;27:2302-2309.

129. de Bruyn JR, Goiko M, Mozaffari M, et al. Dynamic light scattering study of inhibition of nucleation and growth of hydroxyapatite crystals by osteopontin. *PloS one.* 2013;8:e56764.

130. El-Abbadi M, Giachelli CM. Arteriosclerosis, calcium phosphate deposition and cardiovascular disease in uremia: current concepts at the bench. *Curr Opin Nephrol Hypertens.* 2005;14:519-524.

131. Cairns JR, Price PA. Direct demonstration that the vitamin K-dependent bone Gla protein is incompletely gamma-carboxylated in humans. *J Bone Miner Res.* 1994;9:1989-1997.

132. Neve A, Corrado A, Cantatore FP. Osteoblast physiology in normal and pathological conditions. *Cell Tissue Res.* 2011;343:289-302.

133. Plantalech L, Guillaumont M, Vergnaud P, Leclercq M, Delmas PD. Impairment of gamma carboxylation of circulating osteocalcin (bone gla protein) in elderly women. *J Bone Miner Res.* 1991;6:1211-1216.

134. Millar SA, Patel H, Anderson SI, England TJ, O'Sullivan SE. Osteocalcin, vascular calcification, and atherosclerosis: a systematic review and meta-analysis. *Frontiers in Endocrinology.* 2017;8:183.

135. Brylka L, Jahnen-Dechent W. The role of fetuin-A in physiological and pathological mineralization. *Calcif Tissue Int.* 2013;93:355-364.

136. Schafer C, Heiss A, Schwarz A, et al. The serum protein alpha 2-Heremans-Schmid glycoprotein/fetuin-A is a systemically acting inhibitor of ectopic calcification. *J Clin Invest.* 2003;112:357-366.

137. Heiss A, DuChesne A, Denecke B, et al. Structural basis of calcification inhibition by alpha 2-HS glycoprotein/fetuin-A. Formation of colloidal calciprotein particles. *J Biol Chem.* 2003;278:13333-13341.

138. Holt SG, Smith ER. Fetuin-A-containing calciprotein particles in mineral trafficking and vascular disease. *Nephrol Dial Transplant.* 2016;31:1583-1587.

139. Schinke T, Amendt C, Trindl A, Poschke O, Muller-Esterl W, Jahnen-Dechent W. The serum protein alpha2-HS glycoprotein/fetuin inhibits apatite formation in vitro and in mineralizing calvaria cells. A possible role in mineralization and calcium homeostasis. *J Biol Chem.* 1996;271:20789-20796.

140. Ketteler M, Bongartz P, Westenfeld R, et al. Association of low fetuin-A (AHSG) concentrations in serum with cardiovascular mortality in patients on dialysis: a cross-sectional study. *Lancet.* 2003;361:827-833.

141. Schunkert H, Konig IR, Kathiresan S, et al. Large-scale association analysis identifies 13 new susceptibility loci for coronary artery disease. *Nature genetics.* 2011;43:333-338.

142. de Vries PS, Conomos MP, Singh K, et al. Whole-genome sequencing uncovers two loci for coronary artery calcification and identifies ARSE as a regulator of vascular calcification. *Nat Cardiovasc Res.* 2023;2:1159-1172.

143. O'Donnell CJ, Kavousi M, Smith AV, et al. Genome-wide association study for coronary artery calcification with follow-up in myocardial infarction. *Circulation.* 2011;124:2855-2864.

144. Jarinova O, Stewart AF, Roberts R, et al. Functional analysis of the chromosome 9p21. 3 coronary artery disease risk locus. *Arteriosclerosis, thrombosis, and vascular biology.* 2009;29:1671-1677.

145. Almontashiri NA, Antoine D, Zhou X, et al. 9p21.3 Coronary Artery Disease Risk Variants Disrupt TEAD Transcription Factor-Dependent Transforming Growth Factor beta Regulation of p16 Expression in Human Aortic Smooth Muscle Cells. *Circulation.* 2015;132:1969-1978.

146. Almontashiri NAM, Antoine D, Zhou X, et al. 9p21.3 coronary artery disease risk variants disrupt TEAD transcription factor-dependent TGFβ regulation of p16 expression in human aortic smooth muscle cells. *Circulation.* 2015;132:1969-1978.

147. Musunuru K. Enduring mystery of the chromosome 9p21.3 locus. *Circ Cardiovasc Genet.* 2013;6:224-225.

148. Cunnington MS, Santibanez Koref M, Mayosi BM, Burn J, Keavney B. Chromosome 9p21 SNPs Associated with Multiple Disease Phenotypes Correlate with ANRIL Expression. *PLoS Genet.* 2010;6:e1000899.

149. Rivera NV, Carreras-Torres R, Roncarati R, et al. Assessment of the 9p21.3 locus in severity of coronary artery disease in the presence and absence of type 2 diabetes. *BMC Med Genet.* 2013;14:11.

150. Cheng X, Shi L, Nie S, et al. The same chromosome 9p21.3 locus is associated with type 2 diabetes and coronary artery disease in a Chinese Han population. *Diabetes.* 2011;60:680-684.

151. Zhu Y. *Elucidating the Enhancer Code in 9p21 Locus Underlying Age-Related Disease Risks*: ProQuest Dissertations & Theses Global; 2018.

152. Zhu Y, Tazearslan C, Rosenfeld MG, Fiser A, Suh Y. Identification and functional validation of an enhancer variant in the 9p21. 3 locus associated with glaucoma risk and elevated expression of p16INK4a. *Aging cell.* 2023;22:e13908.

153. Pilbrow AP, Folkersen L, Pearson JF, et al. The chromosome 9p21.3 coronary heart disease risk allele is associated with altered gene expression in normal heart and vascular tissues. *PloS one.* 2012;7:e39574.

154. Holdt LM, Hoffmann S, Sass K, et al. Alu elements in ANRIL non-coding RNA at chromosome 9p21 modulate atherogenic cell functions through trans-regulation of gene networks. *PLoS Genet.* 2013;9:e1003588.

155. Jarinova O, Stewart AF, Roberts R, et al. Functional analysis of the chromosome 9p21.3 coronary artery disease risk locus. *Arterioscler Thromb Vasc Biol.* 2009;29:1671-1677.

156. Bown MJ, Braund PS, Thompson J, London NJ, Samani NJ, Sayers RD. Association between the coronary artery disease risk locus on chromosome 9p21.3 and abdominal aortic aneurysm. *Circ Cardiovasc Genet.* 2008;1:39-42.

157. Chowdhury MM, Zielinski LP, Sun JJ, et al. Editor's Choice - Calcification of Thoracic and Abdominal Aneurysms is Associated with Mortality and Morbidity. *Eur J Vasc Endovasc Surg.* 2018;55:101-108.

158. Gade PS, Tulamo R, Lee KW, et al. Calcification in Human Intracranial Aneurysms Is Highly Prevalent and Displays Both Atherosclerotic and Nonatherosclerotic Types. *Arterioscler Thromb Vasc Biol.* 2019;39:2157-2167.

159. Helgadottir A, Thorleifsson G, Magnusson KP, et al. The same sequence variant on 9p21 associates with myocardial infarction, abdominal aortic aneurysm and intracranial aneurysm. *Nature genetics.* 2008;40:217-224.

160. Ernst FD, Uhr K, Teumer A, et al. Replication of the association of chromosomal region 9p21. 3 with generalized aggressive periodontitis (gAgP) using an independent case-control cohort. *BMC medical genetics.* 2010;11:119.

161. Ernst FD, Uhr K, Teumer A, et al. Replication of the association of chromosomal region 9p21.3 with generalized aggressive periodontitis (gAgP) using an independent case-control cohort. *BMC Med Genet.* 2010;11:119.

162. Schaefer AS, Richter GM, Groessner-Schreiber B, et al. Identification of a shared genetic susceptibility locus for coronary heart disease and periodontitis. *PLoS Genet.* 2009;5:e1000378.

163. Zayani Z, Hooshmandi E, Borhani-Haghighi A, et al. Diagnostic potential of LncRNAs-ANRIL and MIAT in the blood of patients with cerebral venous thrombosis. 2023.

164. Park E, Maquat LE. Staufen-mediated mRNA decay. *Wiley Interdisciplinary Reviews: RNA.* 2013;4:423-435.

165. Gong C, Maquat LE. lncRNAs transactivate STAU1-mediated mRNA decay by duplexing with 3′ UTRs via Alu elements. *Nature.* 2011;470:284.

166. Heraud-Farlow JE, Kiebler MA. The multifunctional Staufen proteins: conserved roles from neurogenesis to synaptic plasticity. *Trends in neurosciences.* 2014;37:470-479.

167. Kavousi M, Bos MM, Barnes HJ, et al. Multi-ancestry genome-wide study identifies effector genes and druggable pathways for coronary artery calcification. *Nature genetics.* 2023;55:1651-1664.

168. Sabatini LM, Carlock LR, Johnson GW, Azen EA. cDNA cloning and chromosomal localization (4q11-13) of a gene for statherin, a regulator of calcium in saliva. *Am J Hum Genet.* 1987;41:1048-1060.

169. Amano A, Kataoka K, Raj PA, Genco RJ, Shizukuishi S. Binding sites of salivary statherin for Porphyromonas gingivalis recombinant fimbrillin. *Infect Immun.* 1996;64:4249-4254.

170. Manconi B, Cabras T, Vitali A, et al. Expression, purification, phosphorylation and characterization of recombinant human statherin. *Protein Expr Purif.* 2010;69:219-225.

171. Schlesinger DH, Hay DI, Levine MJ. Complete primary structure of statherin, a potent inhibitor of calcium phosphate precipitation, from the saliva of the monkey, Macaca arctoides. *Int J Pept Protein Res.* 1989;34:374-380.

172. Castagnola M, Congiu D, Denotti G, et al. Determination of the human salivary peptides histatins 1, 3, 5 and statherin by high-performance liquid chromatography and by diode-array detection. *J Chromatogr B Biomed Sci Appl.* 2001;751:153-160.

173. Cowman R, Schaefer S, Oppenheim F, Hay D. Statherin and the proline-rich parotid proteins PRP II and PRP IV as amino nitrogen sources for plaque-forming oral streptococci. *Journal of dental research.* 1979;58:2008-2009.

174. Gilbert M, Stayton PS. Expression and characterization of human salivary statherin from Escherichia coli using two different fusion constructs. *Protein Expr Purif.* 1999;16:243-250.

175. Gururaja TL, Levine MJ. Solid-phase synthesis and characterization of human salivary statherin: a tyrosine-rich phosphoprotein inhibitor of calcium phosphate precipitation. *Pept Res.* 1996;9:283-289.

176. Raj PA, Johnsson M, Levine MJ, Nancollas GH. Salivary statherin. Dependence on sequence, charge, hydrogen bonding potency, and helical conformation for adsorption to hydroxyapatite and inhibition of mineralization. *J Biol Chem.* 1992;267:5968-5976.

177. Cabras T, Inzitari R, Fanali C, et al. HPLC-MS characterization of cyclo-statherin Q-37, a specific cyclization product of human salivary statherin generated by transglutaminase 2. *J Sep Sci.* 2006;29:2600-2608.

178. Boroumand M, Olianas A, Manconi B, et al. Mapping of Transglutaminase-2 Sites of Human Salivary Small Basic Proline-Rich Proteins by HPLC-High-Resolution ESI-MS/MS. *J Proteome Res.* 2020;19:300-313.

179. Deng S, Marmorstein R. Protein N-Terminal Acetylation: Structural Basis, Mechanism, Versatility, and Regulation. *Trends Biochem Sci.* 2021;46:15-27.

180. Kawasaki K, Buchanan AV, Weiss KM. Gene duplication and the evolution of vertebrate skeletal mineralization. *Cells Tissues Organs.* 2007;186:7-24.

181. Kawasaki K, Weiss KM. Mineralized tissue and vertebrate evolution: the secretory calcium-binding phosphoprotein gene cluster. *Proc Natl Acad Sci U S A.* 2003;100:4060-4065.

182. Kawasaki K, Weiss KM. Evolutionary genetics of vertebrate tissue mineralization: the origin and evolution of the secretory calcium-binding phosphoprotein family. *J Exp Zool B Mol Dev Evol.* 2006;306:295-316.

183. Pajic P, Landau L, Gokcumen O, Ruhl S. Emergence of saliva protein genes in the secretory calcium-binding phosphoprotein (SCPP) locus and accelerated evolution in primates. *bioRxiv.* 2024.

184. Romero A, Leurs N, Munoz D, Debiais-Thibaud M, Marcellini S. Divergent Expression of SPARC, SPARC-L, and SCPP Genes During Jawed Vertebrate Cartilage Mineralization. *Front Genet.* 2021;12:788346.

185. de Sousa-Pereira P, Amado F, Abrantes J, Ferreira R, Esteves PJ, Vitorino R. An evolutionary perspective of mammal salivary peptide families: cystatins, histatins, statherin and PRPs. *Archives of oral biology.* 2013;58:451-458.

186. Kawasaki K, Weiss KM. Mineralized tissue and vertebrate evolution: the secretory calcium-binding phosphoprotein gene cluster. *Proceedings of the National Academy of Sciences.* 2003;100:4060-4065.

187. Skorey K, Ly HD, Kelly J, et al. How does alendronate inhibit protein-tyrosine phosphatases? *J Biol Chem.* 1997;272:22472-22480.

188. Patntirapong S, Chanruangvanit C, Lavanrattanakul K, Satravaha Y. Assessment of bisphosphonate treated-osteoblast behaviors by conventional assays and a simple digital image analysis. *Acta Histochem.* 2021;123:151659.

189. Evans KD, Lau ST, Oberbauer AM, Martin RB. Alendronate affects long bone length and growth plate morphology in the oim mouse model for Osteogenesis Imperfecta. *Bone.* 2003;32:268-274.

190. Pols HA, Felsenberg D, Hanley DA, et al. Multinational, placebo-controlled, randomized trial of the effects of alendronate on bone density and fracture risk in postmenopausal women with low bone mass: results of the FOSIT study. Fosamax International Trial Study Group. *Osteoporos Int.* 1999;9:461-468.

191. Weischenfeldt J, Porse B. Bone Marrow-Derived Macrophages (BMM): Isolation and Applications. *CSH Protoc.* 2008;2008:pdb prot5080.

192. Chen HH, Keyhanian K, Zhou X, et al. IRF2BP2 Reduces Macrophage Inflammation and Susceptibility to Atherosclerosis. *Circ Res.* 2015;117:671-683.

193. Carpenter AE, Jones TR, Lamprecht MR, et al. CellProfiler: image analysis software for identifying and quantifying cell phenotypes. *Genome Biol.* 2006;7:R100.

194. O'Rourke C, Shelton G, Hutcheson JD, et al. Calcification of Vascular Smooth Muscle Cells and Imaging of Aortic Calcification and Inflammation. *J Vis Exp.* 2016.

195. Giachelli CM. The emerging role of phosphate in vascular calcification. *Kidney Int.* 2009;75:890-897.

196. Holtwick R, Gotthardt M, Skryabin B, et al. Smooth muscle-selective deletion of guanylyl cyclase-A prevents the acute but not chronic effects of ANP on blood pressure. *Proc Natl Acad Sci U S A.* 2002;99:7142-7147.

197. Madisen L, Zwingman TA, Sunkin SM, et al. A robust and high-throughput Cre reporting and characterization system for the whole mouse brain. *Nat Neurosci.* 2010;13:133-140.

198. Schneider CA, Rasband WS, Eliceiri KW. NIH Image to ImageJ: 25 years of image analysis. *Nat Methods.* 2012;9:671-675.

199. Buchman AR, Berg P. Comparison of intron-dependent and intron-independent gene expression. *Mol Cell Biol.* 1988;8:4395-4405.

200. Xiao JH, Davidson I, Matthes H, Garnier JM, Chambon P. Cloning, expression, and transcriptional properties of the human enhancer factor TEF-1. *Cell.* 1991;65:551-568.

201. Gregory CA, Gunn WG, Peister A, Prockop DJ. An Alizarin red-based assay of mineralization by adherent cells in culture: comparison with cetylpyridinium chloride extraction. *Anal Biochem.* 2004;329:77-84.

202. Vilmundarson RO, Heydarikhormeh N, Duong A, et al. Savior siblings might rescue fetal lethality but not adult lymphoma in Irf2bp2-null mice. *Front Immunol.* 2022;13:868053.

203. Korchynskyi O, ten Dijke P. Identification and functional characterization of distinct critically important bone morphogenetic protein-specific response elements in the Id1 promoter. *J Biol Chem.* 2002;277:4883-4891.

204. Aihara S, Fujimoto S, Sakaguchi R, Imai T. BMPR-2 gates activity-dependent stabilization of primary dendrites during mitral cell remodeling. *Cell Rep.* 2021;35:109276.

205. Vilmundarson RO, Duong A, Soheili F, Chen HH, Stewart AFR. IRF2BP2 3'UTR polymorphism increases coronary artery calcification in men *Frontiers in Cardiovascular Medicine.* 2021;8:687645.

206. Marulanda J, Eimar H, McKee MD, et al. Matrix Gla protein deficiency impairs nasal septum growth, causing midface hypoplasia. *J Biol Chem.* 2017;292:11400-11412.

207. Drissi H, Luc Q, Shakoori R, et al. Transcriptional autoregulation of the bone related CBFA1/RUNX2 gene. *J Cell Physiol.* 2000;184:341-350.

208. Banerjee C, McCabe LR, Choi JY, et al. Runt homology domain proteins in osteoblast differentiation: AML3/CBFA1 is a major component of a bone-specific complex. *J Cell Biochem.* 1997;66:1-8.

209. Ducy P, Zhang R, Geoffroy V, Ridall AL, Karsenty G. Osf2/Cbfa1: a transcriptional activator of osteoblast differentiation. *Cell.* 1997;89:747-754.

210. Bloebaum RD, Lundeen GA, Bachus KN, Ison I, Hofmann AA. Dissolution of particulate hydroxyapatite in a macrophage organelle model. *J Biomed Mater Res.* 1998;40:104-114.

211. Pazar B, Ea HK, Narayan S, et al. Basic calcium phosphate crystals induce monocyte/macrophage IL-1beta secretion through the NLRP3 inflammasome in vitro. *J Immunol.* 2011;186:2495-2502.

212. Laquerriere P, Grandjean-Laquerriere A, Jallot E, Balossier G, Frayssinet P, Guenounou M. Importance of hydroxyapatite particles characteristics on cytokines production by human monocytes in vitro. *Biomaterials.* 2003;24:2739-2747.

213. Nadra I, Mason JC, Philippidis P, et al. Proinflammatory activation of macrophages by basic calcium phosphate crystals via protein kinase C and MAP kinase pathways: a vicious cycle of inflammation and arterial calcification? *Circ Res.* 2005;96:1248-1256.

214. Shanley LC, Mahon OR, O'Rourke SA, et al. Macrophage metabolic profile is altered by hydroxyapatite particle size. *Acta Biomater.* 2023;160:311-321.

215. Wang M, Chen F, Tang Y, et al. Regulation of macrophage polarization and functional status by modulating hydroxyapatite ceramic micro/nano-topography. *Materials & Design.* 2022;213:110302.

216. Martini C, Sosa FN, Malvicini R, Pacienza N, Yannarelli G, Del CVM. Alendronate inhibits triglyceride accumulation and oxidative stress in adipocytes and the inflammatory response of macrophages which are associated with adipose tissue dysfunction. *J Physiol Biochem.* 2021;77:601-611.

217. Rogers MJ, Chilton KM, Coxon FP, et al. Bisphosphonates induce apoptosis in mouse macrophage-like cells in vitro by a nitric oxide-independent mechanism. *J Bone Miner Res.* 1996;11:1482-1491.

218. Dalmeijer GW, van der Schouw YT, Magdeleyns EJ, et al. Matrix Gla protein species and risk of cardiovascular events in type 2 diabetic patients. *Diabetes Care.* 2013;36:3766-3771.

219. Schurgers LJ, Spronk HM, Skepper JN, et al. Post-translational modifications regulate matrix Gla protein function: importance for inhibition of vascular smooth muscle cell calcification. *J Thromb Haemost.* 2007;5:2503-2511.

220. Dupont A, Corseaux D, Dekeyzer O, et al. The proteome and secretome of human arterial smooth muscle cells. *Proteomics.* 2005;5:585-596.

221. Gao BB, Stuart L, Feener EP. Label-free quantitative analysis of one-dimensional PAGE LC/MS/MS proteome: application on angiotensin II-stimulated smooth muscle cells secretome. *Mol Cell Proteomics.* 2008;7:2399-2409.

222. Shanahan CM, Cary NR, Metcalfe JC, Weissberg PL. High expression of genes for calcification-regulating proteins in human atherosclerotic plaques. *J Clin Invest.* 1994;93:2393-2402.

223. de Sousa-Pereira P, Amado F, Abrantes J, Ferreira R, Esteves PJ, Vitorino R. An evolutionary perspective of mammal salivary peptide families: cystatins, histatins, statherin and PRPs. *Arch Oral Biol.* 2013;58:451-458.

224. Bostrom K, Tsao D, Shen S, Wang Y, Demer LL. Matrix GLA protein modulates differentiation induced by bone morphogenetic protein-2 in C3H10T1/2 cells. *J Biol Chem.* 2001;276:14044-14052.

225. Yao Y, Bennett BJ, Wang X, et al. Inhibition of bone morphogenetic proteins protects against atherosclerosis and vascular calcification. *Circ Res.* 2010;107:485-494.

226. Shimokado A, Sun Y, Nakanishi M, et al. Smad3 plays an inhibitory role in phosphate-induced vascular smooth muscle cell calcification. *Experimental and molecular pathology.* 2014;97:458-464.

227. Gonzales CB, Simmons D, MacDougall M. Competing roles of TGFbeta and Nma/BAMBI in odontoblasts. *J Dent Res.* 2010;89:597-602.

228. Baek M, DiMaio F, Anishchenko I, et al. Accurate prediction of protein structures and interactions using a three-track neural network. *Science.* 2021;373:871-876.

229. Bertoni M, Kiefer F, Biasini M, Bordoli L, Schwede T. Modeling protein quaternary structure of homo- and hetero-oligomers beyond binary interactions by homology. *Sci Rep.* 2017;7:10480.

230. Parashar A, Bak K, Murshed M. Prevention of Arterial Elastocalcinosis: Differential Roles of the Conserved Glutamic Acid and Serine Residues of Matrix Gla Protein. *Arterioscler Thromb Vasc Biol.* 2022;42:e155-e167.

231. Bak K, Parashar A, Allgayer R, et al. An inducible model for medial calcification based on matrix Gla protein deficiency. *J Struct Biol.* 2024;216:108144.

232. Fisher JE, Rogers MJ, Halasy JM, et al. Alendronate mechanism of action: geranylgeraniol, an intermediate in the mevalonate pathway, prevents inhibition of osteoclast formation, bone resorption, and kinase activation in vitro. *Proc Natl Acad Sci U S A.* 1999;96:133-138.

233. Li Q, Pratt CH, Dionne LA, et al. Spontaneous asj-2J mutant mouse as a model for generalized arterial calcification of infancy: a large deletion/insertion mutation in the Enpp1 gene. *PloS one.* 2014;9:e113542.

234. Colboc H, Moguelet P, Bazin D, et al. Elastic fiber alterations and calcifications in calcific uremic arteriolopathy. *Sci Rep.* 2023;13:15519.

235. Wilson LM, Rebholz CM, Jirru E, et al. Benefits and Harms of Osteoporosis Medications in Patients With Chronic Kidney Disease: A Systematic Review and Meta-analysis. *Ann Intern Med.* 2017;166:649-658.

236. Marulanda J, Gao C, Roman H, Henderson JE, Murshed M. Prevention of arterial calcification corrects the low bone mass phenotype in MGP-deficient mice. *Bone.* 2013;57:499-508.

237. Chistiakov DA, Killingsworth MC, Myasoedova VA, Orekhov AN, Bobryshev YV. CD68/macrosialin: not just a histochemical marker. *Lab Invest.* 2017;97:4-13.

238. Ashley JW, Shi Z, Zhao H, Li X, Kesterson RA, Feng X. Genetic ablation of CD68 results in mice with increased bone and dysfunctional osteoclasts. *PloS one.* 2011;6:e25838.

239. Ueno M, Maeno T, Nishimura S, et al. Alendronate inhalation ameliorates elastase-induced pulmonary emphysema in mice by induction of apoptosis of alveolar macrophages. *Nat Commun.* 2015;6:6332.

240. Thompson K, Rogers MJ, Coxon FP, Crockett JC. Cytosolic entry of bisphosphonate drugs requires acidification of vesicles after fluid-phase endocytosis. *Mol Pharmacol.* 2006;69:1624-1632.

241. Bernini F, Scurati N, Bonfadini G, Fumagalli R. HMG-CoA reductase inhibitors reduce acetyl LDL endocytosis in mouse peritoneal macrophages. *Arterioscler Thromb Vasc Biol.* 1995;15:1352-1358.

242. Lorza-Gil E, Salerno AG, Wanschel AC, et al. Chronic use of pravastatin reduces insulin exocytosis and increases beta-cell death in hypercholesterolemic mice. *Toxicology.* 2016;344-346:42-52.

243. Behzadi P, Cuevas RA, Crane A, et al. Rapamycin increases murine lifespan but does not reduce mineral volume in the Matrix GLA Protein (MGP) knockout mouse model of medial arterial calcification. *bioRxiv.* 2024.

244. McPherson R, Pertsemlidis A, Kavaslar N, et al. A common allele on chromosome 9 associated with coronary heart disease. *Science.* 2007;316:1488-1491.

245. Helgadottir A, Thorleifsson G, Manolescu A, et al. A common variant on chromosome 9p21 affects the risk of myocardial infarction. *Science.* 2007;316:1491-1493.

246. Assimes TL, Knowles JW, Basu A, et al. Susceptibility locus for clinical and subclinical coronary artery disease at chromosome 9p21 in the multi-ethnic ADVANCE study. *Hum Mol Genet.* 2008;17:2320-2328.

247. Choi SY, Shin E, Choe EK, et al. Genome-wide association study of coronary artery calcification in asymptomatic Korean populations. *PloS one.* 2019;14:e0214370.

248. Gong L, Chen J, Lu J, et al. The 9p21 locus is associated with coronary artery disease and cardiovascular events in the presence (but not in the absence) of coronary calcification. *PloS one.* 2014;9:e94823.

249. van Setten J, Isgum I, Smolonska J, et al. Genome-wide association study of coronary and aortic calcification implicates risk loci for coronary artery disease and myocardial infarction. *Atherosclerosis.* 2013;228:400-405.

250. Dandona S, Stewart AF, Chen L, et al. Gene dosage of the common variant 9p21 predicts severity of coronary artery disease. *J Am Coll Cardiol.* 2010;56:479-486.

251. Kataoka Y, Wolski K, Uno K, et al. Spotty calcification as a marker of accelerated progression of coronary atherosclerosis: insights from serial intravascular ultrasound. *J Am Coll Cardiol.* 2012;59:1592-1597.

252. Matsuura I, Denissova NG, Wang G, He D, Long J, Liu F. Cyclin-dependent kinases regulate the antiproliferative function of Smads. *Nature.* 2004;430:226-231.

253. Herzog DP, Dohle E, Bischoff I, Kirkpatrick CJ. Cell communication in a coculture system consisting of outgrowth endothelial cells and primary osteoblasts. *Biomed Res Int.* 2014;2014:320123.

254. Lo Sardo V, Chubukov P, Ferguson W, et al. Unveiling the Role of the Most Impactful Cardiovascular Risk Locus through Haplotype Editing. *Cell.* 2018;175:1796-1810 e1720.

255. Howe AM, Webster WS. Warfarin exposure and calcification of the arterial system in the rat. *Int J Exp Pathol.* 2000;81:51-56.

256. Alappan HR, Kaur G, Manzoor S, Navarrete J, O'Neill WC. Warfarin Accelerates Medial Arterial Calcification in Humans. *Arteriosclerosis, thrombosis, and vascular biology.* 2020;40:1413-1419.

257. Nuotio K, Koskinen SM, Mäkitie L, et al. Warfarin treatment is associated to increased internal carotid artery calcification. *Frontiers in neurology.* 2021;12:696244.

258. Fryns JP, van Fleteren A, Mattelaer P, van den Berghe H. Calcification of cartilages, brachytelephalangy and peripheral pulmonary stenosis. Confirmation of the Keutel syndrome. *Eur J Pediatr.* 1984;142:201-203.

259. Cranenburg EC, KY VANS-Z, Bonafe L, et al. Circulating matrix gamma-carboxyglutamate protein (MGP) species are refractory to vitamin K treatment in a new case of Keutel syndrome. *J Thromb Haemost.* 2011;9:1225-1235.

260. Weaver KN, El Hallek M, Hopkin RJ, et al. Keutel syndrome: report of two novel MGP mutations and discussion of clinical overlap with arylsulfatase E deficiency and relapsing polychondritis. *Am J Med Genet A.* 2014;164A:1062-1068.

261. Holdt LM, Hoffmann S, Sass K, et al. Alu elements in ANRIL non-coding RNA at chromosome 9p21 modulate atherogenic cell functions through trans-regulation of gene networks. *PLoS genetics.* 2013;9:e1003588.

262. Bapst AM, Dahl SL, Knopfel T, Wenger RH. Cre-mediated, loxP independent sequential recombination of a tripartite transcriptional stop cassette allows for partial read-through transcription. *Biochim Biophys Acta Gene Regul Mech.* 2020;1863:194568.

263. Voet T, Schoenmakers E, Carpentier S, Labaere C, Marynen P. Controlled transgene dosage and PAC-mediated transgenesis in mice using a chromosomal vector. *Genomics.* 2003;82:596-605.

264. Ji HJ, Salzberg SL. Upstream open reading frames may contain hundreds of novel human exons. *PLoS Comput Biol.* 2024;20:e1012543.

7. Appendix 1: List of all primer sequences and templates used in the study

Name	Oligos sequence	length	Functions
oIMR 1084	GCGGTC TGG CAGTAA AAACTATC	23	Genotyping Tagln-Cre mice
oIMR 1085	GTG AAACAG CAT TGC TGTCACTT	23	
oIMR 7338	CTAGGCCACAGA ATTGAA AGATCT	24	
oIMR 7339	GTAGGTGGA AAT TCTAGCATCATC C	25	
STATH-F	GTTTCCATGATTGGAGCTGATTCATC	26	Genotyping STATH transgenic mice
STATH-R	GCGTATCCACATAGCGTAAAAGGAGC	26	
R26-TDR	GCTTGTGATCCGCCTCGGAG	20	Distinguishing homo from heterozygous STATH mice
R26-TDF	CTCTGCTGCCTCCTGGCT TCTGAG	24	
CAG3F	GGGTTCGGCTTCTGGCGTGTG	21	Confirming excision of stop cassettes by Cre
rLxFse	GCTTGGGCTGCAGGTCGAGG	20	
WT- F	GAG AGG CCT GCG ATG ACT AC	20	Genotyping *Mgp*KO mice
Common-R	CGA AAC TCC ACA ACC AAA TGACTG	20	
Mutant-F	CCT TCT ATC GCC TTC TTG ACG	21	
vSTATH-F	GAATTCGCCGCCATGAAGTTC	21	Amplify the cDNA of STATH from plasmid
vSTATH-R	GGATCCTTAAAAGGTATATTGTTGGTATTG	30	
SF-Alu	TTAGAGAACAATTGGTAGAGACG	23	Screen pXJ-40-STATH clones for the statherin Alu
SR-Alu	GTAACCATAAAGAGAAAGGCAG	22	
DF-Alu	CGTTAAACTTTAGCTTGC	18	Determine Alu orientation by sequencing
SR-Alu	GTAACCATAAAGAGAAAGGCAG	22	

8. Appendix 2: Genetic Engineering and Maps of Vectors

Map 1. pcDNATM 3.1 Backbone

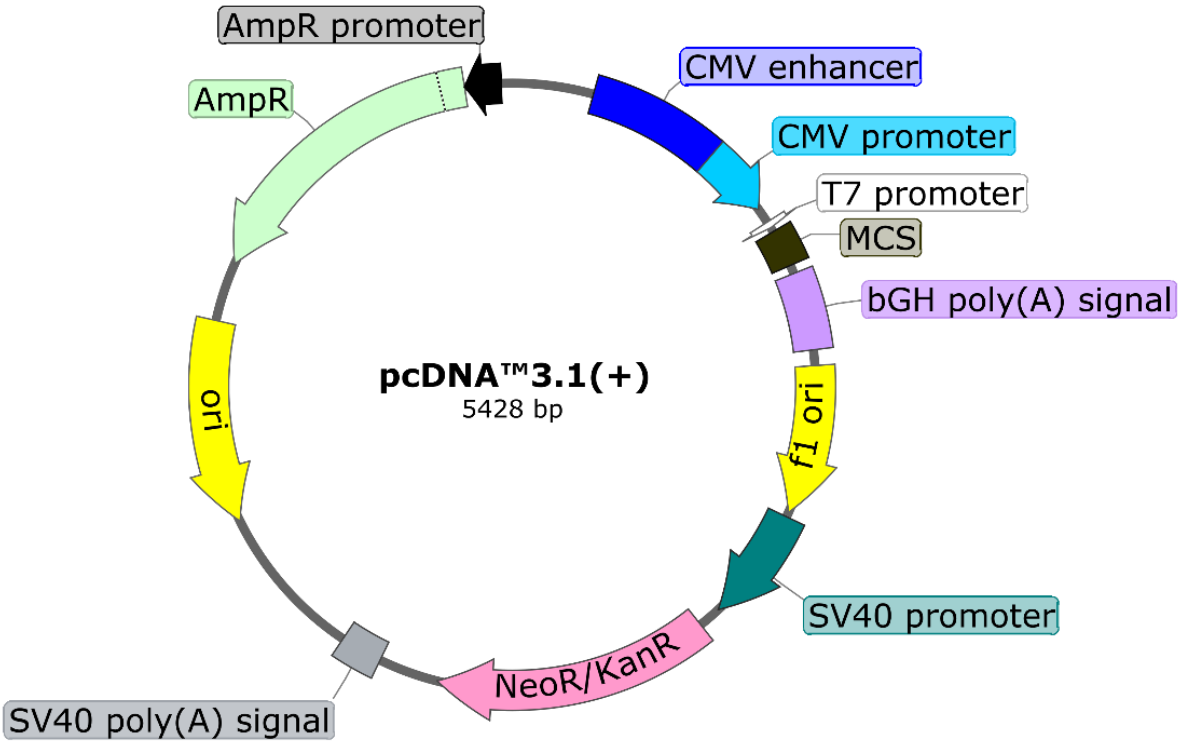

Map 2. pcDNA™ STATH Plasmid

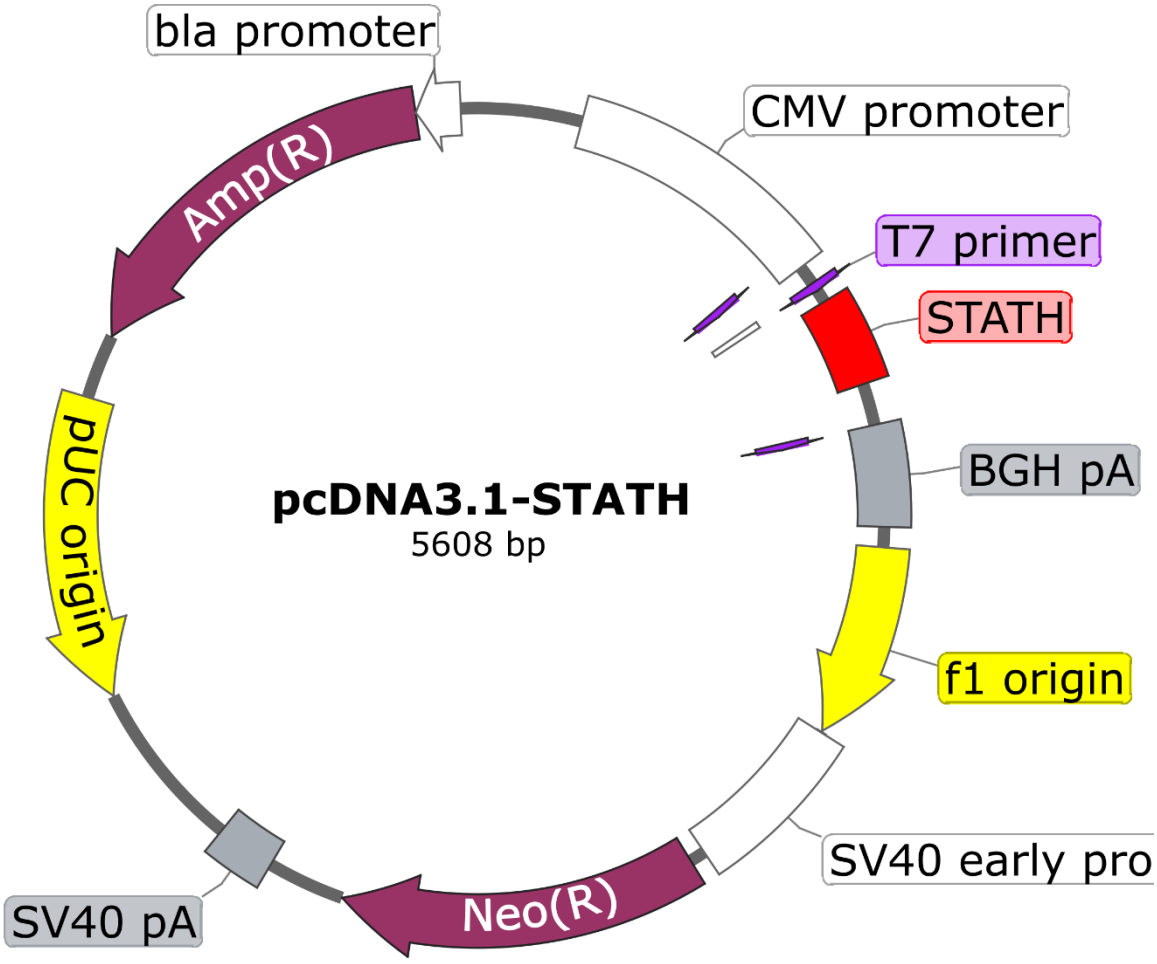

Map 3. pcDNA™ modified STATH Plasmid

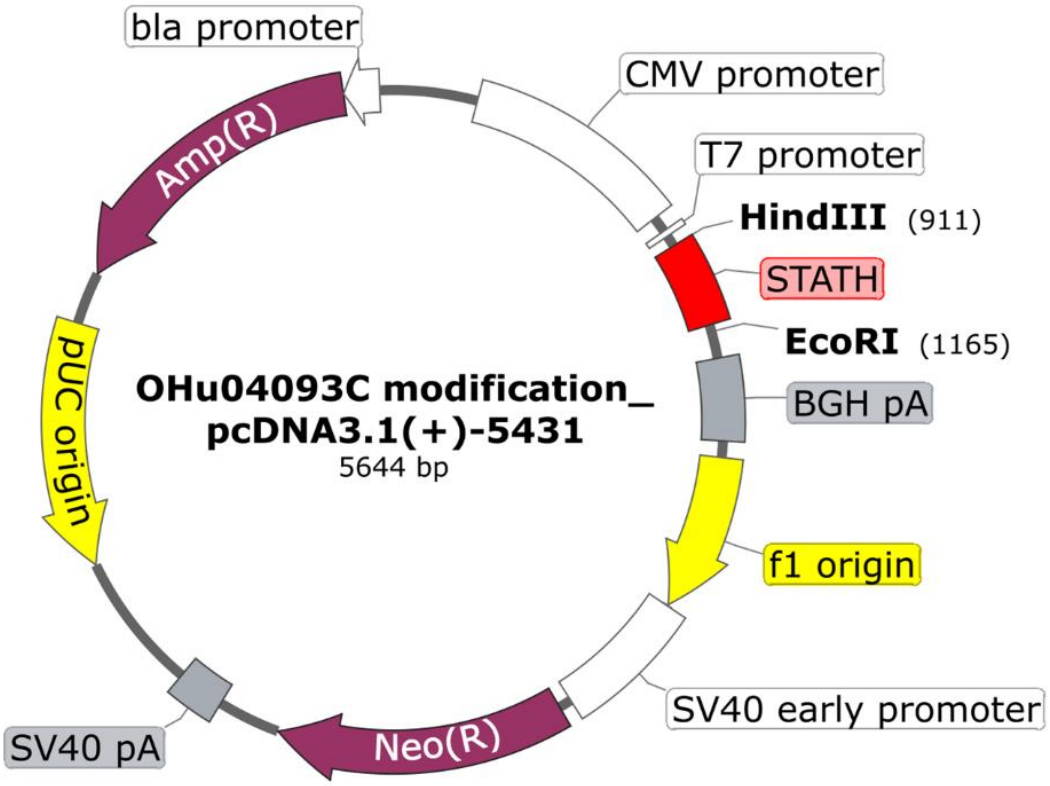

Clone ID: OHu04093C modification

AAGCTTCCTTCTCTTCCCTTCTCTTCCCTTCTCTTCGCCGCCATGAAGTTCCTTGTCTTTGC
CTTCATCTTGGCTCTCATGGTTTCCATGATTGGAGCTGATTCATCTGAAGAGAAATTTTTGCGT
AGAATTGGAAGATTCGGTTATGGGTATGGCCCTTATCAGCCAGTTCCAGAACAACCACTATAC
CCACAACCATACCAACCACAATACCAACAATATACCTTTTAAGGATCC.

1. make 5' UTR longer 2. add KOZAK consensus

Release fragments containing Statherin from modified pcDNA3.1-STATH

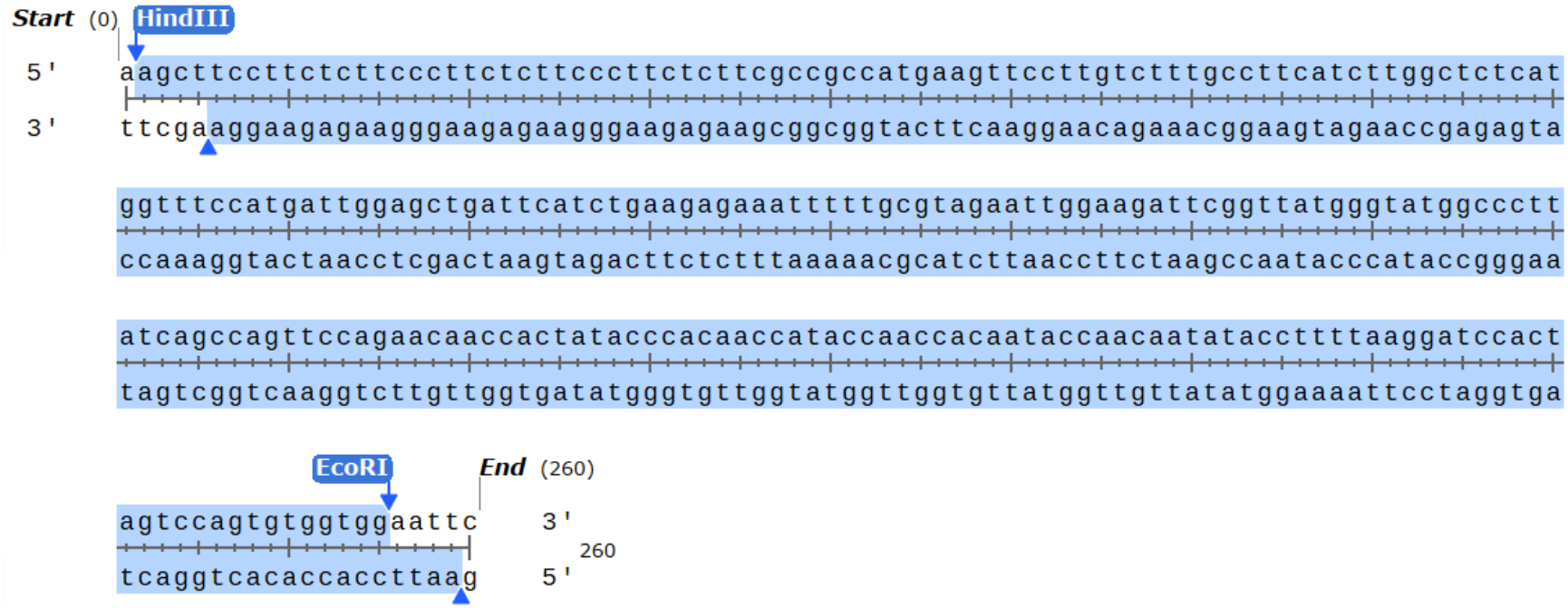

Product of Statherin with primer contains restriction site for Eco RI and Bam HI

Map 4. TOPO PCR Cloning- Statherin

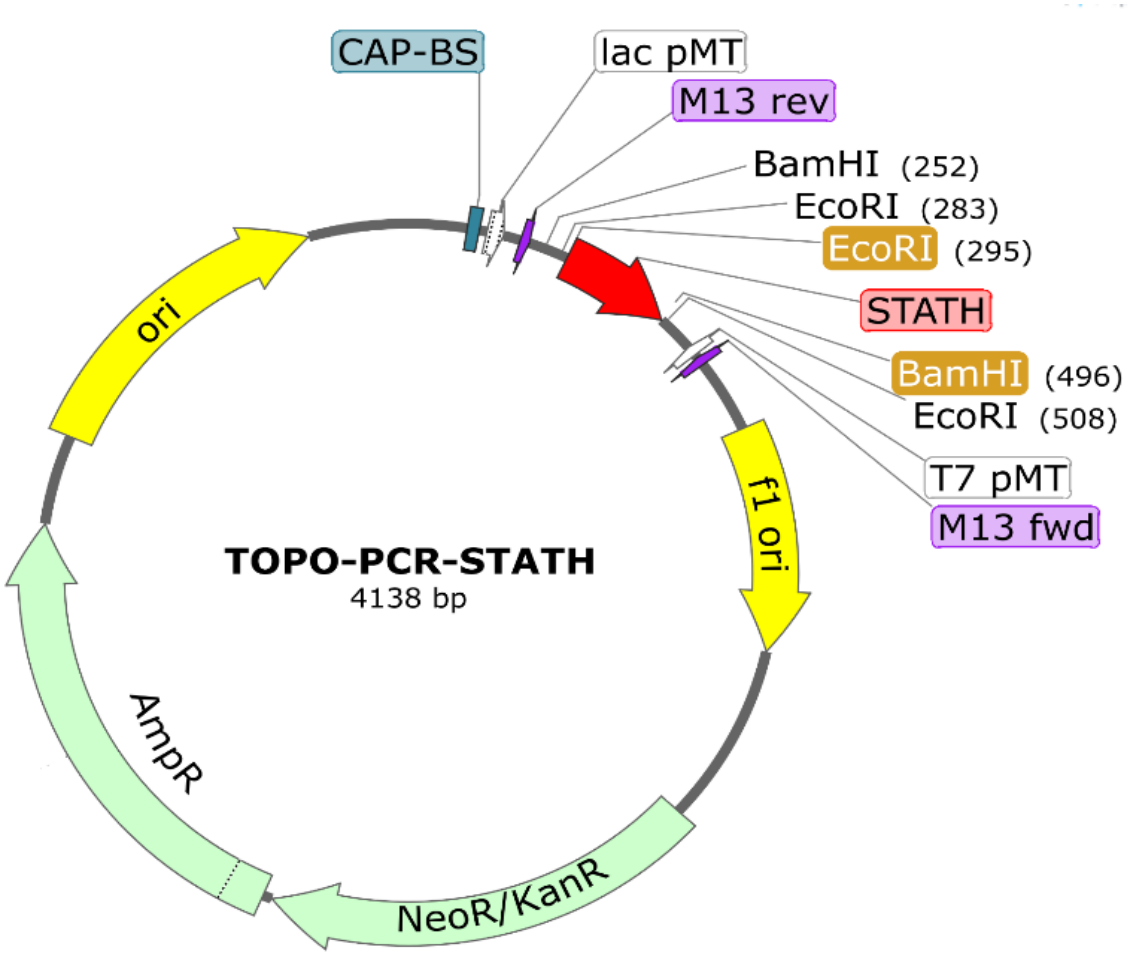

Purification Digested STATH from topo coloning

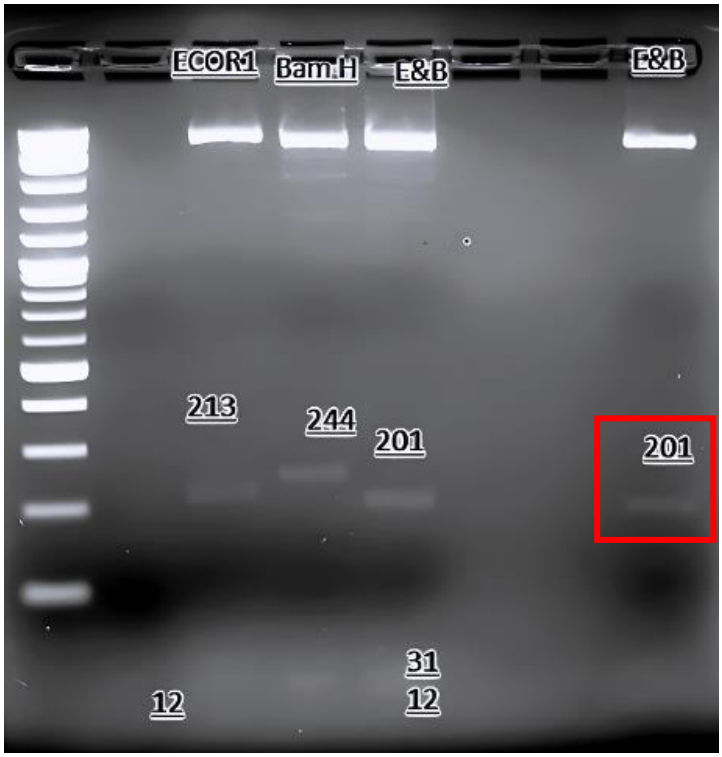

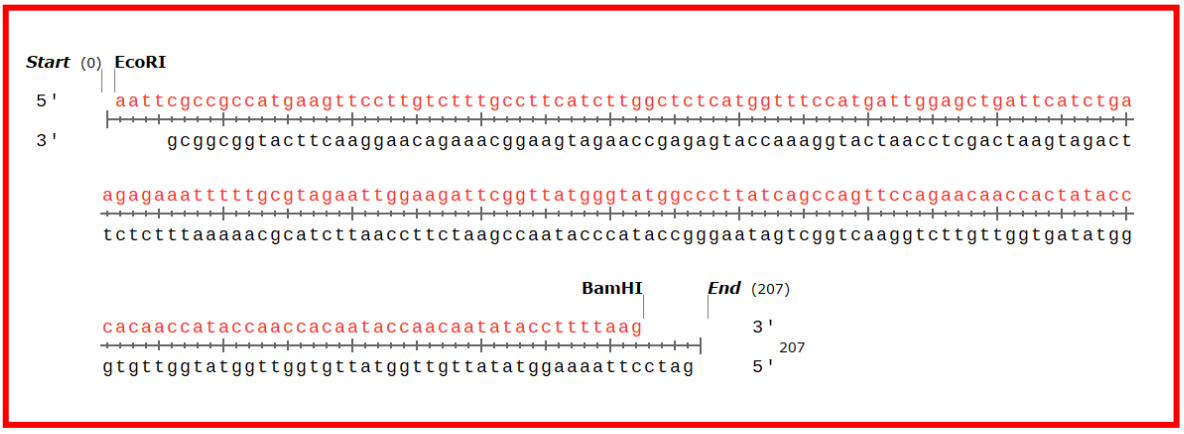

Map 5. pXJ40 Backbone

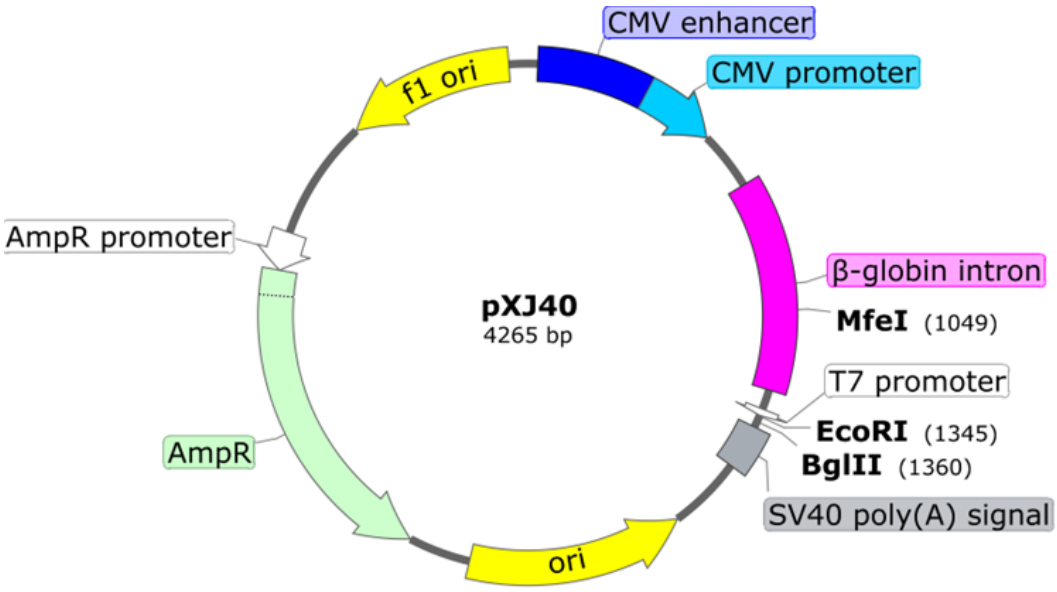

pXJ40 Backbone Digest with EcoRI and Bgl II

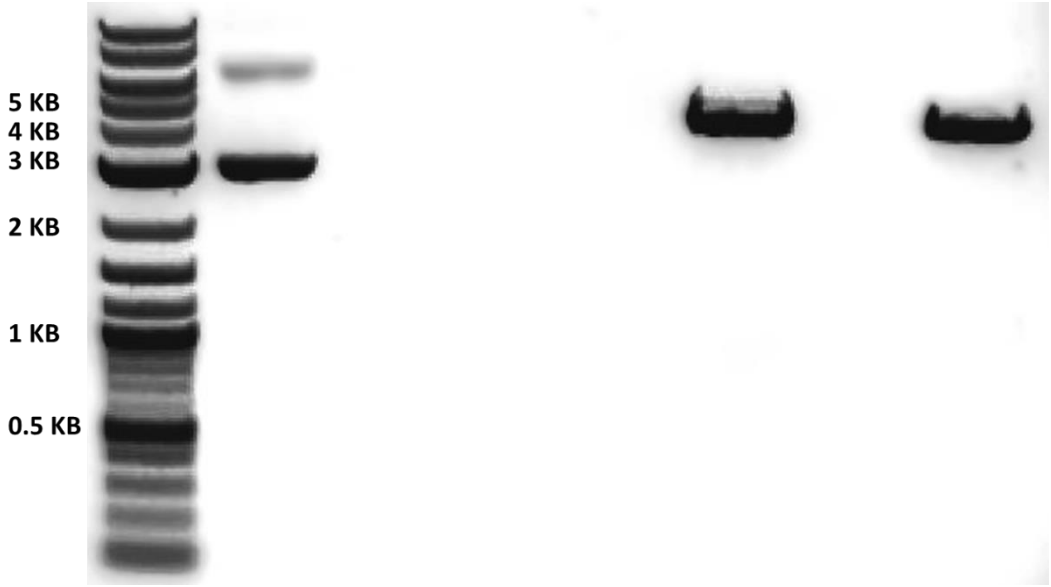

Map 6. pXJ40- STATH

Generation of pXJ40-STATH Expression Voctor

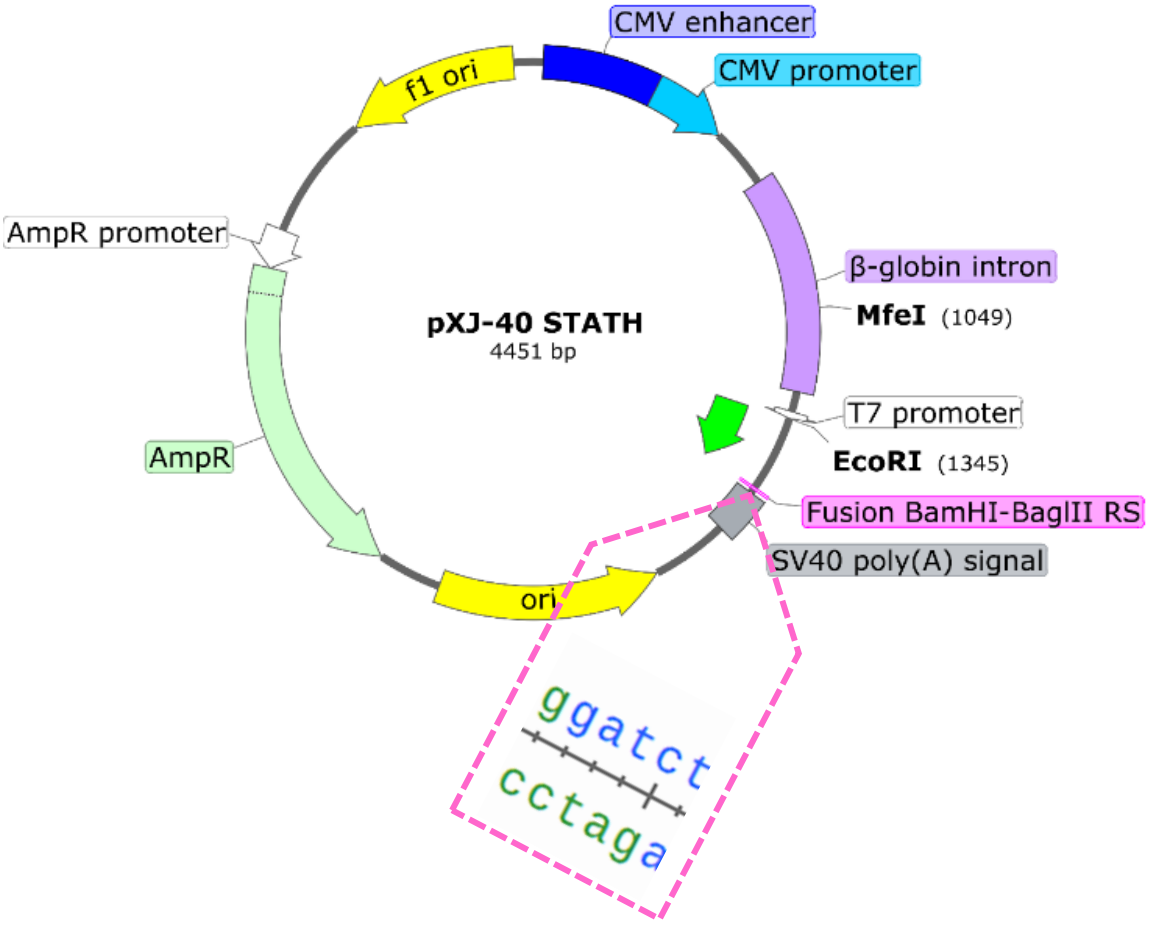

Integration of STATH CSD and Fusion Bam HI and Bagl II Restriction Site

Confirmation of cloning the STATH CSD DNA with PCR

Confirmation of cloning the STATH CSD DNA with sequencing

T7 primer forward and SV40-PA primer

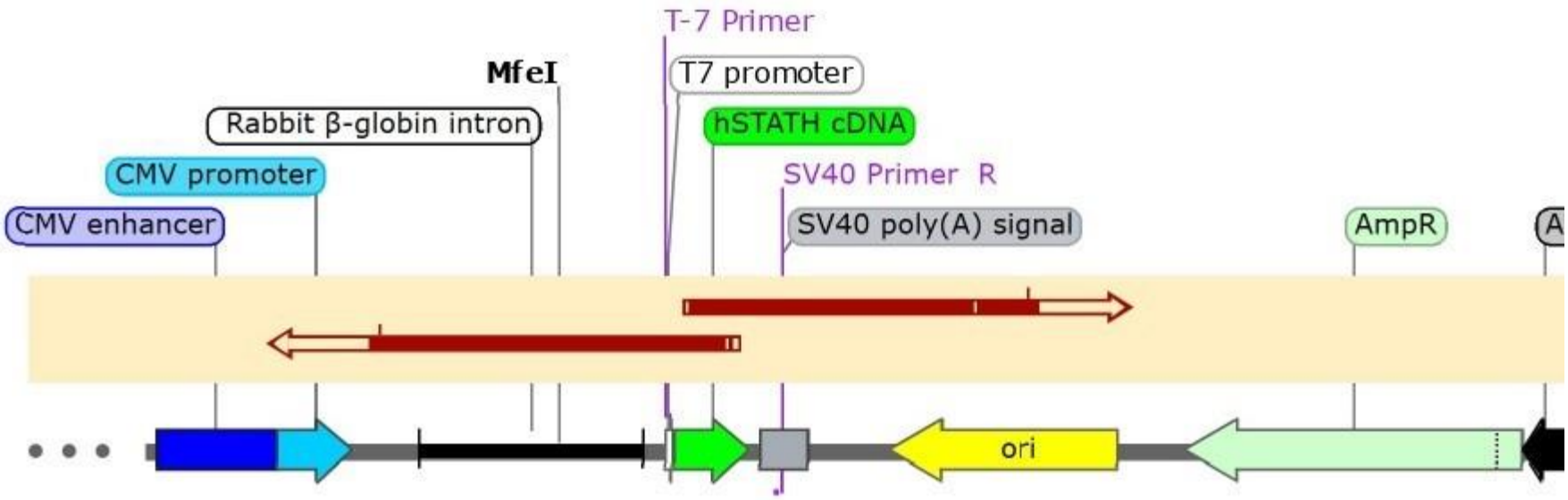

pXJ-40 STATH sequencing

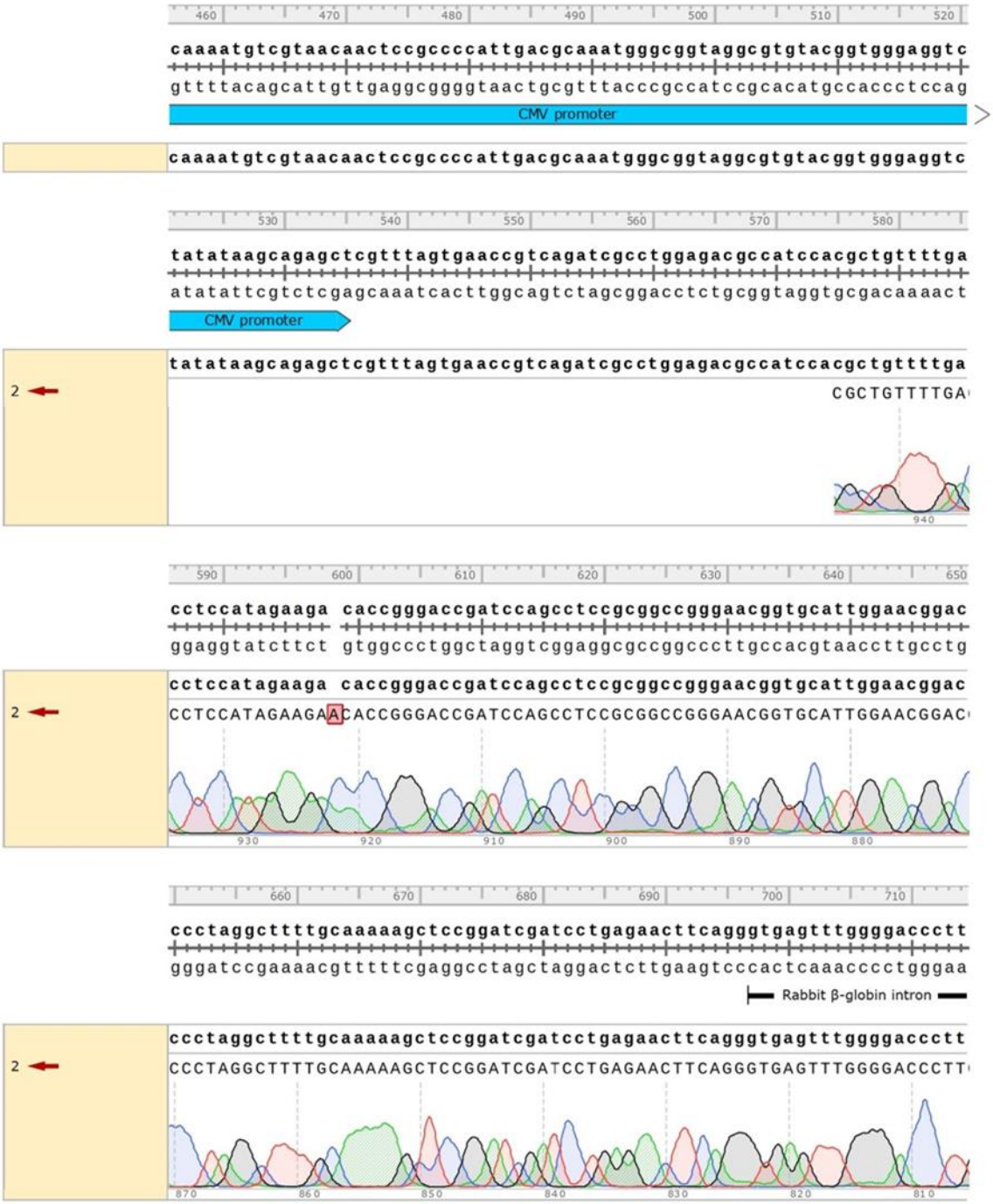

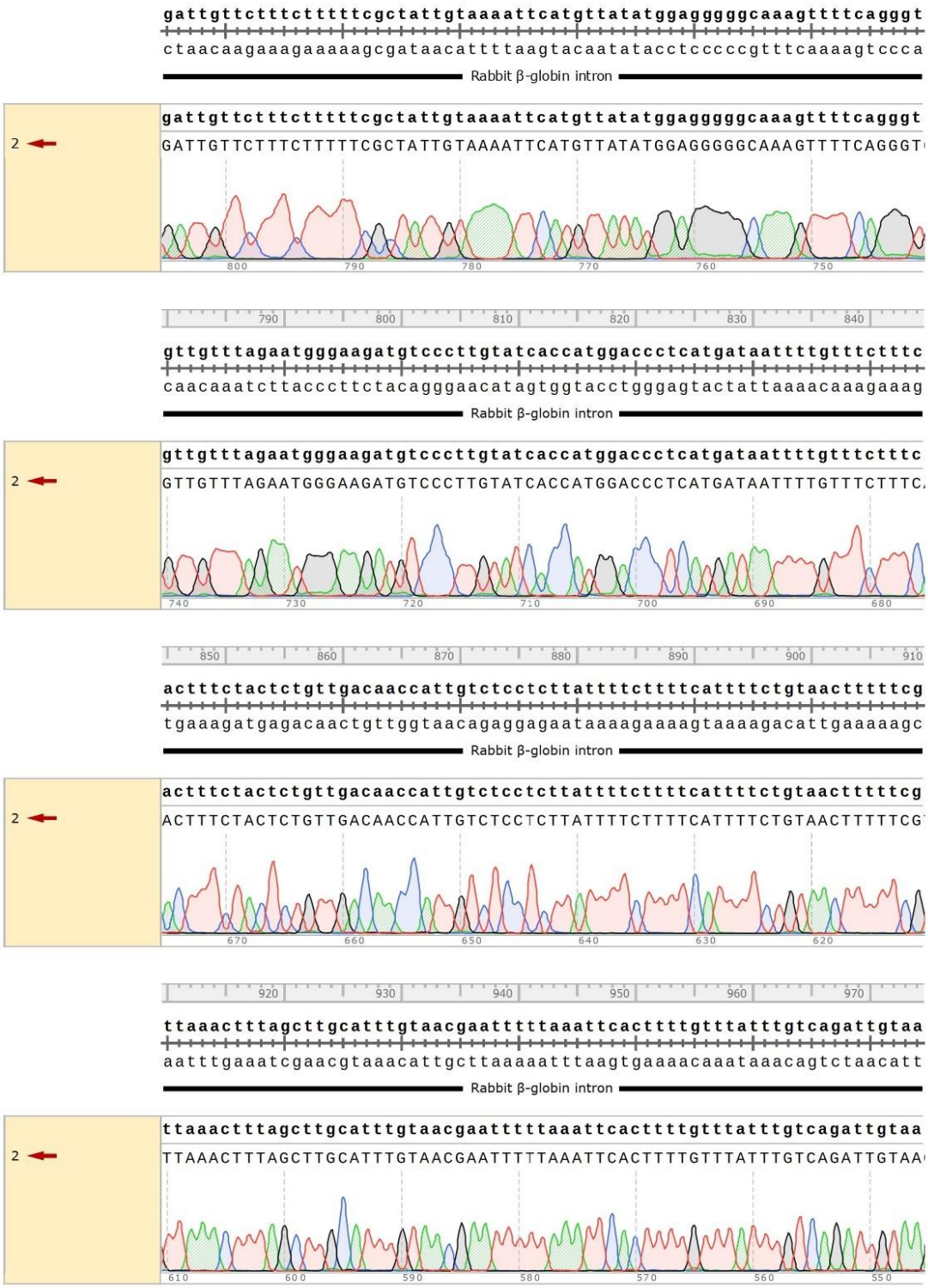
gattgttctttctttttcgctattgtaaaattcatgttatatggaggggcaaagttttcagggt
ctaacaagaaagaaaaagcgataacattttaagtacaatatacctccccgtttcaaaagtccca
Rabbit β-globin intron
2
GATTGTTCTTTCTTTTTCGCTATTGTAAAATTCATGTTATATGGAGGGGGCAAAGTTTTCAGGGT
800 790 780 770 760 750
790 800 810 820 830 840
gttgtttagaatgggaagatgtcccttgtatcaccatggaccctcatgataattttgtttctttc
caacaaatcttacccttctacagggaacatagtggtacctgggagtactattaaaacaaagaaag
Rabbit β-globin intron
2
GTTGTTTAGAATGGGAAGATGTCCCTTGTATCACCATGGACCCTCATGATAATTTTGTTTCTTTC
740 730 720 710 700 690 680
850 860 870 880 890 900 910
actttctactctgttgacaaccattgtctcctcttattttcttttcatttttctgtaacttttcg
tgaaagatgagacaactgttggtaacagaggagaataaaagaaaagtaaaagacattgaaaaagc
Rabbit β-globin intron
2
ACTTTCTACTCTGTTGACAACCATTGTCTCCTCTTATTTTCTTTTCATTTTCTGTAACTTTTTCG
670 660 650 640 630 620
920 930 940 950 960 970
ttaaactttagcttgcatttgtaacgaatttttaaattcacttttgtttatttgtcagattgtaa
aatttgaaatcgaacgtaaacattgcttaaaaatttaagtgaaaacaaataaacagtctaacatt
Rabbit β-globin intron
2
TTAAACTTTAGCTTGCATTTGTAACGAATTTTTAAATTCACTTTTGTTTATTTGTCAGATTGTAA
610 600 590 580 570 560 550

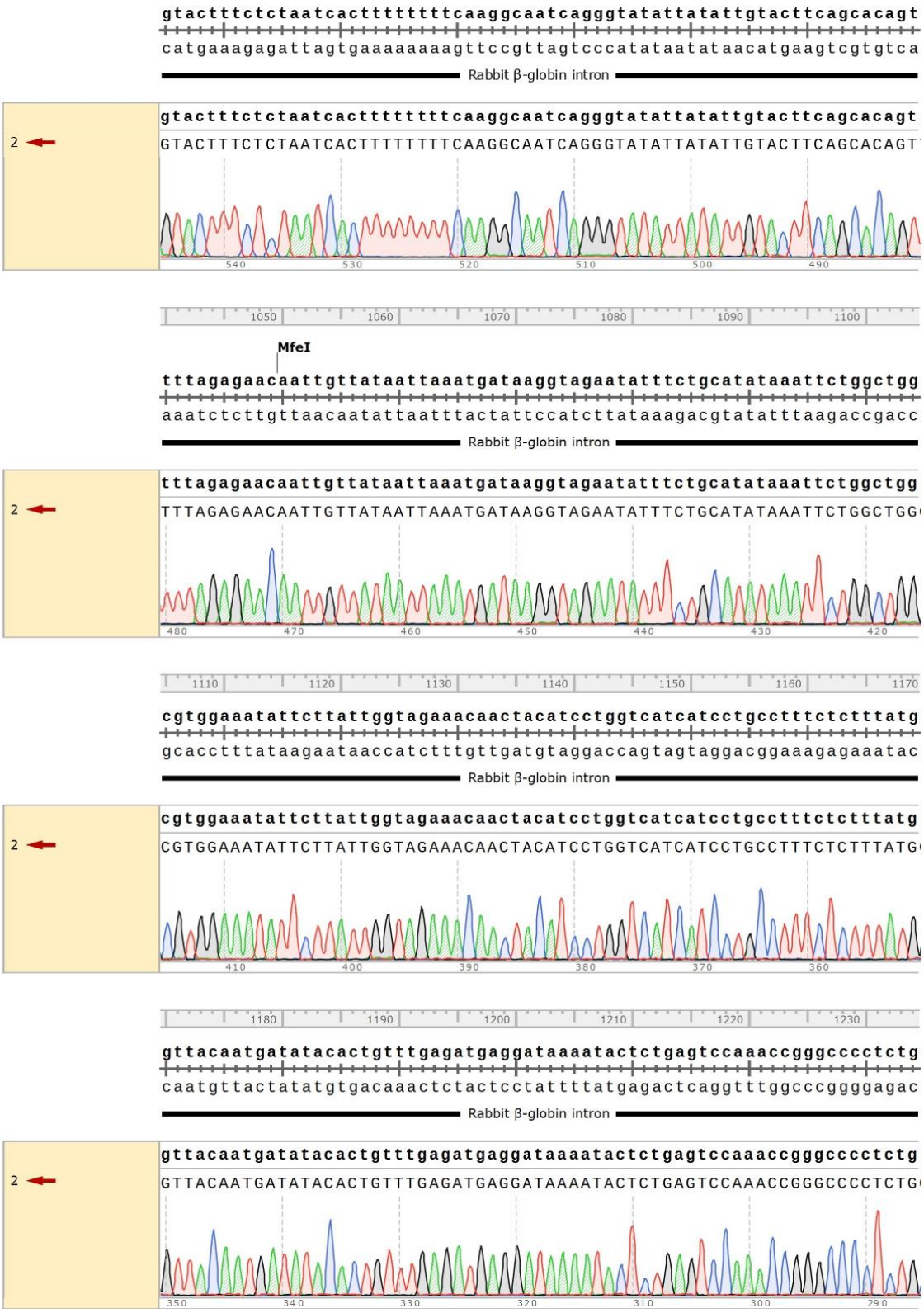
gtactttctctaatcacttttttttcaaggcaatcagggtatattatattgtacttcagcacagt
catgaaagagattagtgaaaaaaaagttccgttagtcccatataatataacatgaagtcgtgtca
Rabbit β-globin intron
2
GTACTTTCTCTAATCACTTTTTTTTCAAGGCAATCAGGGTATATTATATTGTACTTCAGCACAGT
540 530 520 510 500 490
1050 1060 1070 1080 1090 1100
MfeI
tttagagaacaattgttataattaaatgataaggtagaatatttctgcatataaattctggctgg
aaatctcttgttaacaatattaatttactattccatcttataaagacgtatatttaagaccgacc
Rabbit β-globin intron
2
TTTAGAGAACAATTGTTATAATTAAATGATAAGGTAGAATATTTCTGCATATAAATTCTGGCTGG
480 470 460 450 440 430 420
1110 1120 1130 1140 1150 1160 1170
cgtggaaatattcttattggtagaaacaactacatcctggtcatcatcctgcctttctctttatg
gcacctttataagaataaccatctttgttgatgtaggaccagtagtaggacggaaagagaaatac
Rabbit β-globin intron
2
CGTGGAAATATTCTTATTGGTAGAAACAACTACATCCTGGTCATCATCCTGCCTTTCTCTTTATG
410 400 390 380 370 360
1180 1190 1200 1210 1220 1230
gttacaatgatatacactgtttgagatgaggataaaatactctgagtccaaaccgggcccctctg
caatgttactatatgtgacaaactctactcctattttatgagactcaggtttggcccggggagac
Rabbit β-globin intron
2
GTTACAATGATATACACTGTTTGAGATGAGGATAAAATACTCTGAGTCCAAACCGGGCCCCTCTG
350 340 330 320 310 300 290

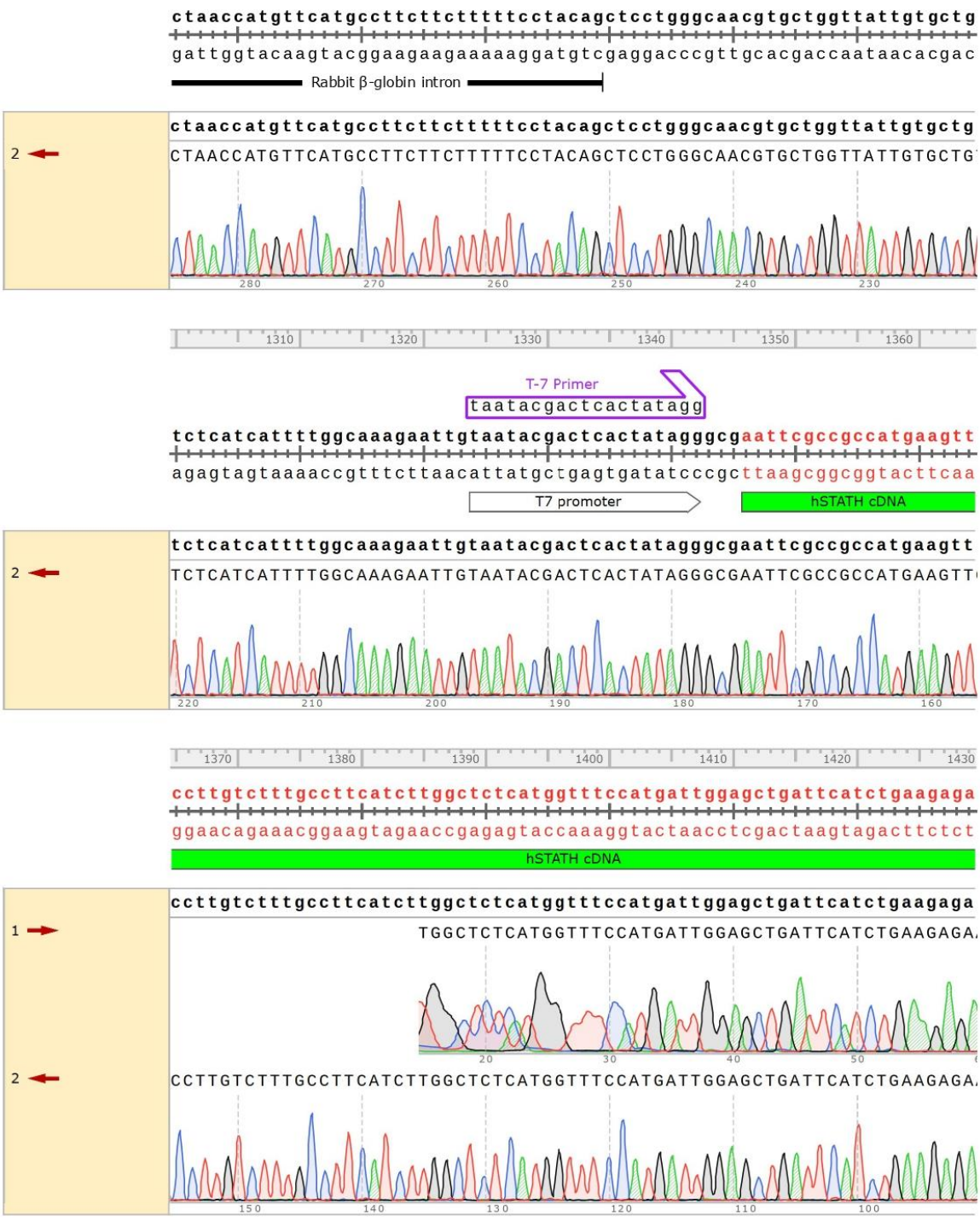
ctaaccatgttcatgccttcttcttttttcctacagctcctgggcaacgtgctggttattgtgctg
gattggtacaagtacggaagaagaaaaaggatgtcgaggacccgttgcacgaccaataacacgac
Rabbit β-globin intron
2
CTAACCATGTTCATGCCTTCTTCTTTTTCCTACAGCTCCTGGGCAACGTGCTGGTTATTGTGCTG
280
270
260
250
240
230
1310
1320
1330
1340
1350
1360
T-7 Primer
taatacgactcactatagg
tctcatcattttggcaaagaattgtaatacgactcactatagggcgaattcgccgccatgaagtt
agagtagtaaaaccgtttcttaacattatgctgagtgatatcccgcttaagcggcggtacttcaa
T7 promoter
hSTATH cDNA
2
TCTCATCATTTTGGCAAAGAATTGTAATACGACTCACTATAGGGCGAATTCGCCGCCATGAAGTT
220
210
200
190
180
170
160
1370
1380
1390
1400
1410
1420
1430
ccttgtctttgccttcatcttggctctcatggtttccatgattggagctgattcatctgaagaga
ggaacagaaacggaagtagaaccgagagtaccaaaggtactaacctcgactaagtagacttctct
hSTATH cDNA
1
TGGCTCTCATGGTTTCCATGATTGGAGCTGATTCATCTGAAGAGA
20
30
40
50
2
CCTTGTCTTTGCCTTCATCTTGGCTCTCATGGTTTCCATGATTGGAGCTGATTCATCTGAAGAGA
150
140
130
120
110
100

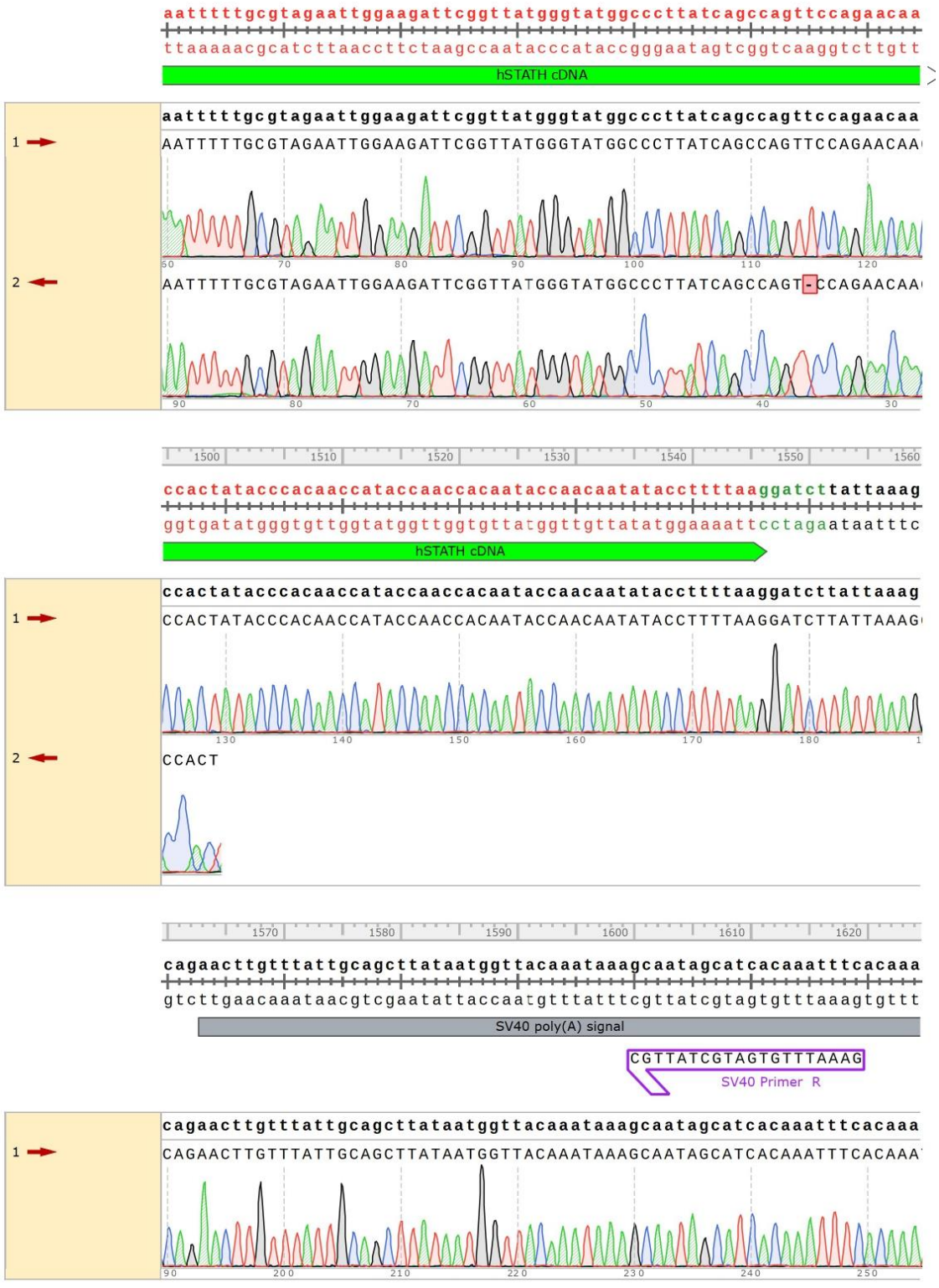
aatttttgcgtagaattggaagattcggttatgggtatggcccttatcagccagttccagaacaa
ttaaaaacgcatcttaaccttctaagccaataccataccgggaatagtcggtcaaggtcttgtt
hSTATH cDNA
1
2
AATTTTTGCGTAGAATTGGAAGATTCGGTTATGGGTATGGCCCTTATCAGCCAGTTCCAGAACAA
AATTTTTGCGTAGAATTGGAAGATTCGGTTATGGGTATGGCCCTTATCAGCCAGT-CCAGAACAA
ccactatacccacaaccataccaaccacaataccaacaatatacctttaaggatcttattaaag
ggtgatatgggtgttggtatggttggtgttatggttgttatatggaaaattcctagaataatttc
hSTATH cDNA
CCACTATACCCACAACCATACCAACCACAATACCAACAATATACCTTTTAAGGATCTTATTAAAG
CCACT
cagaacttgtttattgcagcttataatggttacaaataaagcaatagcatcacaaatttcacaaa
gtcttgaacaaataacgtcgaatattaccaatgtttatttcgttatcgtagtgtttaaagtgttt
SV40 poly(A) signal
CGTTATCGTAGTGTTTAAAG
SV40 Primer R
CAGAACTTGTTTATTGCAGCTTATAATGGTTACAAATAAAGCAATAGCATCACAAATTTCACAAA

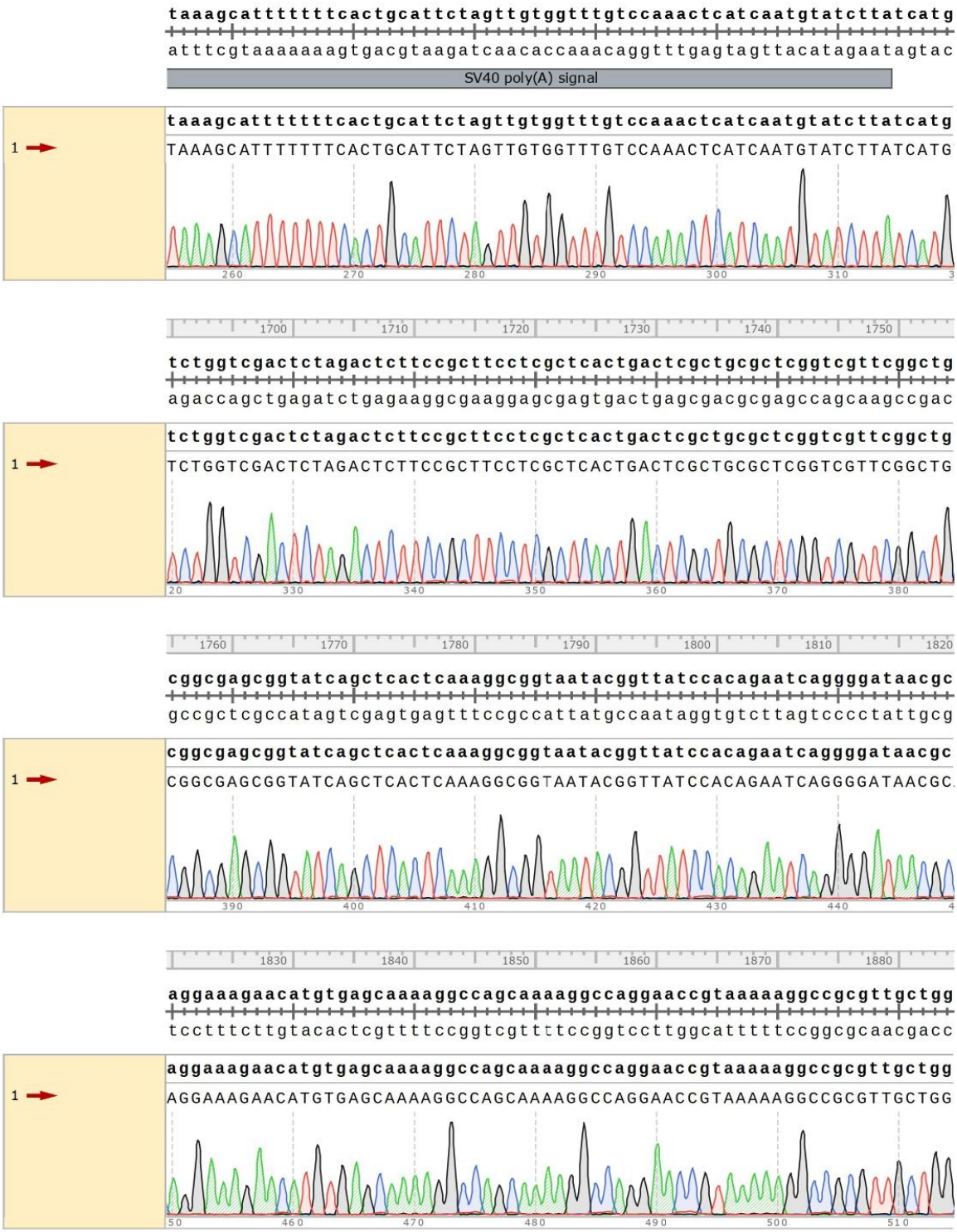
taaagcatttttttcactgcattctagttgtggtttgtccaaactcatcaatgtatcttatcatg
atttcgtaaaaaaaagtgacgtaagatcaacaccaaacaggtttgagtagttacatagaatagtac
SV40 poly(A) signal
1
taaagcatttttttcactgcattctagttgtggtttgtccaaactcatcaatgtatcttatcatg
TAAAGCATTTTTTTCACTGCATTCTAGTTGTGGTTTGTCCAAACTCATCAATGTATCTTATCATG
260
270
280
290
300
310
1700
1710
1720
1730
1740
1750
tctggtcgactctagactcttccgcttcctcgctcactgactcgctgcgctcggtcgttcggctg
agaccagctgagatctgagaaggcgaaggagcgagtgactgagcgacgcgagccagcaagccgac
1
tctggtcgactctagactcttccgcttcctcgctcactgactcgctgcgctcggtcgttcggctg
TCTGGTCGACTCTAGACTCTTCCGCTTCCTCGCTCACTGACTCGCTGCGCTCGGTCGTTCGGCTG
20
330
340
350
360
370
380
1760
1770
1780
1790
1800
1810
1820
cggcgagcggtatcagctcactcaaaggcggtaatacggttatccacagaatcaggggataacgc
gccgctcgccatagtcgagtgagtttccgccattatgccaataggtgtcttagtcccctattgcg
1
cggcgagcggtatcagctcactcaaaggcggtaatacggttatccacagaatcaggggataacgc
CGGCGAGCGGTATCAGCTCACTCAAAGGCGGTAATACGGTTATCCACAGAATCAGGGGATAACGC
390
400
410
420
430
440
1830
1840
1850
1860
1870
1880
aggaaagaacatgtgagcaaaaggccagcaaaaggccaggaaccgtaaaaaggccgcgttgctgg
tcctttcttgtacactcgttttccggtcgtttttccggtccttggcatttttccggcgcaacgacc
1
aggaaagaacatgtgagcaaaaggccagcaaaaggccaggaaccgtaaaaaggccgcgttgctgg
AGGAAAGAACATGTGAGCAAAAGGCCAGCAAAAGGCCAGGAACCGTAAAAAGGCCGCGTTGCTGG
50
460
470
480
490
500
510

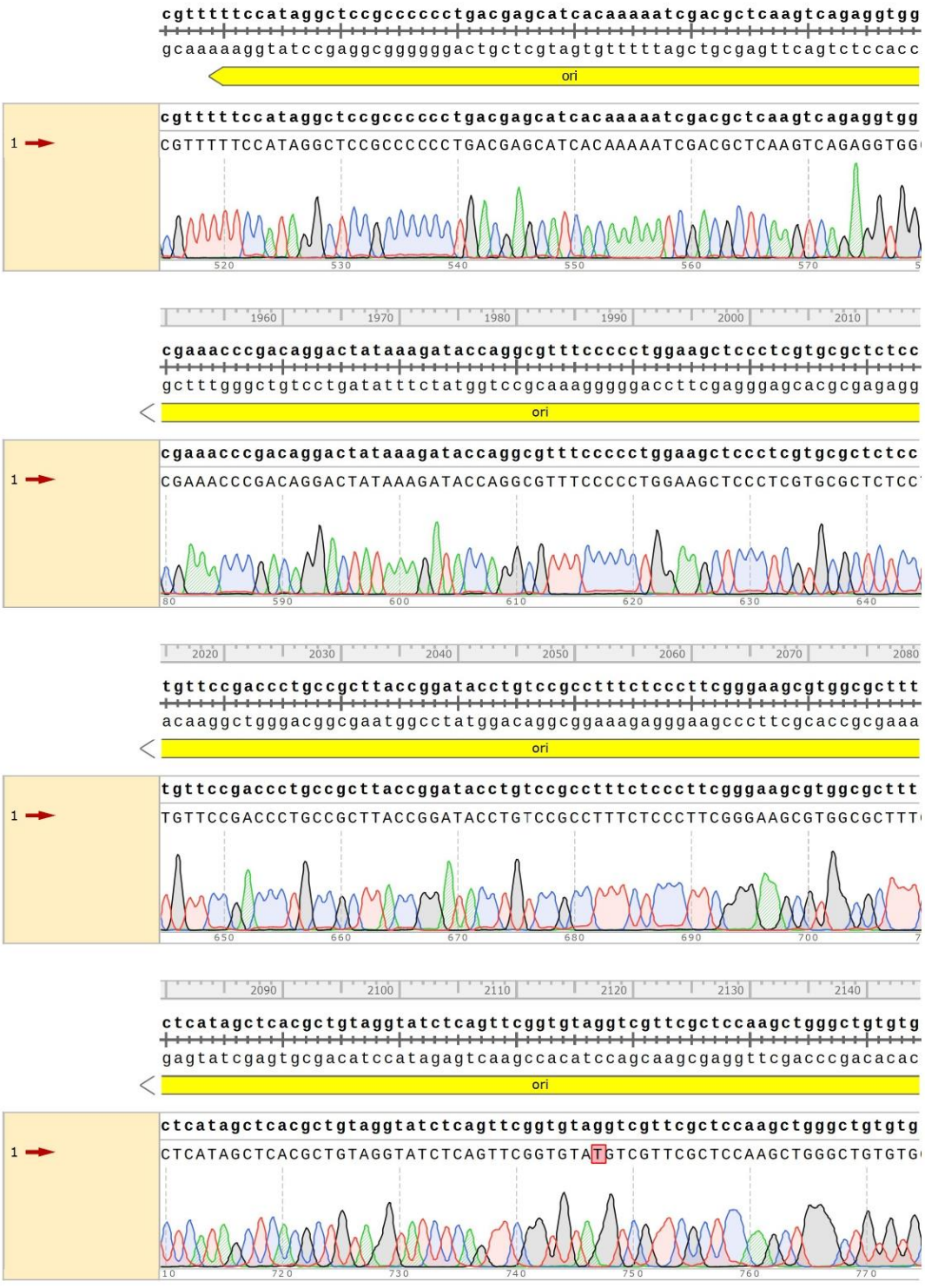
cgtttttccataggctccgccccccctgacgagcatcacaaaaatcgacgctcaagtcagaggtgg
gcaaaaaggtatccgaggcgggggggactgctcgtagtgtttttagctgcgagttcagtctccacc
ori
1
CGTTTTTCCATAGGCTCCGCCCCCCTGACGAGCATCACAAAAATCGACGCTCAAGTCAGAGGTGG
520
530
540
550
560
570
1960
1970
1980
1990
2000
2010
cgaaacccgacaggactataaagataccaggcgtttccccctggaagctccctcgtgcgctctcc
gctttgggctgtcctgatatttctatggtccgcaaaggggggaccttcgagggagcacgcgagagg
ori
1
CGAAACCCGACAGGACTATAAAGATACCAGGCGTTTCCCCCTGGAAGCTCCCTCGTGCGCTCTCC
80
590
600
610
620
630
640
2020
2030
2040
2050
2060
2070
2080
tgttccgaccctgccgcttaccggatacctgtccgcctttctcccttcgggaagcgtggcgcttt
acaaggctgggacggcgaatggcctatggacaggcggaaagagggaagcccttcgcaccgcgaaa
ori
1
TGTTCCGACCCTGCCGCTTACCGGATACCTGTCCGCCTTTCTCCCTTCGGGAAGCGTGGCGCTTT
650
660
670
680
690
700
2090
2100
2110
2120
2130
2140
ctcatagctcacgctgtaggtatctcagttcggtgtaggtcgttcgctccaagctgggctgtgtg
gagtatcgagtgcgacatccatagagtcaagccacatccagcaagcgaggttcgacccgacacac
ori
1
CTCATAGCTCACGCTGTAGGTATCTCAGTTCGGTGTATTGTCGTTCGCTCCAAGCTGGGCTGTGTG
10
720
730
740
750
760
770

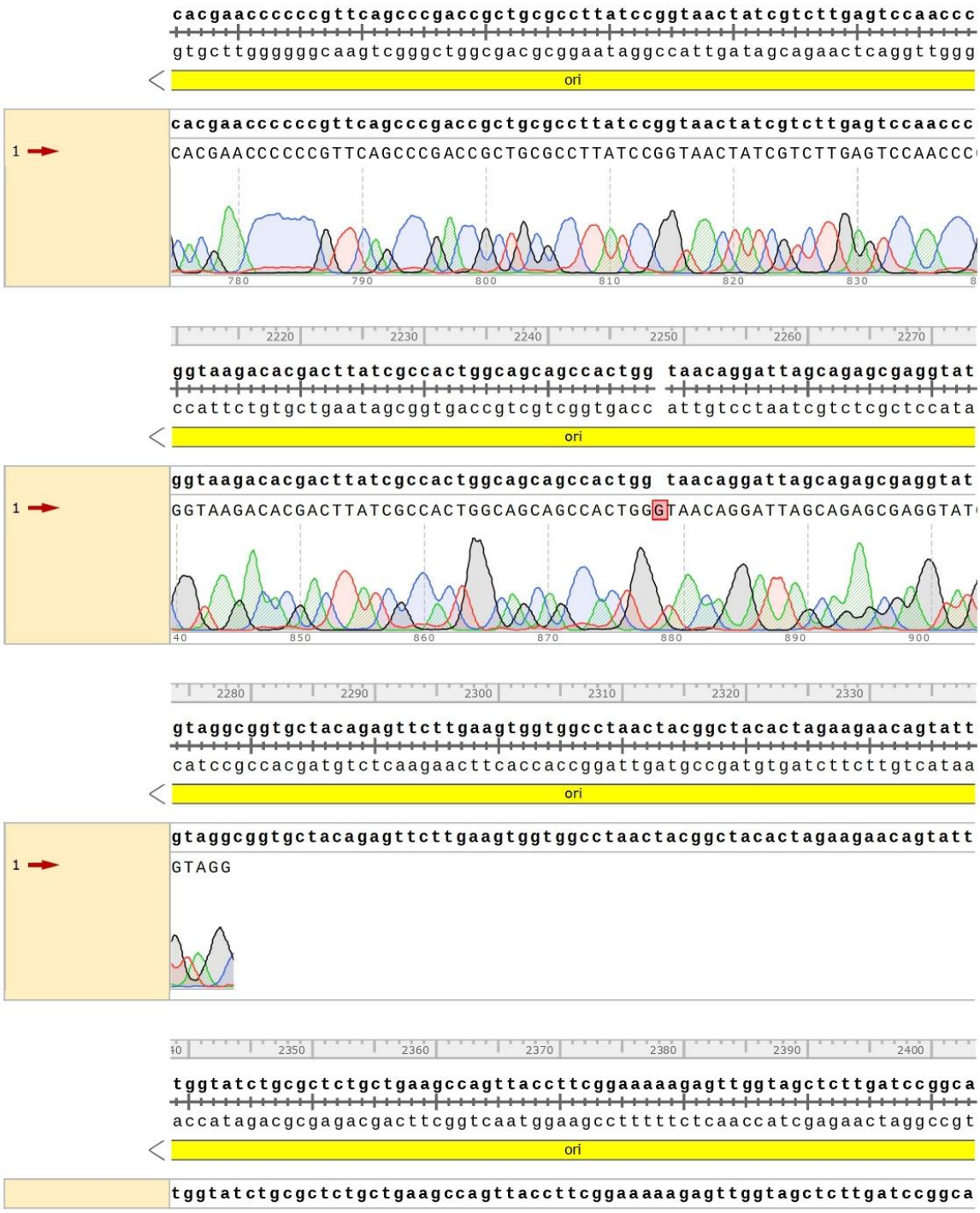
cacgaaccccccgttcagcccgaccgctgcgccttatccggtaactatcgtcttgagtccaaccc
gtgcttgggggcaagtcgggctggcgacgcggaataggccattgatagcagaactcaggttggg
ori
1
cacgaaccccccgttcagcccgaccgctgcgccttatccggtaactatcgtcttgagtccaaccc
CACGAACCCCCCGTTCAGCCCGACCGCTGCGCCTTATCCGGTAACTATCGTCTTGAGTCCAACCC
780
790
800
810
820
830
2220
2230
2240
2250
2260
2270
ggtaagacacgacttatcgccactggcagcagccactgg taacaggattagcagagcgaggtat
ccattctgtgctgaatagcggtgaccgtcgtcggtgacc attgtcctaatcgtctcgctccata
ori
1
ggtaagacacgacttatcgccactggcagcagccactgg taacaggattagcagagcgaggtat
GGTAAGACACGACTTATCGCCACTGGCAGCAGCCACTGGGTAACAGGATTAGCAGAGCGAGGTAT
40
850
860
870
880
890
900
2280
2290
2300
2310
2320
2330
gtaggcggtgctacagagttcttgaagtggtggcctaactacggctacactagaagaacagtatt
catccgccacgatgtctcaagaacttcaccaccggattgatgccgatgtgatcttcttgtcataa
ori
1
gtaggcggtgctacagagttcttgaagtggtggcctaactacggctacactagaagaacagtatt
GTAGG
40
2350
2360
2370
2380
2390
2400
tggtatctgcgctctgctgaagccagttaccttcggaaaaagagttggtagctcttgatccggca
accatagacgcgagacgacttcggtcaatggaagccttttttctcaaccatcgagaactaggccgt
ori
tggtatctgcgctctgctgaagccagttaccttcggaaaaagagttggtagctcttgatccggca

Generation Alu-STATH -pXJ40

Generation of Alu-STATH elements containing of Mfe1 restriction site

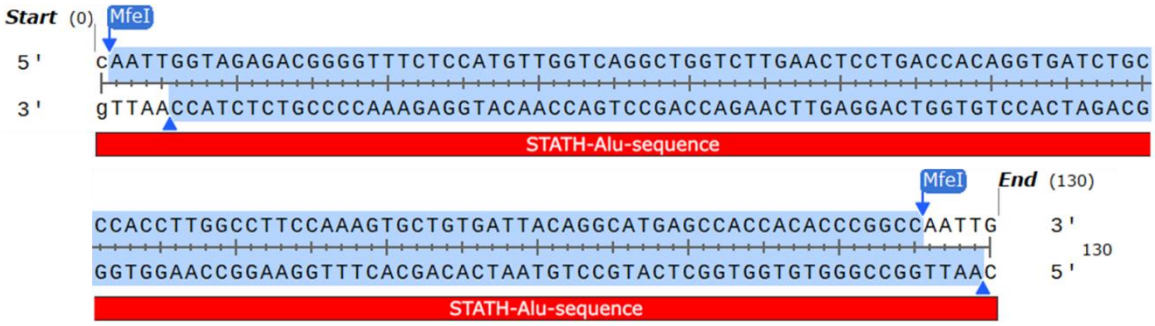

Digestion STATH -pXJ40 with MfeI

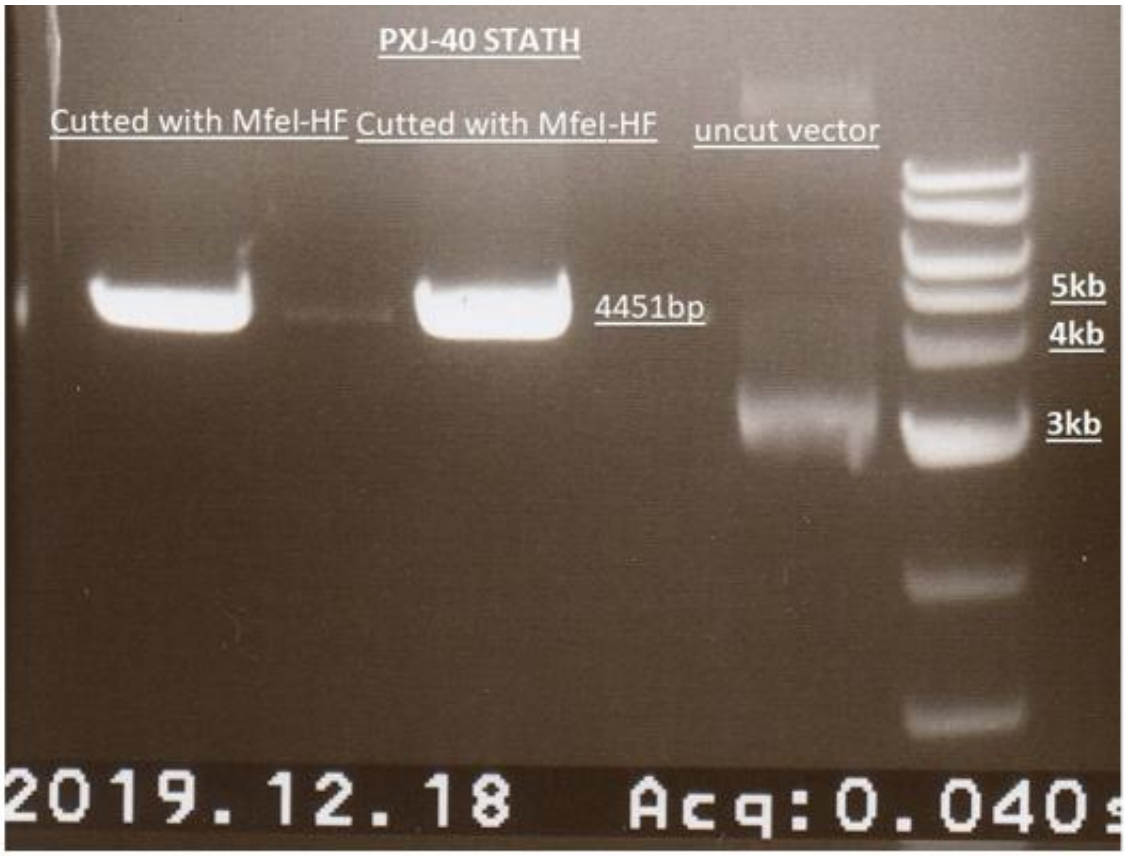

Map 7. Alu-STATH -pXJ40

Subclone Alu STATH elemets into beta globine Mfe1 restriction site

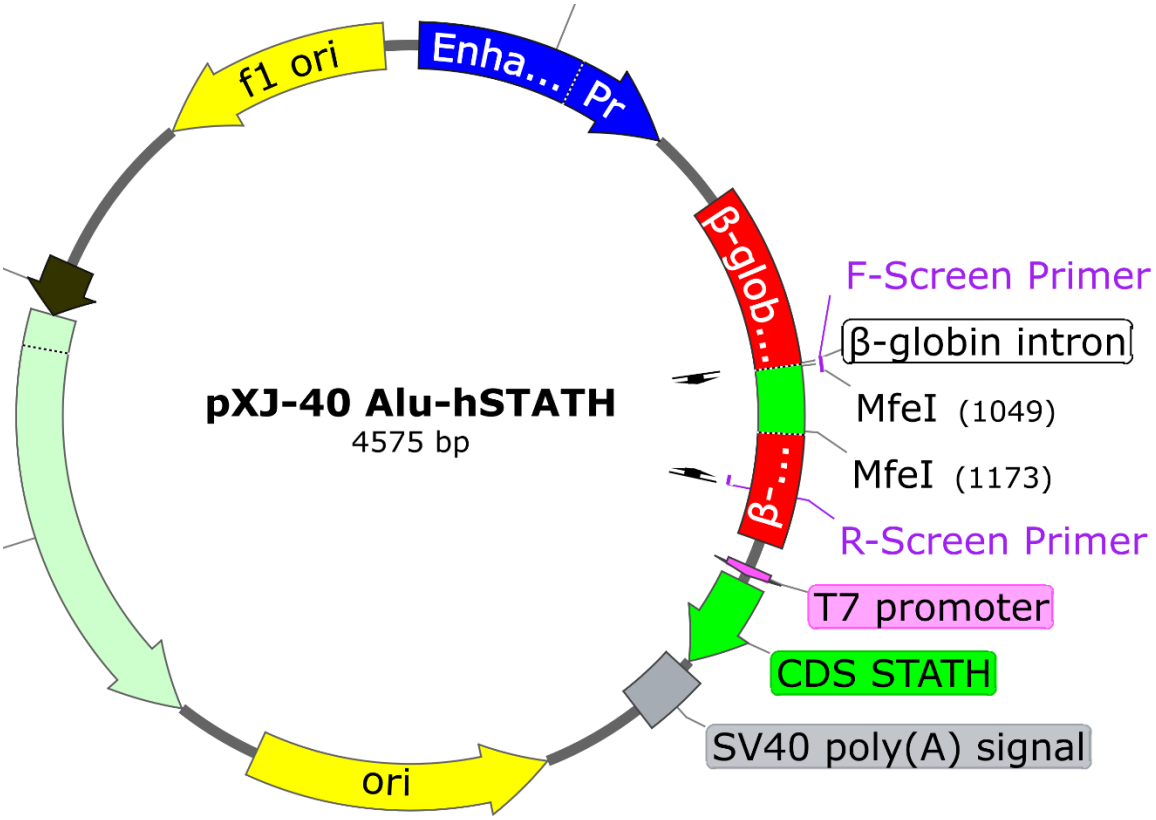

Screening of Alu-STATH insertion Orientations into STATH -pXJ40 by PCR cloning

PCR Cloning Primer Site for Determination of Orinitation

Screening of Alu-STATH insertion Orientations into STATH -pXJ40 by PCR cloning

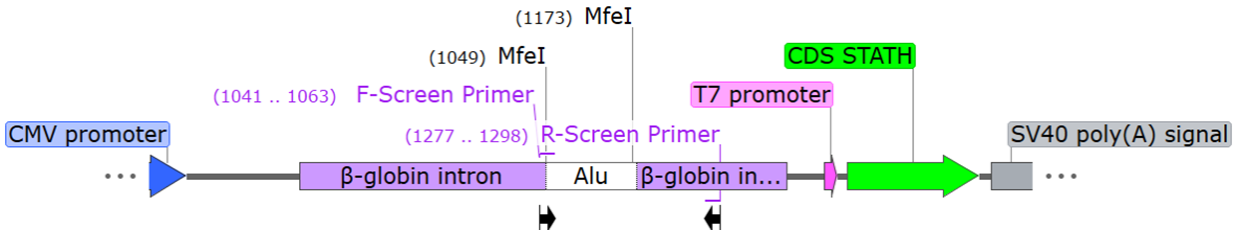

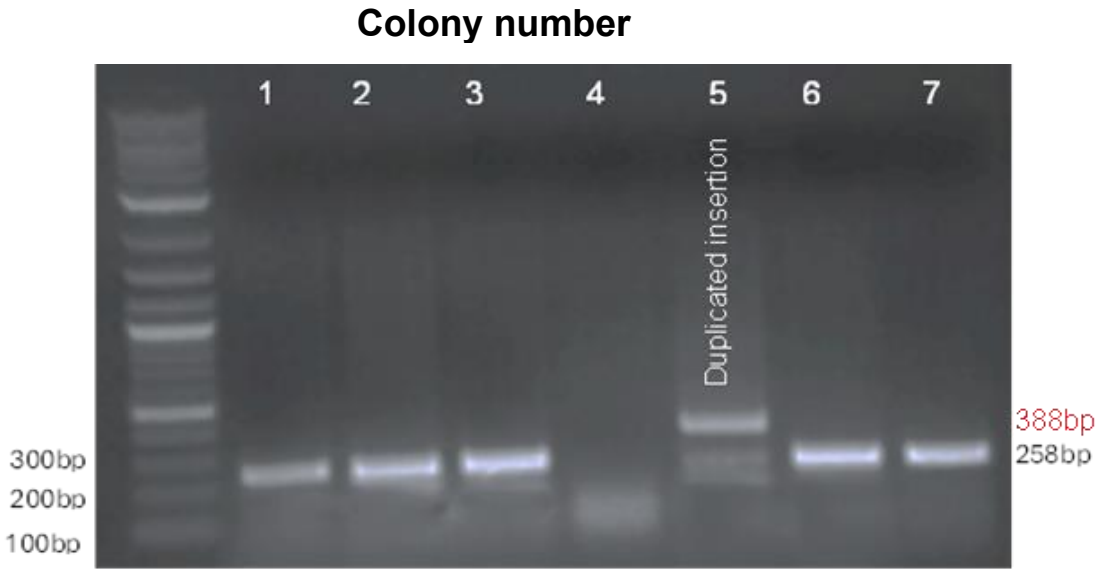

Orientation	Fragment size
Wrong orientation	No band
Correct orientation	258
Doble ALU insert	382
No insert	No band

Sequencing Analysis of Alu-STATH-Pxj40 Vector to confirmation right orientation

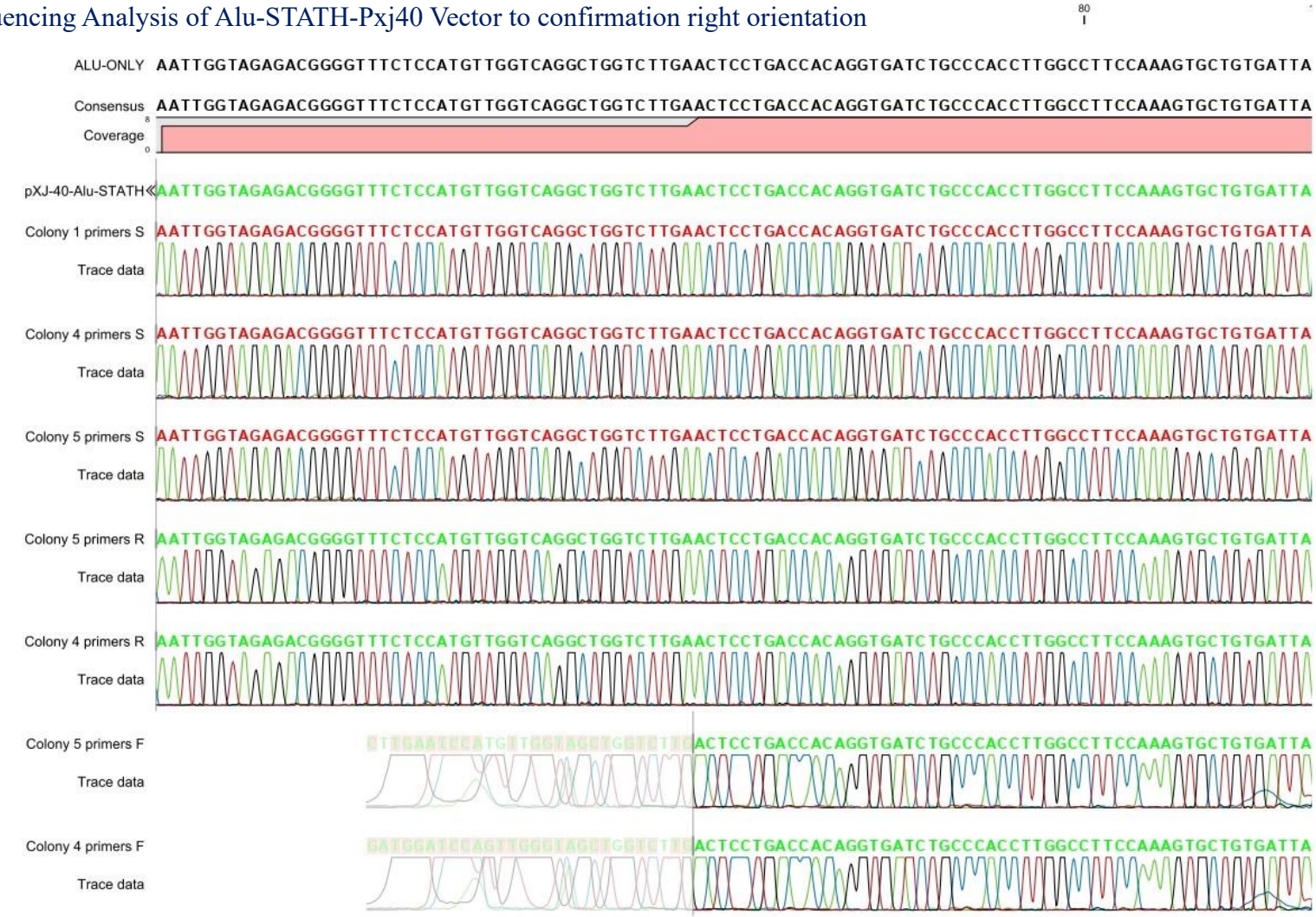

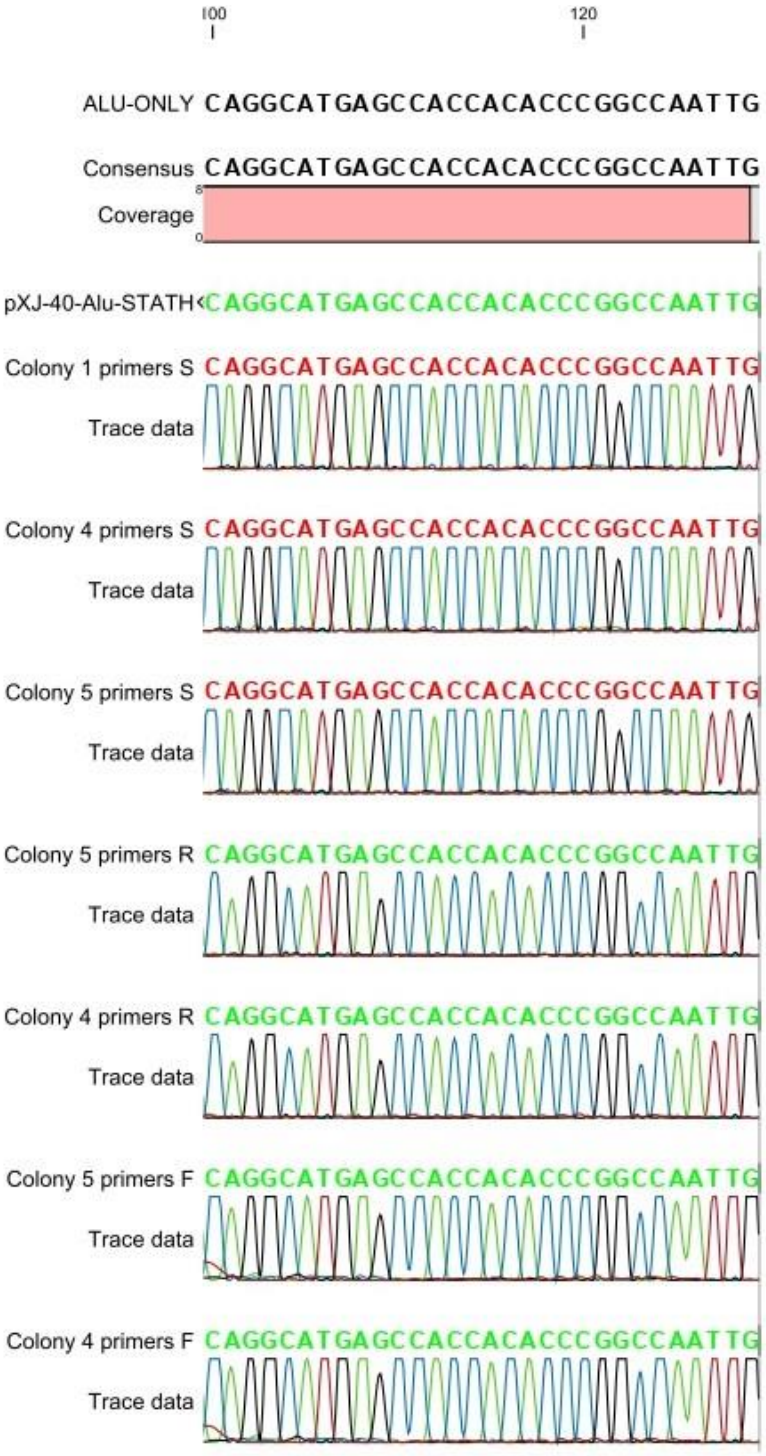
100
120
ALU-ONLY CAGGCATGAGCCACCACACCCGGCCAATTG
Consensus CAGGCATGAGCCACCACACCCGGCCAATTG
Coverage
pXJ-40-Alu-STATH CAGGCATGAGCCACCACACCCGGCCAATTG
Colony 1 primers S CAGGCATGAGCCACCACACCCGGCCAATTG
Trace data
Colony 4 primers S CAGGCATGAGCCACCACACCCGGCCAATTG
Trace data
Colony 5 primers S CAGGCATGAGCCACCACACCCGGCCAATTG
Trace data
Colony 5 primers R CAGGCATGAGCCACCACACCCGGCCAATTG
Trace data
Colony 4 primers R CAGGCATGAGCCACCACACCCGGCCAATTG
Trace data
Colony 5 primers F CAGGCATGAGCCACCACACCCGGCCAATTG
Trace data
Colony 4 primers F CAGGCATGAGCCACCACACCCGGCCAATTG
Trace data

Generation Sp6- ANRIL plasmid

ANRIL EU741058.1 Varint sequences

GenBank: EU741058.1

LOCUS EU741058 688 bp RNA linear PRI 21-JUN-2008

DEFINITION Homo sapiens antisense noncoding RNA in the INK4 locus splice variant (ANRIL), partial sequence, alternatively spliced.

ACCESSION EU741058
VERSION EU741058.1

GCGACATCTGGACACGGCGCGGCGCTGGCGCTGCCGGAGCTGTCGACCCGGC

CTGGCGCCGGACTAGTGTCCCTTTTGATGAGAAGAATAAGCCTCATTCTGATTC

AACAGCAGAGATCAAAGAAAAGACTTCTGTTTTCTGGCCACCAGATATATGTT

ATCTGTGCTTAAAGAATTGAAAAACACACATCAAAGGAGAATTTTCTTGGAAA

GAGAGGGTTCAAGCATCACTGTTAGGTGTGGTGGAATCCTTTCCCGAGTCAGT

ACTGCTTTCTAGAAGAAAACCGGGGAGATCTATTTGGAATGTATCTAACTCCA

AAGAAACCATCAGAGGTAACAGTAGAGACGGGGTTTCACCATGTTGGCCAGA

CTGGTCTTGAACTCCCGACCTCGTGATTCGCCCGCCTCGGCCTCCCAAAGTGC

TGGGATTACAGGTGTGAGACACCACGCCCGGCGGATAGAGAGAATTTTGACA

GGATGATTACGGAGCTAGGAATTTCCTACGAAGCTGGGTGATAAAAGGACATT

GGACAAAAACACAGATAGCTTCATTCTATACCAGGATCCATCACTGATTAGCTG

TATTATATTTGTCTCTACTGTAATTTGAGGAGAATGATACCTGCTTCTCTATCTTG

TTGGGTTTTACAGATGATGTATTGAAAGTTCAATAAAATCTATAAACAAT

Map 8. Sp6- ANRIL EU741058.1 plasmid

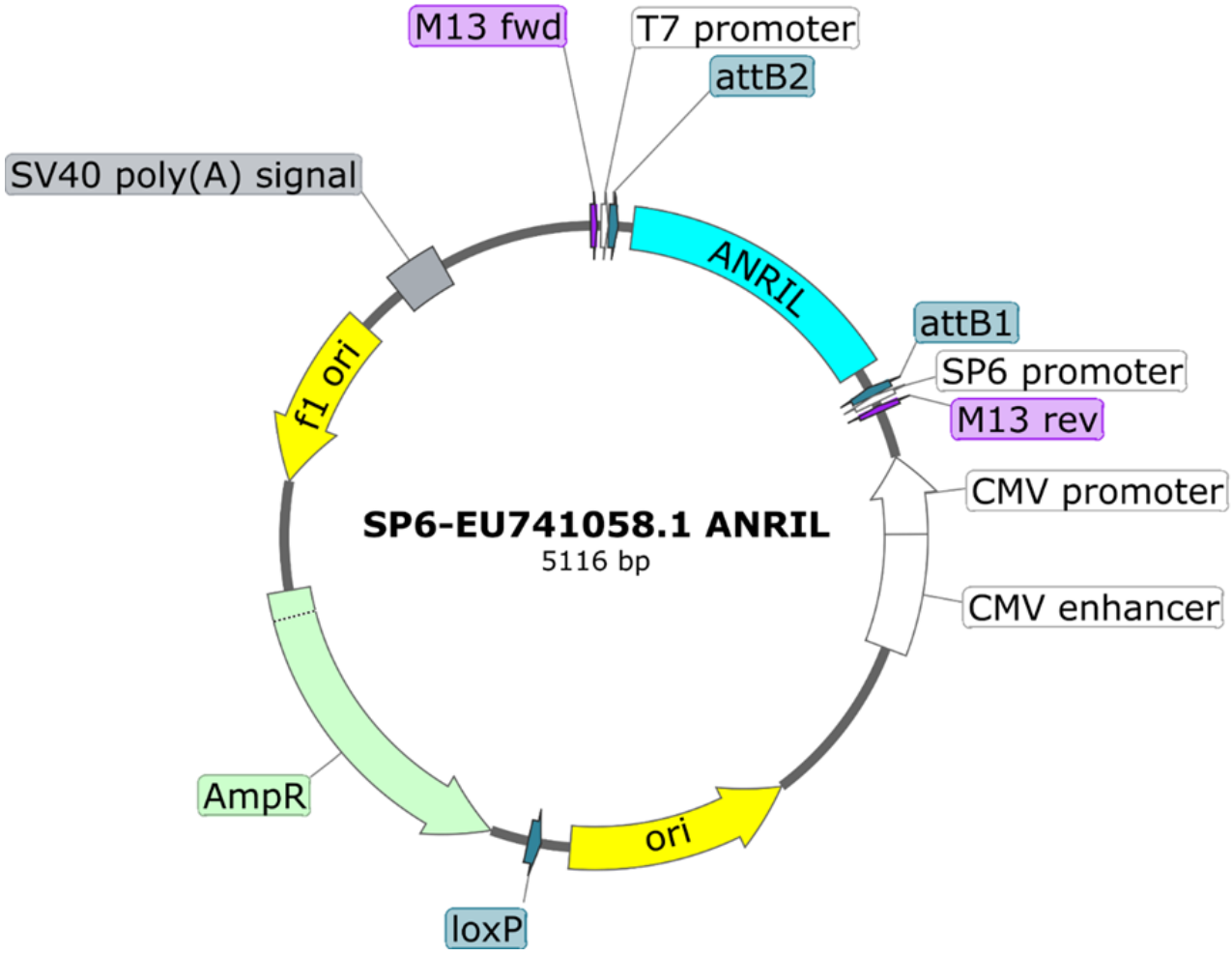

The EU741058 transcript includes exons 1, 5 to 7, and 13 of ANRIL.he single nucleotide polymorphism (SNP) rs1333048 is present in the EU741058 transcript of ANRIL.

Sp6- ANRIL ANRIL EU741058.1 Varint Sequencing Results

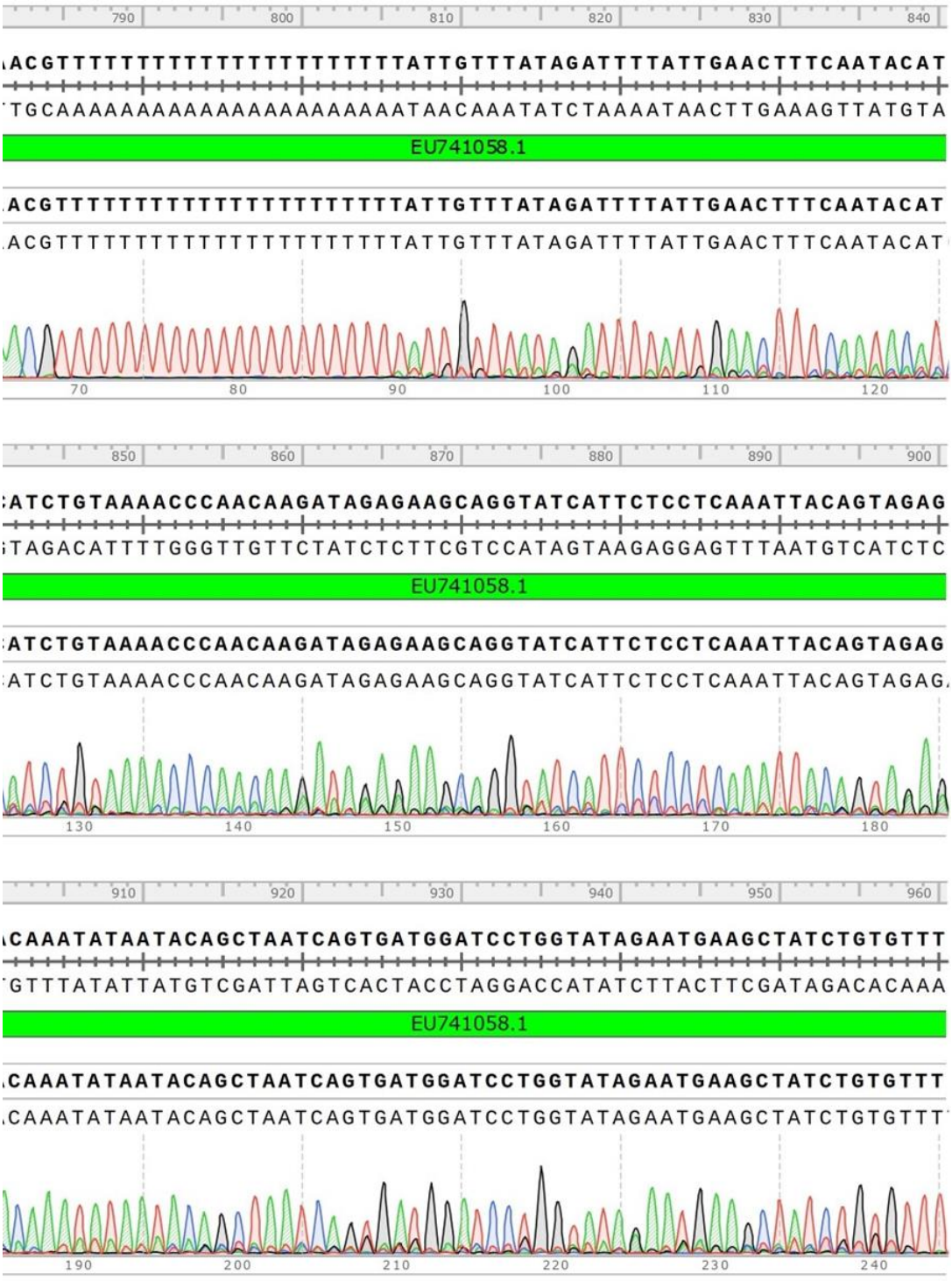
790
800
810
820
830
840
AACGTTTTTTTTTTTTTTTTTTTTTTTATTGTTTATAGATTTTATTGAACTTTCAATACAT
TTGCAAAAAAAAAAAAAAAAAAAAAATAACAAATATCTAAAATAACTTGAAAGTTATGTA
EU741058.1
AACGTTTTTTTTTTTTTTTTTTTTTTTATTGTTTATAGATTTTATTGAACTTTCAATACAT
AACGTTTTTTTTTTTTTTTTTTTTTTTATTGTTTATAGATTTTATTGAACTTTCAATACAT
70
80
90
100
110
120
850
860
870
880
890
900
CATCTGTAAAACCCAACAAGATAGAGAAGCAGGTATCATTCTCCTCAAATTACAGTAGAG
GTAGACATTTTGGGTTGTTCTATCTCTTCGTCCATAGTAAGAGGAGTTTAATGTCATCTC
EU741058.1
CATCTGTAAAACCCAACAAGATAGAGAAGCAGGTATCATTCTCCTCAAATTACAGTAGAG
CATCTGTAAAACCCAACAAGATAGAGAAGCAGGTATCATTCTCCTCAAATTACAGTAGAG
130
140
150
160
170
180
910
920
930
940
950
960
ACAAATATAATACAGCTAATCAGTGATGGATCCTGGTATAGAATGAAGCTATCTGTGTTT
TGTTTATATTATGTCGATTAGTCACTACCTAGGACCATATCTTACTTCGATAGACACAAA
EU741058.1
ACAAATATAATACAGCTAATCAGTGATGGATCCTGGTATAGAATGAAGCTATCTGTGTTT
ACAAATATAATACAGCTAATCAGTGATGGATCCTGGTATAGAATGAAGCTATCTGTGTTT
190
200
210
220
230
240

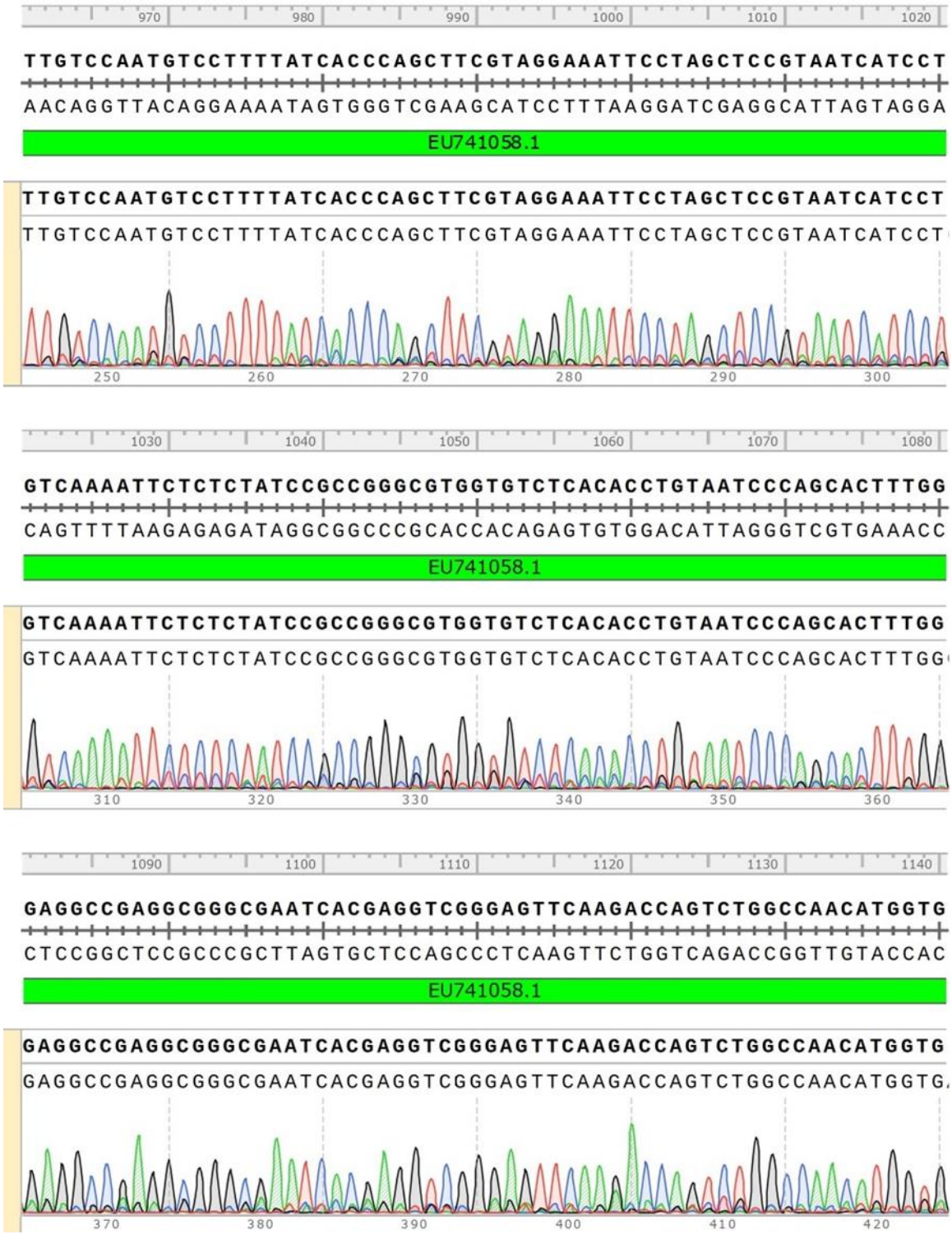
970
980
990
1000
1010
1020
TTGTCCAATGTCCTTTTATCACCCAGCTTCGTAGGAAATTCCTAGCTCCGTAATCATCCT
AACAGGTTACAGGAAAATAGTGGGTCGAAGCATCCTTTAAGGATCGAGGCATTAGTAGGA
EU741058.1
TTGTCCAATGTCCTTTTATCACCCAGCTTCGTAGGAAATTCCTAGCTCCGTAATCATCCT
TTGTCCAATGTCCTTTTATCACCCAGCTTCGTAGGAAATTCCTAGCTCCGTAATCATCCT
250
260
270
280
290
300
1030
1040
1050
1060
1070
1080
GTCAAAATTCTCTCTATCCGCCGGGCGTGGTGTCTCACACCTGTAATCCCAGCACTTTGG
CAGTTTTAAGAGAGATAGGCGGCCCGCACCACAGAGTGTGGACATTAGGGTCGTGAAACC
EU741058.1
GTCAAAATTCTCTCTATCCGCCGGGCGTGGTGTCTCACACCTGTAATCCCAGCACTTTGG
GTCAAAATTCTCTCTATCCGCCGGGCGTGGTGTCTCACACCTGTAATCCCAGCACTTTGG
310
320
330
340
350
360
1090
1100
1110
1120
1130
1140
GAGGCCGAGGCGGGCGAATCACGAGGTCGGGAGTTCAAGACCAGTCTGGCCAACATGGTG
CTCCGGCTCCGCCCGCTTAGTGCTCCAGCCCTCAAGTTCTGGTCAGACCGGTTGTACCAC
EU741058.1
GAGGCCGAGGCGGGCGAATCACGAGGTCGGGAGTTCAAGACCAGTCTGGCCAACATGGTG
GAGGCCGAGGCGGGCGAATCACGAGGTCGGGAGTTCAAGACCAGTCTGGCCAACATGGTG
370
380
390
400
410
420

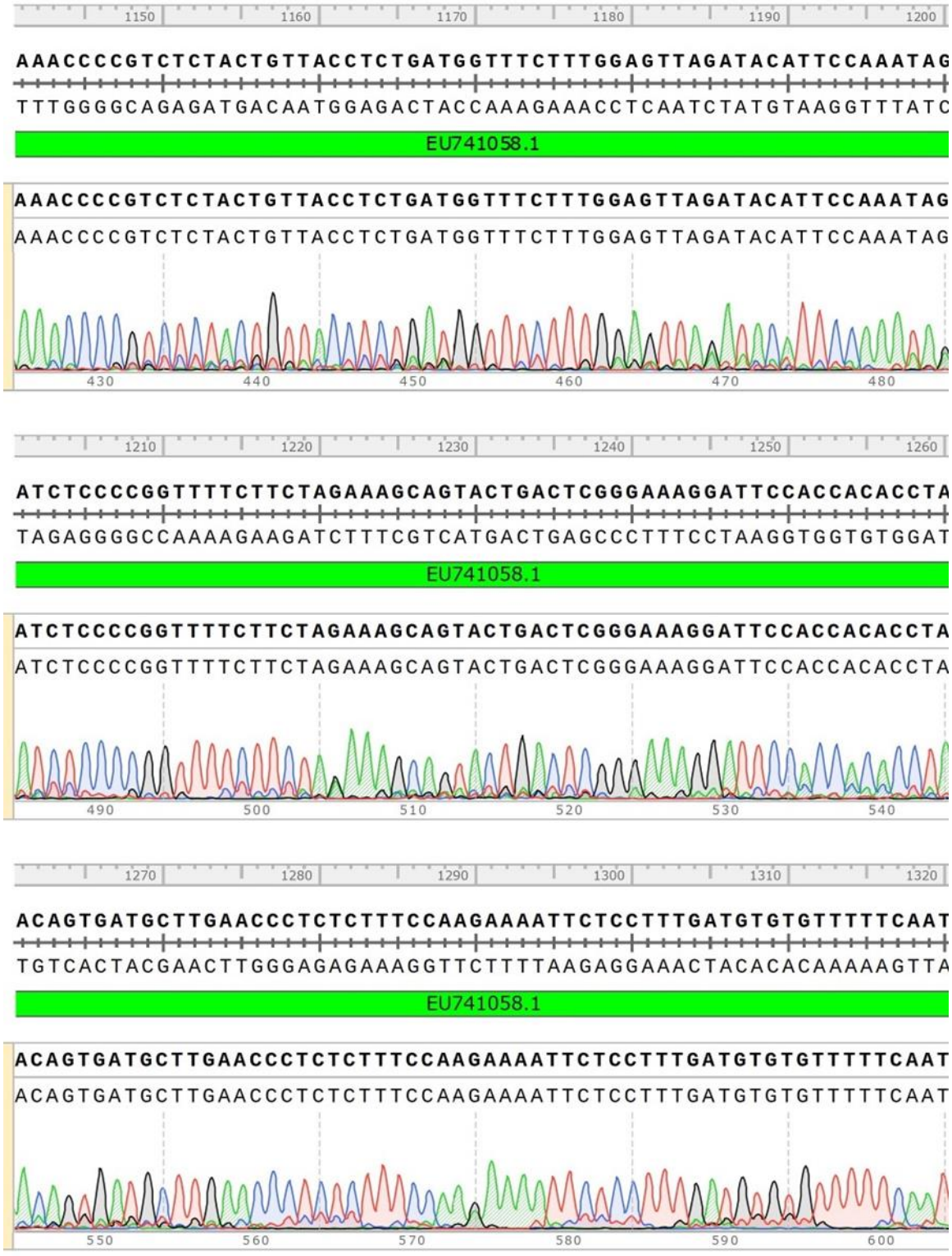
1150
1160
1170
1180
1190
1200
AAACCCCGTCTCTACTGTTACCTCTGATGGTTTCTTTGGAGTTAGATACATTCCAAATAG
TTTGGGGCAGAGATGACAATGGAGACTACCAAAGAAACCTCAATCTATGTAAGGTTTATC
EU741058.1
AAACCCCGTCTCTACTGTTACCTCTGATGGTTTCTTTGGAGTTAGATACATTCCAAATAG
AAACCCCGTCTCTACTGTTACCTCTGATGGTTTCTTTGGAGTTAGATACATTCCAAATAG
430
440
450
460
470
480
1210
1220
1230
1240
1250
1260
ATCTCCCCGGTTTTCTTCTAGAAAGCAGTACTGACTCGGGAAAGGATTCCACCACACCTA
TAGAGGGGCCAAAAGAAGATCTTTCGTCATGACTGAGCCCTTTCCTAAGGTGGTGTGGAT
EU741058.1
ATCTCCCCGGTTTTCTTCTAGAAAGCAGTACTGACTCGGGAAAGGATTCCACCACACCTA
ATCTCCCCGGTTTTCTTCTAGAAAGCAGTACTGACTCGGGAAAGGATTCCACCACACCTA
490
500
510
520
530
540
1270
1280
1290
1300
1310
1320
ACAGTGATGCTTGAACCCTCTCTTTCCAAGAAAATTCTCCTTTGATGTGTGTTTTTCAAT
TGTCACTACGAACTTGGGAGAGAAAGGTTCTTTTAAGAGGAAACTACACACAAAAAGTTA
EU741058.1
ACAGTGATGCTTGAACCCTCTCTTTCCAAGAAAATTCTCCTTTGATGTGTGTTTTTCAAT
ACAGTGATGCTTGAACCCTCTCTTTCCAAGAAAATTCTCCTTTGATGTGTGTTTTTCAAT
550
560
570
580
590
600

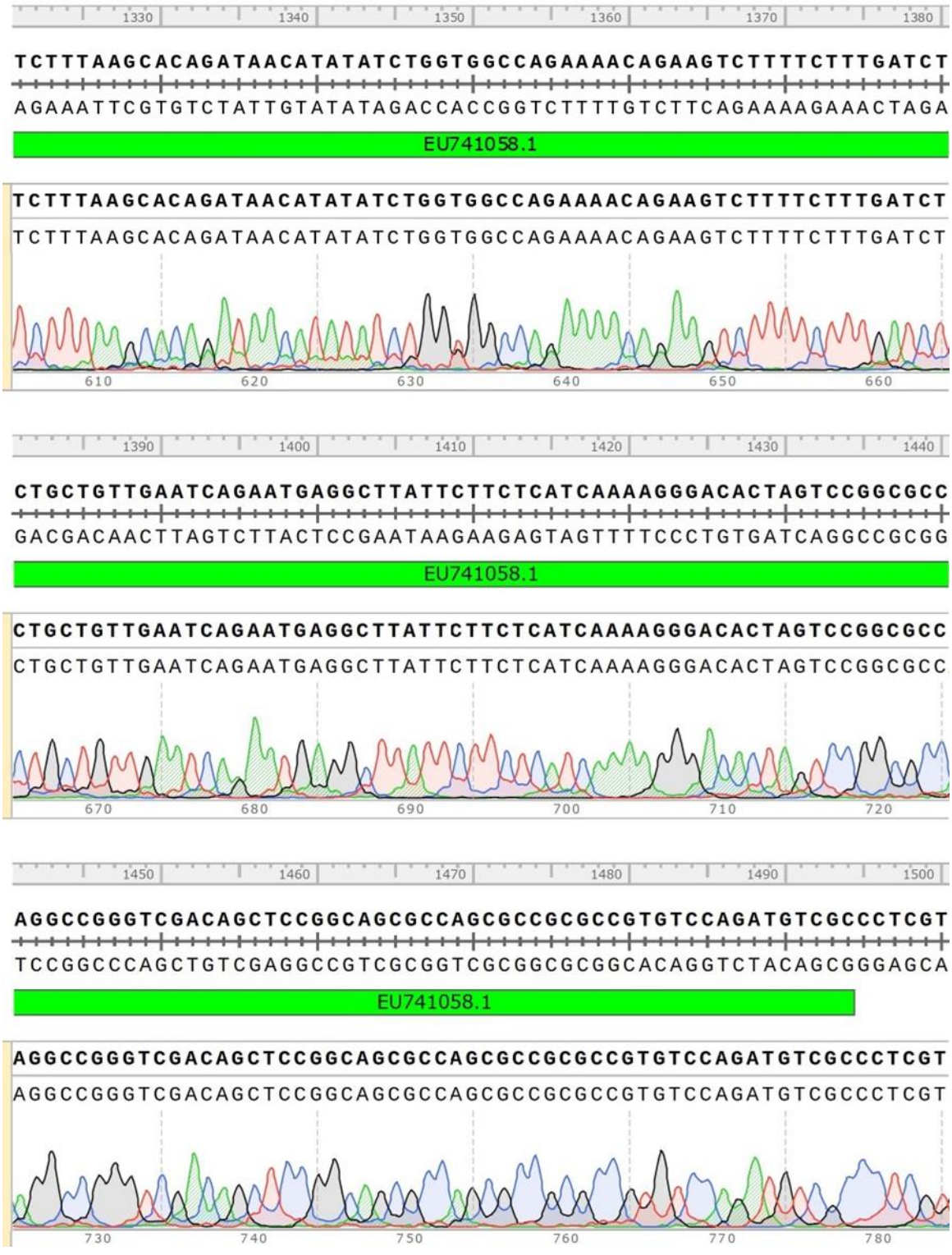
1330
1340
1350
1360
1370
1380
TCTTTAAGCACAGATAACATATATCTGGTGGCCAGAAAACAGAAGTCTTTTCTTTGATCT
AGAAATTCGTGTCTATTGTATATAGACCACCGGTCTTTTGTCTTCAGAAAAGAAACTAGA
EU741058.1
TCTTTAAGCACAGATAACATATATCTGGTGGCCAGAAAACAGAAGTCTTTTCTTTGATCT
TCTTTAAGCACAGATAACATATATCTGGTGGCCAGAAAACAGAAGTCTTTTCTTTGATCT
610
620
630
640
650
660
1390
1400
1410
1420
1430
1440
CTGCTGTTGAATCAGAATGAGGCTTATTCTTCTCATCAAAAGGGACACTAGTCCGGCGCC
GACGACAACTTAGTCTTACTCCGAATAAGAAGAGTAGTTTTCCCTGTGATCAGGCCGCGG
EU741058.1
CTGCTGTTGAATCAGAATGAGGCTTATTCTTCTCATCAAAAGGGACACTAGTCCGGCGCC
CTGCTGTTGAATCAGAATGAGGCTTATTCTTCTCATCAAAAGGGACACTAGTCCGGCGCC
670
680
690
700
710
720
1450
1460
1470
1480
1490
1500
AGGCCGGGTCGACAGCTCCGGCAGCGCCAGCGCCGCGCCGTGTCCAGATGTCGCCCTCGT
TCCGGCCCAGCTGTCGAGGCCGTCGCGGTCGCGGCGCGGCACAGGTCTACAGCGGGAGCA
EU741058.1
AGGCCGGGTCGACAGCTCCGGCAGCGCCAGCGCCGCGCCGTGTCCAGATGTCGCCCTCGT
AGGCCGGGTCGACAGCTCCGGCAGCGCCAGCGCCGCGCCGTGTCCAGATGTCGCCCTCGT
730
740
750
760
770
780

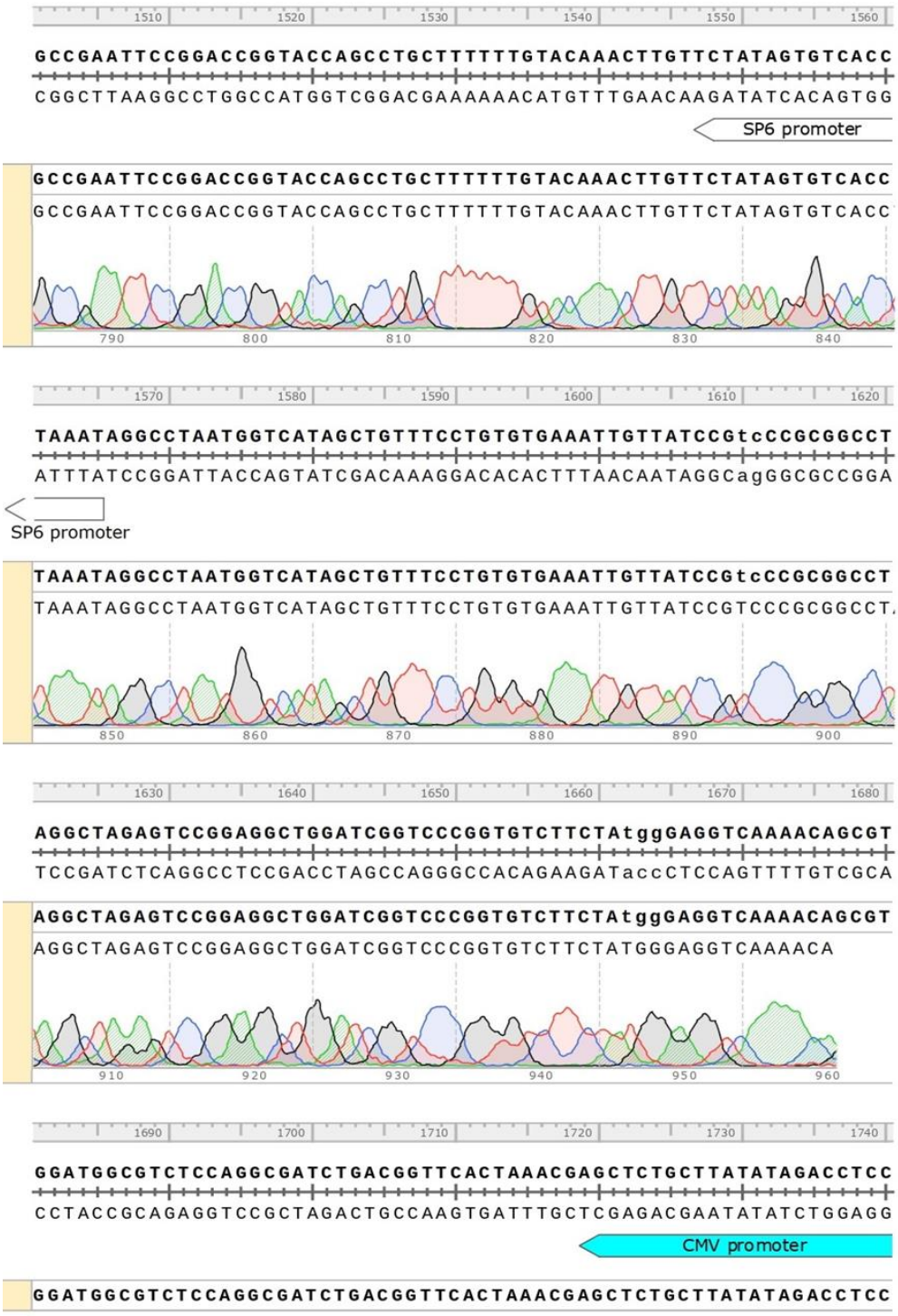
1510
1520
1530
1540
1550
1560
GCCGAATTCCGGACCGGTACCAGCCTGCTTTTTTGTACAAACTTGTTCTATAGTGTCACC
CGGCTTAAGGCCTGGCCATGGTCGGACGAAAAAACATGTTTGAACAAGATATCACAGTGG
SP6 promoter
GCCGAATTCCGGACCGGTACCAGCCTGCTTTTTTGTACAAACTTGTTCTATAGTGTCACC
GCCGAATTCCGGACCGGTACCAGCCTGCTTTTTTGTACAAACTTGTTCTATAGTGTCACC
790
800
810
820
830
840
1570
1580
1590
1600
1610
1620
TAAATAGGCCTAATGGTCATAGCTGTTTCCTGTGTGAAATTGTTATCCGtcCCGCGGCCT
ATTTATCCGGATTACCAGTATCGACAAAGGACACACTTTAACAATAGGCagGGCGCCGGA
SP6 promoter
TAAATAGGCCTAATGGTCATAGCTGTTTCCTGTGTGAAATTGTTATCCGtcCCGCGGCCT
TAAATAGGCCTAATGGTCATAGCTGTTTCCTGTGTGAAATTGTTATCCGTCCCGCGGCCT
850
860
870
880
890
900
1630
1640
1650
1660
1670
1680
AGGCTAGAGTCCGGAGGCTGGATCGGTCCCGGTGTCTTCTAtggGAGGTCAAAACAGCGT
TCCGATCTCAGGCCTCCGACCTAGCCAGGGCCACAGAAGATaccCTCCAGTTTTGTCGCA
AGGCTAGAGTCCGGAGGCTGGATCGGTCCCGGTGTCTTCTAtggGAGGTCAAAACAGCGT
AGGCTAGAGTCCGGAGGCTGGATCGGTCCCGGTGTCTTCTATGGGAGGTCAAAACA
910
920
930
940
950
960
1690
1700
1710
1720
1730
1740
GGATGGCGTCTCCAGGCGATCTGACGGTTCACTAAACGAGCTCTGCTTATATAGACCTCC
CCTACCGCAGAGGTCCGCTAGACTGCCAAGTGATTTGCTCGAGACGAATATATCTGGAGG
CMV promoter
GGATGGCGTCTCCAGGCGATCTGACGGTTCACTAAACGAGCTCTGCTTATATAGACCTCC

Map 9. pGL3 BRE Luciferase BMP4 Response Promotor Sequence-Map

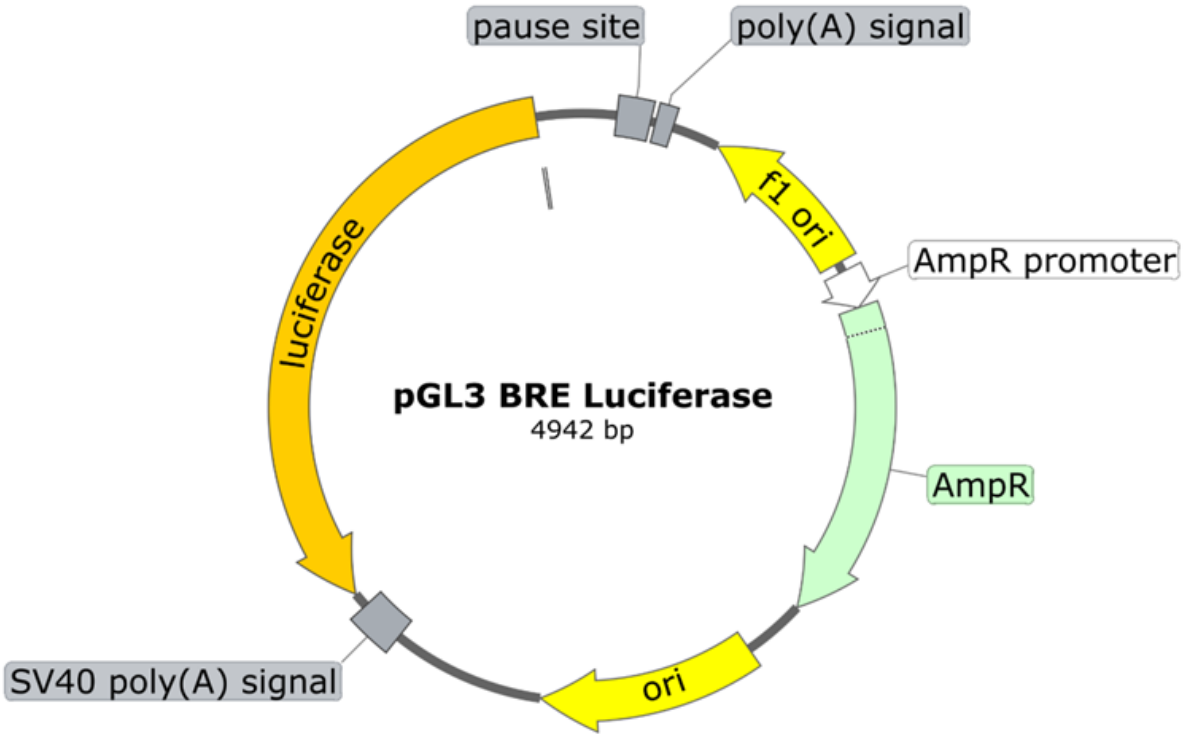

Map 10. pCAG BMP4 Expression plasmids

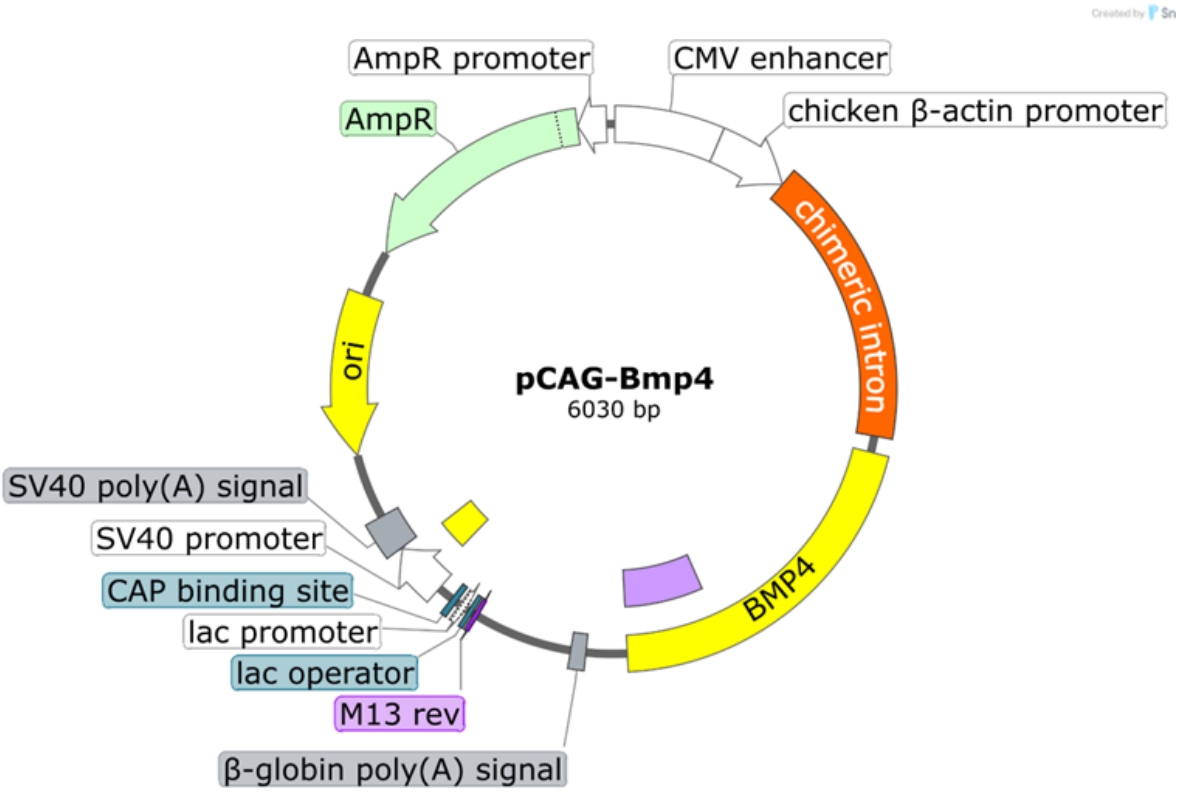

Map 11. pLenti-CMW- RFP-2A-Puro

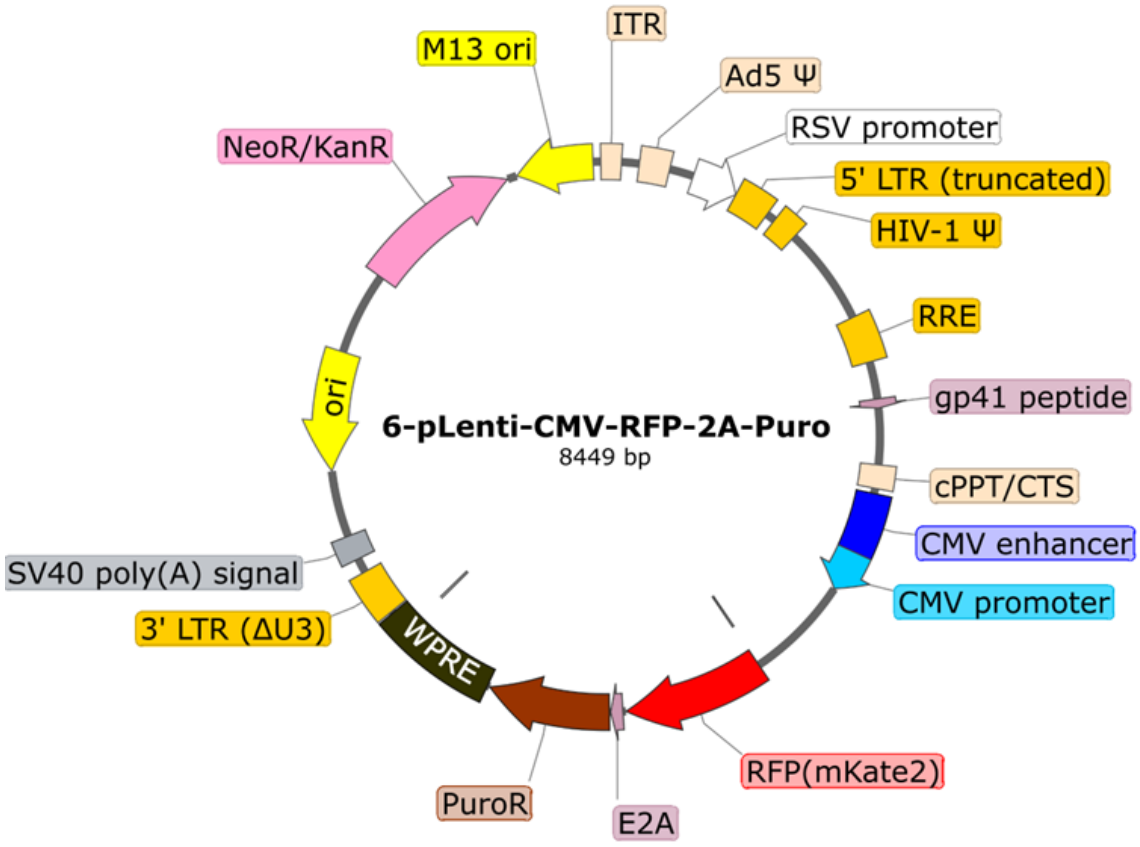

Map 12. pLenti-CMW-β-globin intron STATH-RFP-2A-Puro

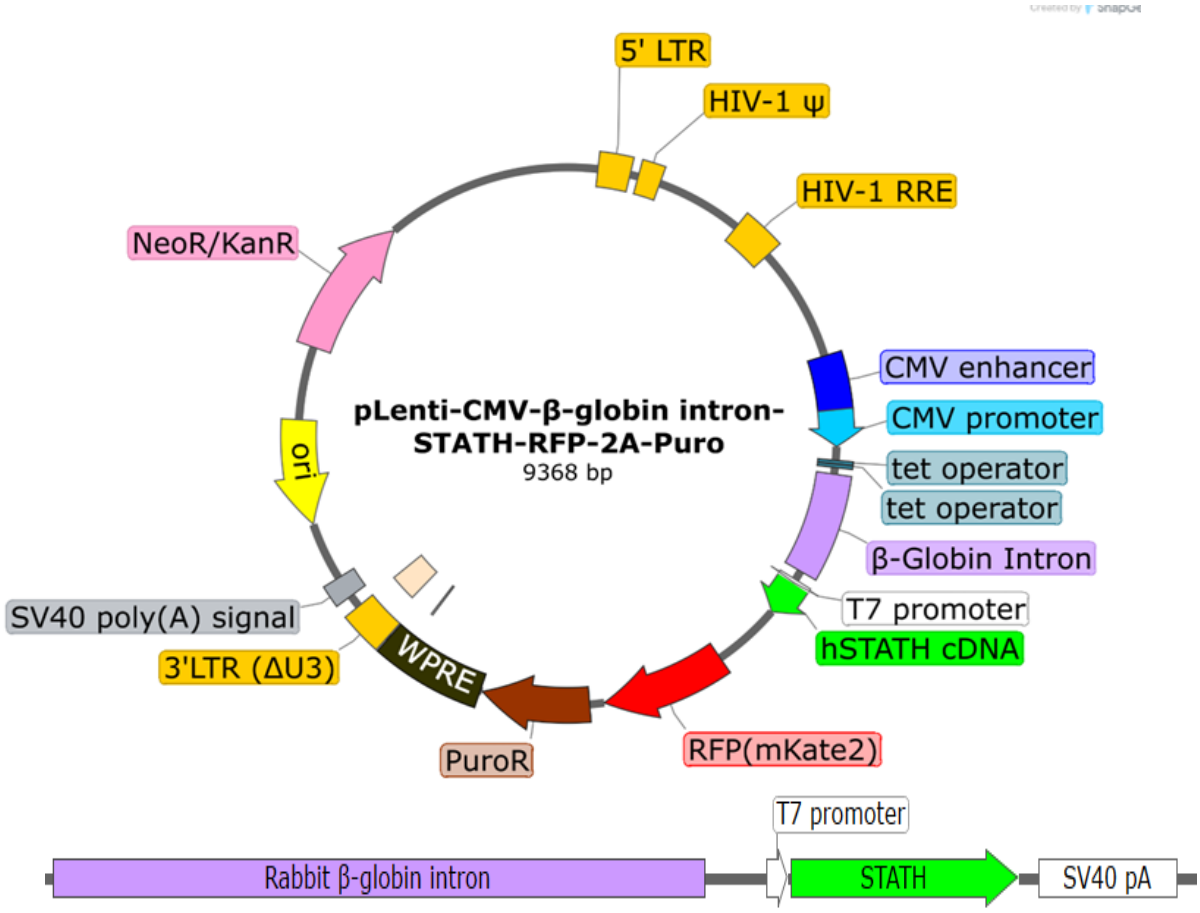

Release fragments of expression statherin elements from pXJ-40 and integration in lentiviral

Transgenic Mice Generation

Map 13. ROSA 26

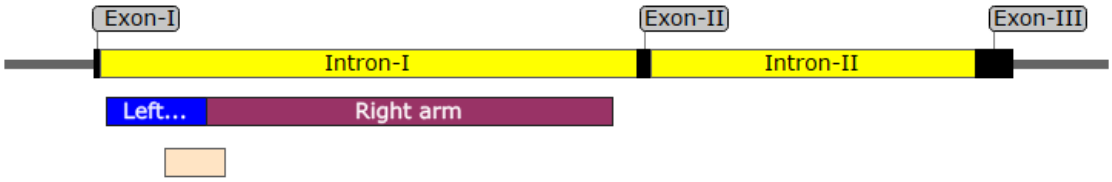

Map 14. Ai9 plasmid: Donor vector backbone for generation transgenic mice

Donor vector for generation transgenic mice design was based on Ai9 (Addgene #22799) (Madisen et al. Nat Neurosci. 13:133-40, 2010)

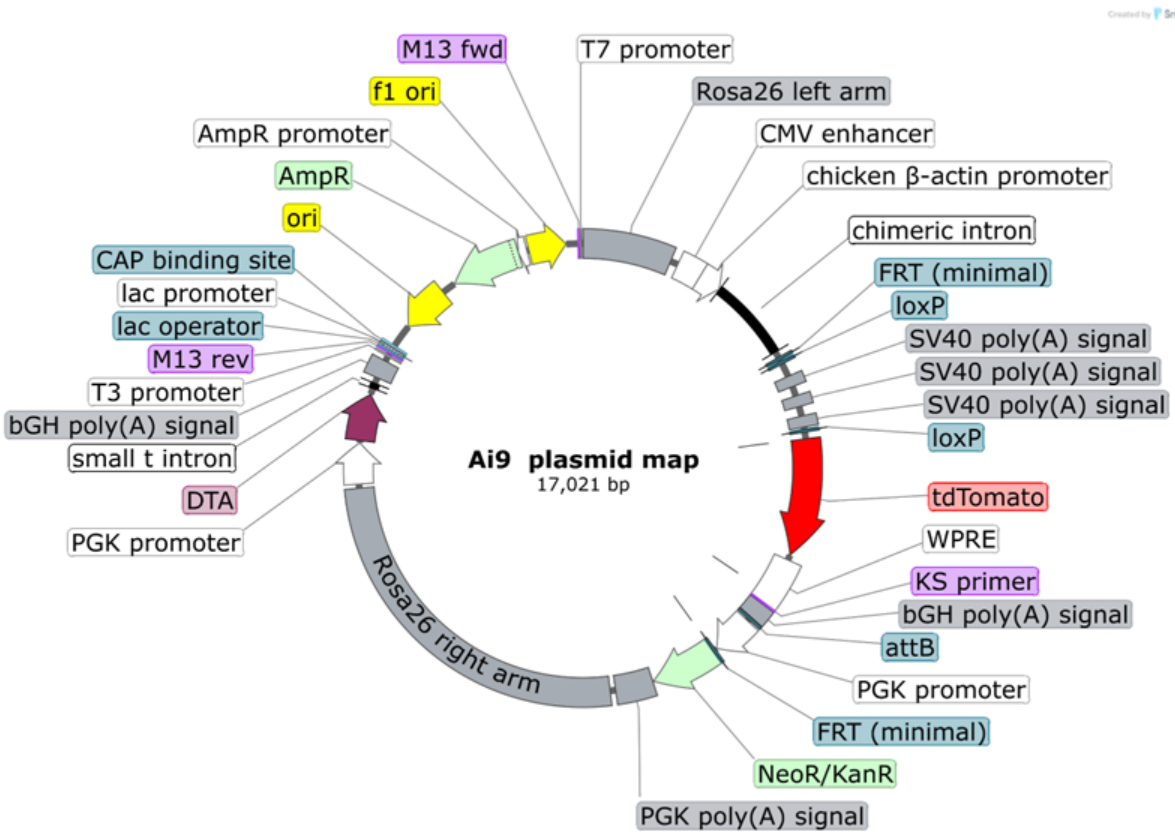

Map 15. Statherin Conditional Overexpression (cOE) donor vector

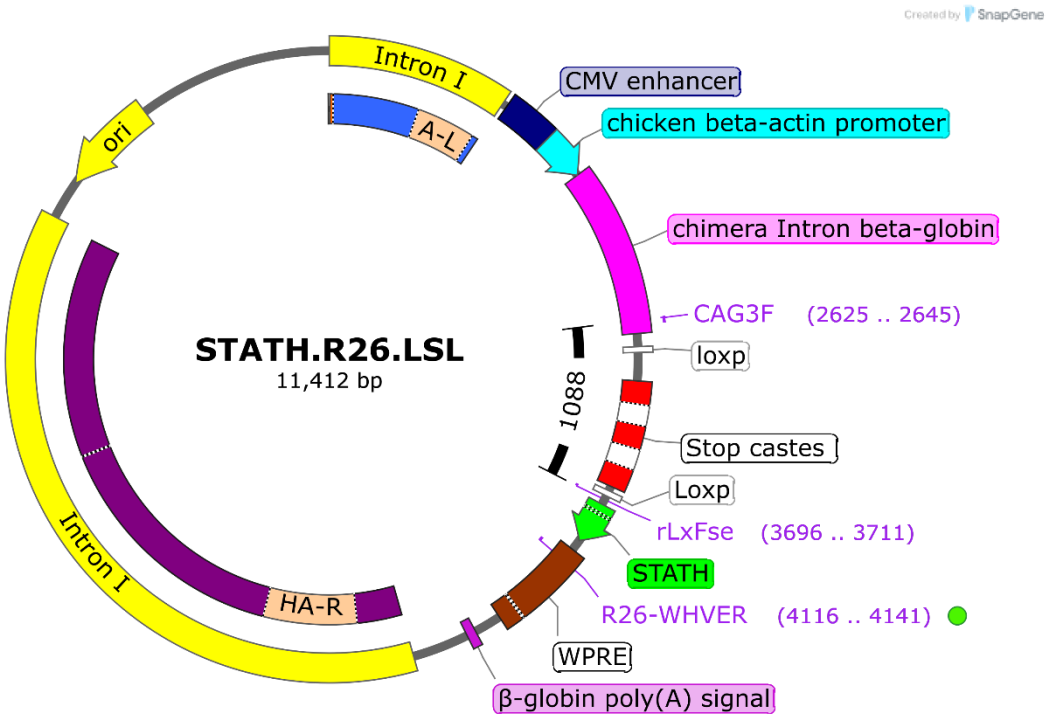

Map 16. Human STATH Transgenic mice cOE Stop flux

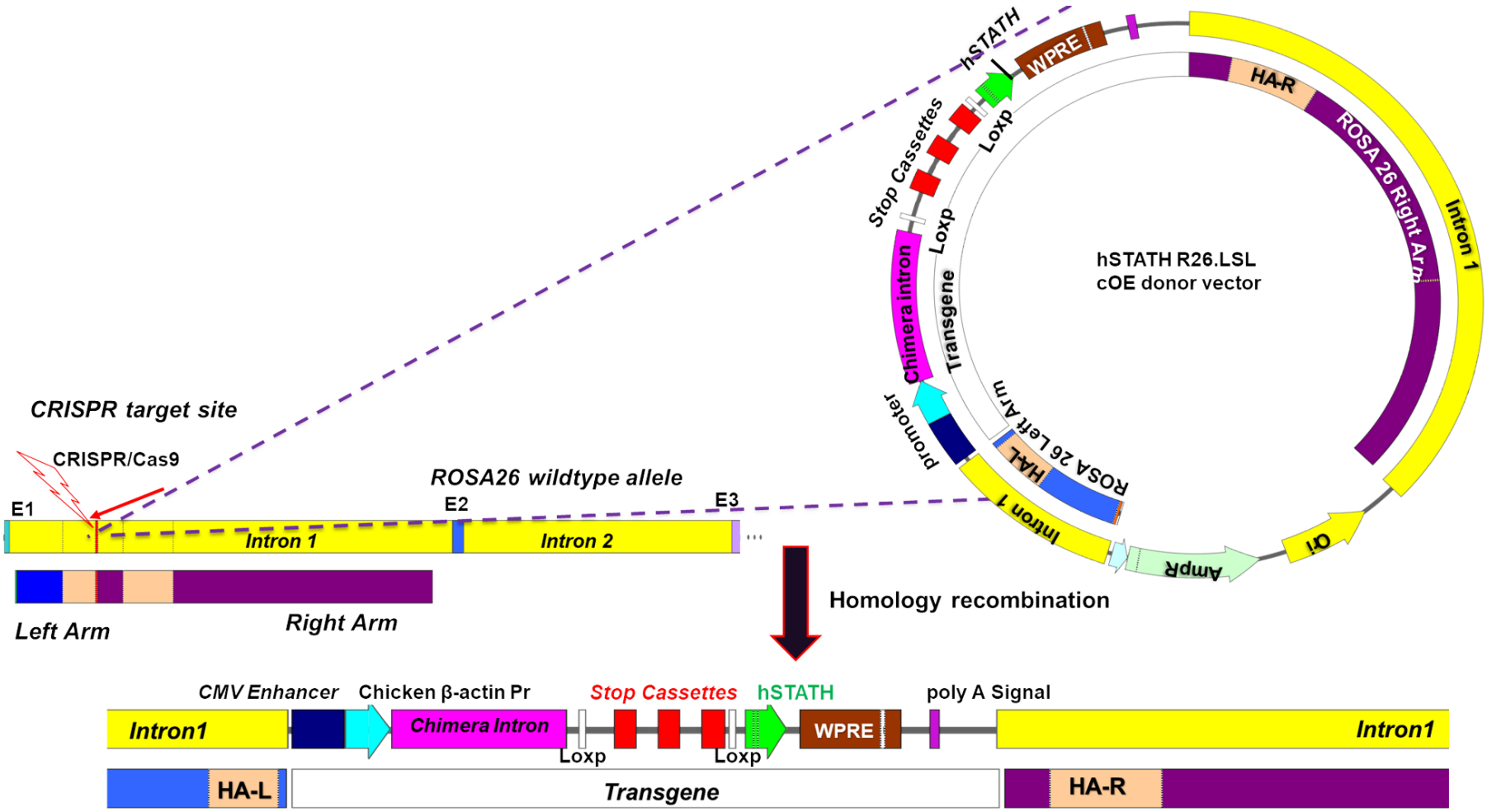

Map 17. Tissue-specific contain smooth muscle expression of human STATH Transgenic mice flux

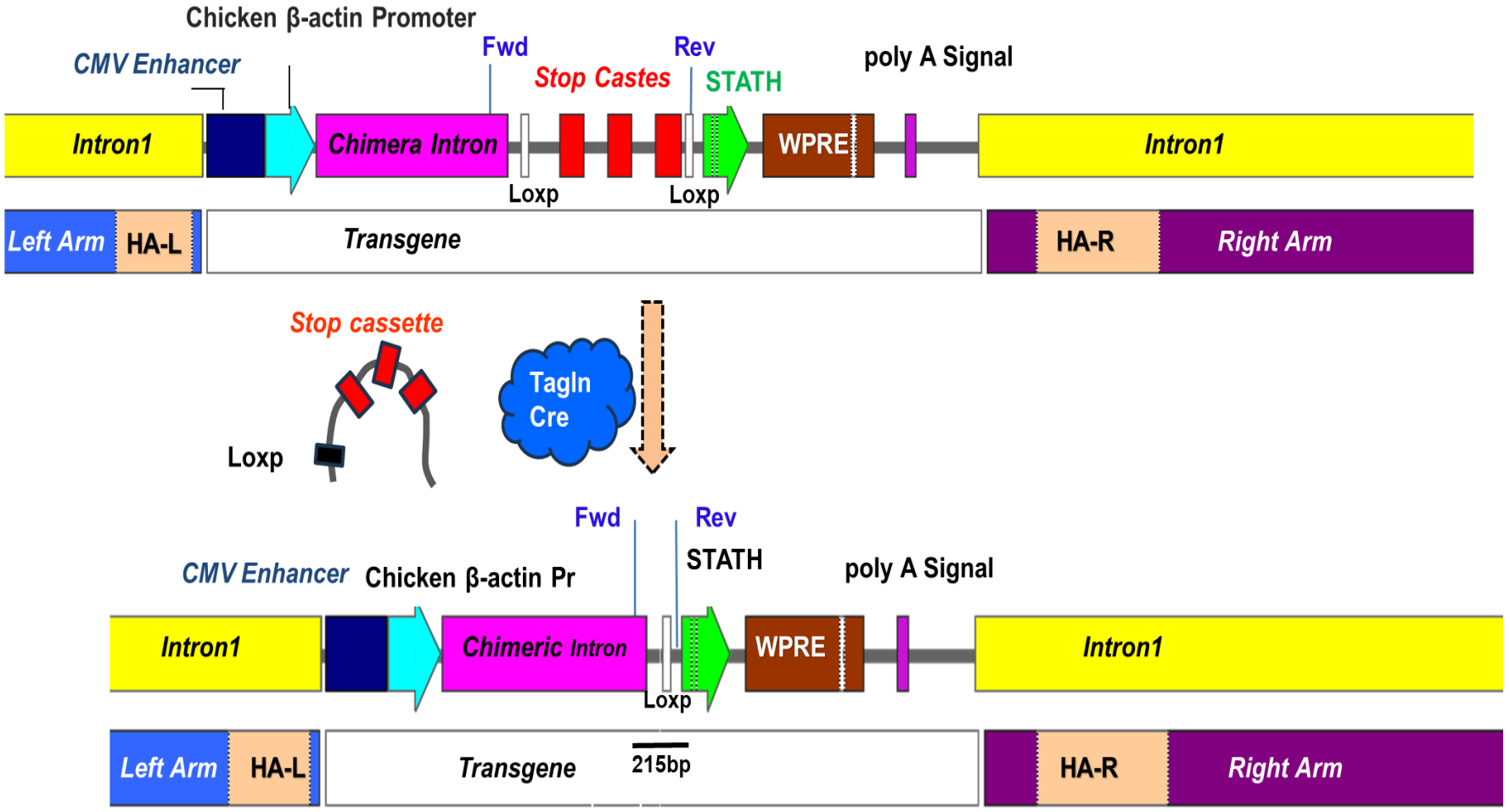

9. Appendix 3 Recombination assay: Sequencing Results of transgenic mice

1. Sequencing Results: Post-Cre Excision Analysis of Recombinant Region

Primers: CAG3F & rLxfse-1

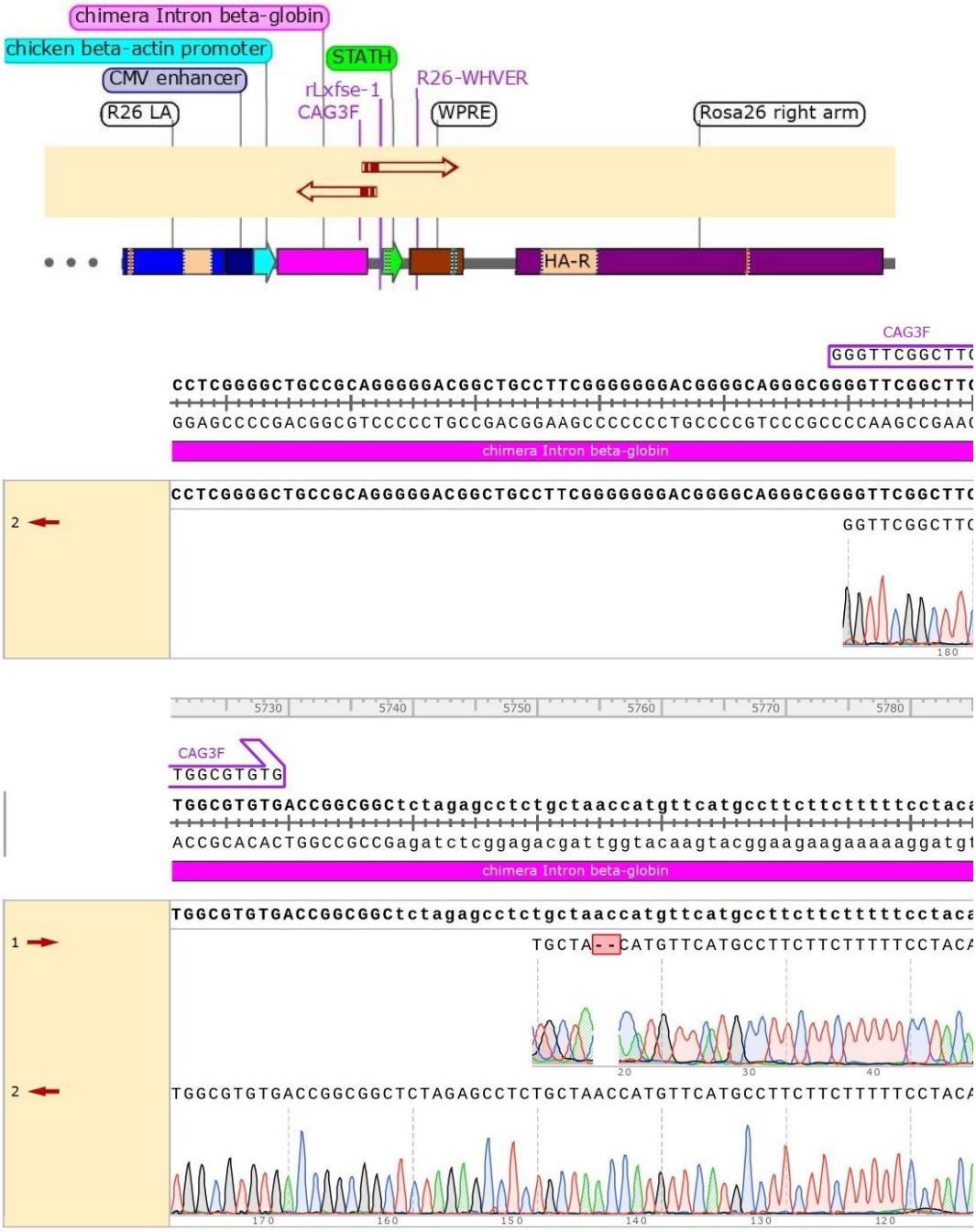

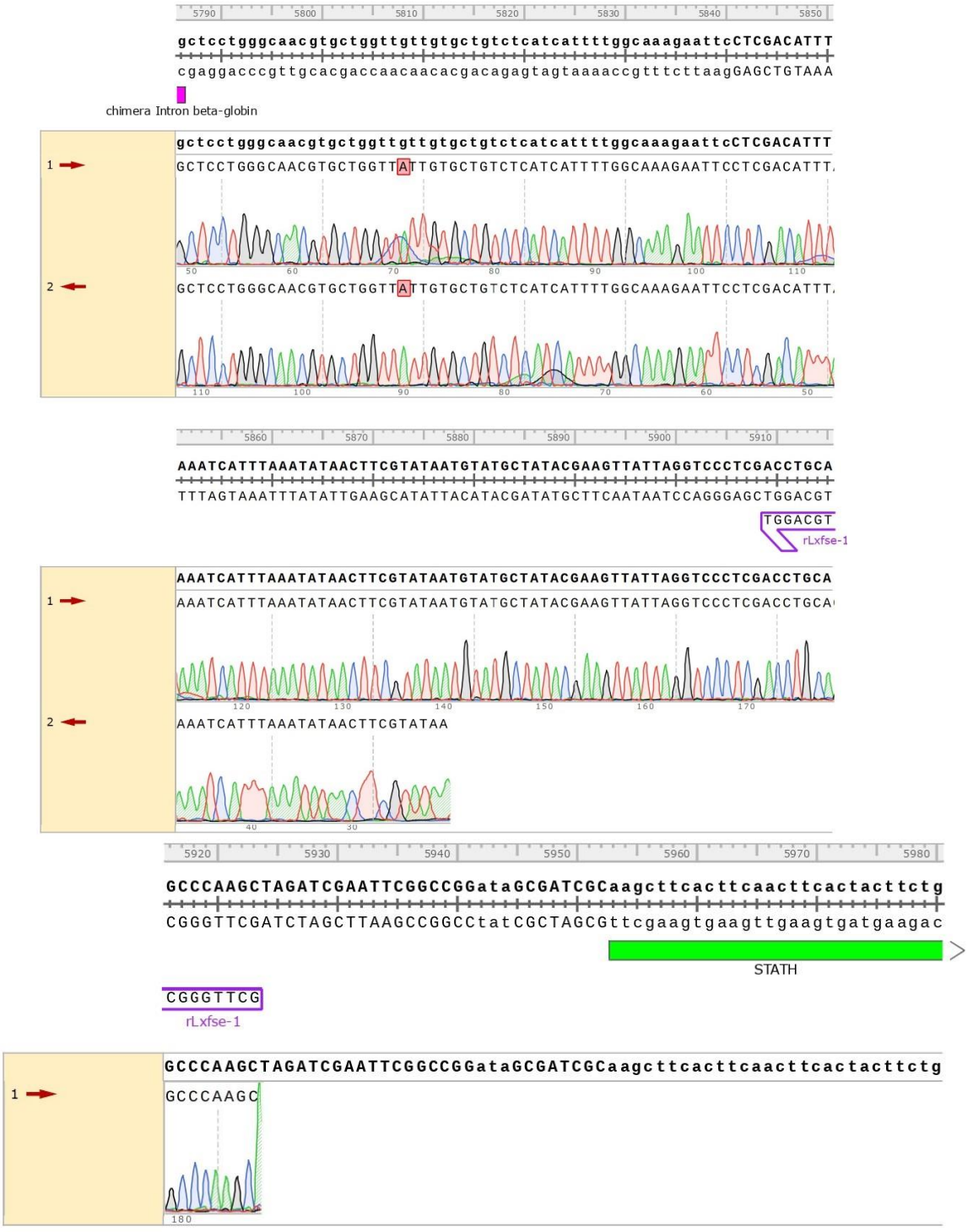
5790
5800
5810
5820
5830
5840
5850
gctcctgggcaacgtgctggttgttgtgctgtctcatcattttggcaaagaattcCTCGACATTT
cgaggacccgttgcacgaccaacaacacgacagagtagtaaaaccgtttcttaagGAGCTGTAAA
chimera Intron beta-globin
gctcctgggcaacgtgctggttgttgtgctgtctcatcattttggcaaagaattcCTCGACATTT
1
GCTCCTGGGCAACGTGCTGGTTATTGTGCTGTCTCATCATTTTGGCAAAGAATTCCTCGACATTT
50
60
70
80
90
100
110
2
GCTCCTGGGCAACGTGCTGGTTATTGTGCTGTCTCATCATTTTGGCAAAGAATTCCTCGACATTT
110
100
90
80
70
60
50
5860
5870
5880
5890
5900
5910
AAATCATTTAAATATAACTTCGTATAATGTATGCTATACGAAGTTATTAGGTCCCTCGACCTGCA
TTTAGTAAATTTATATTGAAGCATATTACATACGATATGCTTCAATAATCCAGGGAGCTGGACGT
TGGACGT
rLxfse-1
AAATCATTTAAATATAACTTCGTATAATGTATGCTATACGAAGTTATTAGGTCCCTCGACCTGCA
1
AAATCATTTAAATATAACTTCGTATAATGTATGCTATACGAAGTTATTAGGTCCCTCGACCTGCA
120
130
140
150
160
170
2
AAATCATTTAAATATAACTTCGTATAA
40
30
5920
5930
5940
5950
5960
5970
5980
GCCCAAGCTAGATCGAATTCGGCCGGataGCGATCGCaagcttcacttcaacttcactacttctg
CGGGTTCGATCTAGCTTAAGCCGGCCtatCGCTAGCGttcgaagtgaagttgaagtgatgaagac
STATH
CGGGTTCG
rLxfse-1
GCCCAAGCTAGATCGAATTCGGCCGGataGCGATCGCaagcttcacttcaacttcactacttctg
1
GCCCAAGC
180

2. Sequencing Results: CAG Promoter to Statherin Terminus Post-Cre Excision

Primers: CAG3F & STATH-R (R-26 WPRE)

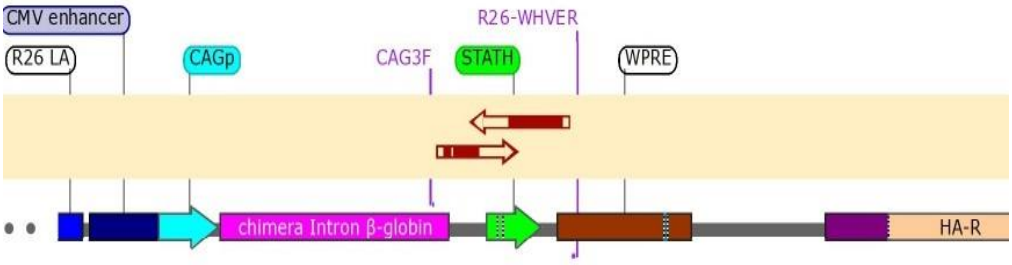

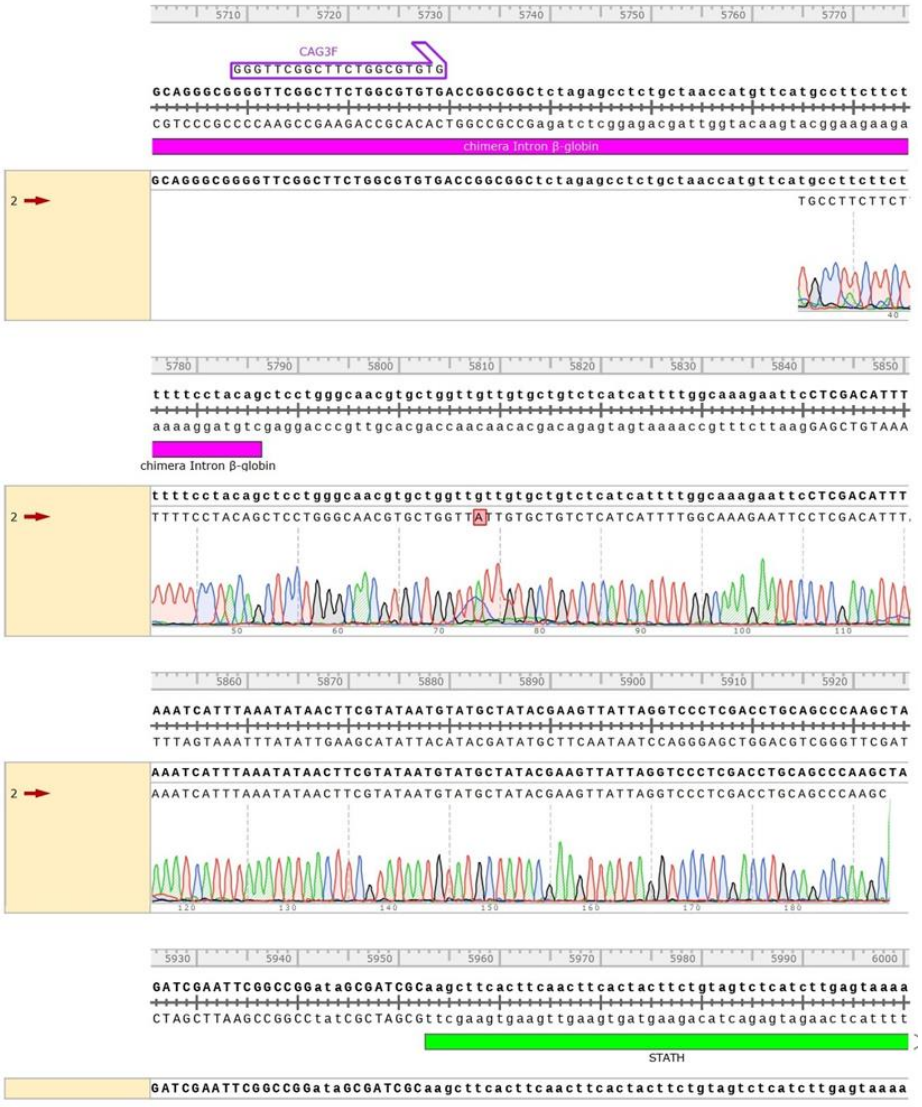

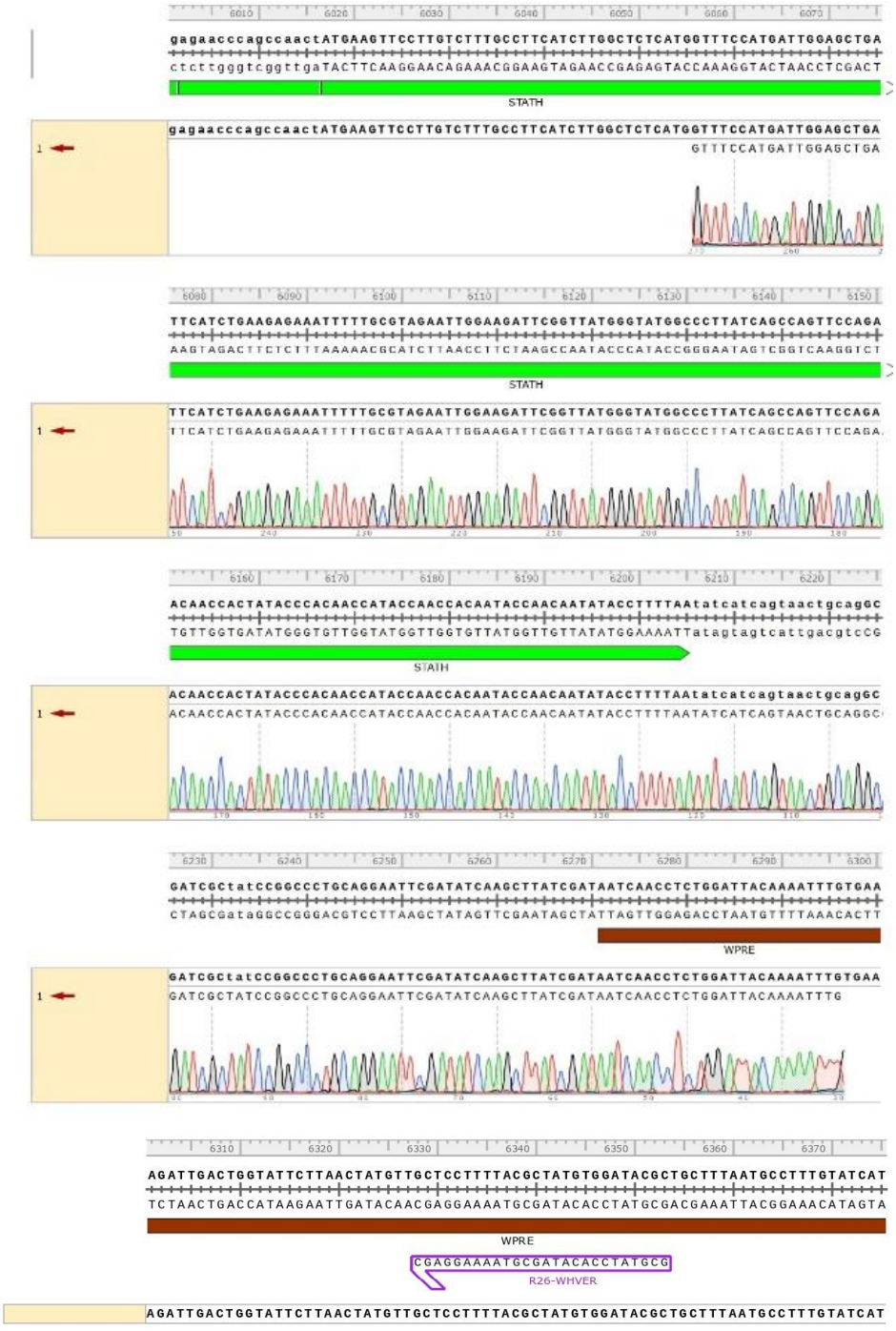
6010
6020
6030
6040
6050
6060
6070
gagaacccagccaactATGAAGTTCCTTGTCTTTGCCTTCATCTTGGCTCTCATGGTTTCCATGATTGGAGCTGA
ctcttgggtcggttgaTACTTCAAGGAACAGAAACGGAAGTAGAACCGAGAGTACCAAAGGTACTAACCTCGACT
STATH
gagaacccagccaactATGAAGTTCCTTGTCTTTGCCTTCATCTTGGCTCTCATGGTTTCCATGATTGGAGCTGA
GTTTCCATGATTGGAGCTGA
1
6080
6090
6100
6110
6120
6130
6140
6150
TTCATCTGAAGAGAAATTTTTGCGTAGAATTGGAAGATTCGGTTATGGGTATGGCCCTTATCAGCCAGTTCCAGA
AAGTAGACTTCTCTTTAAAAACGCATCTTAACCTTCTAAGCCAATACCCATACCGGGAATAGTCGGTCAAGGTCT
STATH
TTCATCTGAAGAGAAATTTTTGCGTAGAATTGGAAGATTCGGTTATGGGTATGGCCCTTATCAGCCAGTTCCAGA
TTCATCTGAAGAGAAATTTTTGCGTAGAATTGGAAGATTCGGTTATGGGTATGGCCCTTATCAGCCAGTTCCAGA
1
6160
6170
6180
6190
6200
6210
6220
ACAACCACTATACCCACAACCATACCAACCACAATACCAACAATATACCTTTTAATatcatcagtaactgcagGC
TGTTGGTGATATGGGTGTTGGTATGGTTGGTGTTATGGTTGTTATATGGAAAATTatagtagtcattgacgtcCG
STATH
ACAACCACTATACCCACAACCATACCAACCACAATACCAACAATATACCTTTTAATatcatcagtaactgcagGC
ACAACCACTATACCCACAACCATACCAACCACAATACCAACAATATACCTTTTAATATCATCAGTAACTGCAGGC
1
6230
6240
6250
6260
6270
6280
6290
6300
GATCGCtatCCGGCCCTGCAGGAATTCGATATCAAGCTTATCGATAATCAACCTCTGGATTACAAAATTTGTGAA
CTAGCGataGGCCGGGACGTCCTTAAGCTATAGTTCGAATAGCTATTAGTTGGAGACCTAATGTTTTAAACACTT
WPRE
GATCGCtatCCGGCCCTGCAGGAATTCGATATCAAGCTTATCGATAATCAACCTCTGGATTACAAAATTTGTGAA
GATCGCTATCCGGCCCTGCAGGAATTCGATATCAAGCTTATCGATAATCAACCTCTGGATTACAAAATTTG
1
6310
6320
6330
6340
6350
6360
6370
AGATTGACTGGTATTCTTAACTATGTTGCTCCTTTTACGCTATGTGGATACGCTGCTTTAATGCCTTTGTATCAT
TCTAACTGACCATAAGAATTGATACAACGAGGAAAATGCGATACACCTATGCGACGAAATTACGGAAACATAGTA
WPRE
CGAGGAAAATGCGATACACCTATGCG
R26-WHVER
AGATTGACTGGTATTCTTAACTATGTTGCTCCTTTTACGCTATGTGGATACGCTGCTTTAATGCCTTTGTATCAT

3. Sequencing Results: STATH- lox-stop-lox (LSL)

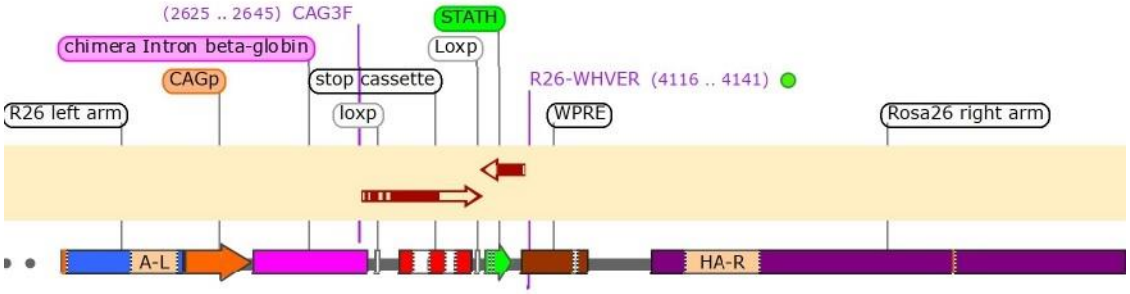

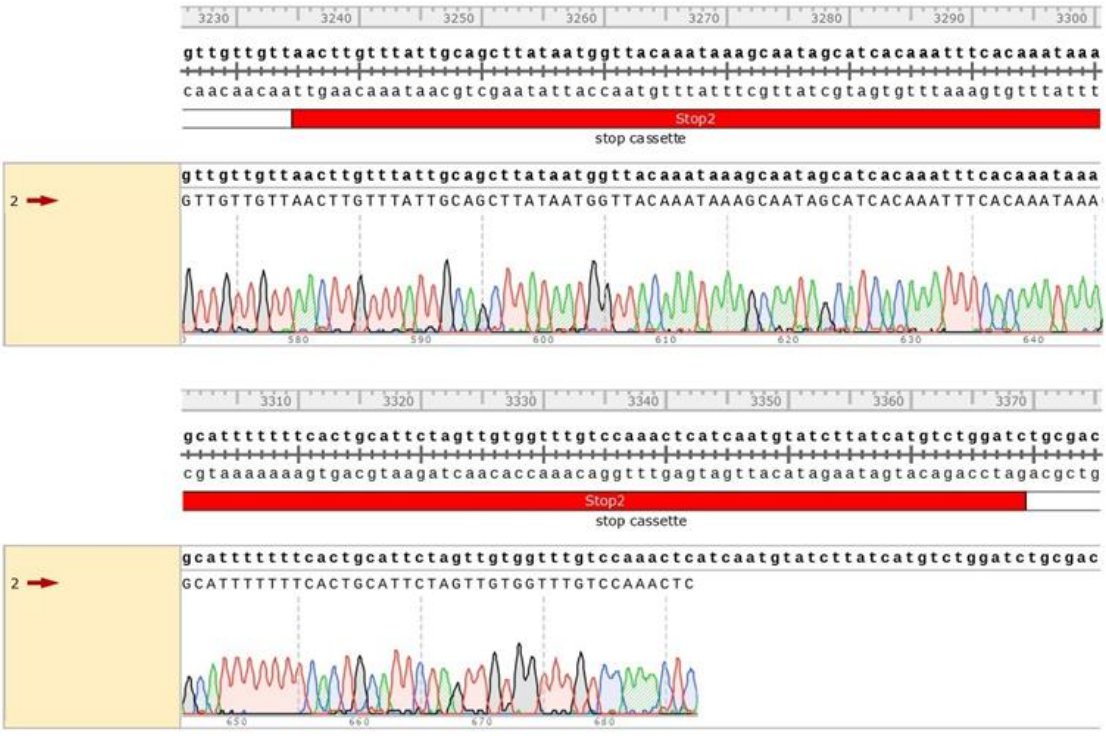

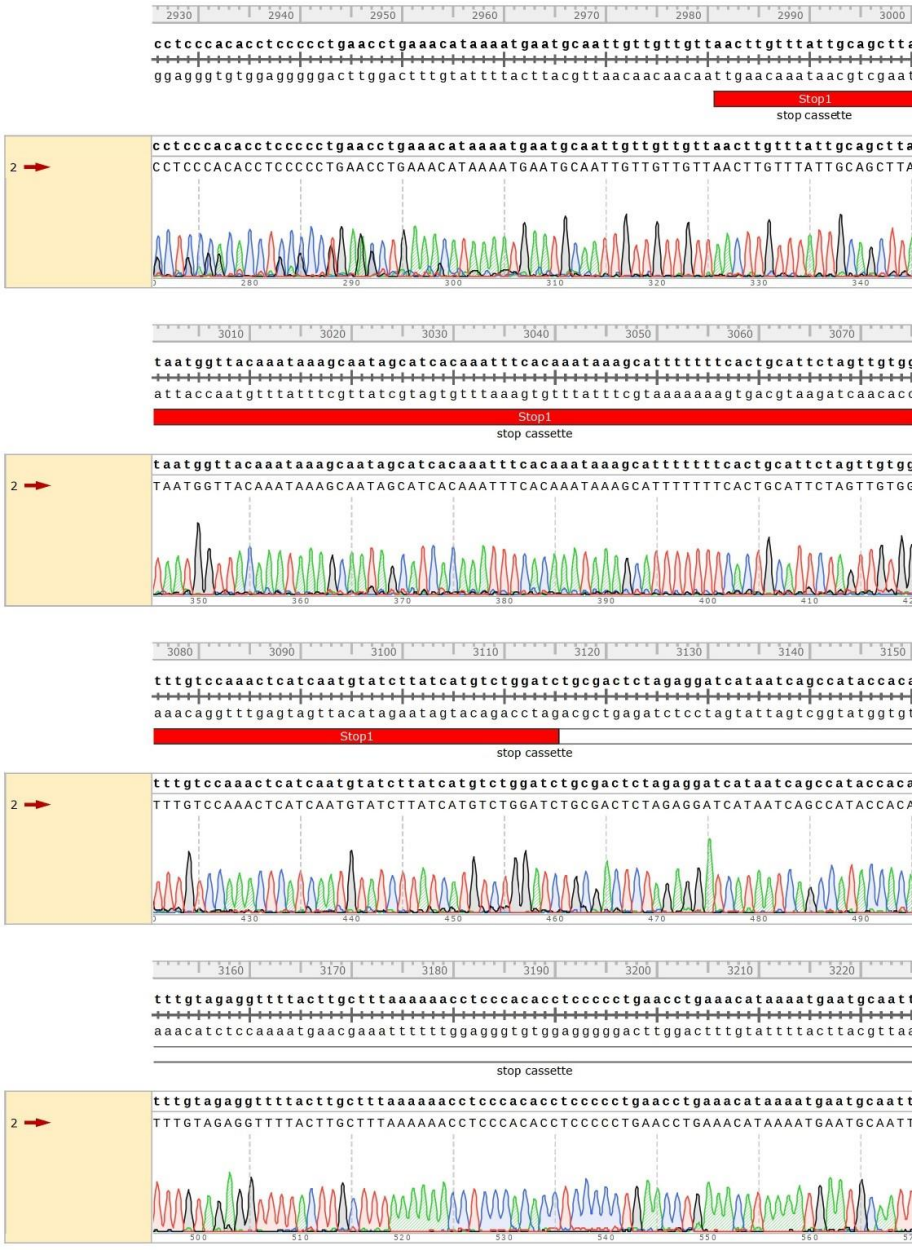
Stop1
stop cassette
2
Stop1
stop cassette
2
Stop1
stop cassette
2
stop cassette
2

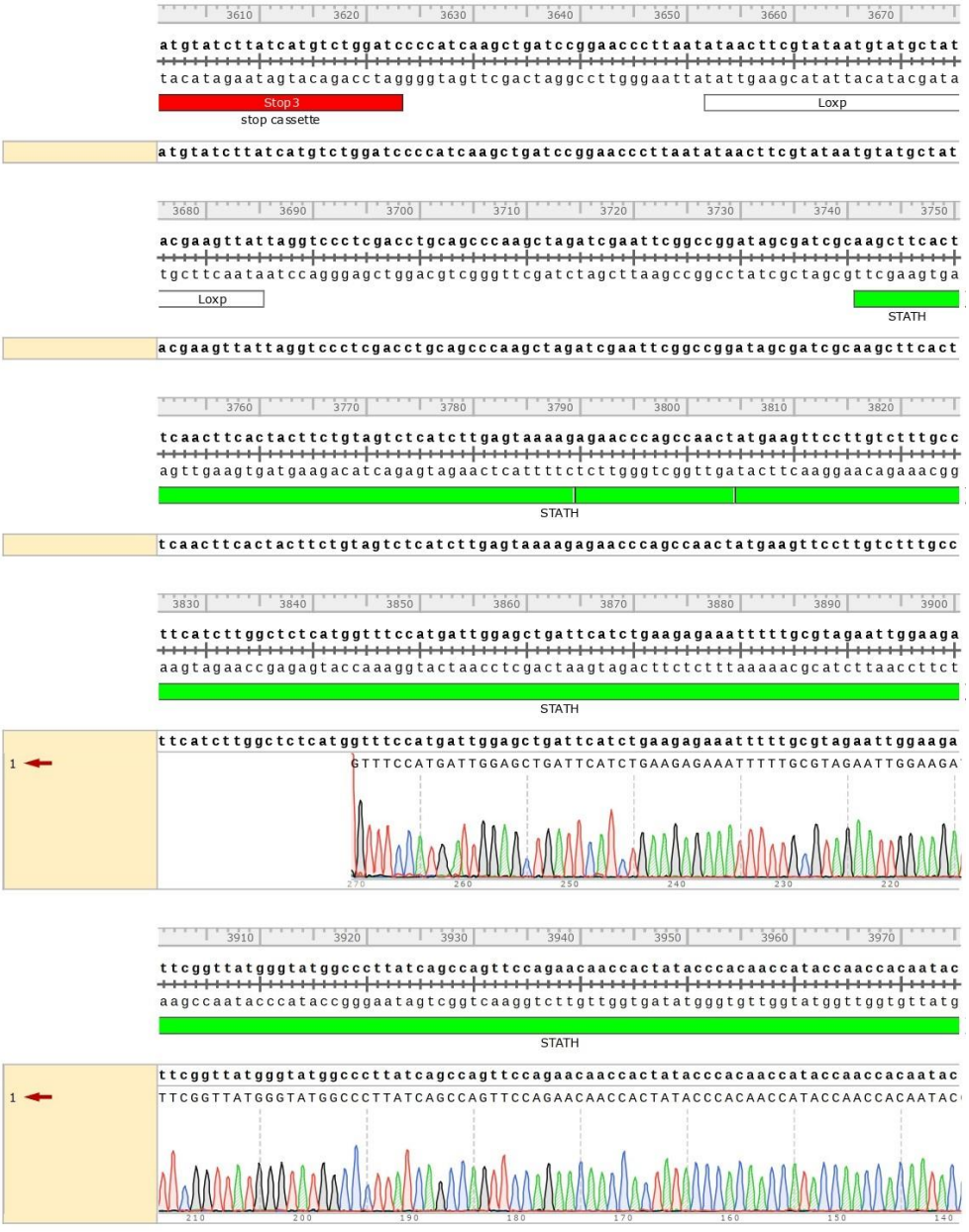
3610
3620
3630
3640
3650
3660
3670
atgtatcttatcatgtctggatccccatcaagctgatccggaacccttaatataacttcgtataatgtatgctat
tacatagaatagtacagacctaggggtagttcgactaggccttgggaattatattgaagcatattacatacgata
Stop 3
stop cassette
Loxp
atgtatcttatcatgtctggatccccatcaagctgatccggaacccttaatataacttcgtataatgtatgctat
3680
3690
3700
3710
3720
3730
3740
3750
acgaagttattaggtccctcgacctgcagcccaagctagatcgaattcggccggatagcgatcgcaagcttcact
tgcttcaataatccagggagctggacgtcgggttcgatctagcttaagccggcctatcgctagcgttcgaagtga
Loxp
STATH
acgaagttattaggtccctcgacctgcagcccaagctagatcgaattcggccggatagcgatcgcaagcttcact
3760
3770
3780
3790
3800
3810
3820
tcaacttcactacttctgtagtctcatcttgagtaaaagagaacccagccaactatgaagttccttgtctttgcc
agttgaagtgatgaagacatcagagtagaactcattttctcttgggtcggttgatacttcaaggaacagaaacgg
STATH
tcaacttcactacttctgtagtctcatcttgagtaaaagagaacccagccaactatgaagttccttgtctttgcc
3830
3840
3850
3860
3870
3880
3890
3900
ttcatcttggctctcatggtttccatgattggagctgattcatctgaagagaaatttttgcgtagaattggaaga
aagtagaaccgagagtaccaaaggtactaacctcgactaagtagacttctctttaaaaacgcatcttaaccttct
STATH
ttcatcttggctctcatggtttccatgattggagctgattcatctgaagagaaatttttgcgtagaattggaaga
1
GTTTCCATGATTGGAGCTGATTCATCTGAAGAGAAATTTTTGCGTAGAATTGGAAGA
270
260
250
240
230
220
3910
3920
3930
3940
3950
3960
3970
ttcggttatgggtatggcccttatcagccagttccagaacaaccactatacccacaaccataccaaccacaatac
aagccaatacccataccgggaatagtcggtcaaggtcttgttggtgatatgggtgttggtatggttggtgttatg
STATH
ttcggttatgggtatggcccttatcagccagttccagaacaaccactatacccacaaccataccaaccacaatac
1
TTCGGTTATGGGTATGGCCCTTATCAGCCAGTTCCAGAACAACCACTATACCCACAACCATACCAACCACAATAC
210
200
190
180
170
160
150
140

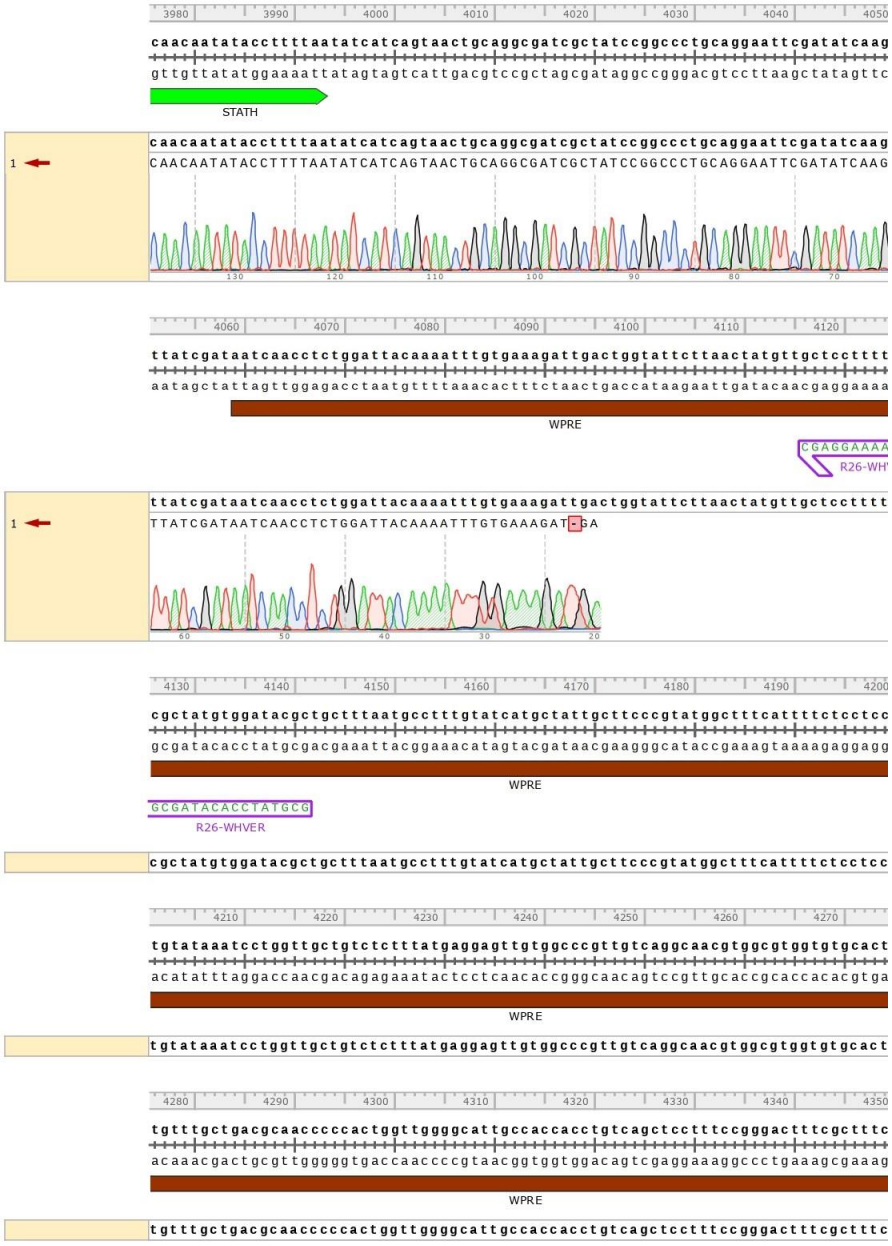
3980
3990
4000
4010
4020
4030
4040
4050
caacaatatacctttaatatcatcagtaactgcaggcgatcgctatccggccctgcaggaattcgatatcaag
gttgttatatggaaaattatagtagtcattgacgtccgctagcgataggccgggacgtccttaagctatagttc
STATH
1
caacaatatacctttaatatcatcagtaactgcaggcgatcgctatccggccctgcaggaattcgatatcaag
CAACAATATACCTTTTAATATCATCAGTAACTGCAGGCGATCGCTATCCGGCCCTGCAGGAATTCGATATCAAG
130
120
110
100
90
80
70
4060
4070
4080
4090
4100
4110
4120
ttatcgataatcaacctctggattacaaaatttgtgaaagattgactggtattcttaactatgttgctccttttt
aatagctattagttggagacctaatgttttaaacactttctaactgaccataagaattgatacaacgaggaaaa
WPRE
CGAGGAAAA
R26-WH
1
ttatcgataatcaacctctggattacaaaatttgtgaaagattgactggtattcttaactatgttgctccttttt
TTATCGATAATCAACCTCTGGATTACAAAATTTGTGAAAGAT-GA
60
50
40
30
20
4130
4140
4150
4160
4170
4180
4190
4200
cgctatgtggatacgctgctttaatgccttttgtatcatgctattgcttcccgtatggctttcattttctcctcc
gcgatacacctatgcgacgaaattacggaaacatagtacgataacgaagggcataccgaaagtaaaagaggagg
WPRE
GCGATACACCTATGCG
R26-WHVER
cgctatgtggatacgctgctttaatgccttttgtatcatgctattgcttcccgtatggctttcattttctcctcc
4210
4220
4230
4240
4250
4260
4270
tgtataaatcctggttgctgtctctttatgaggagttgtggcccgttgtcaggcaacgtggcgtggtgtgcact
acatatttaggaccaacgacagagaaatactcctcaacaccgggcaacagtccgttgcaccgcaccacacgtga
WPRE
tgtataaatcctggttgctgtctctttatgaggagttgtggcccgttgtcaggcaacgtggcgtggtgtgcact
4280
4290
4300
4310
4320
4330
4340
4350
tgtttgctgacgcaacccccactggttggggcattgccaccacctgtcagctcctttccgggactttcgctttc
acaaacgactgcgttgggggtgaccaaccccgtaacggtggtggacagtcgaggaaaggccctgaaagcgaaag
WPRE
tgtttgctgacgcaacccccactggttggggcattgccaccacctgtcagctcctttccgggactttcgctttc

10. Appendix 4: Microarray Results

10.1. List of differentially expressed genes by 9p21.3 genotype in primary human aortic smooth muscle cell

	HR Avg ± SD	HET Avg ± SD	HNR Avg ± SD	HR/HNR	BH	Gene Symbol
Rank	(n=4)	(n=4)	(n=3)			
1	**6.5 ± 0.999**	**260 ± 319**	**176 ± 49.6**	**0.0369**	**1.000E-11**	**STATH**
2	5.5 ± 0.443	6.67 ± 2.43	53.7 ± 23.4	0.102	6.007E-10	EYA4
3	16.4 ± 6.13	95.5 ± 71.2	185 ± 112	0.0886	1.833E-07	MAB21L1
4	43.5 ± 12.4	728 ± 914	382 ± 196	0.114	1.833E-07	PENK
5	15.4 ± 10	261 ± 279	261 ± 128	0.059	6.465E-07	IL13RA2
6	13.4 ± 4.03	31.9 ± 26.1	62.7 ± 10.9	0.214	6.750E-07	HTR2A
7	11.8 ± 3.6	48.9 ± 17.7	50.7 ± 3.77	0.233	8.454E-07	CHRNA5
8	44 ± 19.3	190 ± 114	350 ± 170	0.126	1.628E-05	FERMT1
9	30.2 ± 9.99	80.2 ± 103	135 ± 38.4	0.224	1.628E-05	CPE
10	10.7 ± 2.74	21 ± 17.4	37.3 ± 10.3	0.287	4.465E-05	NR5A2
11	11.3 ± 2.66	24 ± 12.2	33.3 ± 4.36	0.339	4.465E-05	CCDC68
12	16.4 ± 6.81	51.4 ± 19	62.8 ± 12.7	0.261	4.465E-05	ZNF724P
13	242 ± 108	104 ± 81	33.8 ± 11.3	7.16	6.181E-05	BAMBI
14	18.5 ± 2.49	52.6 ± 19	52.7 ± 13.2	0.351	6.181E-05	KIF15
15	74.2 ± 51.7	302 ± 368	521 ± 267	0.142	8.714E-05	PSG4
16	23.4 ± 4.97	52.7 ± 7.25	63.3 ± 3.5	0.37	8.714E-05	MTBP
17	9.51 ± 0.89	17.5 ± 2.56	22.4 ± 2.98	0.425	8.714E-05	FANCB
18	33.7 ± 16.1	74.5 ± 27.8	151 ± 26.2	0.223	1.081E-04	STEAP1B
19	14 ± 2.64	16.5 ± 8.18	38.8 ± 5.74	0.361	1.149E-04	ATL1
20	54.9 ± 11.7	185 ± 45	170 ± 32.4	0.323	1.743E-04	SKA3
21	37.3 ± 4.26	109 ± 80.7	98.8 ± 9.82	0.378	3.892E-04	SKAP2
22	117 ± 34.3	445 ± 145	422 ± 54.2	0.277	5.005E-04	RGS2
23	12.3 ± 5.84	34.2 ± 17	42.7 ± 12.6	0.288	5.005E-04	HOXA2
24	16.1 ± 3.82	42.2 ± 7.96	44.9 ± 6.81	0.359	5.965E-04	C18orf54
25	131 ± 30.2	82.2 ± 75.1	46.1 ± 3.09	2.84	6.312E-04	MYO1D
26	25.7 ± 3.31	51.3 ± 16	66.9 ± 0.981	0.384	7.698E-04	TMC7
27	21 ± 8.79	43.2 ± 15.7	65.1 ± 9.69	0.323	0.00107	KCNK1
28	35.2 ± 16.9	112 ± 30.7	114 ± 14	0.309	0.00107	CLSPN

29	115 ± 11.6	226 ± 104	316 ± 56.1	0.364	0.00107	CTSK
30	68.8 ± 34.1	27 ± 18.6	11.6 ± 3.37	5.93	0.00107	TRPC4
31	50.2 ± 10.1	142 ± 35.6	133 ± 23.5	0.377	0.00107	TTK
32	30.2 ± 12.3	72.5 ± 38.9	87 ± 10.5	0.347	0.00112	ABCC9
33	48.1 ± 12.3	69.3 ± 21.8	128 ± 22.3	0.376	0.00112	B4GALNT1
34	27.3 ± 9.36	76.1 ± 14.7	75.1 ± 3.53	0.364	0.00114	C11orf82
35	67.2 ± 41.2	119 ± 59.4	255 ± 10.8	0.264	0.00126	CPXM2
36	16.5 ± 2.6	37.3 ± 9.08	39 ± 1.99	0.423	0.00126	MTFR2
37	76.1 ± 44.1	25.1 ± 9.96	14.7 ± 0.631	5.18	0.00127	FAM69A
38	24.7 ± 20.9	171 ± 142	241 ± 250	0.102	0.00153	CD24
39	76.8 ± 12.5	200 ± 41.5	212 ± 57.8	0.362	0.00154	CDCA8
40	70.9 ± 12.7	182 ± 38.1	190 ± 15	0.373	0.00154	STIL
41	17.1 ± 4	37.9 ± 12.6	37.3 ± 4.56	0.458	0.00154	ATAD5
42	37.7 ± 12.3	96.1 ± 14.3	104 ± 8.35	0.363	0.00154	XRCC2
43	15.1 ± 3.03	30.7 ± 3.72	35.3 ± 4.19	0.428	0.00164	C5orf34
44	78.3 ± 7.91	229 ± 94.4	189 ± 19.1	0.414	0.00178	HIST1H3A to J
45	47.7 ± 15.8	119 ± 33.6	118 ± 15.7	0.404	0.00185	CLSPN
46	35.6 ± 5.58	60.6 ± 35.5	92.7 ± 20	0.384	0.00185	GBP3
47	33.3 ± 8.71	80.1 ± 16.5	80.9 ± 4.99	0.412	0.00224	BLM
48	112 ± 17.2	261 ± 64.9	299 ± 16.8	0.375	0.00224	ESCO2
49	31.8 ± 7.32	80.5 ± 18.5	79.9 ± 19.9	0.398	0.00229	BRCA1
50	79.2 ± 17.8	43.1 ± 14.8	28.7 ± 8.03	2.76	0.00230	ABCA6
51	18.9 ± 3.26	22.3 ± 13.4	9.24 ± 0.884	2.05	0.00237	GBP2
52	32.1 ± 5.31	70.4 ± 24.9	73.3 ± 8.73	0.438	0.00258	RAD51
53	12.1 ± 4.65	34.7 ± 28.6	44.5 ± 23	0.272	0.00258	ZNF730
54	13.1 ± 1.69	21.7 ± 5.58	25.6 ± 2.11	0.512	0.00258	RAD54B
55	61.5 ± 10.1	163 ± 50.7	172 ± 21.2	0.358	0.00265	CDCA2
56	149 ± 51.4	185 ± 100	457 ± 101	0.326	0.00265	SLC38A5
57	47.5 ± 7.89	117 ± 37.1	113 ± 27	0.42	0.00268	SGOL1
58	68.4 ± 25.3	183 ± 72.1	188 ± 41.8	0.364	0.00269	PBK
59	12.7 ± 3.56	22.2 ± 9.27	28.8 ± 8.65	0.441	0.00282	FRAS1
60	41.1 ± 10.3	107 ± 30.5	108 ± 27.8	0.381	0.00305	NDC80
61	35.1 ± 9.98	67.2 ± 15.7	83 ± 4.22	0.423	0.00370	GINS4
62	200 ± 36.5	274 ± 124	457 ± 55.6	0.438	0.00375	COL12A1
63	15.5 ± 1.39	16.2 ± 4.36	74.6 ± 48.7	0.208	0.00402	UNC13A
64	22.6 ± 6.44	59 ± 15.9	57.8 ± 14.5	0.391	0.00426	RAD51AP1

65	128 ± 10.4	88.6 ± 41.7	56.3 ± 18.3	2.27	0.00427	PRKG1
66	67.3 ± 13.3	152 ± 24.8	154 ± 21.2	0.437	0.00427	WDHD1
67	19 ± 5.16	22.5 ± 5.72	41.8 ± 3.6	0.455	0.00427	DOK6
68	171 ± 61.8	427 ± 198	470 ± 17.1	0.364	0.00427	HIST1H2BM
69	24.6 ± 4	47.2 ± 23.5	54.8 ± 13.6	0.449	0.00427	TRERF1
70	26.5 ± 4.3	51.6 ± 15.4	59 ± 7.27	0.449	0.00427	LRRCC1
71	14.1 ± 2.76	28.1 ± 6.97	30.7 ± 7.38	0.459	0.00427	ERCC6L
72	19.7 ± 2.7	30.8 ± 14.4	39.9 ± 5.47	0.494	0.00465	LRFN5
73	101 ± 15	256 ± 81.1	258 ± 49.3	0.391	0.00465	HJURP
74	26.7 ± 6.67	69.4 ± 16.2	63 ± 12.2	0.424	0.00503	SKA1
75	28.9 ± 14.7	129 ± 79.7	98.2 ± 22.4	0.294	0.00506	ZNF804A
76	42.5 ± 23.3	33.1 ± 34.3	12.3 ± 3.18	3.46	0.00508	NEDD4L
77	825 ± 342	1540 ± 685	1990 ± 107	0.415	0.00508	HAS2
78	130 ± 36.6	86.3 ± 9.81	50.5 ± 10.3	2.57	0.00524	TLE4
79	63.9 ± 6.34	184 ± 81.9	168 ± 75.3	0.38	0.00527	ASPM
80	162 ± 79.8	139 ± 176	45.1 ± 13	3.59	0.00527	GATA4
81	79 ± 10.1	167 ± 31.2	172 ± 9.44	0.459	0.00564	POLD3
82	23.2 ± 6.05	49.1 ± 5.69	48.8 ± 3.45	0.475	0.00618	CENPL
83	60 ± 3	138 ± 29.1	143 ± 19.6	0.42	0.00618	CCNF
84	30.9 ± 17	15.5 ± 12.6	6.37 ± 0.617	4.85	0.00618	GCNT4
85	39.9 ± 8.4	87.9 ± 19.2	89.6 ± 17.8	0.445	0.00624	MIS18BP1
86	3.68 ± 0.618	4.79 ± 0.925	6.15 ± 1.07	0.598	0.00644	ZNF443
87	20.8 ± 3.5	47.8 ± 18.9	50.7 ± 13.3	0.41	0.00653	CDC7
88	80.5 ± 24.3	184 ± 44.8	188 ± 6.47	0.428	0.00657	HIST1H2AB, E
89	36.9 ± 12.4	86.2 ± 35	92.8 ± 24.8	0.398	0.00658	FAM111B
90	72.3 ± 13.6	157 ± 34.7	162 ± 20.9	0.446	0.00658	MELK
91	22.9 ± 2.9	51.5 ± 18.5	51.3 ± 13.7	0.446	0.00658	BRCA2
92	16.1 ± 4.23	26.3 ± 4.63	36.1 ± 5.39	0.446	0.00658	DSCC1
93	2.77 ± 0.207	3.18 ± 0.518	3.89 ± 0.32	0.712	0.00674	IL18
94	48.5 ± 9.89	87.2 ± 47.5	106 ± 9.77	0.458	0.00707	GCNT1
95	56.3 ± 5.83	148 ± 34.4	133 ± 33.7	0.423	0.00710	BUB1B
96	42.6 ± 16.1	102 ± 52.7	106 ± 21.8	0.402	0.00716	NEIL3
97	151 ± 18.4	273 ± 26.1	326 ± 11.5	0.463	0.00716	C9orf64
98	15.8 ± 3.92	37 ± 10.6	33.9 ± 4.2	0.466	0.00719	CCDC15
99	221 ± 78	535 ± 182	549 ± 39.2	0.403	0.00719	HIST1H1B
100	42.4 ± 28.6	88.5 ± 70	140 ± 30.7	0.303	0.00722	PDGFRL

101	21.3 ± 3.63	37.4 ± 6.86	41.7 ± 3.24	0.511	0.00724	HIST1H3G
102	14.7 ± 2.36	29.2 ± 6.98	29 ± 1.66	0.507	0.00784	HIST1H2BC, E, F, G, I
103	14.3 ± 4.26	121 ± 193	51.7 ± 29.8	0.277	0.00813	PARM1
104	42.9 ± 6.95	82.9 ± 15.1	87.2 ± 12.2	0.492	0.00820	PSMC3IP
105	87.4 ± 29.9	214 ± 70.6	208 ± 30.4	0.42	0.00820	FBXO5
106	19.7 ± 2.6	45.5 ± 9.35	43.7 ± 13.5	0.451	0.00828	BORA
107	13.6 ± 3.88	23.1 ± 4.16	26.9 ± 0.879	0.506	0.00900	CHAC2
108	135 ± 182	452 ± 216	710 ± 119	0.19	0.00900	SULT1B1
109	22.7 ± 3.68	40.1 ± 10.5	43 ± 2.93	0.528	0.00903	FAM217B
110	15.6 ± 2.88	32.9 ± 14.2	32.4 ± 5.04	0.481	0.00914	POLE2
111	175 ± 96.7	492 ± 147	445 ± 58.4	0.393	0.00914	GK
112	79.3 ± 16.3	177 ± 33.5	178 ± 34.3	0.446	0.00919	UBE2T
113	75.5 ± 11.9	172 ± 48.8	164 ± 40.1	0.46	0.00949	KIF2C
114	13.7 ± 7.43	32.6 ± 16.4	31.6 ± 6.77	0.434	0.00986	SNHG1 // SNORD22,
115	59.5 ± 16.9	129 ± 30.1	149 ± 36	0.399	0.01001	CENPI
116	86.9 ± 19.7	221 ± 35.9	204 ± 60.6	0.426	0.01003	KIAA1524
117	11.3 ± 3.86	16.5 ± 3.96	23.7 ± 4.95	0.477	0.01060	FLJ31958 // RP11-564C4.6
118	18.9 ± 7.57	74.2 ± 83.6	43.5 ± 8.41	0.434	0.01068	ANO3
119	27.1 ± 7.33	50.8 ± 8.24	59.4 ± 12.1	0.456	0.01068	DLEU1
120	114 ± 93.5	233 ± 313	24.2 ± 16.4	4.71	0.01068	EPB41L3
121	10.3 ± 1.05	16 ± 3.48	18 ± 3.07	0.572	0.01068	CCDC138
122	41.1 ± 6.36	97.5 ± 23.4	89.7 ± 27.2	0.458	0.01068	SGOL2
123	56.9 ± 14.1	121 ± 55	143 ± 30.5	0.398	0.01068	POLR3G
124	61.2 ± 17.8	157 ± 49.4	151 ± 18.3	0.405	0.01068	HIST1H2BC, E, F, G, I
125	9 ± 3.72	14.1 ± 5.66	18.1 ± 2.32	0.497	0.01068	CXorf57
126	48.6 ± 7.67	101 ± 10.3	100 ± 9.93	0.486	0.01098	GINS3
127	56.9 ± 12.2	136 ± 31.5	127 ± 31.2	0.448	0.01145	NCAPH
128	155 ± 23.6	365 ± 134	364 ± 78.6	0.426	0.01154	CEP55
129	96.9 ± 20	209 ± 65	218 ± 57.2	0.444	0.01162	RBL1
130	13.9 ± 1.06	23.7 ± 8.32	26.2 ± 6.86	0.531	0.01218	LOC100288637
131	29.6 ± 3.55	64.9 ± 19.8	61.6 ± 19.8	0.481	0.01218	CDC25C
132	74.6 ± 22.6	143 ± 31.4	152 ± 7.75	0.491	0.01218	ATAD2
133	28.4 ± 9.2	50.9 ± 26.1	63.7 ± 4.58	0.446	0.01230	ADAMTS5
134	13.1 ± 3.74	22.8 ± 5.63	25.5 ± 3.84	0.514	0.01239	ZNF675
135	52.1 ± 15.2	110 ± 32.4	112 ± 14.2	0.465	0.01264	GINS1

136	32 ± 2.31	65.2 ± 22.7	67.4 ± 22	0.475	0.01313	CDCA3
137	6.12 ± 2.86	5.01 ± 1.32	15.5 ± 6.82	0.395	0.01313	GALNT13
138	131 ± 35.7	77.8 ± 14.1	54.7 ± 35	2.39	0.01316	PLA2G16
139	71.1 ± 42.8	127 ± 88	185 ± 14.7	0.384	0.01316	SYT1
140	286 ± 65.2	109 ± 30.3	112 ± 33.2	2.55	0.01321	FAM198B
141	32.3 ± 3.04	55.5 ± 25.5	61.8 ± 15.5	0.523	0.01328	TRERF1
142	146 ± 49.3	76.8 ± 58.1	55 ± 19.2	2.65	0.01351	PRICKLE1
143	62.4 ± 31.4	157 ± 20.6	166 ± 15.6	0.376	0.01351	CDC6
144	23.6 ± 4.65	42.6 ± 11.6	44.3 ± 5.79	0.533	0.01351	EME1
145	53.3 ± 10.5	92.6 ± 12.2	107 ± 17.1	0.498	0.01351	LRRC37A4P
146	6.27 ± 0.312	21.6 ± 25.7	14.7 ± 9.27	0.427	0.01351	DHRS9
147	307 ± 52.5	671 ± 263	698 ± 59.9	0.44	0.01351	HIST1H3A, B, C, D, G,
148	17.1 ± 5.72	35.3 ± 22.5	35.8 ± 7.73	0.478	0.01351	HOXA4
149	9.64 ± 1.24	8.13 ± 0.475	5.83 ± 0.243	1.65	0.01394	MFSD2B
150	87.4 ± 18.1	185 ± 45.8	183 ± 37.2	0.478	0.01408	KIFC1
151	44 ± 12.3	69.1 ± 17	88.1 ± 5.18	0.499	0.01444	HOXA3
152	40.9 ± 14.5	86 ± 45.7	98.3 ± 40.7	0.416	0.01487	MYBL1
153	42.9 ± 12.7	88.9 ± 15.4	93.4 ± 9.08	0.459	0.01492	ORC6
154	60.6 ± 14.9	142 ± 44.7	136 ± 27.1	0.446	0.01524	CDK1
155	17.8 ± 6.01	33.8 ± 16.1	35.6 ± 5.21	0.5	0.01527	MBOAT1
156	58.8 ± 14.5	148 ± 41.5	139 ± 42.6	0.423	0.01530	FAM72A, B, C, D // LOC101060656
157	50.9 ± 30.3	108 ± 28.7	155 ± 58	0.328	0.01548	KCNQ5
158	94.6 ± 57.8	272 ± 92.5	234 ± 28.4	0.404	0.01548	GK
159	22.4 ± 12.5	78.1 ± 52.4	63.9 ± 31.5	0.351	0.01571	PTPN22
160	100 ± 48.3	24.3 ± 15.5	30.8 ± 10.3	3.25	0.01571	DEPTOR
161	61.4 ± 10.9	157 ± 38.1	143 ± 39.5	0.429	0.01572	FAM72B // FAM72C
162	49.4 ± 7.57	116 ± 52.3	112 ± 35.7	0.441	0.01572	CASC5
163	15.2 ± 2.69	23.9 ± 2.84	25.8 ± 1.58	0.589	0.01572	ZNF138
164	9.61 ± 1.09	19.6 ± 1.92	18.6 ± 7.35	0.517	0.01596	HYLS1
165	12.8 ± 8.41	23.1 ± 11	35.6 ± 13.9	0.36	0.01612	LOC654433
166	10.9 ± 2.66	20.2 ± 5.02	19.2 ± 1.03	0.568	0.01655	HIST1H2AE
167	18.8 ± 3.86	30 ± 3.06	34 ± 2.1	0.553	0.01655	PDE7A
168	154 ± 42.4	333 ± 86.2	339 ± 68.2	0.454	0.01661	NCAPG
169	72.8 ± 22.6	178 ± 54.6	160 ± 42.8	0.455	0.01661	CENPK
170	40.6 ± 8.63	79.4 ± 13.8	80.1 ± 7.28	0.507	0.01665	CDCA5

171	32.7 ± 5.22	62.9 ± 13.2	65.1 ± 16.6	0.502	0.01724	MMS22L
172	5.72 ± 1.31	11.1 ± 3.74	9.27 ± 0.616	0.617	0.01766	HIST1H2AJ
173	62.2 ± 9.84	160 ± 61.6	144 ± 31.7	0.432	0.01776	CENPE
174	32.8 ± 11.9	38.4 ± 9.82	68.1 ± 16.7	0.482	0.01806	SLC37A2
175	94.3 ± 19.8	230 ± 64.6	214 ± 44.2	0.441	0.01857	KIF11
176	19.2 ± 0.779	32.6 ± 7.94	32.7 ± 1.31	0.587	0.01857	DCLRE1A
177	117 ± 23.7	243 ± 54.8	239 ± 26.6	0.49	0.01868	TRIP13
178	275 ± 78.8	577 ± 154	595 ± 18	0.462	0.01868	HIST1H3A, B, C, D, E,
179	9.34 ± 1.78	6.57 ± 1.19	5.56 ± 0.492	1.68	0.01886	AKR1B10
180	65.8 ± 21.1	170 ± 63.9	149 ± 49.8	0.442	0.01977	KIF20B
181	42.1 ± 11.2	76.1 ± 23.7	83.9 ± 6.02	0.502	0.02082	OSGEPL1
182	127 ± 18.2	270 ± 89.6	262 ± 69.2	0.485	0.02143	NUSAP1
183	61.3 ± 11.5	154 ± 38.1	141 ± 39.5	0.435	0.02143	FAM72A, C, D // LOC101060656
184	62.6 ± 11.6	158 ± 37.2	145 ± 41.5	0.432	0.02186	FAM72A, B, C // LOC101060656
185	31.6 ± 3.78	48.6 ± 8.25	55.2 ± 3.57	0.572	0.02196	CCDC66
186	52.8 ± 14	88.6 ± 15	99.9 ± 3.92	0.529	0.02228	LNX2
187	55.9 ± 25.7	55.4 ± 60.2	20 ± 0.971	2.8	0.02228	LRRN3
188	71.4 ± 5.5	137 ± 22.6	135 ± 10.8	0.529	0.02246	AURKB
189	21.9 ± 6.13	43.5 ± 4.54	42.5 ± 6.05	0.515	0.02323	FANCM
190	40.3 ± 9.89	76.1 ± 27.8	81.1 ± 15	0.497	0.02362	KNTC1
191	48 ± 11	88.6 ± 14.9	91.4 ± 6.97	0.525	0.02370	SPATA5
192	18.6 ± 2.76	28.1 ± 4.12	31.4 ± 1.58	0.592	0.02385	DCLRE1C
193	18 ± 3.32	30 ± 12.5	31.7 ± 1.84	0.568	0.02388	LPAR3
194	25.1 ± 1.88	49.4 ± 9.58	49.2 ± 10.1	0.51	0.02388	DEPDC1B
195	50.5 ± 18.8	110 ± 28.6	105 ± 3.7	0.481	0.02388	HIST1H2AH
196	37.6 ± 10.4	67.6 ± 14.7	78 ± 19.6	0.482	0.02408	SLC25A19
197	6.1 ± 0.53	11.4 ± 3.61	10 ± 3.04	0.61	0.02414	C12orf56
198	43.4 ± 5.49	64.2 ± 11	73.9 ± 1.72	0.587	0.02414	NR2C2AP
199	210 ± 36.3	448 ± 103	441 ± 90.2	0.476	0.02414	TPX2
200	30.7 ± 3.81	46.6 ± 4.45	54.7 ± 3.78	0.561	0.02417	WDR67
201	63 ± 23.3	140 ± 28.9	141 ± 11.4	0.447	0.02418	MCM10
202	148 ± 21.8	86.3 ± 13.8	72.1 ± 2.61	2.05	0.02418	DDR1
203	1070 ± 383	2090 ± 463	2270 ± 133	0.471	0.02430	ODC1
204	18 ± 4.37	37.7 ± 6.65	33.4 ± 6.86	0.539	0.02602	C1orf112
205	23.5 ± 5.01	45 ± 11.2	43.4 ± 10.8	0.541	0.02605	FANCL

206	138 ± 28.8	297 ± 32.6	280 ± 19.4	0.493	0.02633	NDC1 // TMEM48
207	23.9 ± 6.78	48.1 ± 13	44.2 ± 6.56	0.541	0.02633	GMNN
208	62.5 ± 16.2	102 ± 23.6	142 ± 25.5	0.44	0.02633	ERI1
209	49.7 ± 24.1	92.5 ± 11	102 ± 9.29	0.487	0.02633	UBXN2B
210	100 ± 49.2	265 ± 55.9	244 ± 66.1	0.41	0.02655	RRM2
211	32.9 ± 6.3	56.7 ± 5.69	60.4 ± 4.77	0.545	0.02656	ERI2
212	132 ± 13.4	79.8 ± 11.4	69.2 ± 3.26	1.91	0.02657	DDR1 // MIR4640
213	20.2 ± 3.99	42.9 ± 15.3	39.2 ± 13.3	0.515	0.02676	SPC25
214	150 ± 56.5	300 ± 60.6	327 ± 25.4	0.459	0.02712	NET1
215	8.34 ± 3.19	13.2 ± 3.43	15.9 ± 4.55	0.525	0.02712	PAR5 // SNORD64
216	53.2 ± 23.4	42.4 ± 21.4	21.3 ± 7.41	2.5	0.02735	NCKAP5
217	198 ± 45.4	464 ± 200	448 ± 162	0.442	0.02800	MKI67
218	49.2 ± 10.5	96.4 ± 14.5	94 ± 7.15	0.523	0.02805	SASS6
219	24.8 ± 9.23	45.2 ± 13.1	47.7 ± 8.19	0.52	0.02826	ORC1
220	58.2 ± 22.3	113 ± 27.8	129 ± 22.9	0.451	0.02826	GPAM
221	153 ± 83	68.4 ± 31.6	55.4 ± 1.65	2.76	0.02826	NUAK1
222	76.6 ± 18.2	150 ± 31.3	148 ± 13.9	0.518	0.02826	RFC3
223	25.2 ± 9.47	85.3 ± 79.4	48.5 ± 2.7	0.52	0.02826	SLC16A14
224	82.1 ± 17.5	150 ± 27.1	159 ± 14.8	0.516	0.02826	HIST1H2AG, H, I, K, L, M
225	35.2 ± 9.94	73.5 ± 16.9	69.8 ± 7.18	0.504	0.02833	RMI1
226	165 ± 22.6	344 ± 144	346 ± 86.3	0.477	0.02837	TOP2A
227	8.34 ± 1.68	16.1 ± 10.3	19.5 ± 9.71	0.428	0.02845	GREB1L
228	48.1 ± 24.3	109 ± 34.6	103 ± 11	0.467	0.02847	EXO1
229	28.5 ± 8.23	70.4 ± 24.1	64.2 ± 24.2	0.444	0.02856	KIF14
230	129 ± 47.5	279 ± 41	283 ± 20	0.456	0.02889	DTL
231	70.4 ± 27.2	40.1 ± 30.2	31.8 ± 2.96	2.21	0.02889	FZD7
232	879 ± 145	1550 ± 178	1620 ± 97.2	0.543	0.02970	CLMP // ASAM
233	115 ± 33.3	280 ± 56.6	252 ± 79.3	0.456	0.03073	AURKA
234	32.2 ± 11.5	71.9 ± 54.2	101 ± 81.3	0.319	0.03076	PSG7
235	79.8 ± 15.3	157 ± 38	152 ± 31.6	0.525	0.03308	FAM83D
236	703 ± 376	300 ± 214	250 ± 130	2.81	0.03342	KRT18 // MIR622 // RP11-507F17.1
237	52.7 ± 13.7	109 ± 35.3	105 ± 31.4	0.502	0.03342	TRIM59
238	13.9 ± 2.22	23.3 ± 10.1	22.8 ± 2.8	0.61	0.03342	ZNF273
239	138 ± 15.6	82.9 ± 12.5	70.8 ± 3	1.95	0.03342	DDR1 // MIR4640
240	9.28 ± 2.07	17 ± 6.7	16.1 ± 4.66	0.576	0.03434	MRAP2

241	103 ± 67.5	416 ± 313	298 ± 14.5	0.346	0.03500	GABBR2
242	121 ± 22.4	237 ± 50.6	240 ± 9.79	0.504	0.03514	HIST1H2AG, H, I, K, L, M
243	24 ± 5.74	52.3 ± 15.4	43.5 ± 5.01	0.552	0.03574	MLF1IP
244	110 ± 35	243 ± 102	232 ± 82	0.474	0.03580	LAYN
245	66.9 ± 12.1	149 ± 48.9	144 ± 62.9	0.465	0.03580	HMMR
246	4420 ± 421	4370 ± 135	3060 ± 888	1.44	0.03580	MT-RNR1
247	80.3 ± 13.9	160 ± 36.8	160 ± 33.8	0.502	0.03599	KIFC1
248	4.05 ± 0.676	8.92 ± 2.44	6.18 ± 1.33	0.655	0.03678	ANKRD32
249	114 ± 30.9	285 ± 86.4	260 ± 98.7	0.438	0.03682	CCNB1
250	96.4 ± 38.3	170 ± 42.5	199 ± 9.38	0.484	0.03682	MCM4
251	11.2 ± 2.59	18.1 ± 2.88	19.7 ± 3.66	0.569	0.03714	SFR1
252	46.1 ± 14.1	83.4 ± 50.9	106 ± 57.4	0.435	0.03729	HSPA4L
253	18.2 ± 4.86	48.5 ± 46	35.3 ± 12	0.516	0.03760	CBLN2
254	7.33 ± 0.819	9.58 ± 0.468	10.6 ± 0.579	0.692	0.03776	ZNF678
255	52.6 ± 10.4	101 ± 22.7	96.7 ± 7.02	0.544	0.03857	MSH2
256	63.8 ± 71.4	132 ± 115	174 ± 16.2	0.367	0.03857	CNTN3
257	212 ± 39.3	398 ± 108	412 ± 26.8	0.515	0.03945	ARNTL2
258	23.3 ± 6.42	32.8 ± 10.1	43.9 ± 6.24	0.531	0.03945	CARD11
259	153 ± 9.53	349 ± 98.2	325 ± 110	0.471	0.03946	CKAP2
260	45.1 ± 16.9	84.6 ± 17	87.4 ± 6.76	0.516	0.03962	LOC339803
261	238 ± 62	482 ± 64.8	472 ± 17	0.504	0.04077	MCM8
262	26.8 ± 6.81	47.4 ± 10.9	49.2 ± 2.62	0.545	0.04096	CEP152
263	64.9 ± 34.2	108 ± 22.9	149 ± 13.3	0.436	0.04096	CCNE2
264	76.1 ± 19.1	175 ± 53.8	154 ± 52	0.494	0.04157	SPAG5
265	64.9 ± 28.2	96.3 ± 20.6	166 ± 61	0.391	0.04157	MMP16
266	408 ± 63.3	854 ± 199	794 ± 178	0.514	0.04183	PLK1
267	17 ± 5.3	26.4 ± 3.04	30.1 ± 4.59	0.565	0.04262	NSUN6
268	6.5 ± 0.691	12.7 ± 12.2	13.1 ± 5.91	0.496	0.04274	FAM105A
269	4.18 ± 0.537	4.47 ± 0.241	6.87 ± 2.09	0.608	0.04308	MMP8
270	277 ± 117	486 ± 90.3	596 ± 6.11	0.465	0.04349	PLEK2
271	146 ± 38.1	236 ± 65.5	344 ± 143	0.424	0.04365	FABP5
272	59.2 ± 45.9	32.2 ± 28.9	17.5 ± 1.56	3.38	0.04365	SVEP1
273	58.5 ± 69.9	34.5 ± 18.2	189 ± 104	0.31	0.04366	PLXDC2
274	109 ± 32.8	205 ± 25.6	207 ± 24.1	0.527	0.04457	RFWD3
275	29.2 ± 2.07	42.9 ± 7.52	49.1 ± 5.56	0.595	0.04457	HIST1H2AG, H, I, K,

276	814 ± 364	499 ± 194	303 ± 5.47	2.69	0.04460	EPAS1
277	90.9 ± 23.1	180 ± 31.8	186 ± 16	0.489	0.04465	CENPO
278	42.2 ± 17.8	70.4 ± 28.7	81.5 ± 11.6	0.518	0.04473	PRIM1
279	41.9 ± 14.2	81.9 ± 13.4	81.8 ± 6.92	0.512	0.04473	MGME1
280	132 ± 126	462 ± 499	367 ± 31.8	0.36	0.04473	FGL2
281	24.3 ± 4.78	38.2 ± 6.05	41.2 ± 5.92	0.59	0.04536	ZNF354A
282	494 ± 263	758 ± 506	1080 ± 29.1	0.457	0.04536	FAM180A
283	19.4 ± 3.55	31.1 ± 2.7	32.6 ± 1.13	0.595	0.04577	TUBD1
284	49.4 ± 13.4	77.3 ± 25.3	106 ± 33	0.466	0.04702	GPCPD1
285	125 ± 20.3	219 ± 88.6	238 ± 55.6	0.525	0.04702	HMGB2
286	93.2 ± 7.6	206 ± 69.3	196 ± 71.1	0.476	0.04723	DLGAP5
287	66.1 ± 17.6	131 ± 36	130 ± 21.2	0.508	0.04780	EZH2
288	43.3 ± 11.4	78.3 ± 13.3	80 ± 4.15	0.541	0.04806	CENPJ
289	144 ± 47.2	75.9 ± 14.2	63.2 ± 12.9	2.28	0.04885	FAM43A
290	142 ± 14.5	274 ± 61	269 ± 46.5	0.528	0.04890	RNASEH2A
291	47.4 ± 12.9	83 ± 6.74	83.5 ± 3.79	0.568	0.04891	RNF219
292	58.8 ± 15	132 ± 39	118 ± 25.5	0.498	0.04891	PLK4
293	53.1 ± 11.2	102 ± 20.4	97.9 ± 9.64	0.542	0.04915	GSG2
294	60.5 ± 14.9	111 ± 15.7	120 ± 16.5	0.504	0.04950	TICRR
295	17.4 ± 3.07	28.5 ± 6.06	29.5 ± 8.47	0.59	0.04997	CNTRL

10.2. ASARM motif gene expression profile of VSMCs

Table 1.3. ASARM motif gene expression profile of VSMCs

Rank	HR avg ± SD	HET avg ± SD	HNR avg ± SD	HR/HNR	BH	Gene Symbol
1	6.5 ± 0.999	260 ± 319	176 ± 49.6	0.0369	1E-11	STATH
649	15.8 ± 5.87	10.7 ± 1.08	8.66 ± 1.33	1.82	0.180246	SPP1
4187	117 ± 154	101 ± 131	188 ± 136	0.622	0.748218	MGP
11282	6.06 ± 0.215	5.71 ± 0.153	5.61 ± 0.204	1.08	0.8218768	DSPP
11962	7.98 ± 0.869	7.1 ± 0.714	7.33 ± 0.0757	1.09	0.8300919	IBSP
15342	5.07 ± 0.686	4.68 ± 0.23	4.8 ± 0.141	1.06	0.8764356	DMP1
19560	5.28 ± 0.0972	4.8 ± 0.205	5.22 ± 0.678	1.01	0.9529179	MEPE

10.3. Smooth muscle-specific gene expression profilE

Smooth muscle-specific gene expression profile						
Rank	HR avg ± SD	HET avg ± SD	HNR avg ± SD	HR/HNR	BH	Gene Symbol
4248	1210 ± 960	851 ± 589	626 ± 291	1.93	0.752	ACTA2
6424	152 ± 46.6	255 ± 51.4	187 ± 39	0.813	0.796	SMTN
6525	212 ± 246	116 ± 38.1	94.4 ± 8.23	2.25	0.797	CNN1
19002	1160 ± 633	844 ± 365	968 ± 133	1.2	0.942	TAGLN

11. Rights and Permissions

49 Spadina Ave. Suite 200
Toronto ON M5V 2J1 Canada
www.biorender.com

Confirmation of Publication and Licensing Rights

December 11th, 2024

Subscription Type:	*Student Plan - Academic*
Agreement number:	*HH27NMQU3I*
Publisher Name:	*thesis -uottawa*
Citation to Use:	*Created in BioRender. Soheili, F. (2024) https://BioRender.com/g82i091*

To whom this may concern,

This document is to confirm that Fariborz Soheili has been granted a license to use the BioRender Content, including icons, templates, and other original artwork, appearing in the attached Completed Graphic pursuant to BioRender's Academic License Terms. This license permits BioRender Content to be sublicensed for use in publications (journals, textbooks, websites, etc.).

All rights and ownership of BioRender Content are reserved by BioRender. All Completed Graphics must be accompanied by the following citation: "Created in BioRender. Soheili, F. (2024) https://BioRender.com/g82i091".

BioRender Content included in the Completed Graphic is not licensed for any commercial uses beyond use in a publication. For any commercial use of this figure, users may, if allowed, recreate it in BioRender under an Industry BioRender Plan.

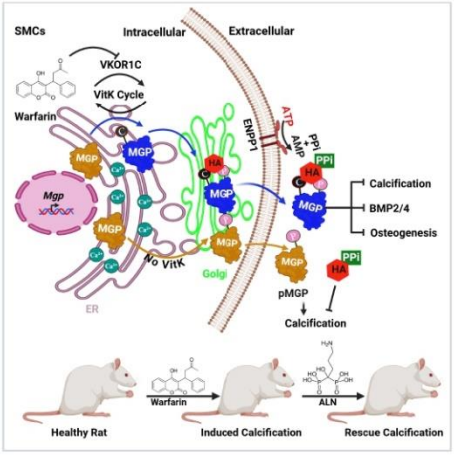

For any questions regarding this document, or other questions about publishing with BioRender, please refer to our BioRender Publication Guide, or contact BioRender Support at support@biorender.com.

49 Spadina Ave. Suite 200
Toronto ON M5V 2J1 Canada
www.biorender.com

Confirmation of Publication and Licensing Rights

December 11th, 2024

Subscription Type:	*Student Plan - Academic*
Agreement number:	*UE27NMQ9M3*
Publisher Name:	*thesis -uottawa*
Citation to Use:	*Created in BioRender. Soheili, F. (2024) https://BioRender.com/z62k900*

To whom this may concern,

This document is to confirm that Fariborz Soheili has been granted a license to use the BioRender Content, including icons, templates, and other original artwork, appearing in the attached Completed Graphic pursuant to BioRender's Academic License Terms. This license permits BioRender Content to be sublicensed for use in publications (journals, textbooks, websites, etc.).

All rights and ownership of BioRender Content are reserved by BioRender. All Completed Graphics must be accompanied by the following citation: "Created in BioRender. Soheili, F. (2024) https://BioRender.com/z62k900".

BioRender Content included in the Completed Graphic is not licensed for any commercial uses beyond use in a publication. For any commercial use of this figure, users may, if allowed, recreate it in BioRender under an Industry BioRender Plan.

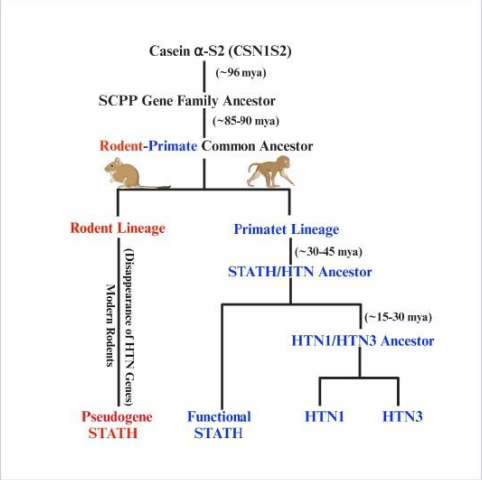

For any questions regarding this document, or other questions about publishing with BioRender, please refer to our BioRender Publication Guide, or contact BioRender Support at support@biorender.com.

49 Spadina Ave. Suite 200
Toronto ON M5V 2J1 Canada
www.biorender.com

Confirmation of Publication and Licensing Rights

December 11th, 2024

Subscription Type:	*Student Plan - Academic*
Agreement number:	*AP27NMSQJS*
Publisher Name:	*thesis -uottawa*
Citation to Use:	*Created in BioRender. Soheili, F. (2024) https://BioRender.com/p07n864*

To whom this may concern,

This document is to confirm that Fariborz Soheili has been granted a license to use the BioRender Content, including icons, templates, and other original artwork, appearing in the attached Completed Graphic pursuant to BioRender's Academic License Terms. This license permits BioRender Content to be sublicensed for use in publications (journals, textbooks, websites, etc.).

All rights and ownership of BioRender Content are reserved by BioRender. All Completed Graphics must be accompanied by the following citation: "Created in BioRender. Soheili, F. (2024) https://BioRender.com/p07n864".

BioRender Content included in the Completed Graphic is not licensed for any commercial uses beyond use in a publication. For any commercial use of this figure, users may, if allowed, recreate it in BioRender under an Industry BioRender Plan.

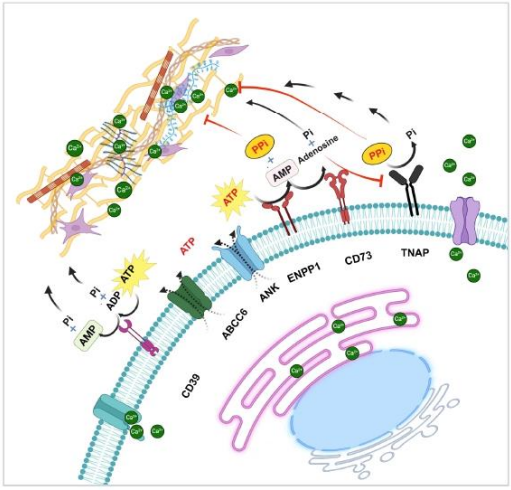

For any questions regarding this document, or other questions about publishing with BioRender, please refer to our BioRender Publication Guide, or contact BioRender Support at support@biorender.com.

Rights and Permissions

49 Spadina Ave. Suite 200
Toronto ON M5V 2J1 Canada
www.biorender.com

Confirmation of Publication and Licensing Rights

December 11th, 2024

Subscription Type:	*Student Plan - Academic*
Agreement number:	*NF27NMUFFV*
Publisher Name:	*thesis -uottawa*
Citation to Use:	*Created in BioRender. Soheili, F. (2024) https://BioRender.com/d19m776*

To whom this may concern,

This document is to confirm that Fariborz Soheili has been granted a license to use the BioRender Content, including icons, templates, and other original artwork, appearing in the attached Completed Graphic pursuant to BioRender's Academic License Terms. This license permits BioRender Content to be sublicensed for use in publications (journals, textbooks, websites, etc.).

All rights and ownership of BioRender Content are reserved by BioRender. All Completed Graphics must be accompanied by the following citation: "Created in BioRender. Soheili, F. (2024) https://BioRender.com/d19m776".

BioRender Content included in the Completed Graphic is not licensed for any commercial uses beyond use in a publication. For any commercial use of this figure, users may, if allowed, recreate it in BioRender under an Industry BioRender Plan.

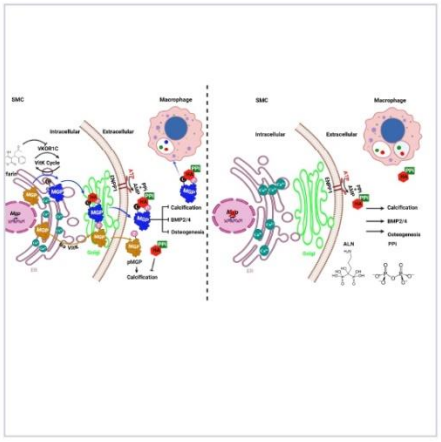

For any questions regarding this document, or other questions about publishing with BioRender, please refer to our BioRender Publication Guide, or contact BioRender Support at support@biorender.com.

49 Spadina Ave. Suite 200
Toronto ON M5V 2J1 Canada
www.biorender.com

Confirmation of Publication and Licensing Rights

December 11th, 2024

Subscription Type:	*Student Plan - Academic*
Agreement number:	*TY27NMSC02*
Publisher Name:	*thesis -uottawa*
Citation to Use:	*Created in BioRender. Soheili, F. (2024) https://BioRender.com/i63f126*

To whom this may concern,

This document is to confirm that Fariborz Soheili has been granted a license to use the BioRender Content, including icons, templates, and other original artwork, appearing in the attached Completed Graphic pursuant to BioRender's Academic License Terms. This license permits BioRender Content to be sublicensed for use in publications (journals, textbooks, websites, etc.).

All rights and ownership of BioRender Content are reserved by BioRender. All Completed Graphics must be accompanied by the following citation: "Created in BioRender. Soheili, F. (2024) https://BioRender.com/i63f126".

BioRender Content included in the Completed Graphic is not licensed for any commercial uses beyond use in a publication. For any commercial use of this figure, users may, if allowed, recreate it in BioRender under an Industry BioRender Plan.

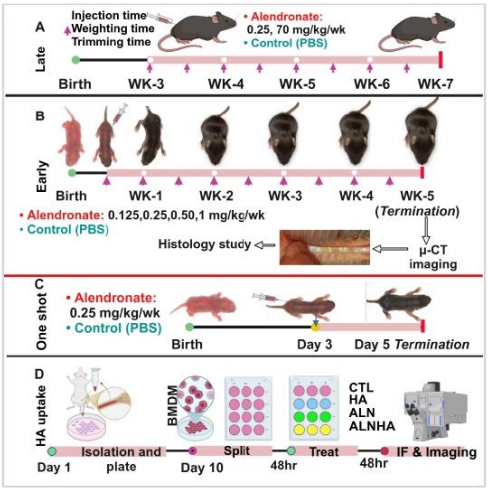

For any questions regarding this document, or other questions about publishing with BioRender, please refer to our BioRender Publication Guide, or contact BioRender Support at support@biorender.com.

SPRINGER NATURE LICENSE TERMS AND CONDITIONS

Dec 17, 2024

This Agreement between Dear sir/Madam I need to reuse this image for my thesis. ("You") and Springer Nature ("Springer Nature") consists of your license details and the terms and conditions provided by Springer Nature and Copyright Clearance Center.

License Number	5926110837815
License date	Dec 11, 2024
Licensed Content Publisher	Springer Nature
Licensed Content Publication	Nature Genetics
Licensed Content Title	Large-scale association analysis identifies 13 new susceptibility loci for coronary artery disease
Licensed Content Author	Heribert Schunkert Nilesh J Samani et al
Licensed Content Date	Mar 6, 2011
Type of Use	Thesis/Dissertation
Requestor type	academic/university or research institute
Format	print and electronic
Portion	figures/tables/illustrations
Number of figures/tables/illustrations	1
Would you like a high resolution image with your order?	no
Will you be translating?	no
Circulation/distribution	1 - 29
Author of this Springer Nature content	no
Title of new work	Student
Institution name	university of ottawa
Expected presentation date	Dec 2024
Portions	Figure 1: Graphical summary (Manhattan plot) of genome-wide association results.
The Requesting Person / Organization to Appear on the License	Dear sir/Madam I need to reuse this image for my thesis.
Requestor Location	Mr. Fariborz Soheili University of Ottawa Heart Institute 40 Ruskin Street 3230 alex stewart lab Ottawa, ON K1Y 4W7 Canada
Billing Type	Invoice
Billing Address	Mr. Fariborz Soheili University of Ottawa Heart Institute 40 Ruskin Street 3230 alex stewart lab Ottawa, ON K1Y 4W7 Canada

SPRINGER NATURE LICENSE TERMS AND CONDITIONS

Dec 17, 2024

This Agreement between I need to reuse this figure for my thesis. ("You") and Springer Nature ("Springer Nature") consists of your license details and the terms and conditions provided by Springer Nature and Copyright Clearance Center.

License Number	5926120029514
License date	Dec 11, 2024
Licensed Content Publisher	Springer Nature
Licensed Content Publication	Nature Cardiovascular Research
Licensed Content Title	Whole-genome sequencing uncovers two loci for coronary artery calcification and identifies ARSE as a regulator of vascular calcification
Licensed Content Author	Paul S. de Vries et al
Licensed Content Date	Dec 4, 2023
Type of Use	Thesis/Dissertation
Requestor type	academic/university or research institute
Format	print and electronic
Portion	figures/tables/illustrations
Number of figures/tables/illustrations	1
Will you be translating?	no
Circulation/distribution	1 - 29
Author of this Springer Nature content	no
Title of new work	Student
Institution name	university of ottawa
Expected presentation date	Dec 2024
Portions	Fig. 1: Manhattan plot for the GWAS of log(CAC + 1).
The Requesting Person / Organization to Appear on the License	I need to reuse this figure for my thesis.
Requestor Location	Mr. Fariborz Soheili University of Ottawa Heart Institute 40 Ruskin Street 3230 alex stewart lab Ottawa, ON K1Y 4W7 Canada
Billing Type	Invoice
Billing Address	Mr. Fariborz Soheili University of Ottawa Heart Institute 40 Ruskin Street 3230 alex stewart lab Ottawa, ON K1Y 4W7 Canada
Total	**0.00 USD**
Terms and Conditions	

Springer Nature Customer Service Centre GmbH Terms and Conditions

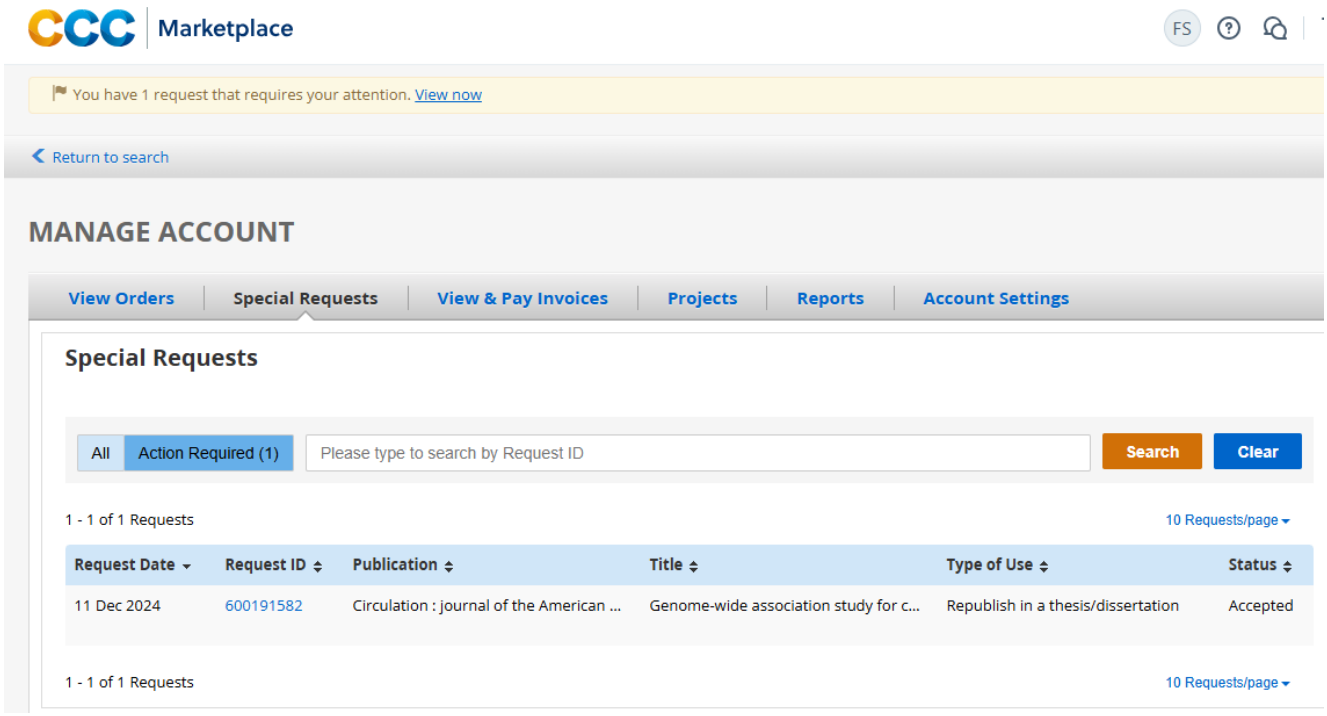
CCC Marketplace
FS
You have 1 request that requires your attention. View now
Return to search
MANAGE ACCOUNT
View Orders
Special Requests
View & Pay Invoices
Projects
Reports
Account Settings
Special Requests
All
Action Required (1)
Please type to search by Request ID
Search
Clear
1 - 1 of 1 Requests
10 Requests/page
Request Date
Request ID
Publication
Title
Type of Use
Status
11 Dec 2024
600191582
Circulation : journal of the American ...
Genome-wide association study for c...
Republish in a thesis/dissertation
Accepted
1 - 1 of 1 Requests
10 Requests/page

12. Curriculum Vitae

Fariborz Soheili M.Sc.

PhD Candidate
University of Ottawa

Academic and Training Background

2018 – 2024 **Ph.D. candidate, Faculty of Medicine, University of Ottawa**
Supervisor: Dr. Alexandre Stewart

2005 – 2007 **M.Sc., Genetics Shahid Chamran University of Ahvaz**
Supervisor: Dr. Hamid GALADARI
Thesis Title: Mutations analysis of P53 gene in patients affected with hepatocellular carcinoma

2010 – 2015 **B.Sc. (Hons), Biology, Razi University, Kermanshah,Iran**
Supervisor: Dr. Sirous Ghobadi

Funding

2022-2024 **University of Ottawa Heart Institute Endowed Award**
$40,000 over 2 years

2021 **Doctoral Admission Scholarship**
$10,000 over 1years
University of Ottawa

2018 – 2022 **Int'l Doctoral Scholarship**
$36,000 over 4 years
University of Ottawa

Honours and Awards

2023 Nicole Bégin-Heick Schol
2023 Fac MED Schol Grad Research
2023 Ontario Student Assistance Program (OSAP)
2023 BMO Financial Grad Bursaries
2022 Endowed Fellowship and Scholarship, UOHI
2022 Langevin-Desrochers Doc Burs
2022 Int'l Doctoral Scholarship
2021 Admissions Scholarship-Doctorate
2020 Int'l Doctoral Scholarship

2019 Langevin-Desrochers Doc Burs
2019 Int'l Doctoral Scholarship
2018 Int'l Doctoral Scholarship
2017 Active Researcher of Sciences Faculty Award,Department of Biology, Chabahar, Iran
2016 Active Researcher of Sciences Faculty Award Department of Biology, Chabahar, Iran
2015 Top university researcher Award Department of Biology, Chabahar, Iran
2010 The Youngest Faculty Achievement Award: Pioneering Generation of Transgenic Mice in Iran
2007 Graduate as Rank 1 University
2005 Rank 9 cell and molecular biology Olympiad

Skill language,
Kurdish (Fluent) Persian (Fluent)
English (Fluent) French (Basic)

Teaching Experience

2011-2018
Faculty member Department of Biology, Chabahar Maritime University, Iran
Course: Genetics, Biochemistry, Cell and Molecular Biology, Embryology, Virology, Evolution. (Biology Students)
Lab course: Genetics I, Genetics II, Molecular biology, Cellular biology, Embryology
Each term (25 student in average/course)
2007-2011
Faculty member, Department Medical Genetics and Anatomy, Medical University of Kurdistan, Kurdistan, Iran
Course: Medical Genetics, Genetic disease council, Cell and Molecular
Biology. (Medical Students; ~35 students/course)

Abstract Publications

Fariborz Soheili, Niloufar Heydarikhorneh, Benjamin Rotstein, Hsiao-huei Chen, Alexandre Stewart (2024), Bisphosphonate therapy improves bone deficits but worsens arterial calcification in Mgp-null mice. **Circulation 150**

F Soheili, N Almontashiri, N Heydarikhorneh, R Vilmundarson, Hsiao-huei Chen, Alexandre Stewart (2024), 9p21. 3 variants drive coronary calcification by suppressing statherin expression. **Circulation 150**

PEER-REVIEWED JOURNAL ARTICLES
https://scholar.google.com/citations?user=ii9y2sMAAAAJ
(n =16; 210 citations; h-index: 7; i10 index: 7),
Fariborz Soheili, Niloufar Heydarikhorneh, Alexandre F. R. Stewart. Alendronate improves dental malocclusion but worsens arterial calcification in Mgp-null mice by modulating macrophage hydroxyapatite uptake to lysosomes. **plos**

Fariborz Soheili, Niloufar Heydarikhorneh, Ragnar O. Vilmundarson, Alexandre F. R. Stewart. Mechanism whereby the chromosome 9p21.3 locus affects arterial calcification. jaha

Fariborz Soheili, L15Q TBX5 gene septal. Revision submitted to Journal of Heart

Asrin Rashidi; Ernst-Martin Füchtbauer; Zakaria Vahabzadeh; Farzad Soleymani; Karim Rahimi; Bahram Nikkho; **Fariborz Soheili,** Fardin Fathi, Oct 2024, Medical Hypotheses the Liver-Heart Nexus: Targeting the Liver to Spare the Heart, Exploring DYRK1B Inhibition in Cancer for Synthetic Lethality with Checkpoint Gene Mutations and Reducing the Dose of Chemotherapeutic Drugs.

Asrin Rashidi, Ernst-Martin Füchtbauer, Zakaria Vahabzadeh, Farzad Soleimani, Karim Rahimi, Bahram Nikkhoo, Shohreh Fakhari, Mohammad Bagher Khadem Erfan, Asaad Azarnezhad, Arash Pooladi, **Fariborz Soheili**, Fardin Fathi, CRISPR/Cas9-mediated knockout of DYRK1B in triple-negative breast cancer cells: implications for cell proliferation, apoptosis, and therapeutic sensitivity, Biochemical Engineering Journal, 2024 Oct, 213

Vilmundarson Ragnar, Duong An, **Soheili Fariborz,** Chen Hsiao-Huei, Stewart Alexandre. IRF2BP2 3′ UTR Polymorphism Increases Coronary Artery Calcification in Men. Frontiers in Cardiovascular Medicine. 2021:1423.

Vilmundarson RO, Heydarikhorneh N, Duong A, Ho T, Keyhanian K, **Fariborz Soheili,** Chen HH, Stewart AF. Savior Siblings Might Rescue Fetal Lethality but Not Adult Lymphoma in Irf2bp2- Null Mice. Frontiers in Immunology. 2022 Jul 4; 13:868053.

Fariborz Soheili*, Zahra Jalili, Mahtab Rahbar, Zahed Khatooni, Amir Mashayekhi, Hossein Jafari. Novel Mutation of GATA4 gene in Kurdish population of Iran with Non-syndromic congenital heart septals defects. Congenit Heart Dis. 2018 Mar;13(2):295-304.

Soheili Fariborz*, Bahram Nikkho, Mazaher Khodabandehloo. Determination of the Physical Status (Episomal/Integral) of HPV by qPCR in Esophageal Squamous Cell Carcinoma. International Journal of Enteric Pathogens. 2017 February; 5(1):1-4.

Soheili Fariborz*, Niloufar Heydarikhormeh, Mahtab Rahbar, Bahram Nikkho, Omid Fotouhi, Abdolrahim Afkhamzadeh, Hossein Jafari & Vahid Bagheri., Human papillomavirus and its clinical relevance in oesophageal squamous cell carcinoma in a Kurdish population in the west of Iran. INFECTIOUS DISEASES, 2016 VOL. 48, NO. 4, 270–273.

Soheili Fariborz *, Parichehr Darabi, Fatemeh Dahmardeh, Nilofar Heidary, Zahra Jalili, Samira Fooladi,Mohammad Saeid Hakhamanesh, and Maseoud Heidarizadeh., Nkx2-5 Mutations in Patients with Nonsyndromic Congenital Heart Disease. Zahedan Journal of Research in Medical Sciences. 2016 January; 18(1): e5873.

Bavi Zainab, Ghaffari Mostafa, Taheri Ali*, **Soheili Fariborz**., The Cytotoxic Effect of Chabahar Coast Marine Algae Gelidiella Acerosa Organic Extracts on Breast (MCF-7) and Colorectal (HT- 29) Cancer Cell Lines. Journal of Rafsanjan University of Medical Sciences. 2017; 16(8): 757-68.

Ghaffari Mostafa, *Taheri Ali, Bavi Zinab**, Soheili Fariborz**., Assessment of Antioxidant Properties of Red Seaweed Gelidiella acerosa of Chabahar Coastal Waters, Iran. Qom University of Medical Sciences Journal J 2017;10(11):34-41.

Soheili Fariborz, Galehdari Hamid*, Foroughmand Ali mohamad, Masjedizadeh Abdolrahim., Lack of Mutation in the Hot Spot Region of the Human P53 Gene in a Number of Iranian Hepatocellular Carcinoma Patients. Iranian Journal of Pathology (2010)5 (3), 116 -120.

Golbar Mohammedreza., Fathi Fardin., Mowla S Javad, **Soheili Fariborz**., Gene Expression Profiling of NCAM, NCAM-L1, N-Cadherin, Ninjurin-1 and Ninjurin-2 during the Course of Differentiation of Murine Neural Stem Cells. Cell Journal (Yakhteh)", 11(4) 2010, 390-99.

Klantar Enayat, **Soheili Fariborz**., Frequency, antimicrobial susceptibility, and plasmid profiles of Escherichia coli pathotypes obtained from children with acute diarrhea, Jundishapur Journal of Microbiology.2011; 4(1): 23-28.

Klantar Enayat, Torabi Vahidah., Salimizand Heiman., **Soheili Fariborz**., Incidence of nosocomial infections caused by P. aeruginosa among burn patients at Kurdistan province. The Southeast Asian Journal of Tropical Medicine and Public Health. 2012 May 1; 43(3):712.

Klantar Enayat, Torabi Vahidah, Salimizand, Heiman, **Soheili Fariborz.**, First Survey of Metallo- β–Lactamase Producers in Clinical Isolates of Pseudomonas aeruginosa from a Referral Burn Center in Kurdistan Province. Jundishapur Journal of Natural

Pharmaceutical Products.2012;7 (1):23-26.

Shakouri Arash, Javanmard, Omelila, **Soheili Fariborz**., Antibacterial Effect of Different Extraction from Organs Sea Urchin, Echinometra Mathaei in Chabahar Beach. Journal of Marine Biology. Ahvaz. Volume 7, Issue 1 (5-2015), 73-Volume 7, Issue 1 (5-2015), 73-82.

Gilan Attaran Fariman, Nasrin Panahloo, **Soheili Fariborz**., Morphology and Molecular Assessment of Two Seastars Species (echinodermata: Asteroidea: Asterinidae) from Chabahar Coastal (oman Sea) Volume 8, Issue 1 (7-2018) [Farsi

Presentations

Soheili F, Heydarikhorneh N, Chen H, Stewart A., Bisphosphonate therapy worsens arterial calcification at *MgpKO* mice. Canadian Lipid & Vascular Summit, Sep 2023

Soheili F, Heydarikhorneh N, Stewart A., how does 9p21.3 contribute to coronary arterial calcification? Cardiovascular Research Day, April 2023

Soheili F, Heydarikhorneh N, Chen H, Stewart A., Bisphosphonate therapy worsens arterial calcification at *Mgp*KO mice. 66th Annual Canadian Society for Molecular Biosciences Meeting (CSMB 2023)

Soheili F, Heydarikhorneh N, Stewart A., Bisphosphonate therapy worsens arterial calcification at
*Mgp*KO mice. Toronto Ottawa Heart Summit, June 2023

Soheili F, Heydarikhorneh N, Stewart A., Bisphosphonate therapy worsens arterial calcification at *Mgp*KO mice. Toronto Ottawa Heart Summit, June 2022

Soheili F, Heydarikhorneh N, Stewart A., Bisphosphonate therapy worsens arterial calcification at *Mgp*KO mice. BMI Scientific Symposium, May 2022,

Soheili F, Heydarikhorneh N, Chen H, Stewart A., Bisphosphonate therapy worsens arterial calcification at *Mgp*KO mice. 25th Toronto Ottawa Heart Summit, June 2021

Soheili F, Dolatabadi F., Frequency of IVS II-1 β-thalassemia mutation in Baloch population of Chabahar city. 3rd international and 15th Iranian Genetics congress. May 13-15, 2018.

Asadollahi V, Soheili F., Neonate Mouse Liver Condition Medium Differentiate Mesenchymal Stem Cells Derived from Amniotic Membrane Placenta into Hepatocyte-like Cells In-vitro. The 2nd International and 4th National Congress of Wound Healing and Tissue Repair. October 25- 27th ,2017

Soheili F., Progress in applications of induced pluripotent stem cell technology. 1st International Joint Conference on New Trends in Biotechnology. April 18-19, 2017
Soheili F., Expression of GATA4, NKX2.5 and OCT4 Genes in Bone Marrow Stem Cells Treat with Algae Extract. International Congress on Stem Cells and Regenerative Medicine 20-22 May 2015 Mashhad, Iran

Soheili F, Heidary N., Comparison of Mesenchymal Stem Cell Isolation Efficiency from Murine Bone Marrow Cells, and Compact Bone. International Congress on Stem Cells and Regenerative Medicine 20-22 May 2015 Mashhad, Iran

Ghafari M, Taheri A, Soheili F, Cytotoxic activity marine algae Sargassum glaucescens coasts of Chabahar on breast cancer cell lines. 26th annual congress of Cancer institute of Iran.25 – 27 November. 2015.

Soheili F, Heidary N., TBX5 gene mutation of exon 6 in non-syndromic congenital heart disease by HRM.18th National and 6th International Congress of Biology in Iran, 26-29 August 2014. Kharazmi University

Shakouri A, Javanmardi O, Soheili F., Antibacterial activity of extract tissues of sea urchin Echinometra mathaei in Chabahar coastal area.18th National and 6th International Congress of Biology in Iran, 26-29 August 2014. - Kharazmi University

Kalantar E, Soheili F., “Frequency of Escherichia coli Pathotypes Obtained from Children with Acute Diarrhea, Northern Conference on Travel Medicine Hamburg May 26 - 29, 2010 (NECTM 2010 in Hamburg)

Soheili F., Galadari H., Identification of a novel missense Mutation in the p53 gene in Iranian Patients with hepatocellular carcinoma. European Human Genetics May 23 – 26, 2009 Vienna, Austria

Soheili F, Galadari H, Mohammadi E., The Suitability of DNA extraction from Archival formalin- fixed paraffin-embedded tissue sections for retrospective genetic toxicology studies.9th Iranian toxicology conference, May 15-17,2007

Soheili F., Galadari H., Pathogenic Mutations analysis of P53 gene in patients affected with hepatocellular carcinoma. The 2nd international congress of biochemistry and

molecular biology. Oct 29-Nov 1,2007

Soheili F., Galadari H., Investigation of the Use of Multiplex-nested-RT-PCR as a Quick Recognition of Common Translocations in Children Leukemia in Khuzestan province. The 2nd international congress of biochemistry and molecular biology. Oct 29-Nov 1,2007

Soheili F, Galadari H., "249ser p53 mutation in archival samples of patient with HCC from Iran.19th Asia pacific

GRADUATE THESIS ADVISOR

Medical University of Kermanshah, Iran

2018, Niloufar Heydari, Differential methylation status of H19 and MEST loci after human sperm cryopreservation from oligospermic patients

Chabahar Maritime University, Iran

2017 Zainab Bavi
Evaluation of the cytotoxic effects of algae extract Acanthophora spicifera and Padina thivyi and DNA fragmentation on cancer cells

2017 Mahboobeh Dini
Evaluation of antioxidant properties and cytotoxic effects of algae extract Sargassum glaucescens acerosa Gelidiella

2016 Javanmard Omelila
Antibacterial activity of sea urchin Echinometra tissues extracts

2016 Mohbeali Anoshirvani The mechanism of interaction of marine anti-cancer medicine with DNA through computational methods

2015 Nasrin Panahloo
Morphology and molecular assessment of two species Sea stars Genus

Medical University of Kermanshah, Iran

2011 Fatemeh Dahmardeh Nkx2.5 gene mutation in congenital heart defects (MSc; 2010)

UNDERGRADUATE THESIS SUPERVISOR

Chabahar Maritime University, Iran

2017 Faezeh Dolatabadi
Frequency of IVS II-1 β-thalassemia mutation in Baloch population

2017 Abdolghafor Houti Incidence of β-thalassemia and α -thalassemia in south of Iran

JOURNAL REVIEWER (34 Articles)

https://www.webofscience.com/wos/author/record/AGP-0393-2022

2021-2023
Cancer Cell International, spring nature, in progress (10)
Anti-Inflammatory & Anti-Allergy Agents in Medicinal Chemistry J

2020-2021
Molecular Medicine Reports - Spandidos Publications (1)
Zahedan Journal of Research in Medical Sciences (1)
Anatolian Journal of Cardiology (1)

2019
The Eurasian Journal of Medicine (1)
Journal of Cellular Biochemistry (1)
Zahedan Journal of Research in Medical Sciences (2)
J Kurdistan University of Medical Sciences (SJKUMS) (2)

2018
International Journal of General Medicine (2)
Zahedan Journal of Research in Medical Sciences (3)
J Kurdistan University of Medical Sciences (SJKUMS) (2)

2012-2017
J Kurdistan University of Medical Sciences (SJKUMS) (7)

RELATED PROFESSIONAL EXPERIENCE

2023-present
Member of Canadian Society for Molecular Biosciences (CSMB)

2023-present
Canadian Trainee representee in Communications and Publications Committee
https://csmb-scbm.ca/about-us/csmb-committees/communications-and-publications-committee/

2023-present
Editor board, Frontiers in microbiome: Nutrition, Metabolism, and the Microbiome
https://www.frontiersin.org/journals/microbiomes/editors
2023- present
Editor board, Cancer Cell International, spring nature, in progress
2008-2011
Member of Endocrinology and Genetic Diseases Committee,
Medical University of Kurdistan, Kurdistan, Iran
2009-2011
Representative of Medical Education Development Center (EDC),
Medical Genetic Departments, Medical University of Kurdistan, Kurdistan, Iran
2002-2005
Member of Undergraduate Students' Union, Razi University

VOLUNTEER ACTIVITY

2022-2024 UOHI Trainee Committee Social Coordinator
2022-2024 UOHI Trainee Committee EDI Coordinator
2014-2016 Teaching biology at Summer high school in Chabahar City
2015-2018 Workshops Molecular biology techniques undergraduate students
2023-2024 Canadian Society for Molecular Biosciences (CSMB)